Applications of Strong Gravitational Lensing:
Utilizing Nature's Telescope for the Study of Intermediate to High Redshift Galaxies

by

H.M. Kaushala T. Bandara
B.Sc.H, University of Toronto, 2006

A Dissertation Submitted in Partial Fulfillment of the
Requirements for the Degree of

DOCTOR OF PHILOSOPHY

in the Department of Physics and Astronomy

Applications of Strong Gravitational Lensing:
Utilizing Nature's Telescope for the Study of Intermediate to High Redshift Galaxies

by

H.M. Kaushala T. Bandara
B.Sc.H, University of Toronto, 2006

Supervisory Committee

Dr. D. Crampton, Co-Supervisor
(Department of Physics and Astronomy, National Research Council Canada)

Dr. C. J. Pritchet, Co-Supervisor
(Department of Physics and Astronomy)

Dr. L. Simard, Departmental Member
(Department of Physics and Astronomy, National Research Council Canada)

Dr. J. Willis, Departmental Member
(Department of Physics and Astronomy)

Dr. C. Bradley, Outside Member
(Department of Mechanical Engineering)

Supervisory Committee

Dr. D. Crampton, Co-Supervisor
(Department of Physics and Astronomy, National Research Council Canada)

Dr. C. J. Pritchet, Co-Supervisor
(Department of Physics and Astronomy)

Dr. L. Simard, Departmental Member
(Department of Physics and Astronomy, National Research Council Canada)

Dr. J. Willis, Departmental Member
(Department of Physics and Astronomy)

Dr. C. Bradley, Outside Member
(Department of Mechanical Engineering)

ABSTRACT

This dissertation presents a detailed analysis of the galaxy-scale strong gravitational lenses discovered by the Sloan Lens ACS (SLACS) survey, with the aim of providing new insight into the processes that affect the evolution of galaxies at intermediate and high redshift. First, we present evidence for a relationship between the supermassive black hole mass and the total gravitational mass of the host galaxy, by utilizing the fact that gravitational lensing allows us to accurately measure the inner mass density profile of early-type lens galaxies and their total masses within an aperture. These results confirm that the properties of the bulge component of early-type galaxies and the resulting supermassive black hole are fundamentally regulated by the properties of the dark matter halo. We then utilize the lensing magnification for a detailed study of the photometric properties (luminosity, size and shape) of SLACS background sources and determine the evolution of the disk galaxy luminosity-size relation since $z \sim 1$. A comparison of the observed SLACS luminosity-size relation to theoretical simulations provides strong evidence for mass-dependent evolution of disk

galaxies since $z \sim 1$. Furthermore, a comparison of the SLACS luminosity-size relation to that of a non-lensing, broad-band imaging survey shows that one can probe a galaxy population that is ~ 2 magnitudes deeper by utilizing the lensing magnification. We continue the detailed study of SLACS background sources by combining the lensing magnification with diffraction-limited integral field spectroscopy to derive two-dimensional kinematic, star formation rate and metallicity distributions of gravitationally lensed galaxies at $z > 0.78$. Integral field spectroscopic observations of the Hα emission line properties of a SLACS source galaxy (SDSS J0252+0039), at $z = 0.98$, show that the lensing magnification and adaptive optics advantages can be effectively combined to derive spatially resolved kinematics and star formation rates of compact, sub-luminous galaxies. Finally, we summarize the results of this dissertation and discuss how the powerful advantages of strong gravitational lensing can be utilized to address various questions about galaxy evolution through upcoming surveys and new telescope facilities.

Contents

List of Tables

List of Figures

ACKNOWLEDGEMENTS

There are many people I would like to offer my thanks for their support during my time at the University of Victoria. Without all of you, this dissertation could not have been completed.

First, I want to thank my supervisor, Dr. David Crampton, for taking me on as a PhD student and providing much advice, encouragement and lots of laughter, as we worked through this thesis.

To my co-supervisor, Dr. Chris Pritchet, for your constant support and encouragement throughout my graduate career.

To Dr. Luc Simard, thank you for providing me with the support and encouragement needed to complete my thesis and move forward in astronomy as a postdoctoral researcher.

To Dr. Chien Peng, thank you for being a fantastic mentor and a friend! Your guidance and friendship throughout the past five years meant the world to me. Not to mention the filing cabinet full of chocolates that you let myself and the other graduate students raid at all times.

Thank you to my supervisory committee, Drs. Jon Willis and Colin Bradley, for their constant support and encouragement throughout my graduate program.

Thank you to Dr. Chris Fassnacht for taking the time to be my external examiner.

To my scientific collaborators for stimulating conversations, and providing useful comments on observing proposals and the resulting papers, which improved them all greatly.

To my fellow astronomy grad students and friends, both near and far, for being such a fantastic group of people. Thank you for the scientific discussions, advice of all kinds and so many great events. A special thank you goes to Sheona Urquhart, Millie Maier, Ryan Leaman and Niko Milutinovich for years of enduring friendship

through good times and bad.

To my non-astronomer friends, especially Nate and Celyne McDonald, Justin and Sherry Trupp and Elysia Leung, for restoring the balance in my life.

To ammi and appachchi (mom and dad), I wouldn't be where I am without the two of you. There aren't enough words to express how much I appreciate the love and support you have given me throughout the years.

To my husband Tim, your love, support and wonderfully infectious sense of humour have made my world a very happy place, even when you were stuck in a Canadian naval frigate in the middle of the Pacific ocean.

To malli (brother), my amazing in-laws and my extended family, thank you for your love, support and pride in me throughout my academic career.

Finally, to the great house of Macallan, the producers of Battlestar Galactica and the developers of "I Can Has Cheezburger?", thank you for a great single-malt, an amazing show and the hilarious cat photos. I couldn't have gotten through my PhD or the postdoctoral application process without them.

DEDICATION

To Ammi and Appachchi

Chapter 1

Introduction

1.1 A Brief Prelude

Galaxies, the "building blocks" of the universe, are gravitationally bound systems of stars, stellar remnants, interstellar dust and gas embedded in a much larger dark matter halos. Within the context of ΛCDM cosmology, galaxies are formed hierarchically by mergers of dark matter halos with baryonic matter settling into the gravitational potential well of the resulting merger remnant. As demonstrated by the well-known Hubble Sequence[1], shown in Figure 1.1, galaxies show a variety of morphological types from elliptical galaxies[2] on the left side of the diagram, lenticular galaxies[3] at the fork, to spiral galaxies[4] on the right side. Elliptical galaxies, which typically contain older stellar populations, are also referred to as "early-type" galaxies[5] and spiral galaxies, which contain young stellar populations, are referred to as "late-type" galaxies. Despite the large variation observed in morphological types, galaxies do not appear as arbitrary combinations of properties such as luminosity, size, stellar mass, stellar velocity dispersion, or rotational velocity. Instead, galaxies

[1] Also known as the Hubble Tuning Fork.

[2] Galaxies which are defined by the existence of a predominant spheroidal component, also referred to as the bulge. Therefore, elliptical galaxies are "bulge-dominated".

[3] S0 type galaxy, which has a bulge component embedded in an extended "disk" of stars.

[4] Galaxies that are defined by characteristic disk components, spiral arms and bar components. Therefore, spiral galaxies are "disk-dominated".

[5] A misnomer that stems from Edwin Hubble's original hypothesis that galaxies evolved from left to right of the Hubble Sequence.

typically obey scaling relations such as the luminosity-size relation, size-stellar mass relation, the Fundamental Plane for early-type galaxies or Tully-Fisher relation for late-type galaxies throughout cosmic times (Barden et al. 2005; Shen et al. 2003; Treu et al. 2006; Djorgovski & Davis 1987; Dressler et al. 1987; Tully & Fisher 1977). Understanding the origin and evolution of these scaling relations is a fundamental aspect of the theoretical studies of galaxies, while observational studies of these scaling relations are important testbeds of the standard paradigm of galaxy formation and evolution. Furthermore, observations provide important constraints on the baryonic processes that affect galaxies, such as star formation, instabilities or feedback, which are still poorly understood. *The primary goal of this thesis involves utilizing the naturally provided advantages of strong gravitational lensing to further understand the evolution of various galaxy scaling relations (and in turn, the baryonic processes that affect the evolution of galaxies) throughout the past 8 billion years*[6]. This chapter is organized as follows: §1.2 gives an introduction to gravitational lensing including a brief history, §1.3 discusses the basic mathematical formalism of gravitational lensing, §1.4 discusses the advantages of gravitational lensing, focusing on the traits that are utilized in this thesis, §1.5 introduces the Sloan Lens ACS survey and §1.6 gives an overview of the motivation behind the various projects of this thesis.

[6]Equivalently, since a redshift of $z \sim 1$.

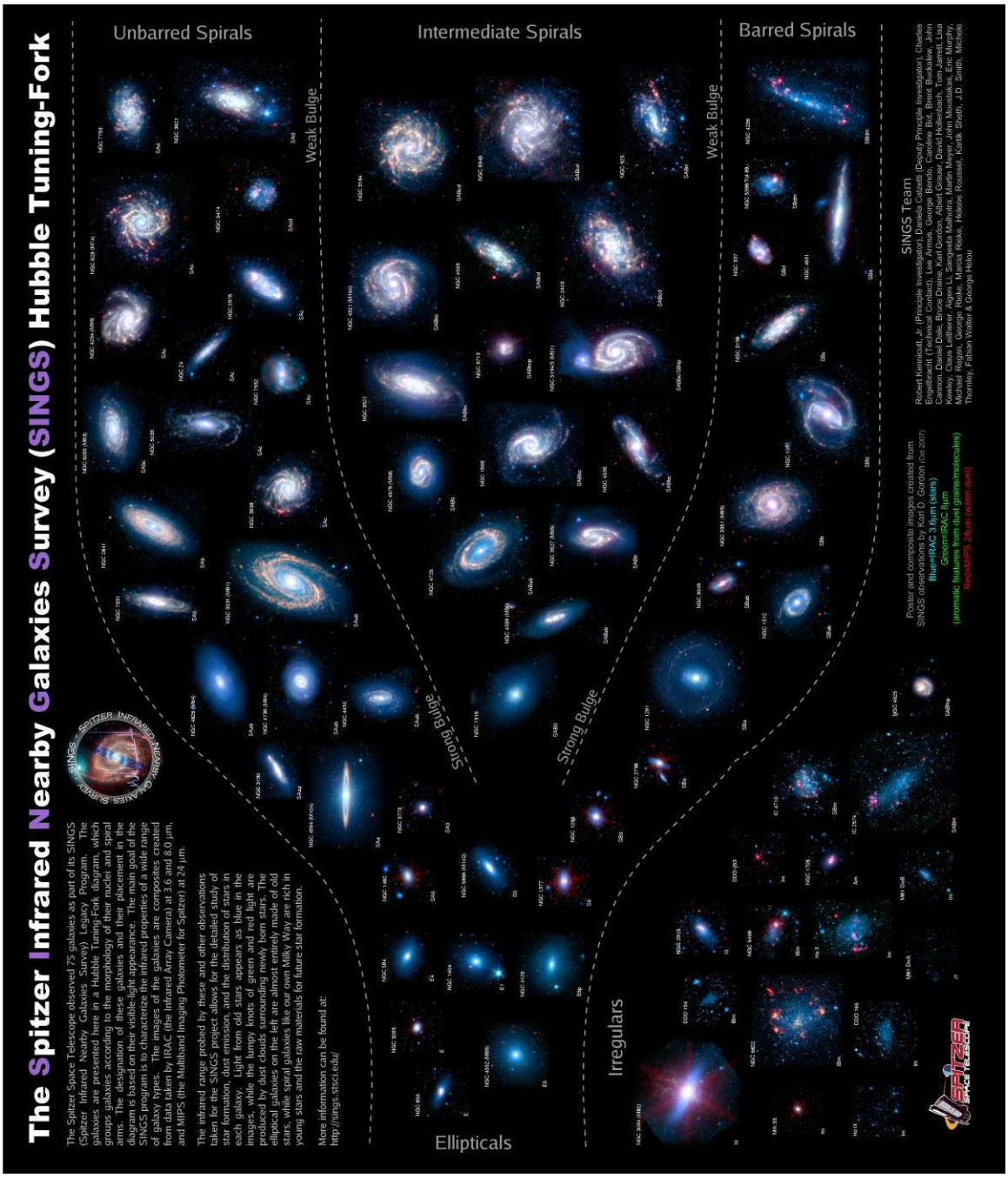

Figure 1.1 The Hubble sequence, rotated 90 degrees counter-clockwise for clarity. The Hubble sequence shown above was constructed using observations of 75 galaxies from the Spitzer Infrared Nearby Galaxies Survey (SINGS). These 75 galaxies were classified as elliptical, lenticular, spiral or irregular according to their morphology from observations in the optical wavelengths. The colour images shown within the Hubble sequence above were constructed from combining imaging observations from three infrared filters: 3.6 μm (blue), 8.0 μm (green), 24 μm (red). **Image Credit: sings.stsci.edu/Publications/sings_poster.html**.

1.2 Gravitational Lensing: A Historical Introduction

One of the predictions of General Theory of Relativity is that light rays are deflected by gravity. The deflection of light rays by the gravitational potential of a massive object, and the resulting observational phenomenon is now commonly known as *gravitational lensing*. Figure 1.2 shows a graphical representation of gravitational lensing, where a light ray propagating from a distant star is deflected when it passes near the limb of the sun. As shown in Figure 1.2, the angular deflection of the light ray causes the apparent position of the star to shift away from the sun.[7] Although gravitational lensing is primarily considered to be a discovery of the 20^{th} century, its theoretical ground work was already in place by the early-19^{th} century. The possibility of gravitational lensing was first explored by various physicists prior to Albert Einstein, including Sir Isaac Newton, Pierre-Simon Laplace and Johann Georg von Soldner. In 1804, Soldner calculated the magnitude of the angular deflection of a light ray passing near the sun using Newtonian physics. In 1915, Einstein fully revised Soldner's work by applying the field equations of General Relativity, which describe the equivalence between the geometry of the space-time continuum and energy density, and calculated that a light ray propagating near the limb of the sun gets deflected by $1\farcs7$. Einstein's result was later confirmed by Sir Arthur Eddington and Frank Watson Dyson, who measured the apparent angular shift of stars close to the limb of the sun during a total solar eclipse in 1919. The agreement between Einstein's calculations and observational evidence provided by Dyson and Eddington was considered to be conclusive evidence in support of the General Theory of Relativity by their contemporaries.

In addition, Eddington further postulated that light rays propagating from the distant object can take multiple paths to the observer under certain conditions. Thus, the gravitational potential of an intervening massive object can deflect the light rays of a single distant object to form multiple images (also referred to as *angular image splitting*). During the following two decades, both Daniel Chwolson and Einstein investigated the possibility of observing angular image splitting by stellar-mass gravitational lenses (i.e. stars lensing stars). In 1936, Einstein concluded that observing the image splitting phenomena by a stellar-mass lens is unlikely since the angular

[7] The angular shift of the observed position shown in this illustration is greatly exaggerated.

shift caused by a less massive lens is too small to be resolved by an optical telescope.

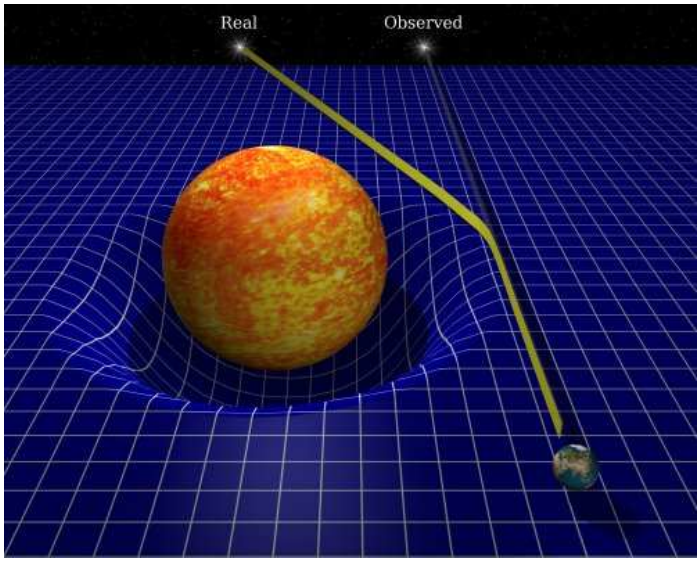

Figure 1.2 An illustration of gravitational lensing. A light ray propagating from a distant star is deflected due to the gravitational potential of the Sun. Therefore, the apparent position of the distant star as perceived by an observer on earth (by following the deflected ray) is shifted by an angle that can calculated using the principles of the General Theory of Relativity. **Image Credit: www.robertdalsanto.com/cosmology.php**

However, research initiated by the Swiss astronomer Fritz Zwicky elevated gravitational lensing from a novel concept to a major sub-field of astronomy today. In 1937, Zwicky applied the virial theorem to the Coma cluster of galaxies to derive the gravitational masses of its individual constituents. Zwicky's calculations yield gravitational masses of $\sim 4 \times 10^{11}\,\mathrm{M}_{\odot}$ for the galaxies in the Coma cluster, which were $\sim 400\times$ more massive than the galaxy masses inferred from the luminous matter component (at that time). Zwicky referred to the unseen matter component of the galaxies as *dunkle materie*, commonly known as dark matter, and postulated that galaxies can act as massive gravitational lenses that produce widely separated, multiple images of background objects (i.e. more distant galaxies) which can be resolved with optical telescopes. Another prediction by Zwicky was that galaxy-scale gravitational lenses not only act as further testbeds of the General Theory of Relativity but also magnify the observed angular size of the background galaxy images. Therefore, a suitably massive gravitational lens can act as a "cosmic telescope" by enabling the discovery of intrinsically faint and distant galaxies, which would otherwise be undetected, through magnification. Zwicky's research was very comprehensive such that

he even calculated the probability of galaxy-scale lensing to be in the order of $\sim 1\%$ for a background galaxy at higher redshifts.

Throughout the late 20^{th} century, all of the predictions made by Zwicky have been observationally confirmed. Today, astronomers observe a large range of the manifestations of gravitational lensing, which include stellar-mass gravitational lenses in the Milky Way (also known as *microlensing*); extragalactic gravitational lenses (individual galaxies, galaxy groups or galaxy clusters deflecting the light from background galaxies) and gravitationally lensed quasar host galaxies (a special case of extragalactic gravitational lensing) etc. Some of the first discoveries of extragalactic gravitational lenses are summarized below.

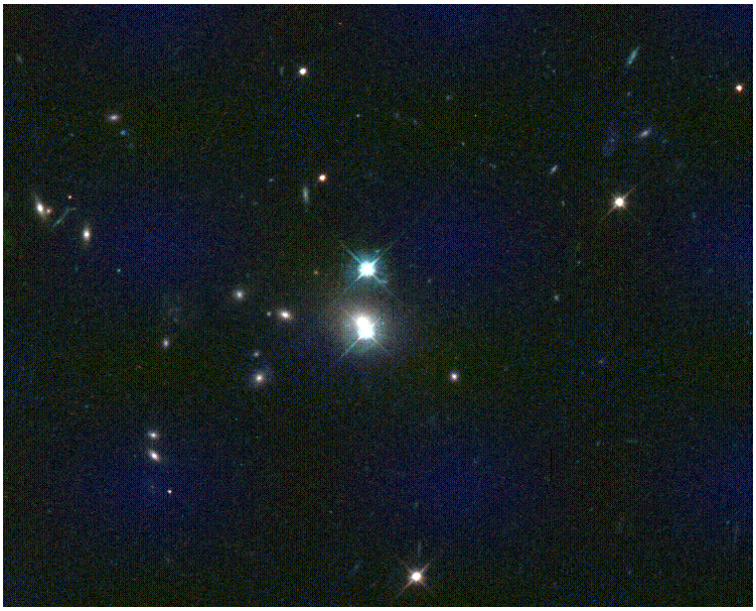

Figure 1.3 A colour image of QSO 0957+561, the first discovery of a gravitational lens. This gravitational lens consists of a galaxy at $z = 0.36$ deflecting the light coming from a quasar at $z = 1.41$ and forming multiple images. Due to the double images of the background quasar, separated by $6\farcs0$, this system is also known as the "Twin Quasar". This image is a composite of three, 2300s observations taken in the V (551 nm) and I (806 nm) filters. **Image Credit: www.astr.ua.edu/keel/agn/q0957.html**

Walsh et al. (1979) discovered the first example of an extragalactic gravitational lens named QSO 0957+ 561, where the gravitational potential of a foreground galaxy forms multiple images of a background quasar. Quasars, highly energetic active galactic nuclei (AGN), are ideal background objects for the discovery and study of extragalactic gravitational lenses for the following reasons: they are distant objects (AGN

activity peaks around the $z \sim 1.5 - 3$ epoch, when the universe was only $\sim 2 - 4$ Billion years old), thus, are more likely to be gravitationally lensed by an intervening galaxy; they are amongst the most powerful and luminous objects in the universe and are easily detected, even at cosmological distances. Figure 1.3 shows QSO 0957+561, which consists of twin images of a gravitationally lensed quasar separated by 6". Evidence that confirm QSO 0957+561 is indeed a gravitationally lensed quasar, not a binary quasar system, are as follows: spectra of the twin images are identical; the flux ratios of the twin images are similar in both optical and radio wavelengths and a foreground galaxy is present between the twin images[8] (the intervening galaxy is not very clear in Figure 1.3 since the luminosity of the twin images overwhelm the luminosity of the foreground galaxy).

Figures 1.4 and 1.5 show the first examples of one of the most spectacular manifestations of gravitational lensing phenomenon: cluster-scale gravitational lenses. Galaxy clusters, the largest gravitationally bound structures in the universe, can act as gravitational lenses that form strongly distorted and elongated *arc*-like images of background galaxies. The formation of luminous arcs due to the gravitational potential of a galaxy cluster requires a special line-of-sight (LOS) alignment between the observer, the galaxy cluster and the distant background galaxy. The first discoveries of giant luminous arcs were made in the galaxy clusters Abell 370 and CL 2244 (Soucail et al. 1987a,b; Lynds & Petrosian 1986), as shown in Figures 1.4 and 1.5 respectively. In addition, Figure 1.4 is also an excellent example of the observational effects of both strong and weak regimes of gravitational lensing. The examples shown so far correspond to the strong regime of the gravitational lensing phenomena (commonly known as *strong gravitational lensing*), which forms strongly distorted and highly magnified multiple images of the background object. The giant luminous arc on the top-right quadrant of Figure 1.4 is caused by strong gravitational lensing; however, we also observe small, blue arcs (commonly known as *arclets*) scattered at various radii from the giant elliptical galaxy in the center of the cluster. Galaxy clusters also weakly distort the shapes of background galaxies that are located at larger projected radii from the cluster center (i.e. the background galaxy, the centroid of the cluster gravitational potential and the observer are not aligned along the LOS), which correspond to the weak regime of gravitational lensing. This effect is referred

[8]The primary lensing object of QSO 0957+561 is a massive early-type galaxy, which is embedded in a galaxy cluster. The large angular separation of the twin images is caused by the additional gravitational potential of the galaxy cluster.

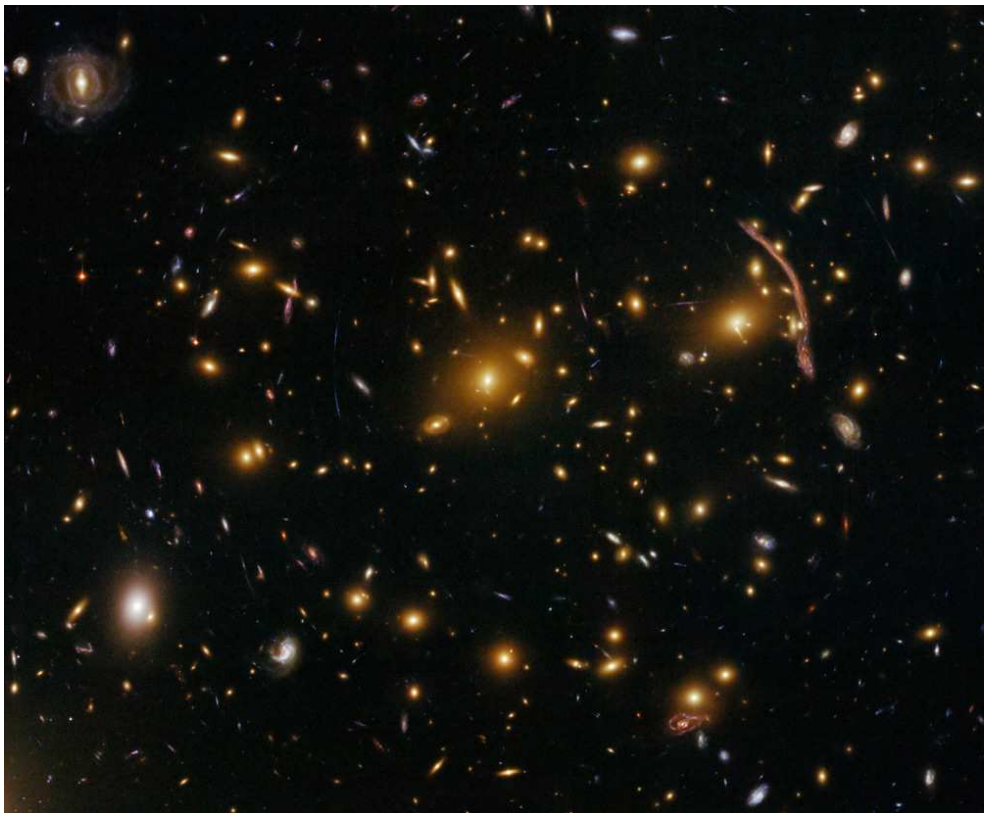

Figure 1.4 A Hubble Space Telescope (*HST*) image of the galaxy cluster Abell 370 (at $z = 0.38$), which shows excellent examples of both regimes of gravitational lensing. The bright arc near the giant elliptical galaxy, on the top-right quadrant of the image, corresponds to an example of strong gravitational lensing by galaxy clusters, where the light propagating from a background galaxy is deflected to form a strongly distorted image. Upon closer inspection of the image, one can discern faint, blue "arclets" at larger radii from the giant, elliptical galaxy at the centre of the image. This phenomenon is known as weak gravitational lensing, where the observed shapes of the background galaxies are weakly distorted (on the order of a few percent) due to the gravitational potential of the intervening galaxy cluster. **Image Credit** : **hubblesite.org/gallery/album/pr2009025ao/**.

to as *weak gravitational lensing*, as evident in Figure 1.4.

The final example of a first discovery shown in this section corresponds to an extremely useful manifestation of strong gravitational lensing: the *Einstein ring*. An Einstein ring is typically caused by a galaxy-scale gravitational lens that deflects the light propagating from a background galaxy. A complete Einstein ring occurs when the background source, the centroid of the foreground galaxy's gravitational potential and the observer align along a common axis, referred to as the *optical axis*. If the background source is slightly offset from the optical axis, a partial Einstein ring is formed. The geometry of Einstein rings will be discussed in detail in the following

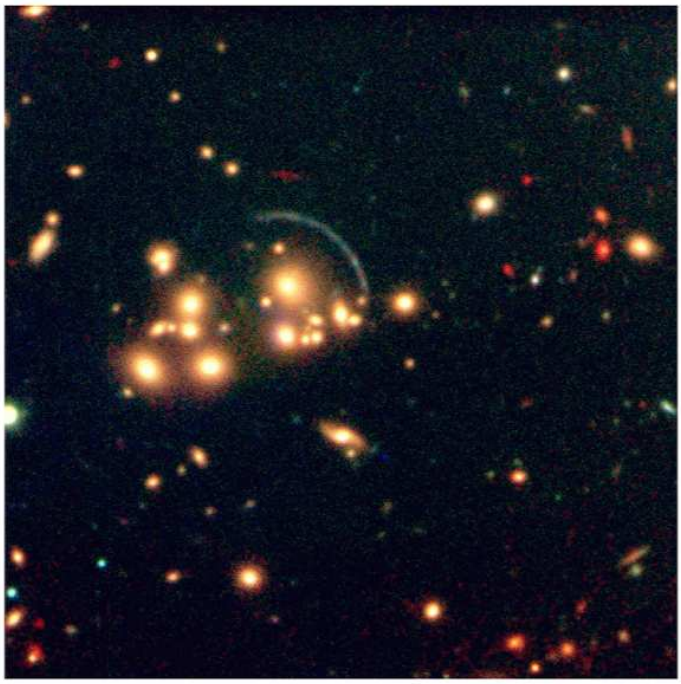

Figure 1.5 A composite image of the galaxy cluster CL2244-02 (at $z = 0.3$), observed with the Very Large Telescope (VLT), using K_s (2160 nm), V (551 nm) and R (658 nm) filters. The bright blue arc near the top-right of the galaxy cluster is formed by a gravitationally lensed galaxy at $z = 2.24$. **Image Credit: www.eso.org/public/images/eso9856d/.**

sections. Figure 1.6(a) and (b) show images of MG1131+0456 and B1938+666, which correspond to the first discovery of a partial Einstein ring (Hewitt et al. 1988) and one of the first discoveries of a complete Einstein ring (King et al. 1998) respectively. Figure 1.6(a) is a radio image of MG1131+0456 observed with the Very Large Array (VLA). The partial Einstein ring of MG1131+0456 is a gravitationally lensed image of a quasar host galaxy. Figure 1.6(b) is a composite image of B1938+666 (initially observed using the MERLIN radio telescope), which consists of *HST* imaging in the F555W (V band), F814W (I band), F160W (H band) filters and Keck II telescope adaptive-optics assisted imaging in the H and K′ bands (Lagattuta et al. 2012).

The following section of this chapter provides a summary of the gravitational lensing formalism. The content is based on three extensive reviews (amongst many) of the lensing theory: Narayan & Bartelmann (1999), Kormann et al. (1994), Keeton (2001a) (and references within). Due to the large overlap of the material, each review is not individually referenced, unless noted otherwise.

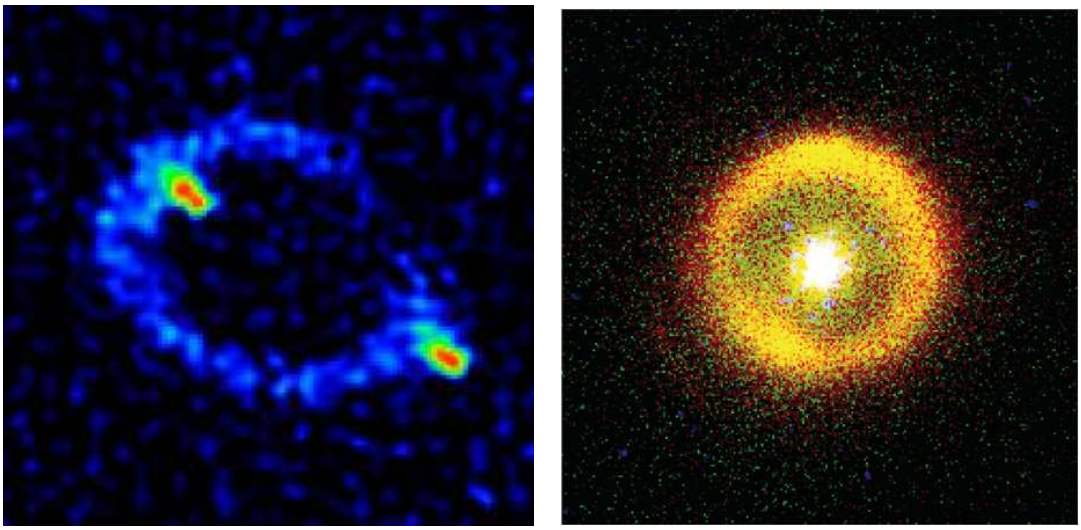

Figure 1.6 *Left:* A radio observation of MG1131+0456, the first discovery of a partial Einstein ring, taken with the Very Large Array (VLA). The Einstein ring feature, with the elongated bright spots at each end, corresponds to a background quasar that is gravitationally lensed by an intervening galaxy. **Image Credit: www.nrao.edu/pr/2000/via20/background/ering**. *Right:* A composite image of the gravitational lens B1938+666 (Lagattuta et al. 2012), one of the first discoveries of a complete Einstein ring (King et al. 1998). The initial discovery of B1938+666 was made with the MERLIN radio telescope array; however, the image shown above corresponds to recent optical and NIR observations of the system with *HST* (in the V, I and H bands) and Keck II adaptive-optics assisted (in the H and K$'$ bands) imaging.

1.3 Gravitational Lensing: The Basics

Although a treatise of the propagation of light in a curved space-time continuum is a complicated theoretical problem, the case of gravitational lensing is simplified due to several assumptions. To derive the lensing formalism, we assume that the universe is homogenous and isotropic (as described by the Friedmann-Lemaitre-Robertson-Walker metric) and the matter inhomogeneities that cause the deflection of light are strictly local perturbations. Therefore, the overall geometry of a gravitational lens can be broken down into three zones as follows:

1. The zone where the light propagates from the background object to the vicinity of the gravitational lens through unperturbed space-time (**zone 1**).

2. The zone near the gravitational lens where the light is deflected (**zone 2**).

3. The zone where the deflected light propagates through unperturbed space-time to the observer (**zone 3**).

Furthermore, to derive the deflection of light in zone 2, we can assume a locally-flat, Minkowskian space-time that is weakly perturbed by the Newtonian gravitational potential of the lens. The two assumptions discussed above are satisfied in all cases of gravitational lensing. For example, consider the galaxy scale gravitational lens SDSS J0252+0039, which consists of a massive, early-type galaxy at $z_{\rm foreground} = 0.28$ deflecting the light from a background galaxy at $z_{\rm background} = 0.98$. The distances from the background source to the lens and from the lens to the observer are ~ 1.1 Gpc and ~ 0.9 Gpc respectively, ~ 4 orders of magnitude larger than the size of a typical giant elliptical galaxy. Thus, zone 2 is restricted to a small local segment of the total light path.

1.3.1 Lensing Formalism

Given the assumptions above, the deflection of light in a locally-flat, Minkowskian space-time that is weakly perturbed a Newtonian gravitational potential can be described in terms of the refractive index[9], n', (Schneider et al. 1992) as shown below.

$$n' \;=\; 1 - \frac{2}{c^2}\,\mathbf{\Phi} = 1 + \frac{2}{c^2}\,|\mathbf{\Phi}| \tag{1.1}$$

Furthermore, the deflection of light in a Newtonian potential is equivalent to the deflection of light by a prism in geometrical optics as shown in Figure 1.7. The Newtonian potential (Φ) in equation 1.1 is negative and defined such that is approaches zero at infinity. In geometrical optics, a refractive index of $n' > 1$ indicates that the effective speed of light inside the prism is reduced to $v = c/n'$, as shown in Figure 1.7. Similarly, the effective speed of light is reduced within the gravitational potential in comparison to the free vacuum as shown below.

$$v \;=\; \frac{c}{n'} \;\simeq\; c - \frac{c}{n'}|\mathbf{\Phi}| \tag{1.2}$$

In gravitational lensing, the deflection angle ($\vec{\hat{\alpha}}$) of light is the integral of the gradient of n' perpendicular to the light path (Narayan & Bartelmann 1999) as shown

[9]The refractive index is typically denoted as n; however, it is denoted as n' in this thesis to avoid confusion with the Sérsic index of a galaxy, a parameter that will be introduced in the following chapters. The prime does *not* imply a derivative of the refractive index.

below. As discussed in the previous section, the deflection angles in gravitational lensing are very small; therefore, instead of integrating $\vec{\nabla}_\perp n'$ along the deflected ray, it is computationally simpler to integrate along the initial unperturbed light ray with the same impact parameter.

$$\vec{\hat{\alpha}} \;=\; -\int \vec{\nabla}_\perp \, n' \, dl \;=\; \frac{2}{c^2} \int \vec{\nabla}_\perp \, \Phi \, dl \tag{1.3}$$

Equation 1.3 refers to the case where the light from the background source is deflected by the gravitational potential of a *single* lens. In the case of multiple lenses along the line-of-sight, the deflected light ray from the first lens becomes the unperturbed light for the second lens (and so on for an arbitrary number of lenses).

The Case of a Point Mass Lens

After establishing the general form of the deflection angle for the propagation of light in a locally-flat space-time, one can compute the deflection angle for the simple case of a point mass (M) lens, whose Newtonian potential is defined as,

$$\mathbf{\Phi}(b, z) \;=\; -\frac{GM}{(b^2 + z^2)^{1/2}} \tag{1.4}$$

where b is the impact parameter of the unperturbed light ray (from zone 1) and z is the distance along the unperturbed light ray from the point of closest approach. A graphical illustration of lensing by a point mass, and the parameters b and z, is shown in Figure 1.8. Therefore, the gradient of $\mathbf{\Phi}(b, z)$ perpendicular to the unperturbed light path is,

$$\vec{\nabla}_\perp \mathbf{\Phi}(b, z) \;=\; \frac{GM\vec{b}}{(b^2 + z^2)^{3/2}} \tag{1.5}$$

where $\vec{b}$ is orthogonal to the unperturbed light ray and points towards M. Inserting equation 1.5 into equation 1.3 then yields,

$$\vec{\hat{\alpha}} \;=\; \frac{2}{c^2} \int \vec{\nabla}_\perp \, \Phi \, dz \;=\; \frac{2}{c^2} \int \frac{GM\vec{b}}{(b^2 + z^2)^{3/2}} dz \;=\; \frac{4GM}{c^2 b} \tag{1.6}$$

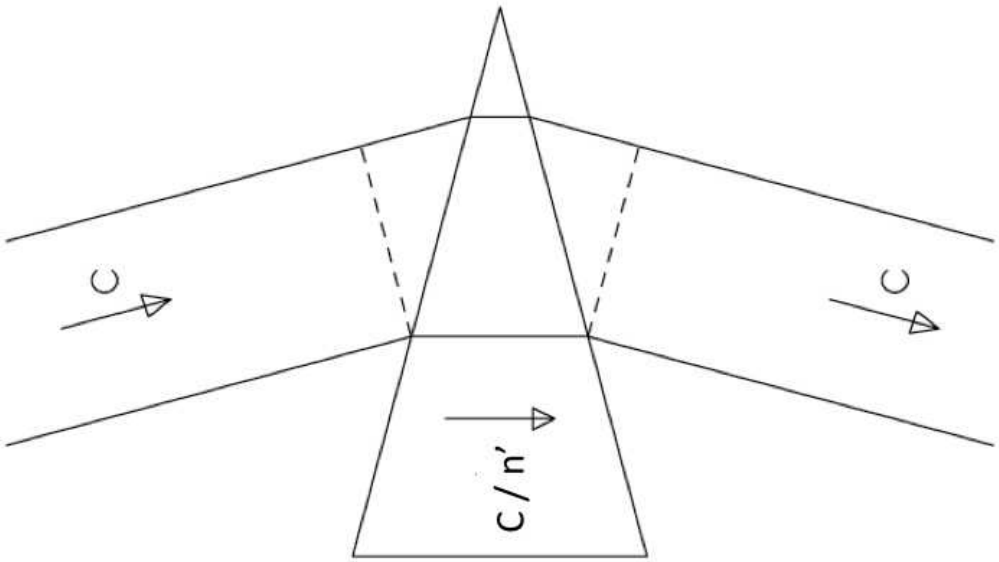

Figure 1.7 Deflection of light inside a prism (Figure 2 of Narayan & Bartelmann (1999)). A refractive index of $n' > 1$ inside the glass prism reduces the effective speed of light to $v = c/n'$, which causes the light to bend around the thick end of the prism.

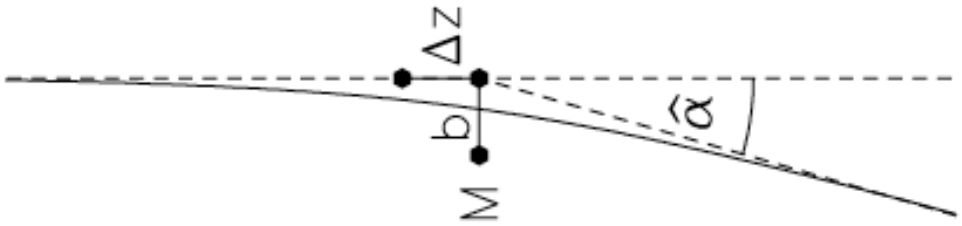

Figure 1.8 Deflection of light by the gravitational potential of a point mass (M) lens (Figure 3 of Narayan & Bartelmann (1999)). The unperturbed ray, propagating from the left, passes the point mass lens (M) at the impact parameter (b) and gets deflected by an angle, $\hat{\alpha}$. Most of the lensing occurs within $\Delta z \sim \pm b$.

The Case of an Extended Lens

We now consider the case where the point mass lens is replaced by a lens with distributed mass, such as an individual galaxy, a galaxy group or a cluster. As shown in Figure 1.8, the deflection of light occurs within $\Delta\, z \sim \pm b$, which is several orders of magnitude smaller than the light travel paths between the background source, lens and the observer. Therefore, the linear diameter of even the largest mass distribution (such as a galaxy cluster) can be considered to be "thin" in comparison to the light paths' length through unperturbed space-time and mass distribution of the lens can be replaced with a "mass sheet" orthogonal to the LOS.

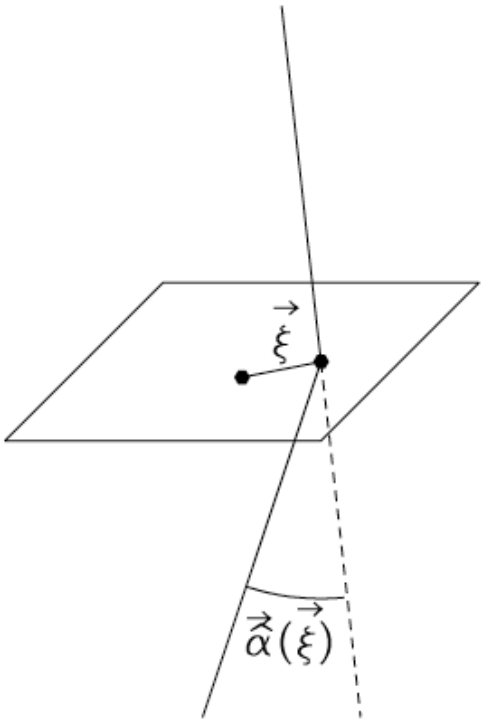

Figure 1.9 An illustration of the *thin lens approximation* (Figure 4 of Narayan & Bartelmann (1999)). An extended mass-distribution, such as a galaxy cluster, can be replaced by a mass-sheet orthogonal to the LOS of the observer since the light travel paths through unperturbed space-time are several orders of magnitude larger than the linear extent of a galaxy cluster. A light ray that intersects the mass-sheet at $\vec{\xi}$ gets deflected by an angle of $\vec{\hat{\alpha}}(\vec{\xi})$.

This is called the *thin lens approximation* and the mass sheet is commonly referred to as the lens plane. The lens plane is illustrated in Figure 1.9, where $\vec{\xi}$ corresponds to a two-dimensional vector. As shown in Figure 1.9, a light ray that intersects the lens plane at $\vec{\xi}$ is deflected by an angle of $\vec{\hat{\alpha}}(\vec{\xi})$. The mass sheet is characterized by the surface mass density as shown below:

$$\Sigma(\vec{\xi}) \;=\; \int \rho(\vec{\xi}, z)\, dz \qquad (1.7)$$

The deflection angle at position $\vec{\xi}$ is, in general, a two-dimensional vector that corresponds to sum of the deflections due to all the mass elements in the lens plane.

$$\vec{\hat{\alpha}}(\vec{\xi}) \;=\; \frac{4G}{c^2} \int \frac{(\vec{\xi} - \vec{\xi'})\Sigma(\vec{\xi'})}{\left|\vec{\xi} - \vec{\xi'}\right|^2} d^2\xi' \qquad (1.8)$$

In the special case of circular symmetry, calculation of the deflection angle can be simplified to a one-dimensional problem by shifting the origin of $\vec{\xi}$ to the center of symmetry. The deflection angle in this case is,

$$\vec{\hat{\alpha}}(\vec{\xi}) \;=\; \frac{4GM(\xi)}{c^2\xi} \tag{1.9}$$

where ξ is the distance from the center of symmetry and M(ξ) is the mass enclosed within ξ defined by,

$$M(\xi) \;=\; 2\pi \int_0^{\xi} \Sigma(\xi')\xi' d\xi'. \tag{1.10}$$

1.3.2 The Lens Equation

The geometry of a typical gravitational lens system is shown in Figure 1.10. The gravitational lens (for an arbitrary mass distribution), shown as the large filled circle, will hereafter be referred to as the *deflector* or the *lens*[10]. The distant object, that is being gravitationally lensed, will hereafter be referred to as the *source*[11]. The lens plane (given by equations 1.7 and 1.8) and equivalently the source plane and the observer plane are also shown in Figure 1.10. The axis connecting the centroid of lens mass distribution and the observer is the optical axis.

The angles α, α_{red}, β and θ correspond to the deflection angle of the light ray, the reduced deflection angle, the angular position of the source (measured w.r.t the optical axis) and the angular position of the image (open circles, measured w.r.t the optical axis). The source and image(s) positions are related by the equation,

$$\beta \;=\; \theta - \alpha_{red}(\theta). \tag{1.11}$$

Equation 1.11 is commonly known as the *lens equation* and, in its general form, is non-linear. Therefore, multiple images (θ) can form for a single source position (β), as shown in Figure 1.10. The variables D_L, D_{LS} and D_S are angular-diameter distances, such that the Euclidean relation $separation = angle \times distance$ holds (and

[10]For extragalactic applications, such as those discussed in the proceeding chapters of this thesis, the massive object will be referred to as the *deflector galaxy*, or more commonly, the *lens galaxy*.

[11]For extragalactic applications, referred to as the *source galaxy*.

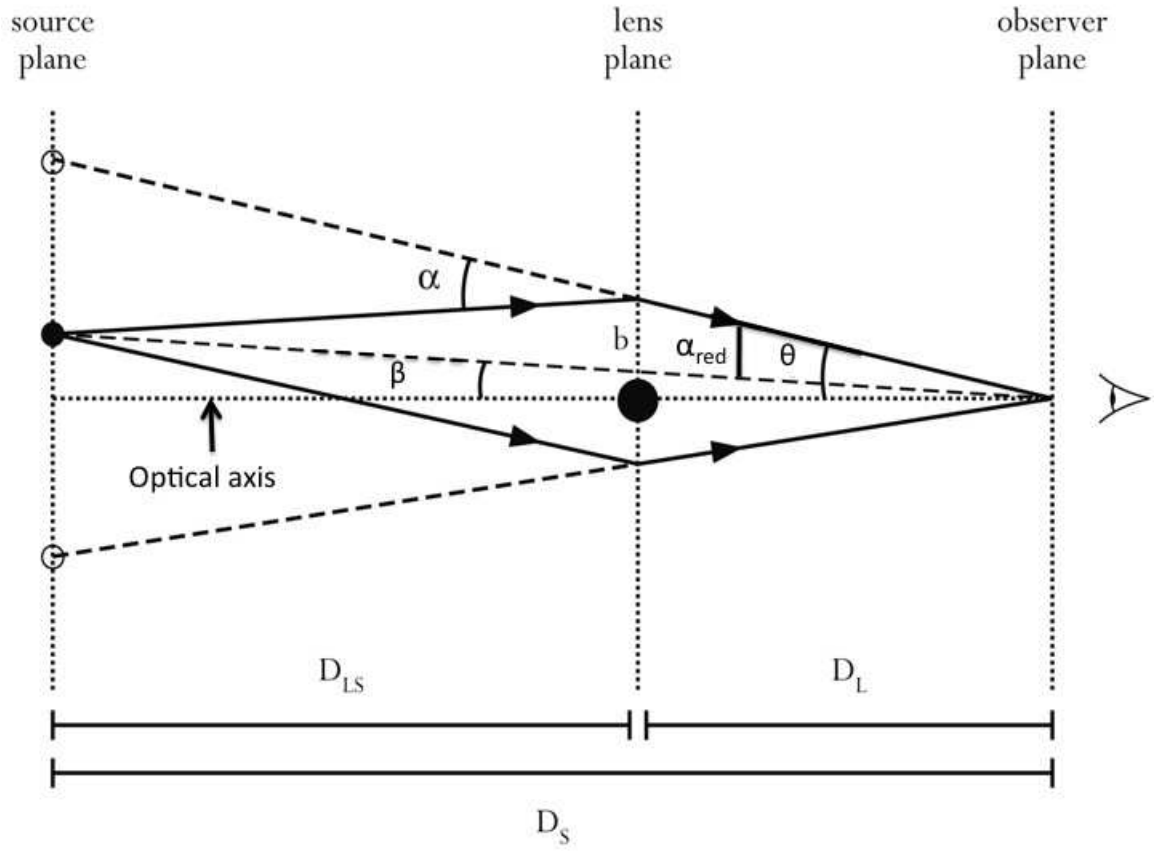

Figure 1.10 The geometry of a typical gravitational lens. Light rays from the background source passing at an impact parameter (b) gets deflected by an angle α. The lens of an arbitrary mass-distribution, is shown by the equivalent lens plane. The axis connecting the centroid of the lens mass-distribution and the observer is the optical axis. The distances between the observer, lens and the source (D_L, D_{LS} and D_S) are defined as angular diameter distances. **Image Credit : en.wikipedia.org/wiki/Einstein_radius**.

$\mathrm{D_{LS}} \neq \mathrm{D_S} - \mathrm{D_L}$). Using the small angle approximation, one can define the following relations between the angles and distances in Figure 1.10:

$$\alpha_{red} = \frac{D_{LS}}{D_S}\,\alpha;\; b = \theta D_L. \tag{1.12}$$

For a circularly symmetric projected mass distribution (ex: a point mass lens), the deflection angle is described by equation 1.6 and rewritten below in terms of the variables shown in Figure 1.10.

$$\alpha = \frac{4GM(<b)}{c^2 b} \tag{1.13}$$

Substituting equation 1.12 and 1.13 into the lensing equation and rearranging yields,

$$\theta^2 - \theta\beta - \frac{4GM}{c^2}\frac{D_{LS}}{D_S D_L} \;=\; 0. \tag{1.14}$$

The quadratic form of equation 1.14 indicates that, for a point mass lens, there are two images of the source:

$$\theta \;=\; \frac{1}{2}\left(\beta \pm \sqrt{\beta^2 + \frac{16GM}{c^2}\frac{D_{LS}}{D_S D_L}}\right) \tag{1.15}$$

Since a point mass lens is circularly symmetric, when a source lies exactly on the optical axis (i.e. $\beta = 0$) it is imaged as a ring. Setting $\beta = 0$ in equation 1.14, we can derive the radius of the ring,

$$\theta_E \;=\; \left[\frac{4GM(<\theta_E)}{c^2}\,\frac{D_{LS}}{D_L D_S}\right]^{1/2} \tag{1.16}$$

This radius is most commonly known as the *Einstein radius* and gravitational lens systems that show ring images are referred to as *Einstein rings*[12]. The Einstein radius is a very useful quantity that determines the geometry of the observed images of a lens system. For example, the angular separation of multiple images is typically on the order of $2\theta_E$. In many cases, the Einstein radius corresponds to the boundary where a source is either singly imaged or multiply imaged. If a source is located inside θ_E (w.r.t the optical axis), it is highly magnified; however, if the source is located outside of the θ_E boundary it is only magnified slightly.

The Case of a Singular Isothermal Sphere

A simple description for the mass distribution of a galaxy is the case where the stars, gas and other mass particles are assumed to behave as an ideal gas in a spherically symmetric gravitational potential. In thermal equilibrium, the temperature (T) is related to the one-dimensional velocity dispersion (σ_v) of the particles by $m{\sigma_v}^2 = kT$, where m corresponds to the mass of the particles. In this case, we also assume that the mass particles are isothermal, such that σ_v is constant throughout the galaxy ($\sigma_v(r) = \sigma_v$). The mass distribution described by the conditions above is known as

[12]The first discovery of this phenomenon was discussed in §1.1.

the *singular isothermal sphere* (SIS) and is described by,

$$\rho(r) \;=\; \frac{{\sigma_v}^2}{2G}\frac{1}{r^2}. \tag{1.17}$$

The rotational velocity of the particles in circular orbits within the gravitational potential is,

$$v_{rot}(r)^2 \;=\; \frac{GM(r)}{r} \;=\; 2{\sigma_v}^2. \tag{1.18}$$

Since σ_v is constant throughout the galaxy, v_{rot} is also constant; thus, the singular isothermal sphere reproduces the flat rotation curves of galaxies. The surface mass density of the SIS model is given by,

$$\Sigma(\xi) \;=\; \frac{{\sigma_v}^2}{2G}\left(\frac{1}{\xi}\right) \tag{1.19}$$

where ξ is the distance from the center of the surface mass density profile. The Einstein radius of the SIS model is defined as,

$$\theta_E \;=\; 4\pi\frac{{\sigma_v}^2}{c^2}\frac{D_{LS}}{D_S}. \tag{1.20}$$

If the source position is located within θ_E (i.e. $\beta < \theta_E$), multiple images are formed at $\theta_\pm = \beta \pm \theta_E$. A third image with zero flux is located at $\theta = 0$; however, it can acquire a finite flux if the center of the lens has a core region with finite density instead of a singularity. If the source is located outside the boundary of θ_E (i.e. $\beta > \theta_E$), only a single image is formed at $\theta = \beta + \theta_E$.

The Critical Surface Mass Density

If the lens plane (as illustrated in Figure 1.9) has a constant surface mass density, the reduced deflection angle is defined as,

$$\alpha_{red} \;=\; \frac{4\pi G\Sigma}{c^2}\,\frac{D_L D_{LS}}{D_S}\,\theta \tag{1.21}$$

where Σ corresponds to the surface mass density. Furthermore, the critical surface mass density is defined as,

$$\Sigma_{cr} \;=\; \frac{c^2}{4\pi G}\,\frac{D_S}{D_L D_{LS}}. \tag{1.22}$$

The critical surface mass density, Σ_{cr}, relates to the other parameters of the lensing equation as follows. If a lens has a constant surface mass density of Σ_{cr}, the reduced deflection angle is $\theta_{red} = \theta$ and $\beta = 0$ for all θ. Thus, all light rays focus perfectly at a single, well-defined focal length. However, similar to an optical lens, a typical gravitational lens shows a variety of aberrations not including chromatic abberation. In reality, light rays are deflected at different impact parameters (b) and focus at different distances on the optical axis. A gravitational lens does not have chromatic abberation because the deflection of light due to its gravitational potential is independent of wavelength. A lens which has $\Sigma > \Sigma_{cr}$ is commonly referred to as being *supercritical* and forms multiple images. For example, the surface mass density inside the Einstein radius is $\Sigma(< \theta_E) \sim \Sigma_{cr}$.

1.4 The Advantages of Gravitational Lensing

As discussed above, manifestations of gravitational lensing result in a variety of interesting observational phenomena. Since their initial discoveries, as discussed in §1.2, gravitational lensing has developed from a novel topic to a powerful tool that can be used to address a variety of important astrophysical questions. This section summarizes the naturally provided advantages of strong gravitational lensing, focusing on the aspects that are specific to this thesis. Briefly, these advantages are,

1. The ability to study the mass density profile of the lens, including a detailed analysis of the luminous and dark-matter contributions to the total mass within a fixed aperture.

2. The magnification of the background source, which often facilitates the discovery of objects that will otherwise be undetected and detailed investigation of the distant background source.

3. The ability to significantly constrain the cosmological parameters such as the Hubble constant (H_0), cosmological constant (Λ) and the density parameter

of the universe (Ω), since the properties of a gravitational lens depend on the age, scale and geometry of the universe. In a pioneering paper, Refsdal (1964) discussed how H_0 can be measured through the observations of a gravitational lens with a variable background source. Since the light travel times are unequal for different light rays, the intrinsic variations of the source will be observed at different times in multiple imaging. Thus, the time delay of the images is proportional to the difference of the light path lengths, which in turn, is proportional to ${H_0}^{-1}$. This advantage is not utilized in this thesis; however, we refer the reader to Fassnacht et al. (1999) for the treatise of an observational application of the method described by Refsdal (1964).

In addition to being a determinant of the lensing geometry, the Einstein radius (θ_E) also provides a direct estimate of the projected mass of the lens within an aperture. In other words, equation 1.16 can be inverted to determine the projected mass of the lens contained within θ_E, provided that there are secure lens and source redshift measurements to calculate the angular diameter distances. Thus, one of the most important advantages of gravitational lensing lies in its ability to measure the *total* mass of a galaxy[13] since the projected mass includes both luminous and dark matter components within θ_E. When combined with the estimates of stellar mass (for example, through broad-band imaging), the lensing mass can be effectively utilized to calculate the contribution of the dark matter component to the central regions of galaxies. While alternative methods of measuring total galaxy masses[14] depend on assumptions about the *state* of the measured mass (for example, that a galaxy cluster must be in virial equilibrium), lensing mass estimates are simpler since the gravitational lensing effect is independent of lens dynamics. Although extragalactic gravitational lenses have more complex mass distributions than the simple examples discussed in §1.3, the method for estimating the lensing mass within θ_E is robust for all applications (Narayan & Bartelmann 1999).

In addition to estimating the total mass within θ_E, gravitational lensing also allows us to determine the mass density profile of the lens. While the ΛCDM model of galaxy formation have very successfully withstood observational tests on the largest scales of the universe[15], smaller scale details such as the inner mass density profile of dark

[13]Equivalently of a galaxy group or cluster at the radius where we observe multiple images.

[14]Such as utilizing dynamics of various tracers at different galactic radii or X-ray measurements.

[15]Such as reproducing the observations of the Cosmic Microwave Background (CMB) and redshift surveys etc.

matter halos are not fully resolved. ΛCDM simulations of Navarro et al. (1996) first proposed the analytical approximation of the well-known NFW inner mass density profile of dark matter halos: $\rho(r) \propto r^{-1}$. Further simulations indicate that the mass density profiles follow a generalized form of $\rho(r) \propto r^{-\beta'}$. This is known as the "generalized NFW" profile (gNFW) with β' predicted to be around 1.4 to 1.5 (Dye & Warren 2008)[16]. However, the predictions of CDM simulations are often discrepant with the observations of the inner mass density profile of galaxies. One of the causes of this discrepancy is the comparison of pure dark matter simulations with observations since the baryons affect the dark matter halo in a non-trivial manner. The presence of baryons in a halo is believed to cause a contraction of the halo, thus steepening the inner slope of the mass density profile. This phenomenon is referred to as the *adiabatic contraction* (Gnedin et al. 2004). In the past decades, a large number of studies have been dedicated to measure the inner mass density profiles of galaxies which, in turn, can be compared with the simulations of galaxy formation. Furthermore, in the past years, gravitational lensing has emerged as a very attractive method to measure the slope of the inner mass density profile of galaxies (Dye & Warren 2008). A detailed analysis of a strong gravitational lens (typically from imaging), called strong lens modeling, involves finding the best-fit model of the source surface brightness profile and the mass density profile of the lens, whose gravitational potential gives rise to the observed multiple images (Peng et al. 2006; Warren & Dye 2003). Various strong lens modeling procedures will be discussed in detail in the proceeding chapters.

Another important advantage of strong gravitational lensing is the magnification of multiple images. Gravitational lensing preserves the surface brightness of the source since the light ray is only deflected (no absorption or emission)[17], leaving the specific intensity of the incident light ray unaffected. However, gravitational lensing changes the apparent solid angle of the source; therefore, to preserve surface brightness, the total flux of the image must also change proportionally. In essence, an expansion in the angular size of the image results in an increase of the total flux of the image as well. Thus, the magnification is defined as,

$$\text{magnification} = \frac{\text{image area}}{\text{source area}} = \frac{\text{image flux}}{\text{source flux}} \tag{1.23}$$

[16]The logarithmic slope of the mass density profile is usually denoted as β, but will be denoted as β' throughout this thesis such that it will not be confused with the lensing angle shown in Figure 1.10.

[17]We assume that extinction due to dust is negligible.

The lens equation, as given by equation 1.11, is a coordinate transformation between the source and lens planes. Therefore, the magnification can be expressed in terms of two parameters of coordinate transformation: *convergence* (κ), the uniform radial expansion of the image[18] and *shear* (γ), stretching of the image along the gravitational equipotential surfaces. The magnification factor (μ) of a gravitational lens is given by,

$$\mu \; = \; \frac{1}{det\; A} \tag{1.24}$$

where A is the Jacobian determinant of the coordinate transformation ($A(\vec{\theta}) = |\delta\vec{\beta}/\delta\vec{\theta}|$). According to equation 1.24, the magnification diverges at each location where the Jacobian vanishes. For a given deflector mass distribution, lens and source redshift, the line connecting the points of infinite amplification on the lens plane is referred to as the *critical line*. Moreover, the lens equation can be inverted to derive the corresponding points of infinite amplification on the source plane. The line connecting these points on the source plane is referred to as the *caustic*. For the case of a circularly symmetric lens, such as a point mass lens, μ is defined as:

$$\mu \; = \; \frac{\theta}{\beta}\frac{d\theta}{d\beta} \tag{1.25}$$

Galaxy-scale gravitational lenses yield typical magnification factors of 10 $\times$, while group- or cluster-scale gravitational lenses can yield magnification factors as high as 40 $\times$ (Marshall et al. 2007). Therefore, even if a faint and small galaxy is gravitationally lensed, under a suitable magnification one can estimate its properties accurately in comparison to the non-lensed case (provided that the mass density profile of the lens is well constrained).

Throughout the past few decades, the magnification effect has been utilized by various studies to discover background galaxies and examine their properties in detail, at ever increasing look-back times (Allam et al. 2007; Bradley et al. 2008; Belokurov et al. 2007; Bian et al. 2010; Koester et al. 2010; Kubo et al. 2009, 2010; Lin et al. 2009; Richard et al. 2011; Yuan et al. 2012; Zitrin et al. 2012). However, such studies typically examine, at most, tens of gravitational lenses at a time since they are rare objects. However, in the recent years, various groups have focused on serendipitous

[18]Therefore, the source is lensed onto an image with the same shape but larger size.

large-scale gravitational lens discovery by "mining" from existing deep- and/or wide-sky surveys. Such lens discoveries fall into two categories (Treu 2010): **(i)** Imaging-based searches (Cabanac et al. 2007), which are useful for detecting sharp multiply-imaged systems (for example, lensed quasars) or systems with extended images of large separation that can be easily deblended. Generally, the lens candidates in these searches are first identified visually, based on the presence of characteristic lensed features, and then confirmed through strong lens modeling. **(ii)** Spectroscopy-based searches, which rely on identifying spectral features of the background source that are superposed on the spectrum of the lens galaxy. The next section discusses a survey that is specifically designed towards discovering a statistically significant sample of galaxy-scale gravitational lenses utilizing data from existing surveys.

1.5 Sloan Lens ACS (SLACS) Survey

For this thesis, we utilize observations of strong gravitational lenses from the Sloan Lens ACS (SLACS) survey, one of the largest and most comprehensive surveys of galaxy-scale lensing conducted to date. In this section, we provide a brief overview of the motivation behind the SLACS survey and discuss the selection method. Further details of the scientific results of this survey can be found in the SLACS series: Paper I through XI (Bolton et al. 2006; Treu et al. 2006; Koopmans et al. 2006; Gavazzi et al. 2007; Bolton et al. 2008a; Gavazzi et al. 2008; Bolton et al. 2008b; Treu et al. 2009; Auger et al. 2009, 2010; Newton et al. 2011).

Within the context of the hierarchical model of galaxy formation, early-type galaxies form through the mergers of late-type galaxies (i.e. "wet" mergers) and also early-type galaxies (i.e. "dry" mergers). Therefore, the structure of early-type galaxies is a fossil record of their formation and evolution, which provides an important testbed for the ΛCDM model. Testing the predictions of the ΛCDM model at kpc-scales, where baryonic and radiative processes have significant effect on the structure of the dark matter halo, requires detailed observations of the mass density profiles of early-type galaxies. Furthermore, early-type galaxies show a great degree of regularity in terms of their photometric and spectroscopic properties as evident from the well known Fundamental Plane, FP[19] (Djorgovski & Davis 1987; Dressler et al. 1987). However,

[19]The Fundamental Plane corresponds to the relationship between the velocity dispersion, effective radius and the surface brightness of early-type galaxies. Together, the three parameters describe a

understanding the deviation of the observed FP from the theoretical expectation of the virial theorem, otherwise known as the "tilt" of the FP, is an important issue. For example, the tilt of the FP implies that early-types galaxies may not always be a self-similar family that obeys the virial theorem and have constant mass-to-light ratios (Auger et al. 2010). In order to examine the processes that cause the tilt of the FP (such as varying stellar populations, mass density profiles or dark matter fractions) one must disentangle the luminous and dark matter profiles of a significant sample of early-type galaxies.

In a nutshell, the SLACS survey was established to fulfill a need for detailed observations of the mass density profiles of a large sample of early-type galaxies to tackle the issues discussed above. Gravitational lensing (a direct measurement of the total mass within the Einstein radius), when combined with measurements of the stellar velocity dispersion profile (a measurement of the mass gradient (Koopmans et al. 2006)), provides a method to disentangle the luminous and dark matter profiles of an early-type galaxy (Bolton et al. 2006)[20]. Without gravitational lensing, it is difficult to separate the luminous and dark matter components of early-type galaxies, since they are pressure supported systems and lack bright kinematic tracers out to large radii[21]. Prior to the SLACS survey, only a handful of gravitational lenses were suitable for a joint lensing and dynamical analysis of early-type lens galaxies, since many of the galaxy-scale gravitational lenses consist of a source galaxy that hosts a bright quasar. Therefore, the luminous multiple images of the quasar can overwhelm the lens galaxy, as evident from Figure 1.3, prohibiting a joint lensing + dynamical analysis. Thus, the SLACS survey was designed specifically for the discovery of galaxy-scale lenses suitable for a joint lensing + dynamical analysis of early-type galaxies (i.e. no lensed quasar systems).

A brief overview of the selection method of SLACS survey, initially outlined in Bolton et al. (2004), is as follows. The targets were initially selected spectroscopically from the Sloan Digital Sky Survey (SDSS) (York et al. 2000) luminous red galaxy (LRG) and MAIN galaxy samples (Eisenstein et al. 2001; Strauss et al. 2002). If a

plane within the general three-dimensional space.

[20]The robust measurement of the total mass within the Einstein radius, when combined with stellar mass estimates, allows one to determine the dark matter mass fraction within the Einstein radius (where $f_{DM} = 1 - f_{\star}$).

[21]Unlike late-type galaxies, which are rotation supported and have kinematic tracers at large radii that can be used to measure the rotational velocity, and in turn, the mass density profile.

galaxy-scale gravitational lens (convolved with the seeing) falls within the 3.″0 SDSS spectroscopic fiber, the observed spectrum is a composite of the lens and source galaxy spectra. During the spectroscopic selection, the best-fit template of the early-type lens galaxy continuum is subtracted from each SDSS spectrum and the residual spectra are scanned for nebular emission lines at a common redshift higher than that of the foreground galaxy. The gravitationally lensed candidates are selected due to the presence of multiple, nebular emission lines (H β, [O II] 3727, [O III] 5007) within the 3.″0 spectroscopic fiber. Prior to the SLACS survey, this emission line based method has been utilized successfully to discover gravitational lenses by a variety of studies including Huchra et al. (1985); Warren et al. (1999a,b); Hall et al. (2000); Hewett et al. (2000); Johnston et al. (2003); Willis et al. (2005). However, the SLACS survey is the largest and the most homogenous survey of emission line based gravitational lens search conducted to date (the successor to SLACS will be discussed later).

Figure 1.11 shows an example of the spectroscopic selection process. Targets whose residual spectra (from the source galaxy) exhibit at least two emission lines are identified as candidates for subsequent imaging followup. By virtue of this selection method, all lens systems have confirmed spectroscopic redshifts for both lens and source galaxies. The lens candidates are then observed under multiwavelength *HST* imaging programs, for confirmation through strong-lens modeling (Bolton et al. 2006; Treu et al. 2006; Koopmans et al. 2006; Gavazzi et al. 2007; Bolton et al. 2008a; Gavazzi et al. 2008; Bolton et al. 2008b; Treu et al. 2009; Auger et al. 2009, 2010; Newton et al. 2011), using the following instruments: Advanced Camera for Surveys (ACS); Wide Field Planetary Camera 2 (WFPC2) and NICMOS.

To date, the SLACS survey has identified $\sim$ 130 lens candidates. Out of these candidates, 85 are lens systems with definitive spectroscopic and imaging confirmation (Bolton et al. 2006, 2008a; Auger et al. 2009) and are referred to as "Grade-A" lenses. Furthermore, there are additional 13 "Grade-B" lens systems (i.e. very likely gravitational lenses). Approximately 80% of the lens galaxies in SLACS survey are massive, elliptical galaxies and $\sim$ 10% show spiral structure. The remainder of the lens galaxies show lenticular (S0) morphology. The stellar masses of the SLACS lens galaxies range from $10^{10.5} M_{\odot}$ to $10^{11.8} M_{\odot}$ (Auger et al. 2009, 2010). Figure 1.12 shows a composite of the *HST* colour images of Grade-A SLACS lenses, which indicates that many of the SLACS lenses contain complete or partial Einstein ring features.

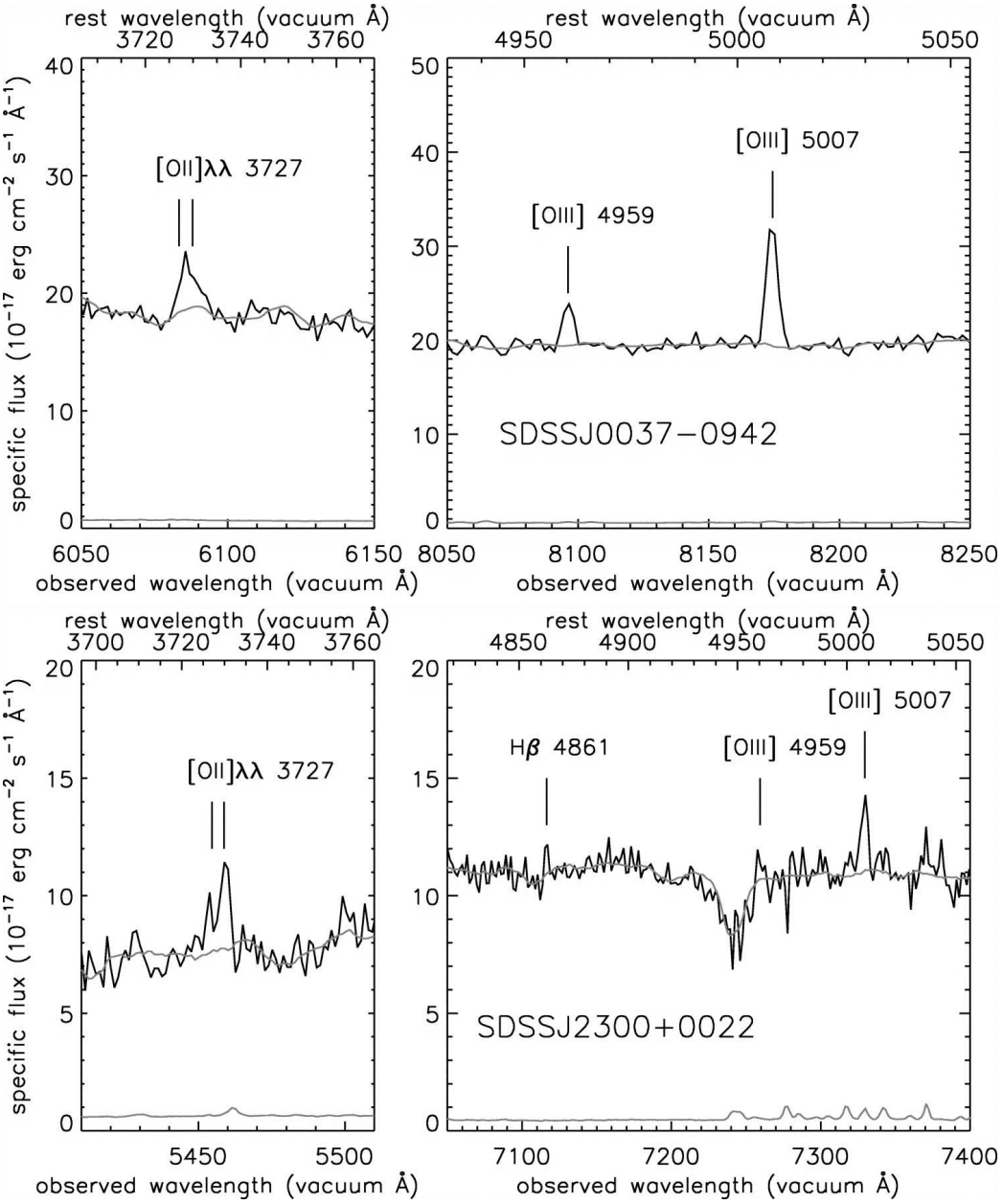

Figure 1.11 *Top row:* SDSS spectrum of the SLACS lens system, SDSS J0037-0942 (Bolton et al. 2006). This gravitational lens consist of an early-type galaxy at $z = 0.20$ deflecting the light from a background galaxy at $z = 0.63$. The upper gray line shows the SDSS fit to the early-type lens galaxy continuum and the lower gray line shows the 1σ noise level. The marked emission lines ([O II] 3727Å, [O III] 4959Å and [O III] 5007Å) originate from the background galaxy. *Bottom row:* SDSS spectrum of the SLACS lens system, SDSS J2300+0022, which consists of a lens galaxy at $z = 0.23$ and a background galaxy at $z = 0.46$.

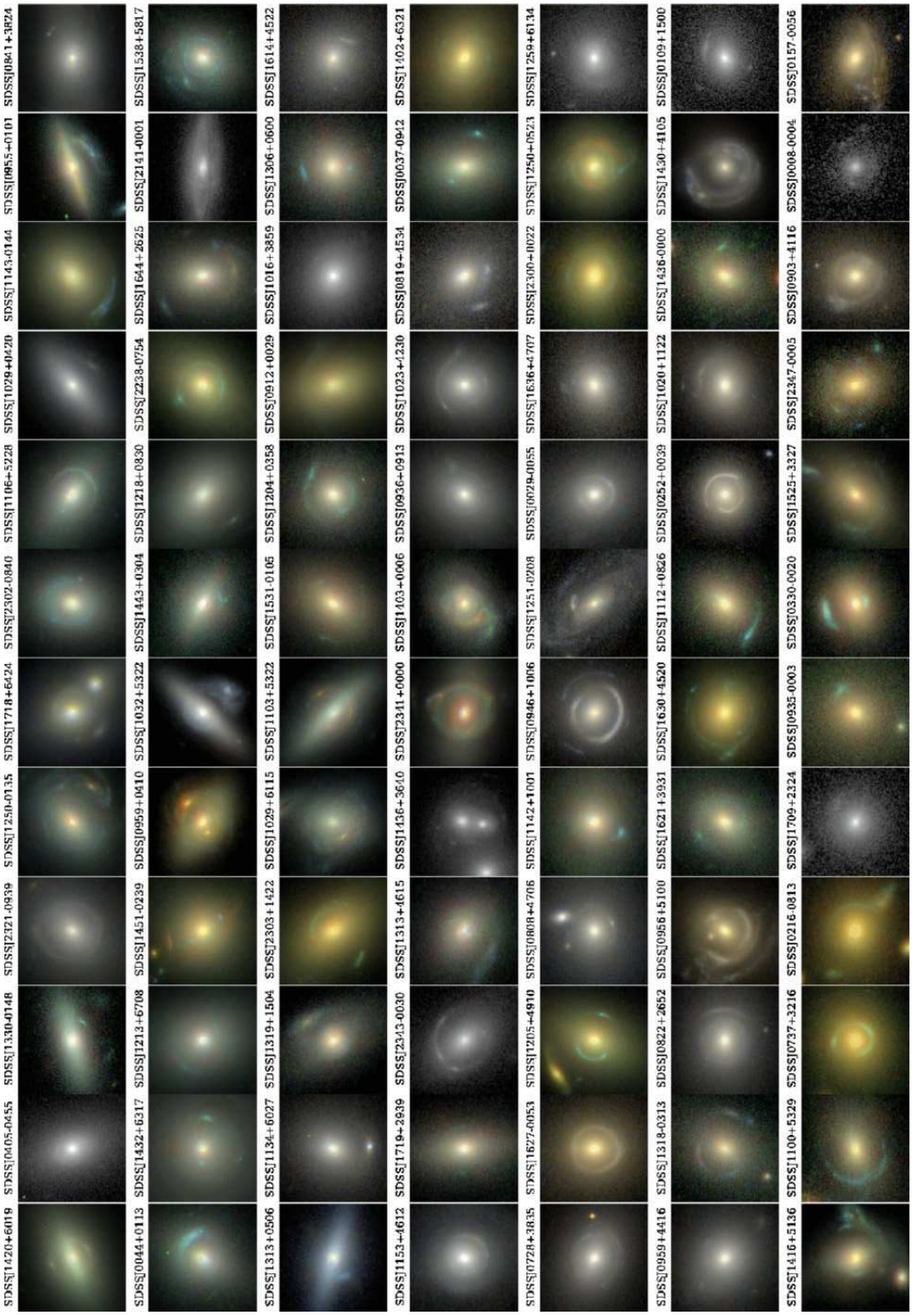

Figure 1.12 A composite made from the colour images of 84 "Grade-A" SLACS lenses (Figure 2 of Auger et al. (2009)). The lens SDSS J1618+4353, which has two lens galaxies, is omitted from this figure.

1.6 Motivation

As discussed in the previous sections, utilizing gravitational lensing as an astrophysics tool dictates that we work with the cosmic alignments that nature has provided us. However, when "mined" in a homogenous manner similar to that of the SLACS survey, large samples of strong gravitational lenses can be used to address a broad range of interesting questions. Thus, a key aspect of this thesis is that the goals of the following chapters were motivated by the availability of the SLACS survey.

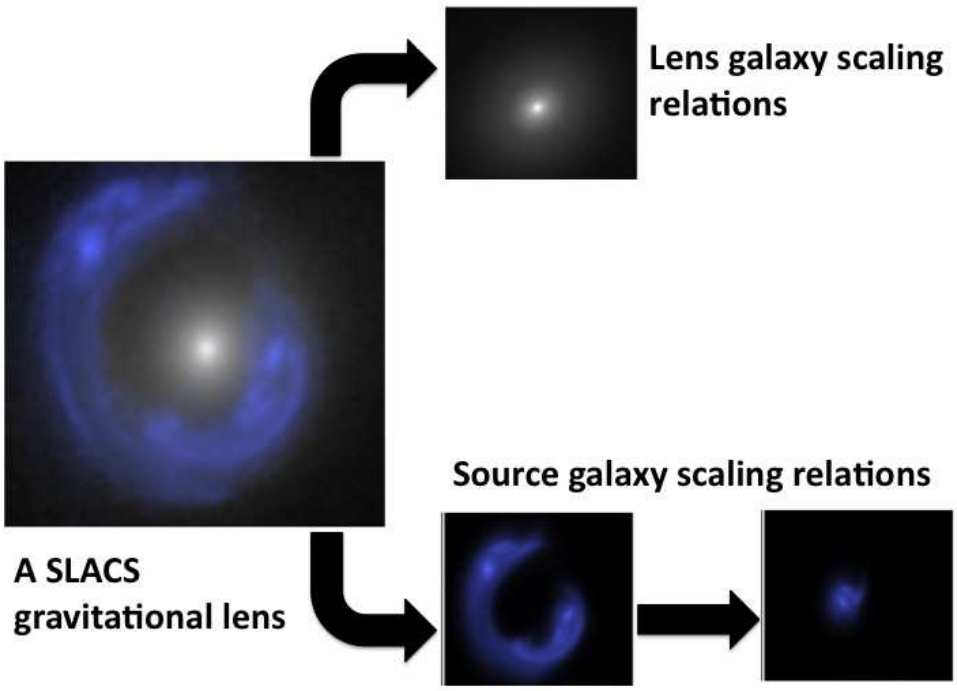

Figure 1.13 Graphical representation of the motivation behind this thesis. This thesis takes *HST* imaging observations from the SLACS survey and dissects each gravitational lens to study lens and source galaxy scaling relations, as enabled by advantages of strong gravitational lensing. These scaling relations enable further investigation of baryonic and non-baryonic processes that affect the evolution of early-type and late-type galaxies. This thesis also initiates further spectroscopic follow-up of SLACS lenses, which will be discussed in Chapter 4.

As illustrated in Figure 1.13, this thesis essentially "dissects" each gravitational lens to extract useful information about the lens and source components, using the advantages discussed in §1.4. In summary, we use the fact that strong gravitational lensing allows us to determine the inner mass density profile and total mass of the lens, to examine early-type lens galaxy scaling relations of the SLACS sample. We

then use the magnification advantage to measure the properties of the SLACS source galaxy population in detail. Both lens and source galaxy scaling relations examined in this thesis give further clues to how various baryonic processes, varying from moderate levels of star-formation to powerful feedback from the central supermassive black holes, affect the evolution of early-type and late-type galaxies. Specifically, the questions addressed with this thesis includes:

1. Does the total gravitational mass of a galaxy fundamentally determine the properties of its supermassive black hole?

2. Can we quantify the improvement in our knowledge of the background galaxy population, that can be expected from a gravitational lensing survey?

3. What can we infer about the evolution of the luminosity-size relation since $z \sim 1$ using the magnification advantage?

4. Can we obtain detail kinematic information of faint and compact galaxies at $z > 0.75$ by combining the magnification advantages with the improved spatial resolution provided by adaptive optics (AO) technology in the infrared regime?

The following three chapters discuss the projects that address the questions discussed above. We assume the following cosmological terms for all computations in this thesis: $\Omega_{\rm M} = 0.3$, $\Omega_{\Lambda} = 0.7$, $\rm H_0 = 70\,h_{70}\,km\,s^{-1}\,Mpc^{-1}$ and $\rm h_{70} = 1$. Unless otherwise noted, all scaling relations in this thesis are defined as linear relationships in log-log space and all logarithms denoted as a base of 10. This research used the facilities of the Canadian Astronomy Data Centre operated by the National Research Council of Canada with the support of the Canadian Space Agency.

Chapter 2

A Relationship Between Supermassive Black Hole Mass and the Total Gravitational Mass of the Host Galaxy

2.1 Introduction

Supermassive black holes (SMBH) are believed to reside in nearly all galaxies (Kormendy & Richstone 1995; Ferrarese & Ford 2005) and the masses of these SMBH (M_{bh}) show correlations with host galaxy properties, implying that SMBH and galaxy formation processes are closely linked (Adams et al. 2001; Cattaneo 2001; Cattaneo et al. 1999; Di Matteo et al. 2005, 2003; El-Zant et al. 2003; Haehnelt & Kauffmann 2000; Hopkins et al. 2005b,a; Silk & Rees 1998; Wyithe & Padmanabhan 2006). Previous studies have shown correlations between M_{bh} and galaxy's effective stellar velocity dispersion ($\sigma_\star$), bulge luminosity (L_{bul}), Sérsic index (n) and stellar mass of the bulge component (M_{bul}) (Ferrarese & Merritt 2000; Gebhardt et al. 2000; Graham et al. 2001; Graham & Driver 2007; Marconi & Hunt 2003). The correlations between M_{bh}, $\sigma_\star$ and L_{bul} are shown in Figure 2.1. Some of the challenges faced by current models of SMBH formation and evolution include reproducing and maintaining these scaling relations regardless of the events that take place during galaxy evolution driven by the process of hierarchical mass assembly (Croton 2009; Wyithe & Loeb 2002, 2003; McLure et al. 2006; Robertson et al. 2006). These scaling relations are not only

important tests of the models of SMBH formation and evolution but also powerful predictive tools from which we can infer SMBH masses of galaxies that are located at higher redshifts.

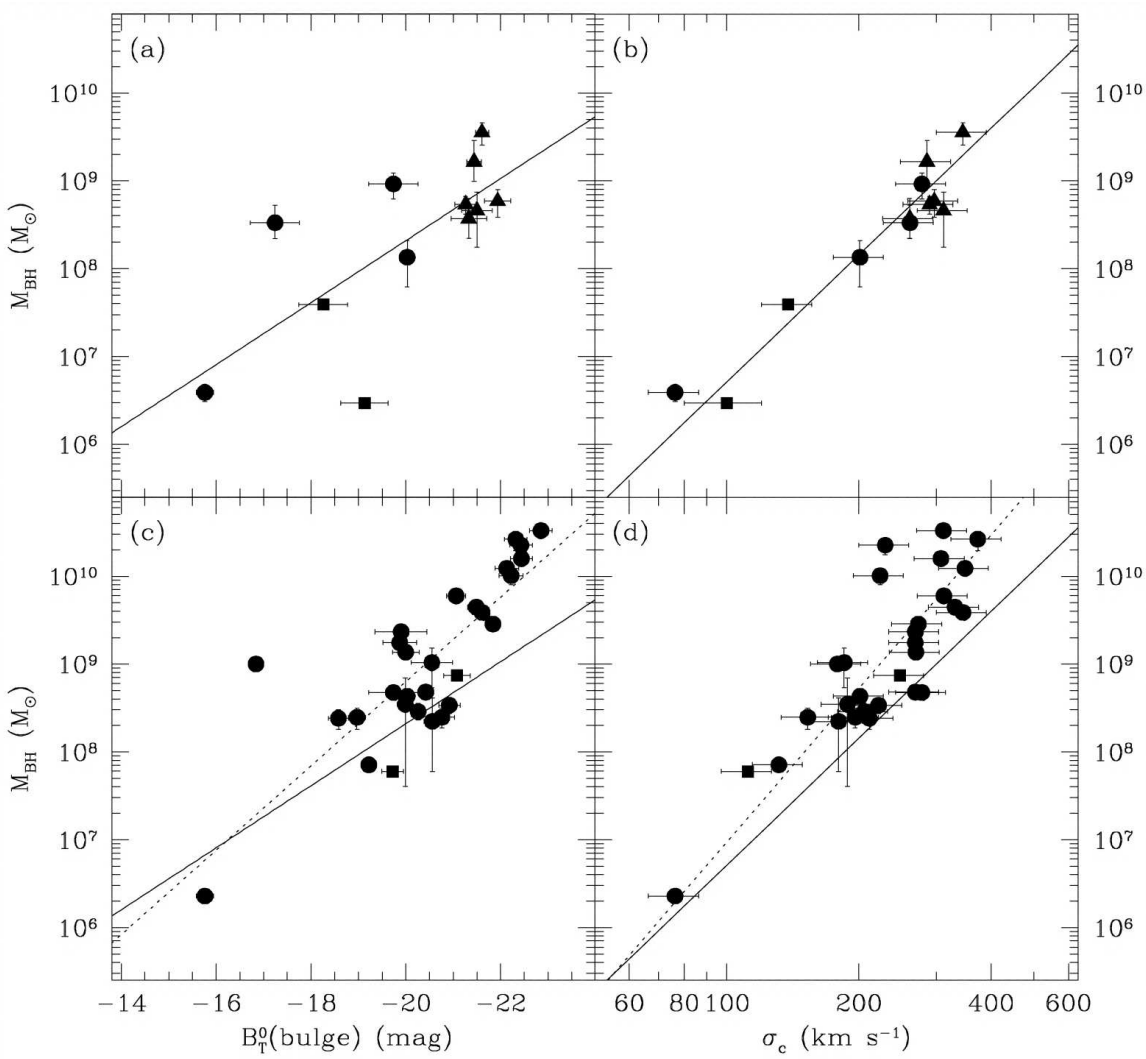

Figure 2.1 Figure 1 of Ferrarese & Merritt (2000), a pioneering study that examined various scaling relations between M_{bh} and the host galaxy properties. Panels (a) and (b) only show measurements of 12 galaxies, which were considered to have the most reliable SMBH mass estimates at the time. Panels (c) and (d) show additional 17 galaxies with less secure SMBH mass estimates. **(a)** M_{bh} vs. absolute B-band luminosity of the host galaxy bulge component. **(b)** M_{bh} vs. stellar velocity dispersion of the bulge component of the host galaxy. **(c)** Same as (a) but for the larger sample of galaxies. **(d)** Same as (b) but for the larger sample of galaxies.

In this paper, we examine the evidence for a scaling relation between M_{bh} and the *total* mass of the host galaxy (denoted as M_{tot}). Most self regulating theoretical

models of SMBH formation predict a fundamental connection between M_{bh} and M_{tot} of the host galaxy (Adams et al. 2001; El-Zant et al. 2003; Haehnelt et al. 1998; Monaco et al. 2000; Silk & Rees 1998). One of the most important predictions of the galaxy models, which study the interaction between the dark matter haloes of galaxies and baryonic matter settling into the gravitational potential to form the bulge and SMBH, is that halo properties determine those of the bulge component and SMBH (Cattaneo 2001; El-Zant et al. 2003; Hopkins et al. 2005b,a). However, observational evidence for such a scaling relation has been sparse since measurement of the total mass is non-trivial.

Results from Ferrarese (2002) examined some of the first *indirect* observational evidence for the existence of a $M_{bh} - M_{tot}$ relation. In Ferrarese (2002), the correlation between bulge velocity dispersion (σ_c) and the observed circular velocity ($v_{c,obs}$), for a sample of 20 elliptical galaxies and 16 spiral galaxies, is translated into an equivalent $M_{bh} - M_{tot}$ correlation. Although σ_c can be translated into M_{bh} through $M_{bh} - \sigma_\star$ relation in a straightforward manner, an estimate of M_{tot} is dependent on the conversion between $v_{c,obs}$ and virial velocity, the velocity of the galactic halo at the virial radius. Ferrarese (2002) uses results from ΛCDM cosmological simulations to derive M_{tot}. The results of Ferrarese (2002) are summarized in Figure 2.2. Following Ferrarese (2002), several studies have examined the $v_{c,obs} - \sigma_c$ relation and its implications for galaxy formation and evolution (Baes et al. 2003; Buyle et al. 2006; Courteau et al. 2007; Pizzella et al. 2005).

The primary goal of this project is to extend the observational evidence to support the $M_{bh} - M_{tot}$ relation using an attractive, alternative, and *direct* method to measure the total mass of the host galaxy. As discussed in §1, in the recent years, strong gravitational lensing has emerged as a powerful tool to probe the mass profiles of objects ranging from individual galaxies to clusters of galaxies (Bolton et al. 2006, 2008a; Dye & Warren 2008; Gavazzi et al. 2008; Halkola et al. 2008; Moustakas et al. 2007). Due to the fact that the deflection of a photon is independent of the deflector's dynamical state, gravitational lensing does not suffer from difficulties associated with dynamical mass measurements of galaxies, where assumptions regarding orbital motions of tracers can lead to complications. Thus, gravitational lensing is a more robust method to estimate the total mass, including dark matter, around early-type galaxies and infer the existence of an isothermal mass profile ($\rho \propto r^{-2}$) in various systems (Dye & Warren 2008; Koopmans et al. 2006).

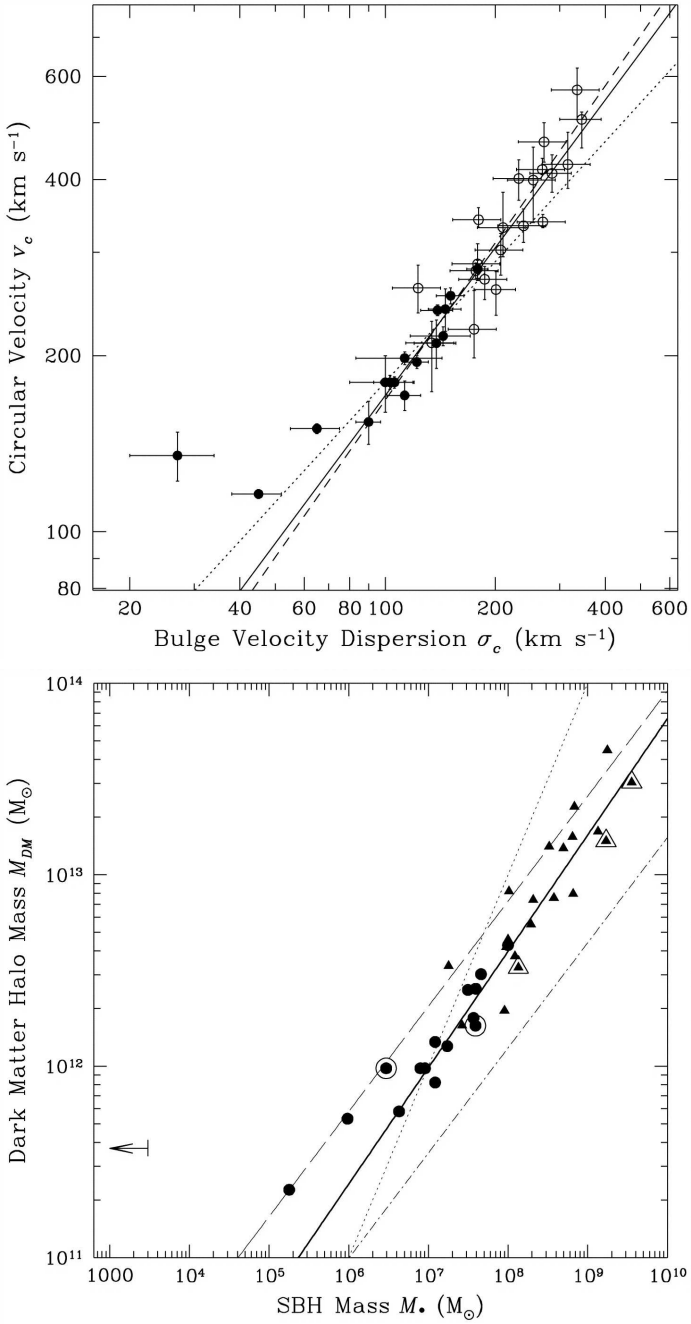

Figure 2.2 *Top:* Correlation between the bulge velocity dispersion (σ_c) and the disk circular velocity (v_c) for a sample of 37 galaxies (Figure 3 of Ferrarese (2002)). The filled circles represent spiral galaxies and the open circles represent elliptical galaxies. The circular velocities of the galaxies are measured from either optical or HI rotation curves. *Bottom:* Same as (a), with σ_c transformed into equivalent SMBH masses using the $M_{bh} - \sigma_c$ relation and v_c transformed into dark matter halo masses following cosmological prescriptions of Bullock et al. (2001). The filled circles are spiral galaxies and filled triangles are elliptical galaxies.

The mass enclosed within the Einstein radius (M_{einst}) which is measured from the lens model that produces the best fit to the observed multiple images, is a direct probe of both luminous and dark mass in a galaxy. In conjunction with velocity dispersion and surface brightness profiles of the lens galaxy, measurement of M_{einst} from a lens model can be used effectively to constrain the luminous and dark matter profiles. In this study, we utilize the M_{einst} as a tracer of the total mass and use the total mass profile of the lensing galaxy to determine the mass contained within a redshift-independent circular aperture.

We also attempt to derive the $M_{bh} - M_{tot}$ relation using purely photometric tracers of M_{bh} and M_{tot}. Therefore, we examine the possibility of using $M_{bh} - n$ relation (Graham et al. 2001; Graham & Driver 2007) as the primary method to estimate black hole masses. Surface brightness profiles of most galaxies, in particular E/S0, can be described by the Sérsic law (Sersic 1968) as follows:

$$\Sigma(r) = \Sigma_e \exp\left(-k[(r/r_e)^{1/n} - 1]\right) \tag{2.1}$$

where $\Sigma(r)$ is the surface brightness at radius r, r_e is the half-light radius of the profile and Sérsic index (n) is the degree of light concentration (shown in Figure 2.3). The well known De Vaucouleurs' profile that describes the surface brightness profile of elliptical galaxies is a special case of the Sérsic profile, where $n = 4$. A Sérsic index of $n = 1$ corresponds to an exponential disk and $n = 0.5$ corresponds to a Gaussian profile. The bulge components of galaxies are usually characterized by $n > 2.5$. Previous studies in the literature indicate that the quantity n varies monotonically with galaxy magnitude. Therefore, the existence of a $M_{bh} - n$ relation can be inferred given the dependence of M_{bh} on the galaxy magnitude (Marconi & Hunt 2003) and the connection between galaxy magnitude and Sérsic index (Jerjen et al. 2000; Graham & Guzmán 2003; Ferrarese et al. 2006).

Graham & Driver (2007) discuss the most recent version of the $M_{bh} - n$ relation and indicate that the dependence between the quantities $\log(M_{bh})$ and $\log(n)$ can be best represented by a log-quadratic relation. The main motivation for using this relation is that measurement of n requires only imaging data, which is easier to acquire than spectroscopic data at a given redshift; therefore, $M_{bh} - M_{tot}$ could be easily extended to large samples of higher redshift gravitational lenses, which may not

have spectroscopic measurements[1]. Furthermore, n is a distant-independent quantity, an added advantage for estimating black hole masses of high redshift galaxies that may not have secure redshift measurements.

This chapter is structured as follows. In §2.2 we present a brief description of the target selection. In §2.3 we describe the following analysis procedures: §2.3.1 Measurements of M_{tot}; §2.3.2: Deriving the connection between M_{bh} and M_{tot} using spectroscopic data (i.e. $M_{bh} - \sigma_\star$ relation); §2.3.3: Deriving the connection between M_{bh} and M_{tot} using imaging data (i.e. $M_{bh} - n$ relation). In §2.4 we present the results of our analysis. In §2.5 and §2.6 we discuss the implications of our results and give some concluding remarks regarding this project.

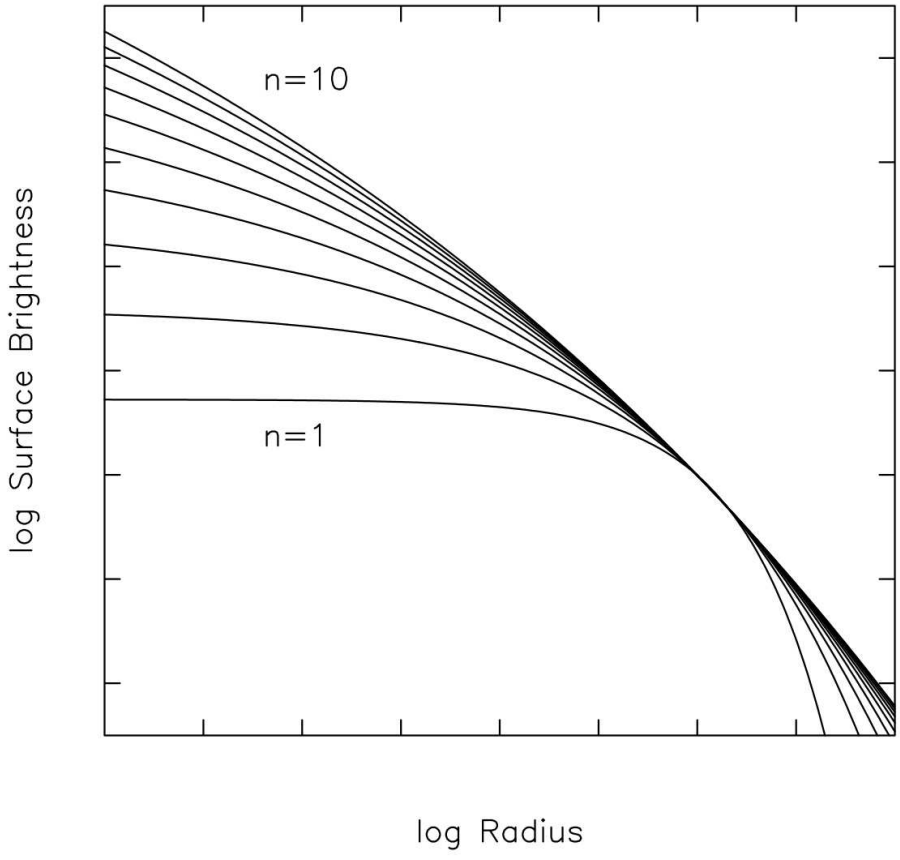

Figure 2.3 Sérsic models with varying Sérsic indices, n, scaled to arbitrary units of the logarithm of the surface brightness.

[1]We refer the reader to Woo et al. (2008) for a spectroscopic study of the evolution of $M_{bh} - \sigma_\star$ relation since $z = 0.57$.

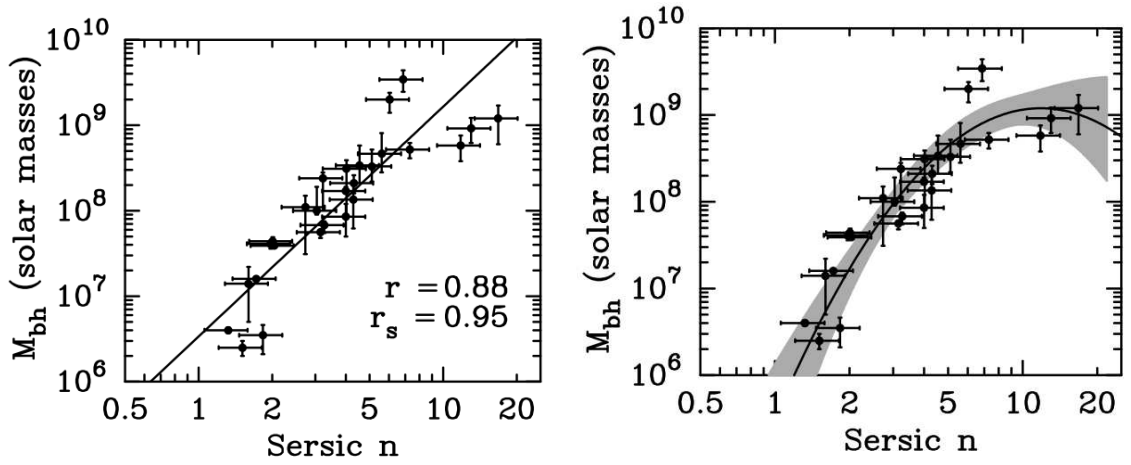

Figure 2.4 *Left:* The correlation between the SMBH mass and the Sérsic index of the galaxy's bulge component (Figure1 of Graham & Driver (2007)), for a sample of 27 galaxies in the local universe (including the Milky Way). The sample consists of 14 galaxies with E-type morphology and 13 galaxies with S0 morphology. The solid black line corresponds to the log-linear fit to the data. *Right:* Same as the left panel, except the solid black line now corresponds to the log-quadratic fit to the data (Figure 2 of Graham & Driver (2007)). The shaded region corresponds to the 1σ confidence region.

2.2 The Sample

The sample of galaxies used in this chapter is a subset of the galaxy-scale strong gravitational lenses from the SLACS survey (Bolton et al. 2006, 2008a), which was first introduced in §1.5. For this project, we use 43 out of the 70 "Grade-A" lenses from Bolton et al. (2008a). The imaging observations for the 43 lenses used in this chapter are from *HST*-ACS programs 10174, 10587 and 10886. We do not use lens systems that do not have a simple lens model due to nearby companion galaxies (7 lens systems) or systems where the stellar velocity dispersion of the early-type lens galaxy ($\sigma_{\rm SDSS}$) is not available (14 lens systems) because the median signal-to-noise (SNR) within the 3.″0 SDSS spectroscopic fiber is too low (Bolton et al. 2008a).

2.3 Data Analysis

The most important advantage of using the SLACS galaxy sample to determine the $\rm M_{bh} - M_{tot}$ relation is that we have an accurate measurement of the total mass profile

of each galaxy. However, SLACS lens galaxies are located at distances ($\langle z_{\rm foreground} \rangle \approx 0.2$) where the SMBH mass cannot be measured directly through its influence on the surrounding gas or stars. Therefore, we use two scaling relations to determine the SMBH masses of the galaxy sample: $M_{\rm bh} - \sigma_\star$ relation (Ferrarese & Merritt 2000; Gebhardt et al. 2000; Gültekin et al. 2009) and $M_{\rm bh} - n$ relation (Graham et al. 2001; Graham & Driver 2007).

2.3.1 Deriving Total Mass of the Host Galaxy

We use the best-fit mass density profiles from the strong lens modeling performed by Bolton et al. (2008a) to obtain $M_{\rm tot}$ of each lens galaxy in the SLACS sample. A summary of the lens modeling process for an extragalactic gravitational lens is given below. Given a deflector potential ($\Phi(x)$), the surface brightness profile (also referred to as the "light profile") of the source galaxy ($\Sigma(u)$) is multiply imaged on the image plane as follows,

$$\mathbf{u} = \mathbf{x} - \nabla_s \Phi(\mathbf{x}) \tag{2.2}$$

while conserving the surface brightness at each location on the source plane (Peng et al. 2006). One of the approaches to strong lens modeling is the backward ray tracing method, which utilizes the fact that regions of the source galaxy that are multiply imaged have the same surface brightness on the image plane. For a trial mass distribution, this method traces image pixels with same the counts back to the same source pixel. The optimal solution for the mass distribution and the source galaxy light profile is obtained by minimizing the dispersion in the image pixel counts for multiply imaged source pixels (Dye & Warren 2008). The alternative method of lens modeling is forward ray tracing, where a single pixel on the source plane is mapped onto multiple locations on the image plane, for a trial mass distribution and a source galaxy light profile. For each iteration, the model lensed image is convolved with the instrumental point spread function (PSF) and compared to the data. The parameters of the mass distribution and source galaxy light profile are adjusted until the model images match the observations and the solutions are optimized using a merit function, such as χ^2 (Dye & Warren 2008).

Bolton et al. (2008a) use a singular isothermal ellipsoid (SIE) model to describe the lens plane which generates the multiple images of the source. To describe the mass density profile of an elliptical lens galaxy, it is sensible to utilize elliptical iso-density contours rather than an idealized, circularly symmetric model. The SIE model breaks the circular symmetry of the SIS model, discussed in the previous chapter, and its projected mass density is,

$$\kappa(x,y) \;=\; \frac{b}{2}\Big[\frac{2q^2}{1+q^2}(x^2+y^2/q^2)\Big]^{-1/2} \tag{2.3}$$

where b is the mass scale and q is the axis ratio of the mass model. The mass scale parameter, b, is approximately the Einstein ring radius of the lens (b_{SIE}). However, this relation is only exact at the $q = 1$ limit (Kochanek et al. 2001; Peng et al. 2006), where b_{SIE} is related to the physical quantities of the mass model by,

$$b_{SIE} \;=\; 4\pi\,\frac{{\sigma_{SIE}}^2}{c^2}\,\frac{D_{LS}}{D_S}. \tag{2.4}$$

The quantity σ_{SIE} is the velocity dispersion of the total mass profile (Kochanek et al. 2001; Bolton et al. 2006, 2008a). The surface brightness profile of the background galaxy is described by single or multiple Sérsic profiles and the model lensed image, for a given SIE model, is produced by forward ray tracing (Bolton et al. 2008a). We use the mass model parameters given by Bolton et al. (2008a), i.e. $\mathrm{b_{SIE}}$, and integrate the best-fit mass profile to obtain the total mass within a projected radius of choice. During the preliminary analysis, we invert the lens equation to compute the total mass inside the Einstein radius ($\mathrm{M_{einst}}$), as a tracer of $\mathrm{M_{tot}}$.

However, $\mathrm{M_{einst}}$ is not a measurement of mass within a *standard* aperture since the linear radius characterized by the Einstein radius for a given mass distribution is redshift dependent. We therefore use $\mathrm{R_{200}}$, the linear radius within which the mean density of the lensing galaxy exceeds the critical density of the universe (ρ_{crit}) by a factor of 200, as a "standard aperture"[2]. The mass contained within a projected radius of $\mathrm{R_{200}}$ ($\mathrm{M_{200}}$) corresponds to,

$$\mathrm{M_{200}} = \frac{4}{3}\pi(\mathrm{R_{200}})^3\,200\rho_{\mathrm{crit}} \tag{2.5}$$

[2]Where $\rho_{\mathrm{crit}} = \frac{3}{8\pi \mathrm{G}}\,\mathrm{H}^2(\mathrm{t})$.

where R_{200} is defined as,

$$R_{200} = \frac{1.73\,\sigma_{200}}{1000\,\mathrm{km/s}\,\sqrt{\Omega_M(1+z_{lens})^3+\Omega_\Lambda}}\,{h_{100}}^{-1}\,\mathrm{Mpc}. \quad (2.6)$$

The quantities σ_{200} and z_{lens} correspond to the velocity dispersion of the total mass profile at R_{200} and the redshift of the early-type lens galaxy. To estimate M_{200}, we assume that the isothermal nature of the total mass profile of SLACS lens galaxies extends up to the virial radius (i.e. R_{200}); therefore, the quantity σ_{200} can be replaced with σ_{SIE} derived from lens modeling (Bolton et al. 2008a).

Adopting an "aperture-corrected" mass measurement (i.e. M_{200}), instead of M_{einst}, does not affect the overall form of the $M_{bh} - M_{tot}$ relation (i.e. the slope and zero-point) discussed in the following sections. Results of Bolton et al. (2008b) show a lack of correlation between the quantities $f \equiv \sigma_{aperture}/\sigma_{SIE}$ and mass or $R_{einst}/R_{aperture}$, where $\sigma_{aperture}$ is the stellar velocity dispersion corrected to an aperture of $R_{aperture}$ and R_{einst} is the Einstein radius. These results are consistent with the near isothermal nature of the *inner* radial profile of early-type lens galaxies. However, a joint strong- and weak-lensing analysis of 22 SLACS lens galaxies by Gavazzi et al. (2007), which detects a weak-lensing signal out to $\sim 300\,h^{-1}$ kpc at a mean redshift of $z = 0.2$, also shows that the total mass density profile of early-type lens galaxies is consistent with isothermal over two orders of magnitude in radius ($\sim 3 - 300\,h^{-1}$ kpc). The results of Gavazzi et al. (2007) are indicative of the luminous and dark matter components of an early-type galaxy "conspiring" to form a isothermal mass distribution out to large radii; thus, the regime probed by joint strong- and weak-lensing analysis is also comparable to the standard aperture (i.e. R_{200}) utilized in this study. Therefore, our assumption of the isothermal nature of early-type lens galaxies, to estimate M_{200} as a proxy for total mass, is justified. We also observe a relationship of $\log(M_{einst}/M_{200}) \propto \log(R_{einst}/R_{200})$, consistent with the fact that an aperture corrected mass measurement does not affect the observed $M_{bh} - M_{tot}$ relation. Furthermore, the use of M_{200} as a tracer of total mass is also consistent with theoretical studies of the $M_{bh} - M_{tot}$ relation (Croton 2009).

To obtain the associated 1-σ error of M_{200}, we use Gaussian error propagation adopting an empirical error of 2% on the measured Einstein radii following Bolton et al. (2008a) ($\langle \delta \log(M_{200}) \rangle \approx 0.01$ dex). Table 1 lists the unique SDSS identifiers for SLACS lenses, redshift of the lens galaxy for each system and the derived values of

M_{200} (hereafter denoted as M_{tot}) for each lensing system.

2.3.2 Estimating SMBH Masses Using Stellar Velocity Dispersion

We first use the $M_{bh} - \sigma_\star$ relation to estimate M_{bh} of the early-type lens sample. The velocity dispersion measurements are derived from the 3.″0 SDSS spectroscopic fiber. The SDSS velocity dispersion measurements are corrected to a standard aperture, of radius equal to $r_e\,/\,8$, using the power-law relation by Jorgensen et al. (1995), similar to previous SMBH and FP studies (Ferrarese & Ford 2005; Treu et al. 2006). The mean difference between SDSS velocity dispersion measurements and the aperture corrected measurements (hereafter denoted as $\sigma_\star$) are $\sim 4\%$; therefore, the aperture correction does not significantly influence the overall form of the $M_{bh} - M_{tot}$ relation discussed in the following sections. We use $M_{bh} - \sigma_\star$ relation by Gültekin et al. (2009), obtained from measurements of M_{bh} from dynamically detected central black holes:

$$\log(M_{bh}/M_\odot) = (8.12 \pm 0.08) + (4.24 \pm 0.41)\log(\sigma_\star/200\,\mathrm{km\,s^{-1}}) \qquad (2.7)$$

with an intrinsic scatter of $\varepsilon_0 = 0.44$ dex.

We assume that errors on $\sigma_\star$ and best-fit coefficients of the $M_{bh} - \sigma_\star$ relation are uncorrelated and use Gaussian error propagation to determine the 1-σ error on the quantity $\log(M_{bh})$[3]. The values of $\sigma_\star$ and its associated error for each lens system and SMBH mass estimates obtained from $M_{bh} - \sigma_\star$ relation are listed in Table 1.

2.3.3 Estimating SMBH Masses Using the Sérsic Index

We also attempt to use the $M_{bh} - n$ relation to estimate M_{bh} of the SLACS lens sample (Graham et al. 2001; Graham & Driver 2007). We perform a careful and detailed decomposition of *HST* ACS images to obtain the Sérsic indices of the SLACS lens galaxies. Although our sample of lens galaxies were observed in at least two ACS filters, mainly F814W and F435W, we exclusively use F814W (Broad I-band) data

[3] $\delta(\log(M_{bh})) = \sqrt{0.08^2 + (\log(\sigma_\star/200\,\mathrm{km\,s^{-1}}))^2\,(0.41^2) + (\delta\log(\sigma_\star/200\,\mathrm{km\,s^{-1}}))^2\,(4.24^2) + 0.44^2}$

due to high SNR of the images. Furthermore, redder magnitudes are a better tracer of mass in comparison to B-band magnitudes. To keep our decomposition method consistent with that of Graham & Driver (2007), we use a two-component model to describe the surface brightness profiles of SLACS lens galaxies. In addition to the general Sérsic profile (given by equation 2.1), to describe the surface brightness of the bulge component in each galaxy, we include a second disk component characterized by a simple exponential profile:

$$\Sigma(\mathrm{r}) = \Sigma_0 \exp(-\mathrm{r}/\mathrm{r_d}) \tag{2.8}$$

where $\Sigma(r)$ is the surface brightness at radius r and r_d is the characteristic exponential scale length.

To obtain the best possible accuracy of the data analysis process, we take particular care during all intermediate steps leading to the bulge-disk composition. Therefore, we obtain the raw images and perform careful cosmic ray removal, distortion correction, manual mask production and determination of the best possible instrumental PSF. We obtain the ACS images from the *HST* archive at The Canadian Astronomy Data Centre (CADC), where the images are processed by CALACS calibration software. Imaging data from programs 10174 and 10587 are 420 s single-exposure snapshot data; therefore, we perform an additional cosmic ray identification step using the L.A.Cosmic software, LACOS (van Dokkum 2001), which distinguishes between undersampled sources and cosmic rays. We then use the MULTIDRIZZLE reduction package (Koekemoer et al. 2003) to obtain distortion-free ACS images, where the distortion solution is applied to correct all pixels to equal areas.

We use the photometry package SExtractor (Bertin & Arnouts 1996) to produce a catalog of galaxies in each ACS image. Furthermore, we use the segmentation images generated by SExtractor, which deblends each source in the field, to produce manual masks of the lensed features around the early-type galaxy before lens modeling. We perform the two-dimensional decomposition of each early-type lens galaxy using Galaxy IMage 2D (GIM2D), which is publicly available to users (Simard et al. 2002). GIM2D uses the Metropolis Algorithm to derive the best-fit parameter values and confidence intervals, for a surface brightness model of choice, through Monte-Carlo sampling of the likelihood function. Since our surface brightness model consists of a bulge and a disk component, we explore the full range of lens galaxy bulge fraction

(B/T = 0.0 - 1.0) such that the Metropolis Algorithm converges to an accurate quantitative morphology of galaxies classified as E/S0-types. On average, we find that most SLACS lens galaxies have a significant bulge component ($\langle$ B/T $\rangle \approx 0.73$) and a bulge plus disk light profile produces a better fit to the lens galaxy, significantly minimizing the residuals when the galaxy model is subtracted from the input galaxy image.

For GIM2D lens models, we take particular care to define the instrumental PSF, which is extremely position- and time- dependent for the ACS. We investigate a variety of models to determine the most suitable PSF for convolution with GIM2D galaxy models. The PSF models are as follows.

1. A star extracted from the field.
2. A PSF produced at the location of the galaxy, in the non-drizzled image, using Tiny Tim software (Krist 1993). We insert the Tiny Tim generated PSF into an empty ACS-WFC field, at the location of the galaxy, and multidrizzle the resulting image to obtain a distortion-free PSF model.
3. A PSF produced at the location of the galaxy using the principle component analysis (PCA) models in the ACS PSF library (Jee et al. 2007).

We examined the residual images produced by subtracting the lens galaxy surface brightness model, each convolved with the PSF models described above, to determine the best-fit PSF for GIM2D lens modeling. The PSF model produced from the ACS library gives the best results, minimizing the core residuals for a fixed surface brightness model. Therefore, we extract the Sérsic indices from the best-fit bulge plus disk decomposition, using the ACS PSF library model for convolution. An example of the difference between residual images produced by various PSF models are shown in Figure 2.5.

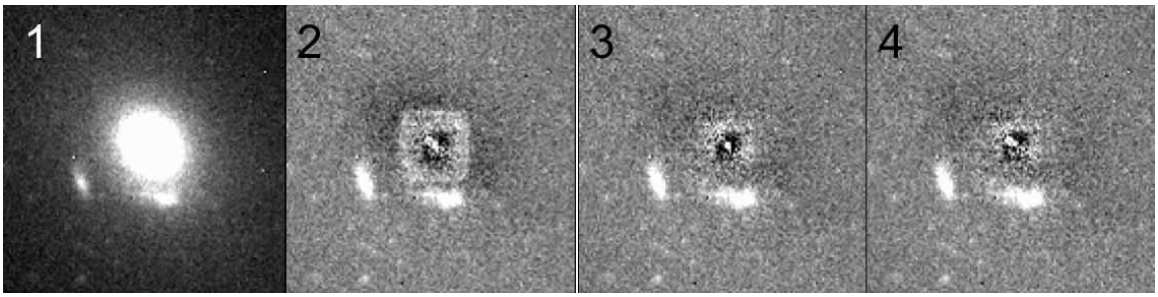

Figure 2.5 Comparison of varying PSFs on GIM2D galaxy models. Panel 1 shows the *HST* ACS image of an example SLACS lens. The contrast of panel 1 is adjusted to show multiple, lensed features around the early-type galaxy. Panels 2, 3, and 4 show the residual images after GIM2D surface brightness model convolved with a Tiny-Tim PSF (panel 2), natural PSF (panel 3) and ACS-library generated PSF (panel 4) is subtracted from the observed image. Residual image where the galaxy model is convolved with a Tiny-Tim PSF shows artifacts such as boxy-core feature, due to the finite size of the Tiny-Tim PSF, evident in panel 2. Statistics of the pixels in panel 2 show that the mean value of the core residuals is comparable to the background level; therefore, the artifact introduced by the finite Tiny-Tim PSF does not significantly affect the quality of the overall fit. In general, we find that both natural and ACS-library generated PSFs produce minimal core residuals. However, most SLACS fields are relatively devoid of stars, suitable for convolution; therefore, we use ACS-library generated PSF for GIM2D galaxy modeling.

We also examine the reliability of the bulge-disk decomposition by comparing our results for the SLACS lens sample to the scaling relations for bulge components of the SDSS galaxies. Since SLACS lenses were initially derived from SDSS LRG and MAIN samples (Eisenstein et al. 2001; Strauss et al. 2002), structural parameters measured from ACS imaging should be in agreement with that of the SDSS bulge population. Figure 2.6 shows the comparison of effective bulge radius (R_e), absolute I-band magnitude of the bulge component ($M_{I,bulge}$) and aperture-corrected bulge velocity dispersion (σ_{ap}) of the SLACS lens galaxies to the SDSS bulge parameters. We construct the scaling relations for SDSS galaxies from the bulge-disk decomposition of 77523 galaxies (provided by Luc Simard) and velocity dispersions from the SDSS database. The structural parameters derived from ACS imaging are in good agreement with those of SDSS galaxies, which confirms the accuracy of our bulge-disk decomposition (in addition to the minimal residuals seen in the galaxy images after subtracting the galaxy models). The outlier in Figure 2.6 is SDSS J0959 + 0410, a disk galaxy with a small bulge fraction (B/T = 0.14). Previous studies, which examine the positions of bulges with disk-like features (also referred to as *pseudobulges*) in structural parameter space find that pseudobulges with low B/T deviate from the scaling relations of classical bulges (Fisher & Drory 2008).

Using the best-fit parameter for n (of the bulge component) from GIM2D models,

we estimate the SMBH masses using the log-quadratic $M_{\rm bh} - n$ relation (Graham & Driver 2007):

$$\log(\mathrm{M_{bh}}/\mathrm{M_\odot}) = (7.98 \pm 0.09) + (3.70 \pm 0.46)\log(n/3)\cdots \\ -(3.10 \pm 0.84)[\log(n/3)]^2 \tag{2.9}$$

with an intrinsic scatter of $\varepsilon_0 = 0.18$ dex. Similar to Graham & Driver (2007), we assume a measurement error of 20% on the values of n to obtain the 1-σ error on $\log(\mathrm{M_{bh}})$ as shown:

$$\delta\log(\mathrm{M_{bh}}) = \sqrt{\mathrm{x}^4 + \frac{\mathrm{x}^2}{4} + 0.09^2 + \frac{[3.70 - 6.20\,\mathrm{x}]^2\,(\delta \mathrm{n}/\mathrm{n})^2}{(\ln 10)^2} + 0.18^2}, \tag{2.10}$$

where $\mathrm{x} = \log(n/3)$. Table 1 lists the Sérsic indices and bulge fractions of the SLACS lenses from GIM2D modeling, estimates of $\mathrm{M_{bh}}$ for each lens system.

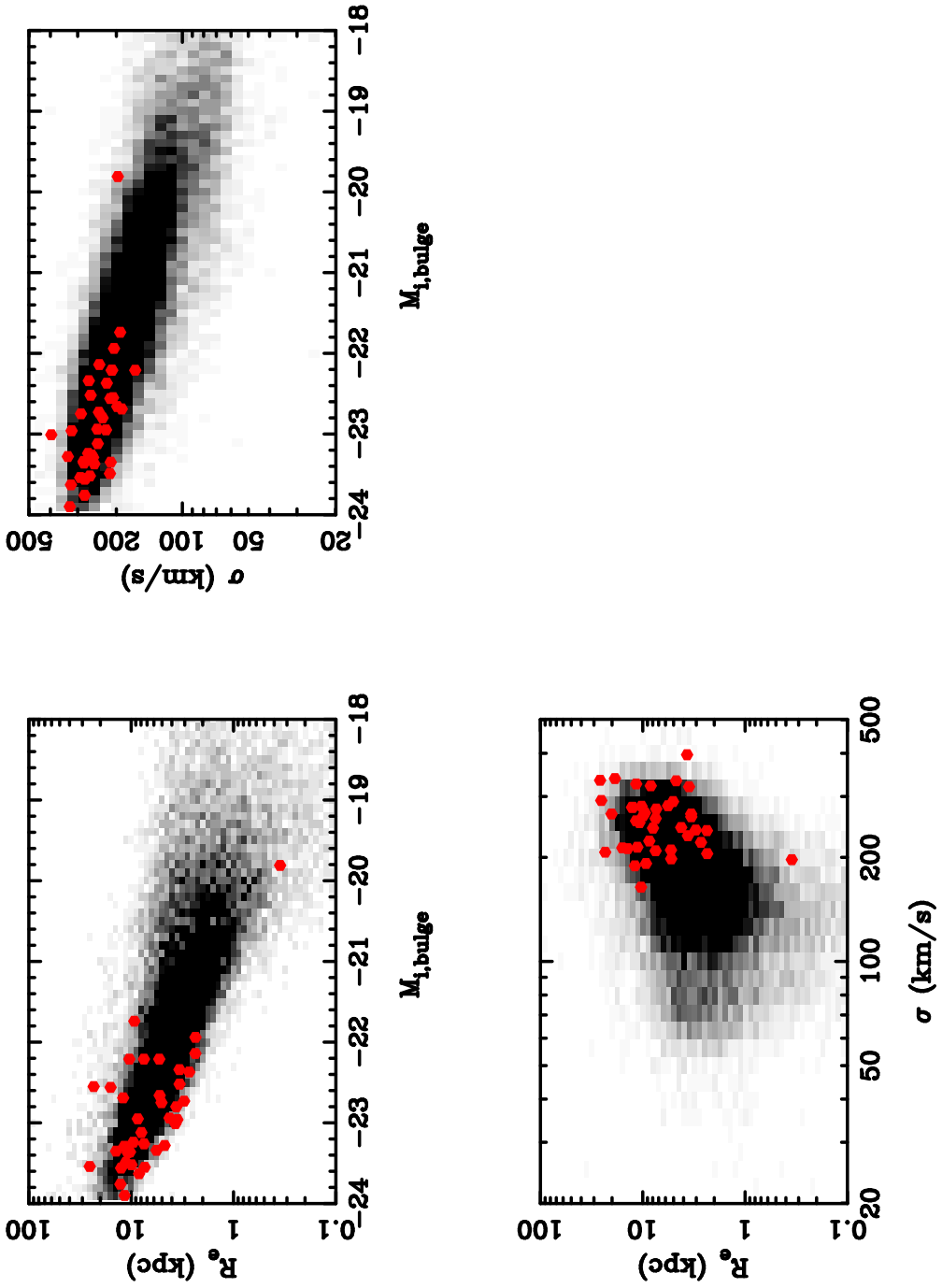

Figure 2.6 Comparison of SLACS lens galaxy measurements to the scaling relations for bulge components of SDSS galaxies. The red circles indicate the best-fit values for the following structural parameters of the SLACS lenses: effective bulge radius (R_e), absolute I-band magnitude of the bulge ($M_{I,bulge}$) and aperture corrected bulge velocity dispersion (σ). The scaling relations for the bulge components of SDSS early-type galaxies are constructed from a sample 77523 galaxies and are shown with the gray-scale. The gray-scale is scaled to 20% of the peak value of the central distribution to show that the structural parameters of the SLACS lenses lie well within the distribution that encompasses the SDSS galaxies. The outlier in this figure is SDSS J0959 + 0410.

Table 1. SLACS lens galaxy sample and its SMBH properties

System (1)	z_{lens} (2)	b_{frac} (3)	Sérsic (n) (4)	$M_{bh,n}$ ($M_\odot$) (5)	σ_{ap} (km/s) (6)	$M_{bh,\sigma}$ ($M_\odot$) (7)	M_{200} ($M_\odot$) (8)
SDSS J0029-0055	0.23	0.76	6.41 ± 1.28	7.29×10^8	235.86 ± 18.54	2.65×10^8	1.04×10^{13}
SDSS J0037-0942	0.20	0.94	4.47 ± 0.89	3.38×10^8	282.43 ± 14.17	5.69×10^8	2.40×10^{13}
SDSS J0216-0812	0.33	0.43	2.91 ± 0.58	8.50×10^7	356.24 ± 24.61	1.52×10^9	4.03×10^{13}
SDSS J0252+0039	0.28	0.58	10.64 ± 2.12	1.19×10^9	169.18 ± 12.38	6.48×10^7	1.27×10^{13}
SDSS J0330-0020	0.35	0.88	7.85 ± 1.85	9.65×10^8	217.42 ± 21.54	1.88×10^8	1.51×10^{13}
SDSS J0728+3835	0.21	0.95	6.36 ± 1.27	7.21×10^8	218.03 ± 11.21	1.90×10^8	1.73×10^{13}
SDSS J0737+3216	0.32	0.85	6.10 ± 1.22	6.70×10^8	341.91 ± 17.20	1.28×10^9	2.41×10^{13}
SDSS J0822+2652	0.24	0.81	4.98 ± 1.00	4.41×10^8	269.55 ± 15.61	4.67×10^8	2.00×10^{13}
SDSS J0912+0029	0.16	1.00	3.30 ± 0.66	1.35×10^8	329.39 ± 16.17	1.09×10^9	4.36×10^{13}
SDSS J0935-0003	0.35	0.27	2.75 ± 0.55	6.89×10^7	428.32 ± 37.36	3.33×10^9	4.46×10^{13}
SDSS J0936+0913	0.19	0.79	5.88 ± 1.18	6.27×10^8	250.43 ± 12.37	3.42×10^8	1.48×10^{13}
SDSS J0946+1006	0.22	0.40	2.19 ± 0.44	2.61×10^7	284.95 ± 22.75	5.91×10^8	2.32×10^{13}
SDSS J0955+0101	0.11	0.77	8.57 ± 1.71	1.05×10^9	193.13 ± 13.08	1.14×10^8	1.21×10^{13}
SDSS J0956+5100	0.24	0.90	7.72 ± 1.54	9.48×10^8	330.61 ± 16.83	1.11×10^9	3.24×10^{13}
SDSS J0959+0410	0.13	0.14	2.09 ± 0.42	2.10×10^7	226.97 ± 14.98	2.25×10^8	1.08×10^{13}
SDSS J0959+4416	0.24	0.64	3.65 ± 0.73	1.87×10^8	259.69 ± 20.22	3.99×10^8	1.65×10^{13}
SDSS J1020+1122	0.28	0.58	4.38 ± 0.88	3.20×10^8	298.15 ± 19.03	7.16×10^8	2.76×10^{13}
SDSS J1029+0420	0.10	0.84	5.87 ± 1.17	6.24×10^8	215.58 ± 11.29	1.81×10^8	9.82×10^{12}
SDSS J1106+5228	0.10	0.79	5.70 ± 1.14	5.90×10^8	273.07 ± 13.55	4.94×10^8	1.49×10^{13}
SDSS J1112+0826	0.27	0.67	2.62 ± 0.52	5.63×10^7	344.43 ± 21.53	1.32×10^9	3.08×10^{13}
SDSS J1134+6027	0.15	0.53	3.44 ± 0.69	1.55×10^8	256.76 ± 12.89	3.80×10^8	1.51×10^{13}
SDSS J1142+1001	0.22	0.48	3.71 ± 0.74	1.98×10^8	238.99 ± 23.79	2.81×10^8	1.68×10^{13}
SDSS J1143-0144	0.11	0.90	3.38 ± 0.68	1.46×10^8	269.91 ± 13.04	4.70×10^8	2.52×10^{13}
SDSS J1204+0358	0.16	0.72	4.96 ± 0.99	4.37×10^8	283.45 ± 18.05	5.78×10^8	1.72×10^{13}
SDSS J1205+4910	0.22	0.78	5.58 ± 1.12	5.66×10^8	287.77 ± 14.34	6.17×10^8	2.37×10^{13}
SDSS J1213+6708	0.12	0.89	10.41 ± 2.08	1.19×10^9	283.14 ± 14.54	5.76×10^8	1.70×10^{13}
SDSS J1250+0523	0.23	0.70	8.57 ± 1.71	1.05×10^9	258.15 ± 14.34	3.89×10^8	1.46×10^{13}
SDSS J1402+6321	0.20	1.00	5.94 ± 1.19	6.38×10^8	265.73 ± 16.92	4.40×10^8	2.61×10^{13}
SDSS J1403+0006	0.19	0.66	10.23 ± 2.05	1.18×10^9	213.50 ± 17.04	1.74×10^8	1.18×10^{13}
SDSS J1416+5136	0.30	0.55	2.67 ± 0.53	6.07×10^7	260.54 ± 27.14	4.04×10^8	2.31×10^{13}
SDSS J1420+6019	0.06	0.75	3.27 ± 0.65	1.29×10^8	213.46 ± 10.41	1.74×10^8	9.39×10^{12}
SDSS J1430+4105	0.29	0.74	4.28 ± 0.86	3.00×10^8	335.24 ± 33.32	1.18×10^9	3.76×10^{13}
SDSS J1443+0304	0.13	0.89	10.04 ± 2.01	1.17×10^9	213.43 ± 11.23	1.74×10^8	9.46×10^{12}
SDSS J1451-0239	0.13	0.93	5.49 ± 1.10	5.46×10^8	225.94 ± 14.18	2.21×10^8	1.17×10^{13}
SDSS J1525+3327	0.36	0.58	4.40 ± 0.88	3.23×10^8	274.71 ± 27.05	5.06×10^8	3.03×10^{13}
SDSS J1531-0105	0.16	1.00	5.45 ± 1.09	5.37×10^8	280.78 ± 14.09	5.55×10^8	2.35×10^{13}
SDSS J1538+5817	0.14	0.86	9.31 ± 1.86	1.12×10^9	189.86 ± 12.05	1.06×10^8	1.17×10^{13}
SDSS J1627-0053	0.21	0.67	4.42 ± 0.88	3.27×10^8	305.19 ± 15.79	7.91×10^8	2.11×10^{13}
SDSS J1630+4520	0.25	0.86	4.11 ± 0.82	2.68×10^8	287.64 ± 16.67	6.15×10^8	3.02×10^{13}
SDSS J1636+4707	0.23	0.64	3.29 ± 0.66	1.33×10^8	247.07 ± 16.04	3.23×10^8	1.53×10^{13}
SDSS J2238-0754	0.14	0.80	4.49 ± 0.88	3.41×10^8	205.23 ± 11.40	1.47×10^8	1.44×10^{13}
SDSS J2303+1422	0.16	0.97	4.13 ± 0.83	2.71×10^8	257.14 ± 16.13	3.83×10^8	2.57×10^{13}
SDSS J2341+0000	0.19	0.52	7.43 ± 1.49	9.02×10^8	204.24 ± 12.83	1.44×10^8	1.87×10^{13}

Note. — Col. (1): The unique SDSS spectrum identifier for the lens system. Col (2): Redshift of the early-type lens galaxy (Bolton et al. 2008a) Col. (3): Bulge fraction of the early-type galaxy from the best-fit bulge-disk decomposition. Col (4): The bulge Sérsic index from the best-fit bulge-disk galaxy decomposition. Col. (5): Black hole mass estimated from the $M_{bh} - n$ relation. The 1-σ error on the quantity $\log(M_{bh,n})$ is a function of n and its measurement errors and can be computed as shown by Graham & Driver (2007). Col. (6): Velocity dispersion of the lens galaxy, from the SDSS database corrected to a standard aperture of $r_e/8$. Col. (7): Black hole mass estimated from the $M_{bh} - \sigma$ relation. The 1-σ error on the quantity $\log(M_{bh,\sigma_\star})$ is a function of $\sigma_\star$ and its measurement errors and can computed following a similar methodology to Graham & Driver (2007). Col. (8): Total mass of the lensing galaxy within the projected radius of R_{200}, where mass profile of the lensing galaxy is derived from the lens modeling results of Bolton et al. (2008a). The typical 1-σ error on the quantity $\log(M_{tot})$ is ≈ 0.01 dex.

2.4 Results

2.4.1 $M_{bh,\sigma_\star}$ – M_{tot} Relation

In the following section, we combine the correlation between the primary observable quantities ($\sigma_\star - M_{tot}$ relation) with $M_{bh} - \sigma_\star$ relation to derive the $M_{bh} - M_{tot}$ relation. A tight correlation between the quantities $\log(\sigma_\star/200\,\mathrm{km\,s^{-1}})$ and $\log(M_{tot})$ is apparent from Figure 2.7. From Spearman's rank test, we obtain a correlation coefficient (r_s) of 0.84 (degrees of freedom = 41), which indicates a strong positive correlation between the quantities $\log(\sigma_\star/200\,\mathrm{km\,s^{-1}})$ and $\log(M_{tot})$, with a 99.99% confidence level that the correlation has not occurred by chance.

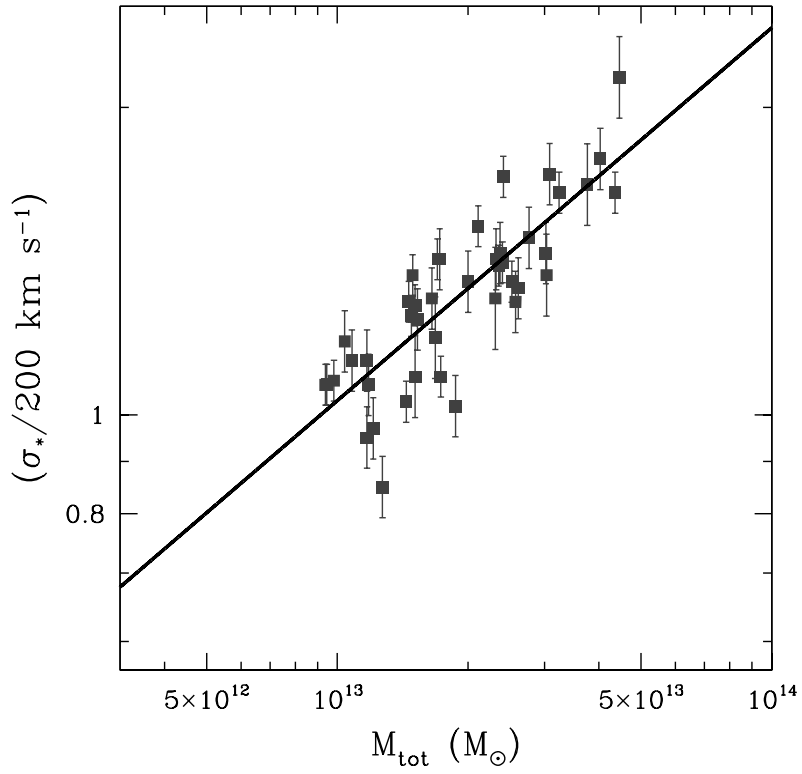

Figure 2.7 The correlation between $\sigma_\star$ and M_{tot}, for the sample of early-type SLACS lenses. Velocity dispersion values from SDSS pipeline are corrected to an aperture of radius equal to $r_e/8$ using the empirical relation of Jorgensen et al. (1995). The error bars correspond to the 1-σ error of the aperture corrected velocity dispersion, from Gaussian error propagation, taking the measurement errors of SDSS velocity dispersions into account. Total masses of the SLACS lenses are derived from strong lens modeling parameters of Bolton et al. (2008a). The 1-σ errors of M_{tot}, which are smaller than the data points, are incorporated into the fitting routines but not shown in this plot. The solid line correspond to the best-fit $\sigma_\star - M_{tot}$ relation for all SLACS lenses in the logarithmic space.

To quantify this correlation, we use the χ^2-fitting routine by Weiner et al. (2006), which implements a generalized form of the least-squares fitting routine by Press et al. (1992). Weiner et al. (2006) routine accounts for intrinsic scatter (ε_0) beyond the observational errors, for a relation of interest, by adding ε_0 in quadrature to the error in the dependent variable. Initial fits to the observed relation between $\log(\sigma_\star/200\mathrm{kms}^{-1})$ and $\log(\mathrm{M_{tot}})$, incorporating observational errors in both variables, gives a large reduced χ^2 value ($\chi_{\mathrm{red}}{}^2 \approx 3.0$) indicative of intrinsic scatter in the relation. Therefore, we perform the fits by incorporating observational errors in both variables and intrinsic scatter in the y-variable. The value of ε_0 is determined by requiring that $\chi_{\mathrm{red}}{}^2$ is unity. The results of the fitting routine gives the following best fit correlation:

$$\log\left(\sigma_\star/200\,\mathrm{km\,s^{-1}}\right) = (0.014 \pm 0.013) + (0.365 \pm 0.038)[\log\left(\mathrm{M_{tot}}/\mathrm{M_\odot}\right) - 13.0] \quad (2.11)$$

with an intrinsic scatter of 0.037 dex in $\log(\sigma_\star/200\,\mathrm{km\,s^{-1}})$. Combining equations 2.7 and 2.11, we derive the following $\mathrm{M_{bh}} - \mathrm{M_{tot}}$ relation:

$$\log\left(\mathrm{M_{bh}}/\mathrm{M_\odot}\right) = (8.18 \pm 0.11) + (1.55 \pm 0.31)\,[\log\left(\mathrm{M_{tot}}/\mathrm{M_\odot}\right) - 13.0] \quad (2.12)$$

Figure 2.8 shows $\sigma_\star$ transformed into SMBH masses using equation 2.7. We assume that measurement errors of the velocity dispersions and best-fit coefficients of the $\mathrm{M_{bh}} - \sigma_\star$ relation are uncorrelated and use Gaussian error propagation to determine the 1-σ error on the quantity $\log(\mathrm{M_{bh}})$. We also perform a direct fitting step to $\mathrm{M_{tot}}$ and the secondary observable quantity, $\mathrm{M_{bh}}$, to confirm the validity of the derived $\mathrm{M_{bh}} - \mathrm{M_{tot}}$ relation. We find $\log(\mathrm{M_{bh}}/\mathrm{M_\odot}) = \alpha + \beta(\log(\mathrm{M_{tot}}/\mathrm{M_\odot}) - 13.0)$ with $(\alpha, \beta) = (8.17 \pm 0.13, 1.57 \pm 0.39)$ and $\chi_{\mathrm{red}}{}^2 \approx 0.2$, which is in agreement with the result shown in equation 2.12.

2.4.2 $\mathrm{M_{bh,n}} - \mathrm{M_{tot}}$ Relation

In this section, we discuss the $n - \mathrm{M_{tot}}$ relation of the SLACS lenses, shown in Figure 2.9, and Figure 2.10 which shows n converted to SMBH masses using equation 2.10 (Graham & Driver 2007). Similar to §2.4.1, we use Gaussian error propagation (assuming a measurement error of 20% on n) with intrinsic scatter of the $\mathrm{M_{bh}} - \mathrm{M_{tot}}$ relation ($\varepsilon_0 = 0.18$ dex) added in quadrature, to determine the 1-σ error of the quan-

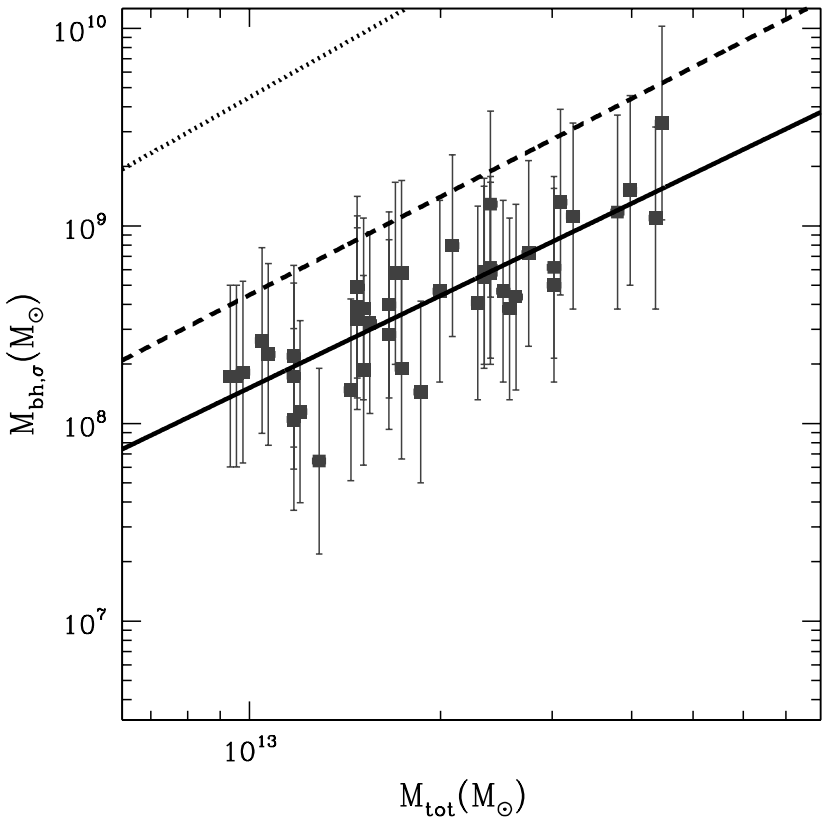

Figure 2.8 Same as Figure 2.7 with $\sigma_\star$ converted into M_{bh} using $M_{bh} - M_{tot}$ relation (Gültekin et al. 2009). The error bars correspond to 1-σ error on the quantity $\log(M_{bh})$. The solid line corresponds to the $M_{bh} - M_{tot}$ relation for all SLACS lenses derived using the $\sigma_\star - M_{tot}$ and $M_{bh} - M_{tot}$ relations. The dashed line represents the resulting $M_{bh} - M_{tot}$ relation obtained by Ferrarese (2002), where M_{tot} is computed from cosmological simulations (Bullock et al. 2001) relating the the observed circular velocity ($v_{c,obs}$) to the virial velocity of the host halo (v_{vir}). The dotted line shows the resulting $M_{bh} - M_{tot}$ relation if M_{tot} is computed using $v_{c,obs} = 1.8\, v_{vir}$ (Ferrarese 2002).

tity $\log(M_{bh})$. Results of Graham & Driver (2007) indicate that $M_{bh} - n$ relation is comparable to the $M_{bh} - \sigma_\star$ relation; therefore, we expect both scaling relations to yield $M_{bh} - M_{tot}$ relations with similar level of scatter. If the expected equivalence between $M_{bh} - n$ and $M_{bh} - \sigma_\star$ relations hold, we can then extend the $M_{bh} - M_{tot}$ relation to gravitational lens samples which span a higher dynamical range in the total mass at various redshifts. Unfortunately, however, the trends observed in Figures 2.9 and 2.10 are very different from the strong positive correlations shown in Figures 2.7 and 2.8.

From a Spearman's rank test, we obtain a weak negative $n - M_{tot}$ correlation

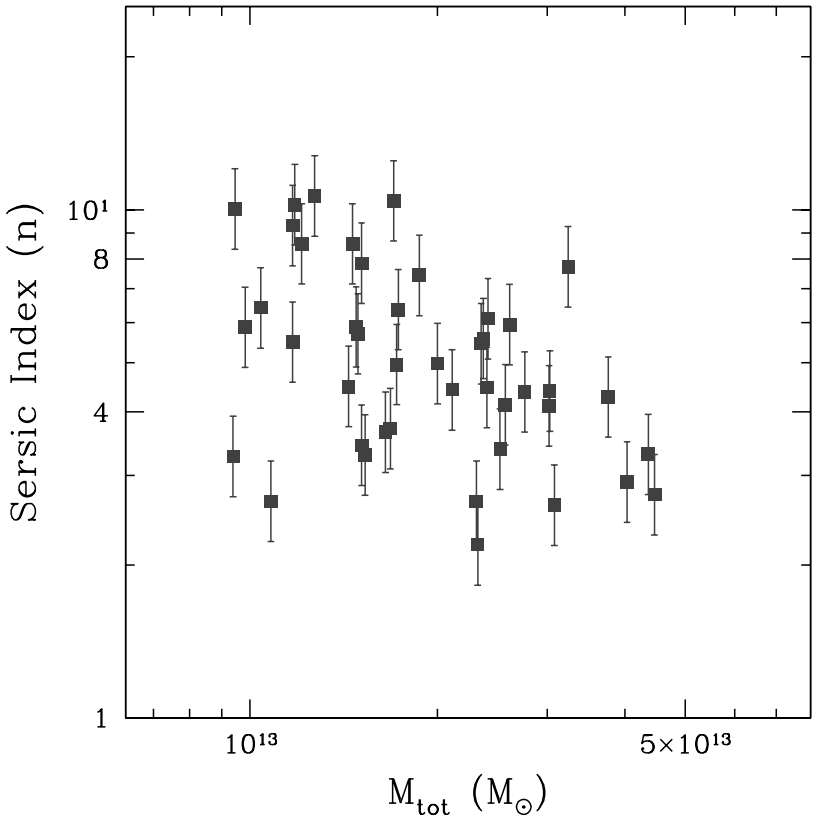

Figure 2.9 The correlation between bulge n and M_{tot}, for the sample of early-type SLACS lens galaxies. The Sérsic indices are derived from the best-fit bulge+disk decomposition of the SLACS lenses. The error bars correspond to the measurement errors on the quantity n. Total masses of the SLACS lenses are derived from strong lens modeling parameters of Bolton et al. (2008a). The 1-σ errors of M_{tot}, which are smaller than the data points, are incorporated into the fitting routines but not shown in this plot.

($r_s \approx -0.42$ for degrees of freedom = 41) for the trend observed in Figure 2.9 with only a 95% confidence level that the correlation has not occurred by chance. A Spearman's rank test performed on the $M_{bh} - M_{tot}$ relation shows similar statistical properties to that of the $n - M_{tot}$ relation. Before concluding if the correlation observed in Figure 2.8 is a better representation of a $M_{bh} - M_{tot}$ relation, we investigate various possibilities that may cause the inconsistency observed between Figures 2.8 and 2.10.

First, we attempted to reproduce the $M_{bh} - n$ relation, obtained by Graham & Driver (2007), for the SLACS lens sample. In Figure 2.11, we plot $M_{bh,\sigma_\star}$ values for the SLACS lenses, versus the corresponding Sérsic indices from the bulge-disk decomposition. The log-quadratic $M_{bh} - n$ relation by Graham & Driver (2007) is

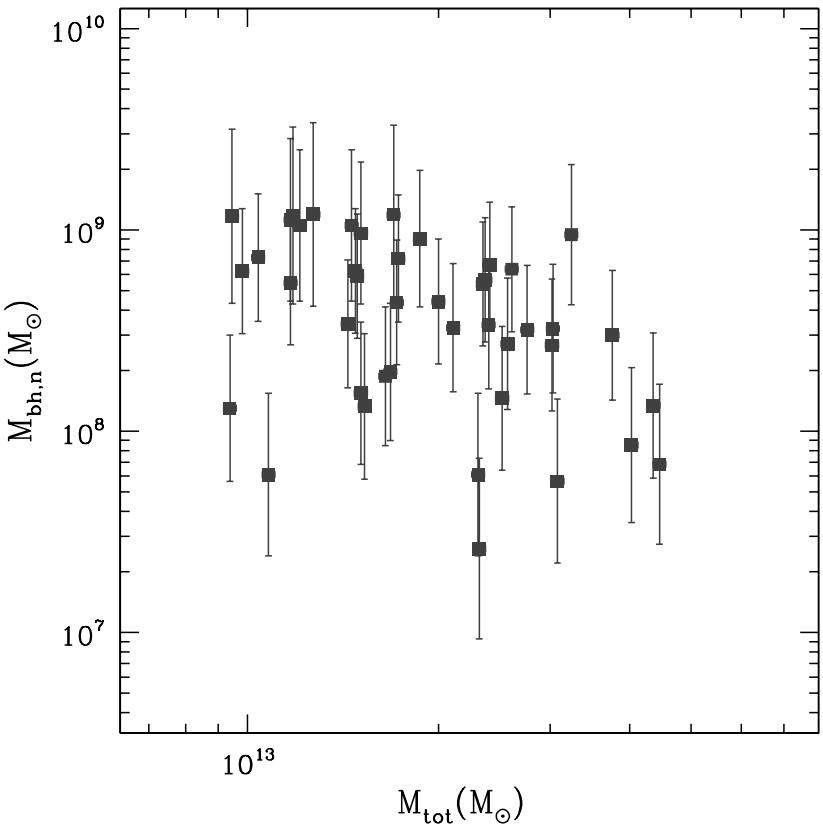

Figure 2.10 Same as Figure 2.9 with n converted into M_{bh} using $M_{bh} - n$ relation (Graham & Driver 2007). The error bars correspond to 1-σ error on the quantity log(M_{bh}).The 1-σ error of M_{tot} is smaller than the data points, and is not shown in the plot.

overlaid on the SLACS data for comparison. Figure 2.11 clearly indicates that the log-quadratic M_{bh} − n relation cannot be reproduced with the $M_{bh,\sigma_\star}$ and n values for the SLACS lens sample. A weak but different correlation between $M_{bh,\sigma_\star}$ and n is apparent from Figure 2.11. We perform a Spearman's rank test and derive a weak, negative correlation, $r_s \approx -0.44$ at the 5% significance level, between these quantities.

The correlation observed in Figure 2.11 is in contrast to the log-linear or log-quadratic $M_{bh} - n$ relation discussed in literature (Graham & Driver 2007). Previous studies of morphology and scaling relations of bulge dominated galaxies indicate that n scales monotonically with the galaxy bulge magnitude (equivalently, bulge luminosity (Ferrarese et al. 2006)). If this correlation holds, we expect n to correlate positively with M_{bh} due the dependence between M_{bh} and L_{bul} (Marconi & Hunt

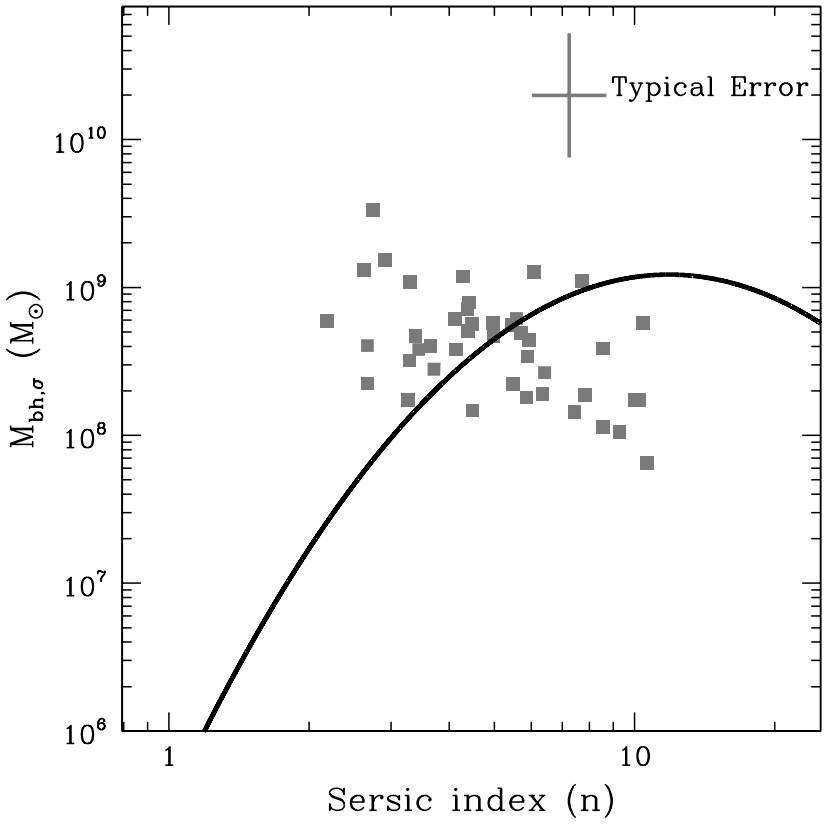

Figure 2.11 Comparison of log-quadratic $M_{bh} - n$ relation to SLACS data. M_{bh} values are derived from the $M_{bh} - \sigma_\star$ relation and Sérsic indices are best-fit results from the GIM2D bulge-disk decomposition. Error bars on the legend represent the typical 1-σ uncertainty of log (M_{bh}), derived from Gaussian error propagation using measurement errors from the SDSS velocity dispersions ($\langle \delta \log (M_{bh}) \rangle \approx 0.42$ dex), and a measurement error of 20% on the quantity n. The log-quadratic relation by Graham & Driver (2007) is shown by the solid black line.

2003; Ferrarese et al. 2006). Since Figure 2.11 contradicts the existence of a log-quadratic $M_{bh} - n$ relation, we also test the correlation between n and I-band bulge magnitude ($M_{bulge,I}$) for the SLACS lens sample. The results of GIM2D bulge-disk decomposition of SLACS galaxies are shown in Figure 2.12. A Spearman's rank test to determine degree of correlation between $M_{bulge,I}$ and n shows that there is only a very weak correlation between the two quantities ($r_s \approx -0.20$); furthermore, the rank correlation we observe between $M_{bulge,I}$ and n is significant at a level larger than 5%.

Although we do not observe a direct correlation between galaxy bulge magnitude and the Sérsic index, our results are limited by the narrow range of absolute magnitudes ($-24 < M_{bulge,I} < -20$) in the SLACS lens sample. Furthermore, our

results are consistent with those of Bolton et al. (2008b), who also find that n for all SLACS lenses is uncorrelated with the measurements of lensing mass, dynamical mass, luminosity and velocity dispersion of the sample. Given the trend observed in Figure 2.12, we cannot confidently expect M_{bh} to correlate with n for the SLACS sample as claimed by previous studies (Graham et al. 2001; Graham & Driver 2007). The possible origin of $M_{bh} - n$ relation has not been examined theoretically and is beyond the scope of this paper. For the remainder of this study, we use the $M_{bh} - \sigma_\star$ relation to determine the black hole masses.

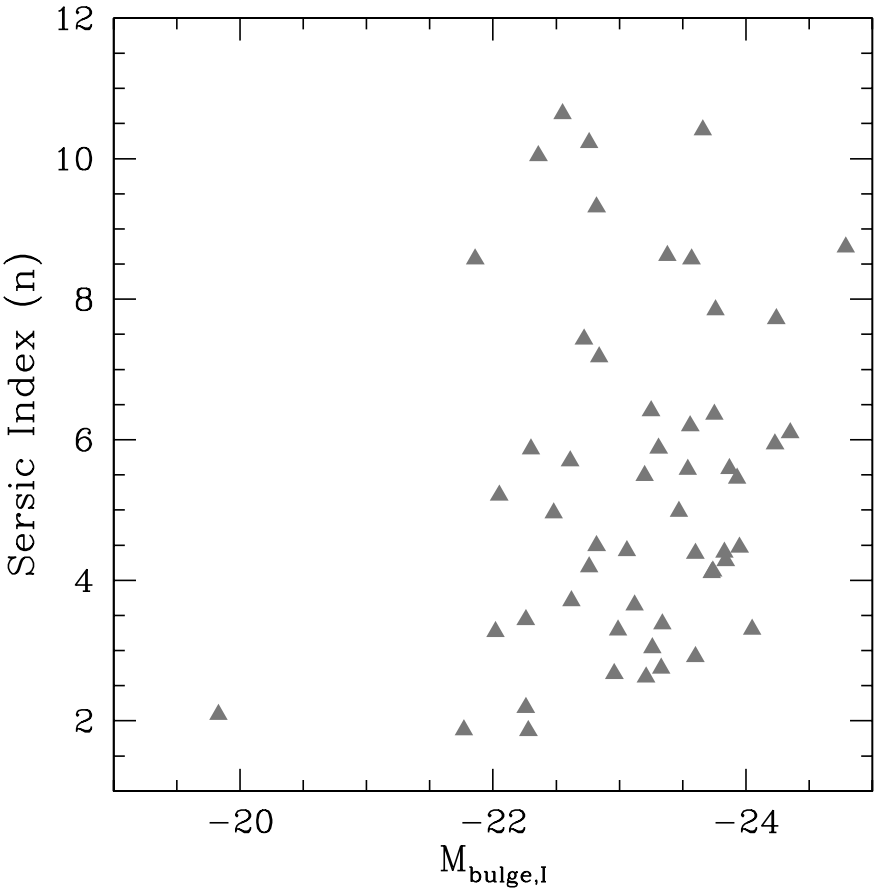

Figure 2.12 The correlation between absolute I-band magnitude ($M_{bulge,I}$) and the Sérsic index (n) of the bulge component for SLACS lens sample. The values of n are best-fit parameters derived from the bulge+disk decomposition using GIM2D. The values of $M_{bulge,I}$ are the best-fit, dust extinction- and k-corrected parameters from the bulge+disk decomposition. The absolute magnitudes are quoted in the AB-magnitude system and we perform the k-correction assuming a E/S0 galaxy template. The I-band Galactic dust extinction correction values for each system, based on Schlegel et al. (1998) maps, were obtained from Bolton et al. (2008a).

2.5 Towards a $M_{BH} - M_{TOT}$ Relation

The correlation observed between M_{bh} and M_{tot}, in Figure 2.8, is in remarkable agreement with theoretical predictions (Croton et al. 2006; Croton 2009; Silk & Rees 1998; Wyithe & Loeb 2002, 2003) and local observations (Ferrarese 2002) of the $M_{bh} - M_{tot}$ relation. In the following section, we compare our results to several black hole formation scenarios posed by various theoretical studies and examine the implications of our findings. Equation 2.12, which quantifies the trend observed in Figure 2.8, shows that M_{bh} scales non-linearly with M_{tot} and that efficiency of black hole formation increases with total mass. Theoretical models that reproduce the observed luminosity function of high-redshift quasars (Adams et al. 2003; Cattaneo 2001; Hopkins et al. 2005b; Springel et al. 2005b; Volonteri et al. 2003) predict that M_{bh} scales as a power law of the circular velocity of the galactic halo (denoted as $v_{c,halo}$ and also referred to as virial velocity) in which the black hole resides:

$$M_{bh} \propto {v_{c,halo}}^{\gamma} \tag{2.13}$$

The $M_{bh} - v_{c,halo}$ relation shown above can be converted into an equivalent $M_{bh} - M_{tot}$ relation by considering the dependence between $v_{c,halo}$ and halo mass (equivalent to M_{tot} in this study), $v_{c,halo} \propto {M_{halo}}^{1/3}$. The resulting correlation between M_{bh} and M_{halo} is as follows:

$$M_{bh} \propto {M_{halo}}^{\gamma/3} \tag{2.14}$$

The circular velocity of a given halo mass is redshift-dependent; therefore, an important aspect of this analytical prediction is the evolution of the $M_{bh} - M_{halo}$ relation with time (Croton 2009; Wyithe & Loeb 2002, 2003).

The slope of the $M_{bh} - M_{halo}$ relation, γ / 3, is a valuable indicator of various formation scenarios which result in observed black hole populations. In the process of hierarchical mass assembly, formation of SMBH is driven by mergers of galaxy haloes. A linear relation between M_{bh} and M_{halo}, where $\gamma = 3$, results from a formation scenario where the black holes residing in the merging haloes coalesce without additional gas accretion. A slope of $\gamma > 3$ is characteristic of a merger where the growth of the resulting black hole is dominated by an accretion process where a

significant gas fraction from the merger product is driven in to the central accreting region (Cattaneo 2001; Cattaneo et al. 1999; Di Matteo et al. 2005, 2003; Haehnelt & Kauffmann 2000; Haehnelt et al. 1998; Wyithe & Loeb 2002, 2003). Within this formation scenario, the fraction of baryons accreted on to the central regions that feed the black hole is significantly larger for more massive haloes, due to a deeper potential well; therefore, massive haloes host larger SMBH.

In Figure 2.13, we plot two analytical predictions for the $M_{bh} - M_{tot}$ relation (Croton 2009; Wyithe & Loeb 2003), which correspond to two formation scenarios, for three different epochs ($z = 0.0, 1.0, 5.0$).

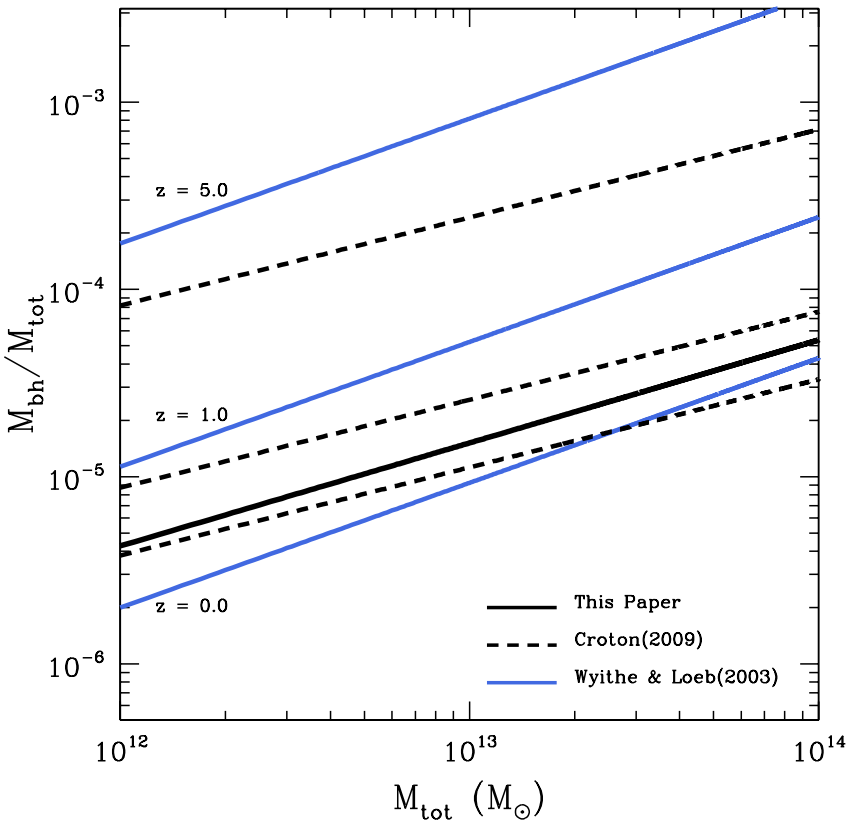

Figure 2.13 The evolution of the $M_{bh} - M_{tot}$ relation from various analytical predictions for $z = 0.0, 1.0, 5.0$. The pale blue, solid lines are predictions from Wyithe & Loeb (2003), where $M_{bh} \propto {M_{tot}}^{1.67}$. The dashed lines are predictions from Croton (2009), where $M_{bh} \propto {M_{tot}}^{1.47}$, for the same epochs as Wyithe & Loeb (2003) (epochs increasing in the same order as shown in the labels for Wyithe & Loeb (2003)). The thick, solid black line is a comparison of the observed $M_{bh} - M_{tot}$ relation from the SLACS lens sample (equation 2.12), at $\langle z \rangle \approx 0.2$.

Both types of evolutionary tracks indicate that M_{bh} increases with the total mass of the host galaxy at any given redshift and that a galaxy of given total mass hosts a more massive black hole at a higher redshift relative to a lower redshift. Within the context of hierarchical mass assembly in ΛCDM cosmology, the decrease in the growth of M_{bh} relative to M_{tot} at lower redshifts can be caused by processes such as a decrease in merger rates and the gas fraction that is available to fuel the central SMBH.

Another important physical process involved in the evolution of $M_{bh} - M_{tot}$ relation is the feed-back regulated growth of SMBH (Di Matteo et al. 2005; Hopkins et al. 2005a; Silk & Rees 1998; Springel et al. 2005a). A black hole shines at a fraction, η, of its Eddington luminosity (L_{Edd}) following a merger and returns a fraction of this energy into the surrounding galactic gas. A black hole shining at its limiting L_{Edd} can unbind the surrounding galactic gas if the energy liberated from the black hole is sufficient to overcome the gravitational binding energy of the gas. As the mass of a black hole increases through merger driven processes discussed above, the energy output can approach the limit where it is sufficient to unbind the entire galactic gas. The unbound galactic gas that escapes into the halo is heated beyond the virial temperature and cannot cool during the dynamical time of the quasar; therefore, this mechanism can eventually terminate the accretion process that feeds the central black hole.

The growth of a SMBH via a merger-driven, feed-back regulated mechanism implies a relation of $M_{bh} \propto {v_{c,halo}}^5$ (the required rate of energy deposition to unbind a self-gravitating system is proportional to ${v_{c,halo}}^5/G$) (Wyithe & Loeb 2002, 2003), leading to a slope of ≈ 1.67 in the $M_{bh} - M_{tot}$ relation. Evolutionary tracks shown in solid blue lines in Figure 2.13 (Wyithe & Loeb 2003) are examples of the formation scenario described above. The evolutionary tracks with a shallower slope, similar to the dashed lines shown in Figure 2.13 (Croton 2009), may be indicative of a modified feed-back regulated growth mechanism. If the galactic gas heated by the energy output of the black hole cools before the black hole reaches its critical Eddington limit, additional energy (up to a factor of $c/v_{c,halo}$) would be required to unbind the cool gas component. This formation scenario leads to dependence of $M_{bh} \propto {v_{c,halo}}^4$, resulting in a slope of ≈ 1.33 in the $M_{bh} - M_{tot}$ relation. It is worth noting that Croton (2009) assumes the $M_{bh} - \sigma_\star$ relation by Tremaine et al. (2002), $M_{bh} \propto \sigma^{4.02}$, which yields a relation of $M_{bh} \propto {M_{tot}}^{1.39}$. Therefore, we recompute the results of Croton (2009)

using the $M_{bh} - \sigma_\star$ relation used throughout this study (Gültekin et al. 2009), which gives a dependence of $M_{bh} \propto {M_{tot}}^{1.47}$.

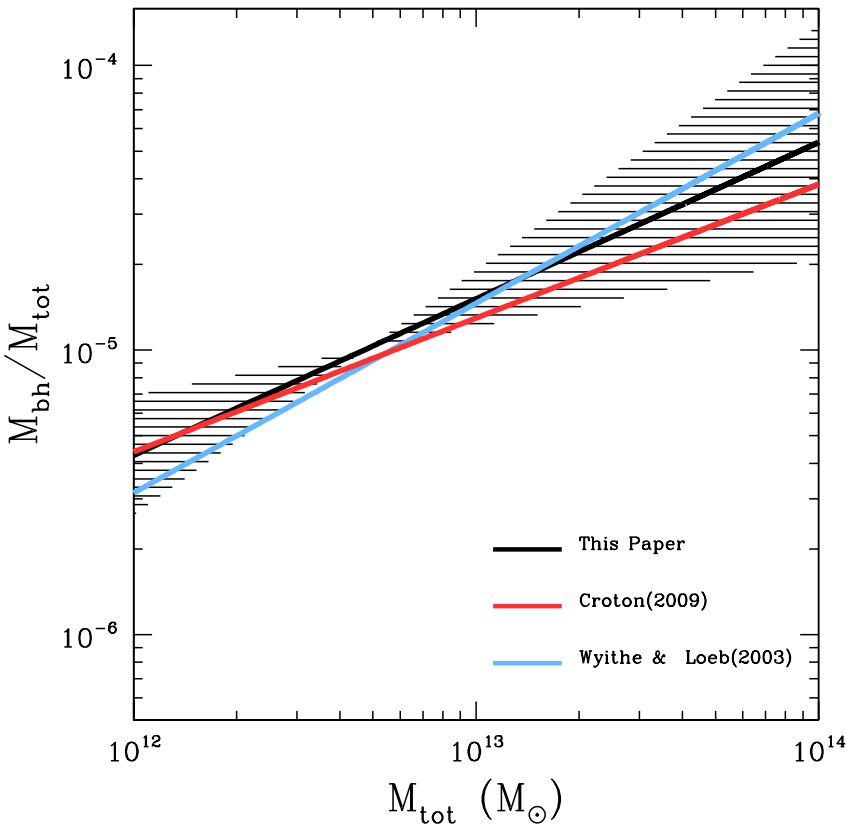

Figure 2.14 Comparison of the observational $M_{bh} - M_{tot}$ relation to theoretical predictions of the $M_{bh} - M_{tot}$ relation at $z = 0.2$, the mean redshift of the SLACS lens sample. The solid black line correspond to the best-fit result from this study and the shaded region shows the 1-σ upper and lower limits of the $M_{bh} - M_{tot}$ relation. The solid red and blue lines correspond to the theoretical predictions of Croton (2009) and Wyithe & Loeb (2003) of the $M_{bh} - M_{tot}$ relation respectively.

Within the context of formation and evolution of SMBH, it is extremely important to accurately determine the parameters that quantify the slope and the evolution of $M_{bh} - M_{tot}$ relation. These parameters provide significant insight into the dominant formation scenarios that lead to the observed black hole populations at various redshifts. Due to the narrow range of redshifts in the SLACS lens sample, the $M_{bh} - M_{tot}$ relation we derive can be considered as an evolutionary track for the mean redshift of the SLACS sample ($\langle z \rangle \approx 0.2$), as shown in Figure 2.13 (solid black line). The $M_{bh} - M_{tot}$ relation we derive from the SLACS lens sample provides a unique opportunity to compare the theoretical tracks with observational evidence of

the $M_{bh} - M_{tot}$ relation. This is shown in Figure 2.14, where we compare the observational $M_{bh} - M_{tot}$ relation to the theoretical predictions of the $M_{bh} - M_{tot}$ relation at $z = 0.2$. The dashed region indicates the upper and lower 1-σ bounds of the observational form of the $M_{bh} - M_{tot}$ relation found in this study. Inspection of Figure 2.14 shows that our results are in excellent agreement with analytical predictions of feedback regulated growth. However, from our results, it is difficult to distinguish the importance of gas cooling in the black hole formation process.

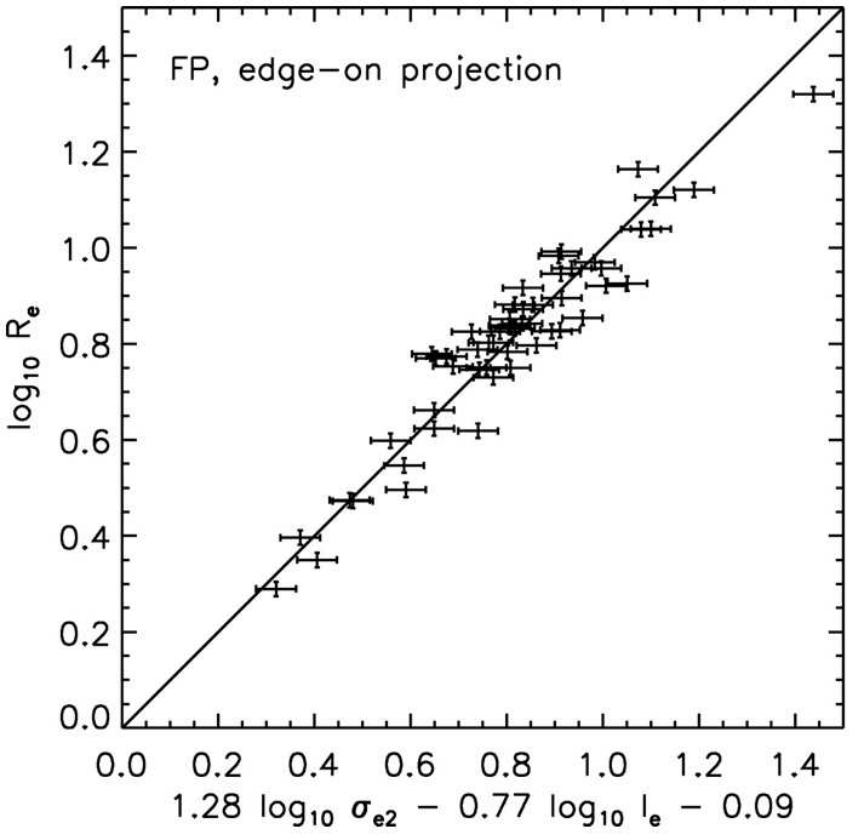

Figure 2.15 The edge-on projection of the FP of 53 SLACS lens galaxies (Figure 2 of Bolton et al. (2008b)). The units of σ_{e2} (stellar velocity dispersion), I_e (surface brightness) and R_e (half light radius) are 100 $km\ s^{-1}$, kpc^{-2} and kpc respectively. The solid black line correspond to the best-fit FP projection.

The $M_{bh} - M_{tot}$ relation found in this study is strongly suggestive that halo properties determine those of the galaxy and its black hole. This link is also observed in the FP, the two-dimensional projection of the three-dimensional space defined by surface brightness (I_e), effective radius (R_e) and central velocity dispersion (σ_e), of

early-type galaxies (Djorgovski & Davis 1987). Results of Bolton et al. (2008b) show that a sample of 53 SLACS lenses define a FP that is consistent with the general population of early-type galaxies from SDSS as shown in Figure 2.15:

$$\mathrm{R_e} \propto \sigma_\mathrm{e}{}^{1.28}\, \mathrm{I_e}{}^{-0.77} \tag{2.15}$$

The ratio $\mathrm{f} \equiv \sigma_\mathrm{e}/\sigma_\mathrm{SIE}$ for the SLACS lenses is $\mathrm{f} = 1.1019 \pm 0.008$ (Bolton et al. 2008b; Treu et al. 2006), also known as the "bulge-halo conspiracy", indicative of a universal isothermal mass profile. Therefore, we can replace the quantities $\mathrm{R_e}$ and σ_e in the FP with $\mathrm{R_{200}}$ and σ_SIE. Combining this with equations 2.5 and 2.7, we derive:

$$\mathrm{M_{bh}} \propto \mathrm{M_{tot}}{}^{1.30}\, \mathrm{I_e} \tag{2.16}$$

Ignoring the dependence of equation 2.16 on $\mathrm{I_e}$, since it only varies weakly relative to the other variables, we can extract the connection between $\mathrm{M_{bh}}$ and $\mathrm{M_{tot}}$ from the FP of SLACS lenses. The slope of 1.30 of the $\mathrm{M_{bh}} - \mathrm{M_{tot}}$ relation derived from the SLACS FP (Bolton et al. 2008b) is in agreement with our results within the 1-σ bounds. The manifestation of a $\mathrm{M_{bh}} - \mathrm{M_{tot}}$ relation within the FP of the SLACS lenses further strengthens the existence of the observed $\mathrm{M_{bh}} - \mathrm{M_{tot}}$ relation. We require *direct* measurements of both $\mathrm{M_{bh}}$ and $\mathrm{M_{tot}}$ to fully compare the manifestation of $\mathrm{M_{bh}} - \mathrm{M_{tot}}$ relation within the FP and its implications for regularity of early-type galaxy formation scenarios.

An additional advantage of the results from this study lies within the method used to derive $\mathrm{M_{tot}}$. The traditional method of estimating total gravitational mass of a galaxy, used in black hole studies, is to convert the *observed* circular velocity (from galaxy rotation curves) into the velocity of the galactic halo (also referred to as the *virial* velocity). The inferred total mass of a galaxy differs depending on the method used to relate observed circular velocity to the virial velocity. The effect on the $\mathrm{M_{bh}} - \mathrm{M_{tot}}$ relation from varying assumptions of the connection between observed circular velocity ($\mathrm{v_{c,obs}}$) and virial velocity ($\mathrm{v_{vir}}$), discussed in Ferrarese (2002), is also shown in Figure 2.8. The dashed line shows the best-fit $\mathrm{M_{bh}} - \mathrm{M_{tot}}$ relation obtained by Ferrarese (2002) using cosmological prescriptions of Bullock et al. (2001) to relate $\mathrm{v_{c,obs}}$ and $\mathrm{v_{vir}}$ ($\mathrm{M_{bh}} \propto \mathrm{M_{tot}}{}^{1.65}$) and the dot-dashed line shows the resulting relation where $\mathrm{v_{c,obs}} = 1.8\, \mathrm{v_{vir}}$ ($\mathrm{M_{bh}} \propto \mathrm{M_{tot}}{}^{1.82}$). From the relations obtained by Ferrarese

(2002), it is evident that the slope of the $M_{bh} - M_{tot}$ is affected by the method assumed to relate $v_{c,obs}$ and v_{vir}. Gravitational lens modeling is independent of such dynamical assumptions and provides an elegant alternative method to determine the total mass. Therefore, the $M_{bh} - M_{tot}$ relation characterized by this independent method is not only a complementary comparison to existing observational evidence but also provides valuable insight to determine the dominant physical processes of SMBH growth.

2.6 Summary

We use a sample of 43 early-type galaxies, which exhibit galaxy-scale strong gravitational lensing, to derive the scaling relation between black hole mass, M_{bh}, and the total mass, M_{tot}, of the host galaxy. In this study, we use the results of gravitational lens modeling to directly measure the total mass of the galaxy rather than converting the observed circular velocity into a total mass, the traditional method that is used in black hole studies. We use two alternative scaling relations, $M_{bh} - \sigma_\star$ and $M_{bh} - n$ to estimate the black hole masses of the lens sample. We obtain a tight correlation between $\sigma_\star$ and M_{tot} in the log-log space. In conjunction with the $M_{bh} - \sigma_\star$ relation, we derive the observational form of the $M_{bh} - M_{tot}$ relation that is consistent with no intrinsic scatter. We do not find a significant correlation between n and M_{tot}. From a variety of tests, we find that we cannot confidently estimate black hole masses with the $M_{bh} - n$ relation for our sample of galaxies. The scaling relation we observe between M_{bh} and M_{tot} is non-linear and is in agreement with theoretical predictions of the growth of black holes and observational studies of the local $M_{bh} - M_{tot}$ relation. The observed $M_{bh} - M_{tot}$ relation is also consistent with the studies of the FP of SLACS lenses, which is suggestive of a unified scenario where the properties of the host halo determine those of the resulting galaxy and black hole formed through hierarchical merging. The observed non-linear correlation between M_{bh} and M_{tot} indicates that massive halos are more efficient in forming black holes and the slope of the $M_{bh} - M_{tot}$ relation is suggestive of a merger-driven, feed-back regulated process for the growth of black holes.

Chapter 3

Witnessing the Differential Evolution in Luminosity and Size of Disk Galaxies via Gravitational Lensing

3.1 Introduction

Quantifying the evolution of the basic properties of galaxies such as luminosity, size and stellar mass is crucial to constrain the models of galaxy formation and evolution. In the ΛCDM model of galaxy formation, dark matter haloes are formed by hierarchical clustering and the baryonic material condenses and cools within the halo after the dark matter reaches equilibrium. In the context of disk galaxy formation, tidal torques impart angular momentum to the dark matter halo and its baryons, and the resulting angular momentum is conserved as the gas condenses into a disk galaxy (Fall & Efstathiou 1980). These models of galaxy formation predict various relationships between galaxy luminosity, size and stellar mass such as the luminosity-size relation and size-stellar mass relation. However, the exact shapes of these relations are complicated by star formation, feedback (such as supernovae driven outflows) or various instabilities (Dutton et al. 2007; Shen et al. 2003). Therefore, comparing detailed observations of these scaling relations with galaxy formation models at various cosmic

times is important to test the standard paradigm and understand the processes that affect the baryonic matter on galactic scales.

The luminosity-size and size-stellar mass relations in the local universe have been well established by studies (Shen et al. 2003) using the SDSS observations (York et al. 2000). Analysis of 140,000 galaxies in the SDSS sample by Shen et al. (2003) show that the size distribution of both early-type and late-type galaxies at a given luminosity (equivalently stellar mass) is well approximated by a log-normal function. Furthermore, Shen et al. (2003) also find that above a characteristic r-band luminosity of $M_{r,0} \sim -20.5$ (equivalently $\mathrm{M}_0 \sim 10^{10.6}\,\mathrm{M}_\odot$) the size of a late-type galaxy, R, scales steeply with mass ($R \propto \mathrm{M}^{0.39}$), while below the characteristic luminosity this relation is much shallower ($R \propto \mathrm{M}^{0.14}$).

Although the forms of luminosity-size and size-stellar mass relations are well understood in the local universe, measuring these scaling relations become more uncertain in the intermediate ($0.1 \leq z \leq 1$) and high-redshift ($z > 1$) regimes. High resolution observations, using *HST*, for a large sample of intermediate to high redshift galaxies are enabled by surveys such as the Galaxy Evolution from Morphologies and SEDs (GEMS survey, Barden et al. (2005)) and the Great Observatories Origins Deep Survey (GOODS, Giavalisco et al. (2004)). Over the past decade, many studies have used such observations to quantify galaxy scaling relations and determine the evolution of high-redshift galaxies into the locally observed population (Barden et al. 2005; Kanwar et al. 2008; Melbourne et al. 2007; Ravindranath et al. 2004; Simard et al. 1999; Trujillo & Aguerri 2004; Trujillo & Pohlen 2005).

After considering the selection affects, recent studies of disk galaxies (Barden et al. 2005; Melbourne et al. 2007; Trujillo & Pohlen 2005) find that the luminosity-size relation undergoes significant evolution since $z \sim 1$. However, it is difficult to quantify the type and the degree of evolution in the luminosity-size relation since galaxies may undergo pure size evolution, pure luminosity evolution or a combination of the two. Melbourne et al. (2007) construct the luminosity-size relation of blue galaxies in the Team Keck Redshift Survey (TKRS) of the GOODS North (GOODS-N) field, and find that blue galaxies exhibit size-dependent luminosity evolution, which matches the sample to the local galaxy population. The results of Melbourne et al. (2007) indicate that intermediate- and large-sized galaxies evolve $M_B \sim 1.5$ mag, since $z \sim 1$, while small galaxies exhibit much larger evolution in luminosity ($M_B \sim 2.55$ mag). The

large observed evolution in the luminosity of small galaxies, in comparison to intermediate and large galaxies, may require a complex evolutionary scenario. Although most studies assume that the shape of the luminosity-size relation remains constant with redshift, a changing luminosity-size relation may be required at the regime of faint and compact galaxies to explain the observed evolutionary trends. However, even with *HST* resolution, it is difficult to accurately measure the luminosities and sizes of faint, compact galaxies at higher redshifts.

Gravitational lensing, which magnifies the size and flux of a distant galaxy, provides us with a powerful advantage to extend the study of galaxy scaling relations over cosmic times. As discussed in chapter 1, galaxy-scale gravitational lensing yields a typical magnification of $10\times$ (Marshall et al. 2007), while group- or cluster-scale gravitational lenses can yield magnifications as high as $40\times$. Therefore, if a faint and compact galaxy is gravitationally lensed, one can estimate its luminosity and size accurately in comparison to the non-lensed case, provided that the deflector potential is well constrained.

In this project, we exploit the magnification advantage to study the lensed galaxy population of the SLACS survey. The goals of this project are outlined below. We first perform detailed lens modeling of the galaxy-scale SLACS lenses to reconstruct the *lensed* galaxy morphologies and measure their properties such as luminosity, size and Sérsic index. We then construct the luminosity-size relation of the disk-dominated ($n \leq 2.5$) and bulge-dominated ($n > 2.5$) SLACS lensed galaxies. We show that lensing provides ~ 2 magnitude boost in sensitivity over non-lensing surveys, which enables one to examine the fainter (also the most numerous) galaxy population at intermediate to high redshifts. We also compare the luminosity-size relation of the disk-dominated galaxies (i.e. late-types) in the SLACS sample to the luminosity-size relation of local disk-dominated galaxies to examine the evidence for evolution since $z \sim 1$.

This chapter is structured as follows. In §3.2 we give a description of the observations including a description of the data reduction process. We discuss the lens modeling procedure in §3.3. In §3.4, we compare our lens modeling results with the another team's determination, which is informative because we use different analysis techniques. In §3.5, we examine the advantages of a lensing survey by comparing the SLACS sample to a non-lensing, broad-band imaging survey. We also compare the

SLACS lensed galaxies to the local galaxy population and discuss possible evolutionary trends in §3.6 and present the summary of this study in §3.7. Unless otherwise noted, the apparent magnitudes quoted in this chapter are given in the AB magnitude system and the absolute magnitudes are given in the Vega magnitude system.

3.2 Description of the Observations

3.2.1 The Sample

We analyze 62 (out of 63) Grade-A SLACS lenses presented in Bolton et al. (2008a), denoted as B08, that were observed using the wide-field channel (WFC) of the Advanced Camera for Surveys through the F814W filter. In these lenses, source galaxies of interest span a redshift range of $0.20 \leq z \leq 1.20$ with a median redshift of $z = 0.61$. The foreground deflector galaxies (i.e. lens galaxies) have a median redshift of $z = 0.21$ (Bolton et al. 2008a). Our sample consists of 40 deep- ($\sim$ 2000 s) and 22 shallow-F814W ($\sim$ 420 s) observations. Each deep-F814W observation is split into multiple dithered observations (Bolton et al. 2006, 2008a).

3.2.2 Data Reduction

We obtain ACS-F814W images of the 62 SLACS lenses from the *HST* archive of CADC, where the frames are pre-processed by the CALACS calibration pipeline. We perform the following intermediate reduction steps on all frames, taking particular care to keep the reduction procedure as uniform as possible across all images[1].

Sky Subtraction

The SLACS observations are taken such that each lens is located at the centre of the WFC1 aperture of ACS (Auger et al. 2009). Each quadrant (2048×2048 pixels) of the two WFC detectors is read out separately by four amplifiers. Each amplifier has its own bias level offset, which may not be properly removed from the calibrated WFC1

[1]The data reduction for this project was done independently of the data reduction discussed in chapter 2.

and WFC2 frames. Figure 3.1 shows an example of this effect for an observation in the F775W filter. The surface brightness profiles of extended objects, such as galaxies, that occupy both quadrants of a WFC frame can suffer from this offset in the sky level (Sirianni et al. 2003). Similarly, lensing analysis is sensitive to errors in the sky level since Einstein rings of many SLACS lenses lie near the boundary of the two quadrants in WFC1. Therefore, we take special care to remove the offset in the sky level between the quadrants.

We use the following IRAF-based procedure to remove the offset between sky levels in each quadrant of the WFC frames. First, we extract each quadrant from the WFC frames and perform cosmic ray rejection using the LACOS software (van Dokkum 2001), which distinguishes between undersampled sources and cosmic rays. We then convolve the cosmic ray rejected quadrant with a Gaussian kernel and derive the modal value of the resulting pixel distribution. We impose a 3σ clipping factor on the pixel distribution to avoid any bright objects in a given quadrant. Thus, the modal value of the pixel distribution is an estimate of the sky level in each quadrant.

For deep I-band images, we subtract the sky value from each original quadrant and combine the resulting quadrants into WFC1 and WFC2 frames. We use the cosmic ray rejected quadrants (using LACOS) only to determine the sky level but perform the final cosmic ray rejection using multiple dithered images. For shallow I-band images, we subtract the sky level from each *cosmic ray rejected* quadrant and combine the resulting quadrants into WFC1 and WFC2 frames. The resulting WFC1 and WFC2 frames, for both deep and shallow images, have a uniform sky-background. Figure 3.2 shows an example of a deep, F814W observation of the SLACS lens, SDSS J0252+0039, both before and after the sky subtraction procedure.

Multidrizzling

We use the PYRAF reduction package Multidrizzle (Koekemoer et al. 2003) to rectify ACS image distortion, where the distortion solution is applied to map individual, sky-subtracted ACS frames onto a uniform grid with a pixel scale of $0\farcs05$ and a pixel fraction of 1.0 (i.e. the input pixel size is not "shrunk"). Using Multidrizzle, the multiply-dithered ~ 2000 s images are combined into a single exposure image, rejecting cosmic rays. Finally, we scale the science image of the final drizzled product by the exposure time.

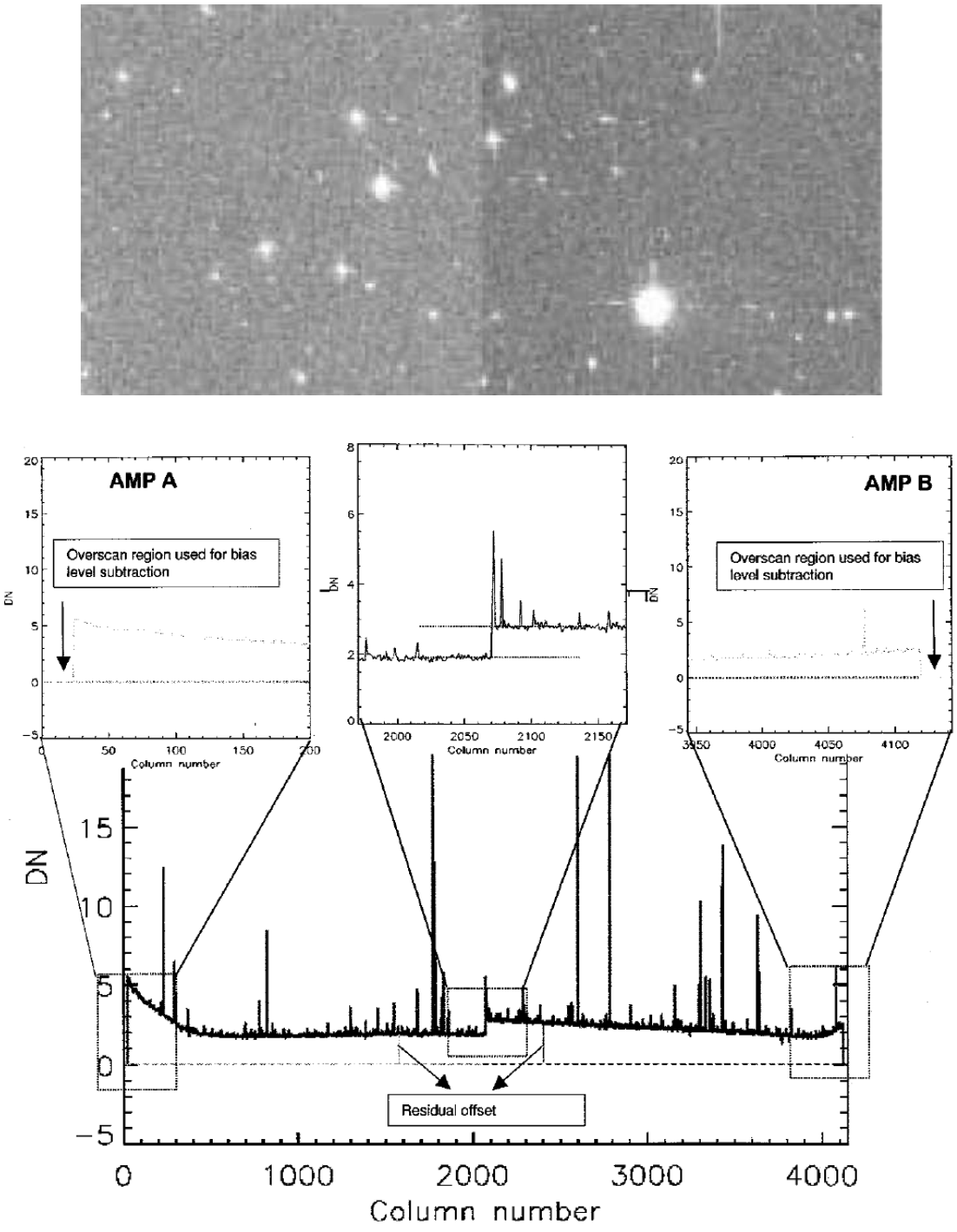

Figure 3.1 *Top:* A calibrated F775W observation that shows the bias level offset in the WFC1 detector, which is caused by the read-out of WFC1 detector by two separate amplifiers (Figure 1 Sirianni et al. (2003)). *Bottom:* Horizontal profile of the bias level offset in the WFC1 detector (Figure 2 of Sirianni et al. (2003)).

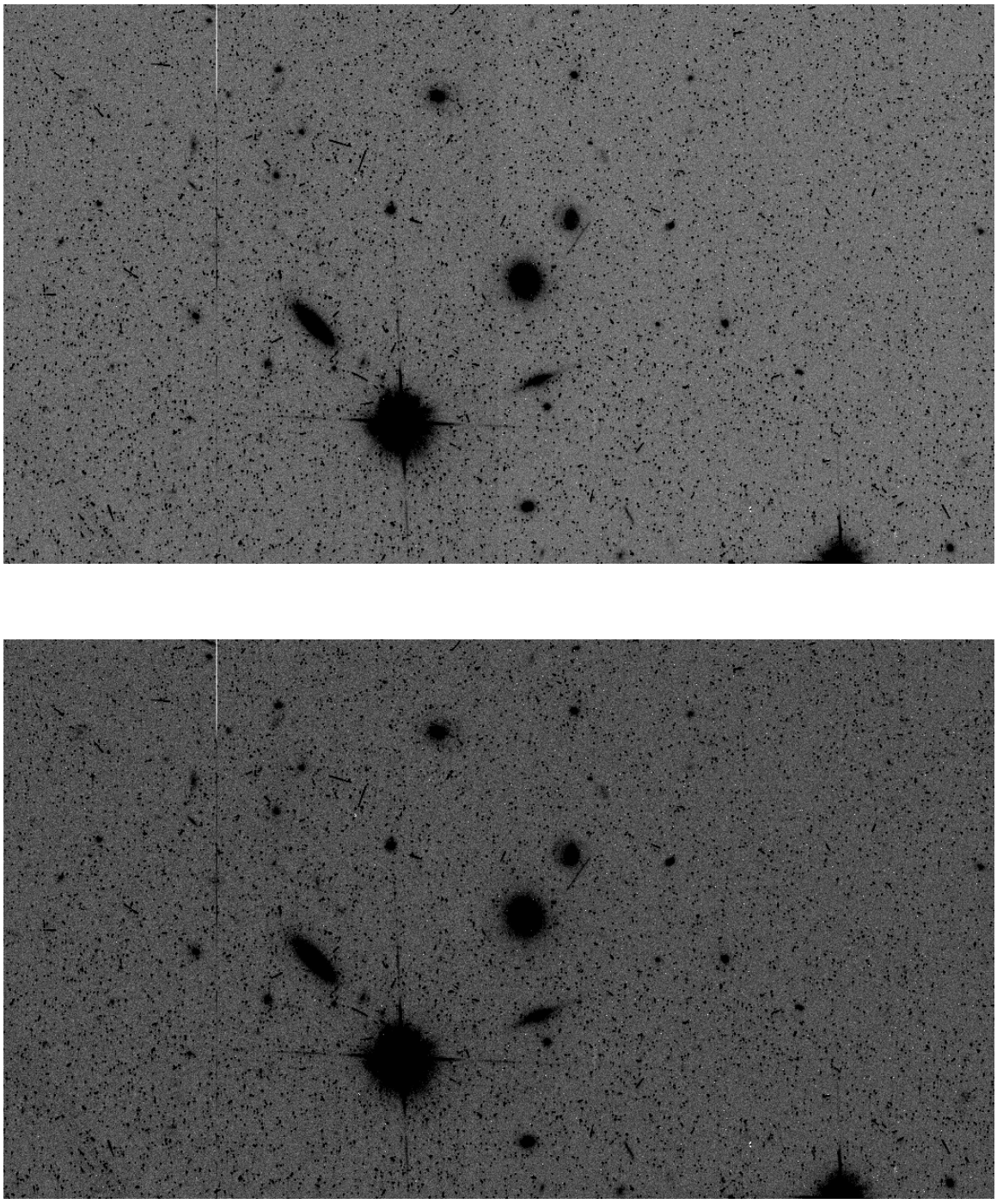

Figure 3.2 *Top:* A calibrated F814W observation ($\sim 2000s$) of the SLACS gravitational lens, SDSS J0252+0039, that shows the bias level offset in the WFC1 frame. *Bottom:* The WFC1 frame after the sky subtraction procedure. The final cosmic ray rejection process, for a deep observation, is performed during multidrizzling.

3.2.3 PSF Characterization

The best-fit gravitational lens model (referred to as the *lens model* throughout this chapter) must be convolved with the instrumental PSF for comparison with the data. We investigate three models of the ACS PSF to determine the most suitable one for convolution with the lens models. It is important to consider different models since the ACS PSF varies both spatially and temporally. This is similar to the procedure utilized in Bandara et al. (2009), discussed in the previous chapter (with improved PSF template libraries). The PSF models are:

1. A star extracted from the I-band image, referred to as PSF1.
2. A PSF produced at the location of the lens in WFC1 with the Tiny Tim software (Krist 1993), which produces PSF models based on the optical train of *HST* and ACS. We insert the Tiny Tim PSF into an empty WFC field and run Multidrizzle using identical parameters to that of the science frames. We then extract a cut-out of the Tiny Tim PSF from the distortion-corrected image, referred to as PSF2.
3. A PSF produced at the location of the lens in WFC1 using the principle component analysis models (PCA) in the ACS PSF library (Jee et al. 2007), referred to as PSF3.

Each PSF model discussed above has unique advantages and disadvantages. The temporal variation of the *HST* PSF occurs due to the short-term "breathing" and long-term aging of the telescope (Krist 1993). The PSF1 model reflects the exact temporal conditions at the time of the observation and is subjected to an identical reduction procedure as the science image (i.e. sky subtraction, cosmic ray rejection, and multidrizzling). Although, we take particular care to reduce PSF2 and PSF3 models in an identical manner to the science image, PSF1 is the only model which has undergone the same reduction steps in a natural way. PSF1 is not spatially identical to the PSF at the location of the lens; nevertheless, Häussler et al. (2007) show that the spatial variation of the ACS PSF is a negligible source of uncertainty when fitting normal galaxies.

Both PSF2 and PSF3 reproduce the spatial dependence of the ACS PSF well; however, these models cannot reproduce the temporal dependence of the ACS-PSF.

Due to the lack of a model that perfectly matches the ACS PSF both spatially and temporally, we determine the most suitable PSF by examining the residual images where a convolved lens galaxy light model is subtracted from the I-band image of the lens. An example is shown in Figure 3.3. As evident from Figure 3.3, for a given lens galaxy light model, PSF1 and PSF3 yield the best results by minimizing the core residuals that can be caused by an incorrect PSF model. The finite size of PSF2 introduces a "boxy" artifact in the core region of the lens, which is evident in Figure 3.3. Since many SLACS fields are devoid of unsaturated stars suitable for convolution, we select PSF3, which ensures a uniform convolution for all lens models.

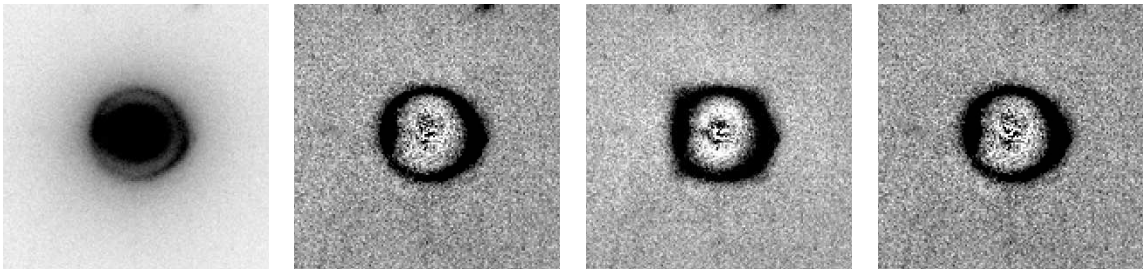

Figure 3.3 Effects of varying PSFs on LENSFIT models. *From left to right:* **(1)** ACS-F814W image of SDSS J1627-0053, with the contrast adjusted to show the lensed features around the early-type lens galaxy. The remaining panels show the residual image of the lens system after the light profile of the lens galaxy, convolved with various PSFs, is subtracted from the ACS-F814W image. **(2)** Residual image after the natural PSF (PSF1) convolved lens galaxy model is subtracted. **(3)** Residual image after the Tiny-Tim PSF (PSF2) convolved lens galaxy model is subtracted. **(4)** Residual image after the ACS library PSF (PSF3) convolved lens galaxy model is subtracted. Overall, we find that PSF1 and PSF3 produce minimal core residuals; however, most SLACS fields are devoid of unsaturated stars that are suitable for convolution with LENSFIT models. Therefore, we use PSFs generated from the ACS PSF library for strong lens modeling. All images are $7\farcs5 \times 7\farcs5$.

3.3 Lensing Analysis

In the following section, we discuss the strong lens modeling procedure utilized for the analysis of the 62 SLACS lenses. As discussed in chapters 1 and 2, strong lens modeling involves finding the mass model of the lens galaxy that can accurately lens a background galaxy (on the source plane) on to the image plane, while simultaneously fitting the lens galaxy light profile (Warren & Dye 2003; Bolton et al. 2008a). We use LENSFIT (Peng et al. 2006), an extension of the galaxy decomposition software GALFIT (Peng et al. 2002), for strong lens modeling. We present a brief description

of the strong lens modeling methodology utilized in LENSFIT below, and refer the reader to Peng et al. (2006) for a detailed description.

The primary difference between various strong lens modeling software lies on the method used to reconstruct the *unlensed* light profile of the source galaxy. LENSFIT, similar to the studies of Bolton et al. (2008a); Marshall et al. (2007) and Moustakas et al. (2007), assumes a parametric light profile for the source galaxy (Peng et al. 2006), while studies such as Dye & Warren (2005); Koopmans (2005); Suyu et al. (2006) and Warren & Dye (2003) describe the source galaxy light profile on a pixelized grid. We refer the reader to Warren & Dye (2003) for further information about lens modeling where the linear inversion of a pixelized light distribution is utilized. Lens modeling based on pixelized-grid reconstruction still requires the source galaxy to be fit with a parametric function to derive the luminosity and size for comparison purposes. Therefore, our technique is analogous to two-dimensional parametric fitting of large non-lensing galaxy surveys.

The parametric de-projection of the source galaxy light profile utilized by LENSFIT is a 1-1 mapping technique, where each pixel on the image plane is mapped to a single position on the source plane (following the conservation of surface brightness in gravitational lensing). This is in contrast to the forward ray-tracing method, which is a 1-to-N mapping technique, where a single pixel on the source plane is mapped onto multiple positions on the image plane, as specified by the assumed $\Phi(x)$[2]. LENSFIT optimizes the model parameters using the Levenberg-Marquardt non-linear least squares method of Press et al. (1992). In the following sections, we discuss the three main components of LENSFIT: description of the *mass model*, *lens galaxy subtraction* and description of the *source galaxy*.

3.3.1 Description of the mass model

For the mass model, which describes the mass distribution of the lens galaxy, we follow the previous lens modeling studies which include the SLACS series (Auger et al. 2009; Bolton et al. 2006, 2008a; Gavazzi et al. 2007; Marshall et al. 2007; Moustakas et al.

[2]It should be noted that the 1-N lens mapping technique, i.e. selecting a source position $\mathbf{u}$ and trying to find the image positions x_i, is mathematically difficult in contrast to the 1-1 lens mapping technique since no algorithm is guaranteed to find all the roots of the two-dimensional lens equation (Keeton 2001b). Please refer to Keeton (2001b) for a detailed discussion.

2007; Peng et al. 2006) and assume a SIE mass model (Kormann et al. 1994; Keeton & Kochanek 1998). Results of various studies show that the mass models of galaxy-scale strong gravitational lenses are well approximated by the SIE model (Koopmans et al. 2006; Treu & Koopmans 2004). Furthermore, with the use of a SIE mass model, we can directly compare our results to other studies of SLACS lenses, even those with a different method of source galaxy reconstruction. We model each SLACS lens galaxy with a single SIE model (i.e. the multiply lensed images are produced by a *single* deflector potential) with an external shear field to model the tidal effects by objects nearby or along the LOS of the lens.

The SIE model used in LENSFIT is characterized by the following 7 parameters: mass model centroid (x_{SIE}, y_{SIE}), Einstein radius (b_{SIE}), axis ratio of the elliptical mass model (q_{SIE}), position angle of the major axis measured E from N (PA_{SIE}), external shear (γ_{SIE}) and the position angle of the external shear component measured E from N PA_{γ}). The shear component of the lensing coordinate transformation (γ), discussed in §1.4, is due to the contributions from the ellipticity of the mass model (q_{SIE}) and the external shear (γ_{SIE}) induced by the presence of interloper galaxies along the LOS of the deflector.

Initial Parameter Estimates of the mass model

For lens modeling, we assume the following initial parameters for the SIE mass model. We initially hold the centroid of the mass model (x_{SIE}, y_{SIE}) fixed to that of the lens galaxy light profile centroid. This assumption is consistent with previous studies which find that the stellar component dominates the mass profile of an early type galaxy in the central region and that the dark matter component must also be aligned with the stellar spheroid in this regime (Bolton et al. 2008a). Since the mass model is best constrained by lensed features that span a large range of azimuthal angles, lenses that exhibit complete or nearly complete Einstein rings are ideal candidates to test whether the mass model and the lens galaxy light profile centroids are aligned. Therefore, we select a subset of 35 lenses with complete or nearly complete Einstein rings and allow (x_{SIE}, y_{SIE}) to vary freely during the optimization to determine how well the assumption above holds.

From the optimizations where the mass model centroid varies freely, we find that

the 35 lenses discussed above are in excellent agreement with our initial assumption. For example, the maximum shift between (x_{SIE}, y_{SIE}) and the lens galaxy centroid is $\sim 0\farcs05$ for the subset of lenses mentioned above. This corresponds to a single *HST*-ACS pixel and is consistent with no shift in comparison to other systematic errors such as those associated with lens galaxy subtraction and an incorrect PSF model. Therefore, our initial choice to constrain the mass model centroid to that of the lens galaxy light profile is well justified. Our method is also consistent with that of B08. Although the justification for fixing the mass model centroid to that of the lens galaxy light profile centroid is strong for the SLACS sample, it is also possible to treat (x_{SIE}, y_{SIE}) as a free parameter depending on the individual lens system[3].

We use the angular sizes of the Einstein rings and arcs in the I-band images as an initial estimate of b_{SIE}; furthermore, we use the axis ratio and the orientation angle of the lens galaxy light profile as initial estimates for q_{SIE} and PA_{SIE}. In models where the lens galaxy light profile is described by several Sérsic components, the brightest component is used as the reference for the initial estimates. For the external shear component, we assume an initial estimate of $\gamma_{ext} = 0.01$ and set the initial orientation angle (of γ_{ext}) to be aligned with the interloper galaxies in the field.

3.3.2 Lens Galaxy Subtraction

The deflection model of equation 2.2 is non linear, which allows for multiple images[4] to form on the image plane. Therefore, the lens modeling procedure often requires fitting faint multiple images in the data. SLACS lens galaxies are primarily bright, early-type galaxies whose light profiles are typically well described through a set of parametric functions. However, the lens galaxy light does contaminate the faint lensed features since the Einstein ring radii of the SLACS lenses ($R_{einst} \sim 1\farcs0 - 1\farcs5$) are smaller than the typical effective radii of the early-type lens galaxies (Bolton et al. 2006, 2008a). Furthermore, some of the lensed features are embedded near the central region of the lens galaxy on the image plane. Therefore, it is important to remove the light profile of the lens galaxy, either prior to- or during- the lens modeling.

[3]There is observational evidence for an offset between the mass model centroid and lens galaxy light profile for one of the SLACS lenses, SDSS J0946+1006 (Gavazzi et al. 2008).

[4]In other words, the roots of the two-dimensional lens equation.

LENSFIT Lens Galaxy Subtraction Method

We use the Sérsic profile (Sersic 1968) to model the surface brightness of the lens galaxy[5]. The elliptically symmetric Sérsic profile has a total of 7 fitting parameters in LENSFIT: position of the Sérsic component (x_s, y_s), half-light radius (r_{hl}), apparent magnitude (m_I), the Sérsic index (n), axis ratio of the elliptical profile $(q = b/a)$ and the position angle of the major axis measured E from N (PA).

This method is similar to the study of Moustakas et al. (2007), which uses a tilted two-dimensional Moffat profile to model the lens galaxy light profiles of the gravitational lenses discovered in the DEEP2 Extended Groth Strip. The capabilities of LENSFIT include fitting the lens galaxy light profile while optimizing the mass model and source galaxy light profile simultaneously. Before simultaneously optimizing the light profile of the lens galaxy, it is often useful to first provide an initial estimate; otherwise, large residuals can make it difficult "see" the fainter lensed features. Below, we summarize the steps taken to determine the initial model for the lens galaxy light profile before optimizing all components simultaneously (i.e. mass model, source galaxy and lens galaxy light profiles):

1. We use SExtractor (Bertin & Arnouts 1996) to produce a catalog of the objects in each ACS I-band image. We use the segmentation image produced by SExtractor, which deblends objects in each image, as a mask of non-essential objects in the fitting region.

2. We "unmask" the gravitational lens from the SExtractor segmentation image and run LENSFIT to obtain an approximate solution of the lens galaxy Sérsic profile. During these steps, the optimization of the source galaxy and mass model is not performed and LENSFIT operates as the GALFIT package (Peng et al. 2002).

3. We subtract the PSF convolved model of the lens galaxy light profile from the I-band image and examine the residual. Typically, lensed features are visible

[5]

$$\Sigma(r) = \Sigma_e \exp\left(-\kappa(n)\left[(r/r_{hl})^{1/n} - 1\right]\right) \tag{3.1}$$

where $\Sigma(r)$ is the surface brightness at a given radius r, r_{hl} is the half-light radius of the profile and n is the concentration parameter.

in the residual image after the initial trial. We then use the residual image to produce manual masks of the lensed features.

4. We repeat the Sérsic profile fitting procedure, with the masked lensed features, until a clean lens galaxy subtraction is obtained using multiple components if necessary. The overall best-fit model is determined by the χ^2 merit function, where a good solution typically correspond to a χ^2 of unity, and a visual inspection of the residual image.

5. We do not use an arbitrarily large number of Sérsic components to model the lens galaxy, since some galaxies have low-order angular structure that cannot be easily removed, even using multiple components. Such galaxies are easily identifiable because adding extra Sérsic components do not affect the overall quality of the fit (both residual image and the χ^2 statistic). Typically, 1-4 Sérsic components suffice to derive a clean lens galaxy subtraction.

6. Certain fields contain several interloper galaxies near the LOS of the lens, which may result in contamination of the lens galaxy light leading to an inaccurate light profile. For such fields, we also model the interloper galaxies simultaneously using single or multiple Sérsic components.

7. After the best-fit lens galaxy light profile is obtained, we perform the complete strong-lens modeling procedure which includes the optimization of the source galaxy light profile and the mass model. The lens galaxy profile derived from the steps discussed above acts as the initial estimate for the final optimization process and reduces some of the complexities of strong lens modeling.

Alternative Methods of Lens Galaxy Subtraction

Previous studies of the SLACS lenses (Bolton et al. 2006, 2008a; Marshall et al. 2007) use the radial B-spline fitting method, first introduced in Bolton et al. (2006) (referred to as B06), to remove the lens galaxy light. The B-spline models fit the radial light profiles of early-type galaxies and can effectively remove low-order angular structure due to the inclusion of multipole terms (Bolton et al. 2008a). We refer the reader to B06 for detailed information about the B-spline fitting method.

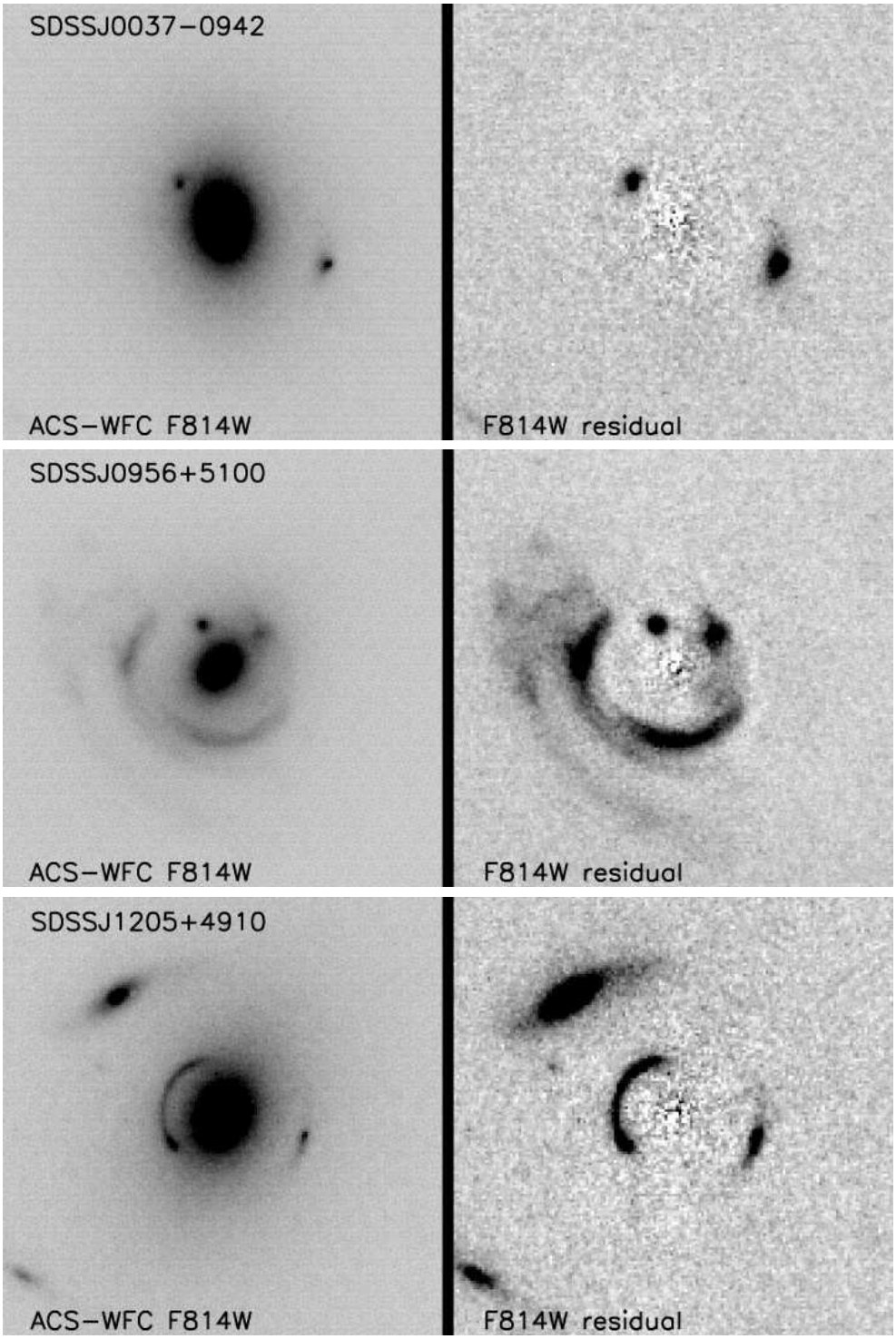

Figure 3.4 *Left panels: HST*-ACS imaging of a subset of SLACS lenses taken in the F814W filter. *Right panels:* Demonstration of the B-Spline lens galaxy subtraction method utilized in B06 (based on Figure 2 of B06).

As shown in Figure 3.4, the B-spline method produces visually clean lens galaxy subtracted images of lenses. However, because the lens galaxy is removed independently of the source galaxy, B-splines can partially remove the source galaxy light (Marshall et al. 2007) causing one to infer a fainter and more compact source galaxy relative to its true morphology. A better solution is to simultaneously deblend the lens and source galaxy using parametric profiles, a technique used in LENSFIT. Equivalently, an alternative lens modeling method is to simultaneously deblend the lens and source galaxy light profiles using B-spline (for the lens galaxy) and Sérsic models (for the source galaxy). As described above, with LENSFIT, multiple Sérsic components are necessary to obtain a clean subtraction and reduce systematics.

This process is generally reliable because the lens galaxy profile shape, being highly symmetric and monotonically declining, is different from the source galaxy which modulates both radially and azimuthally on the image plane in predictable ways. In simulations to quantify how reliable it is to decouple overlapping, non-lensed galaxies, Häussler et al. (2007) show that no amount of masking is a suitable substitute for simultaneous fitting of galaxies even when a large number of free parameters are involved. An additional benefit of the parametric analysis is that it allows us to quantify the systematic errors that arise from different assumptions about the model profiles as discussed in Peng et al. (2010).

3.3.3 Description of the Source Galaxy

The primary goal of this study is to derive the luminosities, half-light radii and Sérsic indices of the source galaxies, which can then be compared to the non-lensed galaxy population. Therefore, it is sensible to describe the source galaxy in terms of a light profile that is commonly observed over a large range of redshifts. Therefore, we also model the source galaxy using the Sersic (1968) profile. Without the intervening effect of gravitational lensing, modeling of the source galaxy profile is similar to the galaxy decomposition procedure of GALFIT (Peng et al. 2002).

Multiple Source Galaxy Components

Our main interest is to compare the sizes and luminosities of the deprojected source galaxies with non-lensed galaxies from $0 \leq z \leq 1.2$. However, the definition of size is complicated when some of the lensed sources are fractured into multiple components. There are two main issues to consider in this analysis: it is important from the standpoint of lens modeling to accurately reproduce the source, no matter how clumpy or disjointed, because such information is useful for constraining the mass model accurately. However, from the standpoint of comparing the lensed galaxies to non-lensed galaxies, we want only a simplified representation (i.e. a single Sérsic profile excluding clumps), which mirrors the analysis techniques of other studies (Barden et al. 2005; Marshall et al. 2007; Melbourne et al. 2007; Newton et al. 2011). To properly deal with the incongruous requirements, we developed the following method.

Similar to §3.3.2, we begin the lens modeling procedure by using a single Sérsic component to describe the source galaxy light profile and adding further components as required to obtain the best-fit lens model. Since the SLACS lenses are selected due to the presence of nebular emission lines (Bolton et al. 2006, 2008a), it is likely that some of the source galaxies contain star forming regions which show up as "knots" on the image plane. It is difficult for LENSFIT, or any lens modeling code based on parametric light profiles, to fully model these regions. Therefore, such features may appear on the residual images even after assuming a complex source galaxy profile. Furthermore, the final reconstruction of the lensed galaxies on the source plane show that some SLACS sources resemble *fractured systems* or *galaxy groups* (collectively referred to as *multiple systems*); therefore, it is very important that the choice of source galaxy components reflect multiple systems or galaxy group morphology, when required.

Even with the assumption of multiple source galaxy components, we follow the lens modeling equivalent to "Ockham's Razor" such that we do not add an arbitrarily large number of Sérsic components to model the source galaxy. For a system with substantial residuals, such as those resulting from star-forming regions, we do not add further Sérsic components if the overall fit does not improve (both in the residual image and the χ^2 statistic). Using the method described above, we find that $\sim 67\%$ of the SLACS lenses require multiple Sérsic components to fully model the background source (discussed below). As discussed in the following sections, our lens modeling

results are also in good agreement with that of B08.

Information derived from the substructures in the source galaxy light profile as described above, in principle, yield the best-fit mass model. To obtain the overall *global* properties of the source galaxies for comparison with non-lensing studies, we perform an additional LENSFIT run by using a single Sérsic component to describe the source galaxy light profile and holding the best-fit mass model and the lens galaxy light profile fixed. During the preliminary analysis, we only consider the global properties of the source galaxy population derived using the method described above. However, SLACS sources with multiple Sérsic components can be divided into the following criteria, through visual classification of the source plane reconstruction: systems where an individual galaxy has multiple concentric (or nearly concentric) components such as a bulge and a disk; a fractured source or a group of galaxies which show potential signs of interaction (i.e. multiple systems). The latter two groups have characteristic multiple offset Sérsic components and we refer to these sources as "group" systems for the remainder of this paper. For the 15 lenses whose source morphology correspond to a multiple system, it is sensible to consider the luminosity, size and Sérsic index of individual subcomponents rather than the global properties of the system.

The total error budget of lens modeling is dominated by systematic uncertainties and Marshall et al. (2007), which examine a single SLACS source galaxy in detail, shows that systematic uncertainties of lens modeling are primarily incurred from the assumption of the lens model density slope and the method of lens galaxy subtraction. The systematic uncertainties of source galaxy apparent magnitude and size due to the uncertainty in the lens model density slope are (Marshall et al. 2007),

$$\sigma_{m_{AB}} \approx 2.2\sigma_m \text{ and } \frac{\sigma_{\mathrm{r_{hl}}}}{\mathrm{r_{hl}}} \approx \sigma_{\mathrm{m}} \tag{3.2}$$

where σ_m, $\sigma_{m_{AB}}$ and $\sigma_{r_{hl}}$ correspond to the intrinsic spread of the power-law indices of the lens model density profile, systematic uncertainties of source galaxy size and apparent magnitude. The Sérsic index of the source galaxy is unaffected by the lens model density profile since it only changes the magnification of the source galaxy (Marshall et al. 2007). We adopt a value of $\sigma_m = 0.12$ (Koopmans et al. 2006), which yields systematic uncertainties of ~ 0.26 mag and $\sim 12\%$ for the source galaxy apparent magnitude and size respectively.

Next, we compute the magnitude of the systematic uncertainties of source galaxy parameters due to the lens galaxy subtraction method of LENSFIT. As discussed in §3.3.2, SLACS lens galaxies are typically described by 1-3 Sérsic components (up to 4 in several systems). We select a subset of 30 SLACS lenses whose lens galaxy is best described by 2-4 Sérsic components and "degrade" each model by successively removing lens galaxy components until the lens model is left with only a single lens galaxy component. We then track the differences between the global source galaxy parameters of the best-fit solution and the successively degraded iterations.

Figure 3.5a, 3.5b and 3.5c show the distributions of the deviates of source galaxy luminosity (Δm_{f814w}), size ($\Delta r_{hl}/r_{hl}$) and Sérsic index (Δn) due to incomplete lens galaxy subtraction in the iterations discussed above. The standard deviation of each distribution is an estimate of the *ensemble* systematic error incurred due to the lens galaxy subtraction method of LENSFIT. Therefore, the ensemble systematic errors (from the fits shown as solid black lines in Figure 3.5) in source galaxy apparent magnitude, size and Sérsic index correspond to ~ 0.28 mag, $\sim 24\%$ and ~ 0.1 respectively. Although the *individual* systematic errors of source galaxy parameters due by lens galaxy subtraction can be systematically lower, we adopt the ensemble systematic errors as a conservative proxy. Finally, we add both sources of systematic uncertainties in quadrature to derive the total systematic uncertainty in source galaxy luminosity, size and Sérsic index, which corresponds to $\sigma_{m_{AB}} \sim 0.38$ mag, $\sigma_{r_{hl}}/r_{hl} \sim 0.27$ and $\sigma_n \sim 0.1$ respectively.

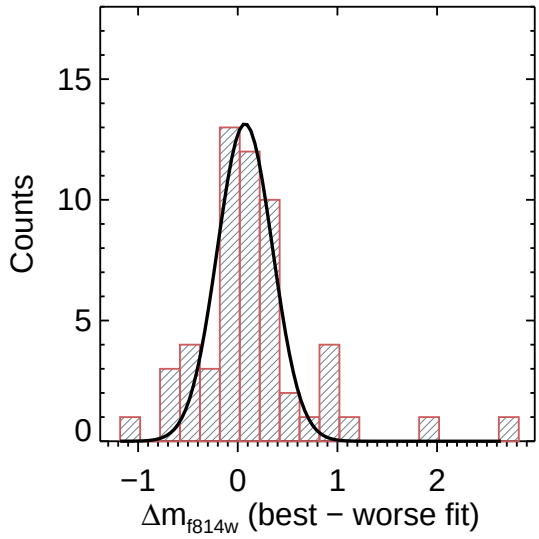

(a) Systematic error in luminosity.

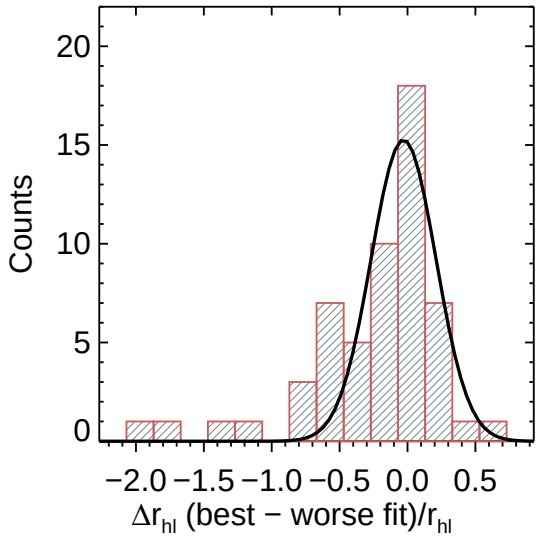

(b) Systematic error in size.

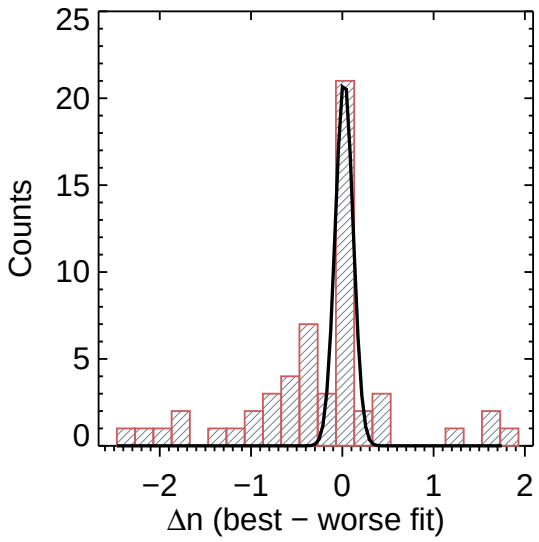

(c) Systematic error in Sérsic index.

Figure 3.5 The distribution of the deviates of global source galaxy parameters, due to incomplete lens galaxy subtraction. The deviates are defined as the difference between the best-fit global solution and a degraded solution. The standard deviation of each distribution, derived from gaussian fits to each distribution (shown as solid black lines), corresponds to the ensemble systematic uncertainty of each parameter caused by the lens galaxy subtraction. **(a)** Distribution of the deviates of source galaxy apparent magnitude, quoted in the AB system. **(b)** Distribution of the deviates of source galaxy size (expressed as a fraction of the half-light radius from the best-fit solution). **(c)** Distribution of the deviates of source galaxy Sérsic index.

Initial Parameter Estimates for the Source Galaxy

The initial estimates for the source galaxy parameters are fairly straightforward. For lenses that exhibit complete or partial Einstein rings, the initial position of the source galaxy must be close to the centroid of the lens galaxy light profile, which we use as an initial guess. For all systems, we assume the following initial parameters for the source galaxy light profile: $m_I \sim 24$ mag (AB system), $n \sim 1$ and $r_{hl} \sim 0\farcs1$. A unique solution from lens modeling is less sensitive to the initial estimates of the parameters in comparison to input priors. To avoid "pseudo-degeneracies" in the solution, we use caution not to input too few or too many components than required by the data. We refer the reader to Peng et al. (2010) for an extensive discussion of pseudo-degeneracies within the context of galaxy fitting.

3.4 Lens Modeling Results & Comparisons

In the following section, we present the results of the LENSFIT procedure and compare them to the studies by the SLACS team (Bolton et al. 2008a; Marshall et al. 2007; Newton et al. 2011). The best-fit mass model parameters, which were obtained using multiple source components (when required), are shown in Table 2. The properties of the source galaxies and the corresponding errors are shown in Table 3. Figure 3.6 shows the results of lens modeling for a subset of SLACS lenses and demonstrates that LENSFIT can be used effectively to model lenses of varying complexity. Figure 3.7 shows the source-plane reconstruction of a subset of "normal" galaxies and Figure 3.8 shows the reconstruction of 15 sources whose morphology corresponds to a "group".

Table 2. SIE mass model parameters of SLACS lenses derived by LENSFIT

System (1)	b_{SIE} ($''$) (2)	q (SIE) (3)	PA(SIE) (4)	γ_{ext} (5)	$PA(\gamma)$ (6)	$N_{sources}$ (7)	Image type (8)
SDSS J0008-0004	1.12	0.77	149.56	0.04	−32.26	2	d
SDSS J0029-0055	0.94	0.86	117.29	0.03	−9.27	2	d
SDSS J0037-0942	1.51	0.91	−153.53	0.03	2.98	2	s
SDSS J0044+0113	0.76	0.68	317.49	0.03	−57.91	2	s
SDSS J0109+1500	0.75	0.55	107.43	0.13	6.79	1	s
SDSS J0157-0056	0.78	0.48	−147.58	0.17	−68.60	3	d
SDSS J0216-0813	1.22	0.74	36.62	···	···	2	d
SDSS J0252+0039	1.03	0.90	−63.28	0.02	40.17	3	d
SDSS J0330-0020	1.10	0.75	25.00	0.03	−69.44	3	d
SDSS J0405-0455	0.78	0.94	251.43	0.04	18.57	1	s
SDSS J0728+3835	1.23	0.74	−26.94	0.06	68.69	3	d
SDSS J0737+3216	0.96	0.90	25.99	0.09	−2.94	2	d
SDSS J0822+2652	1.12	0.83	140.83	0.05	53.98	2	d
SDSS J0841+3824	1.40	0.78	158.76	0.01	39.92	2	d
SDSS J0903+4116	1.30	0.87	−120.23	0.02	−16.93	3	d
SDSS J0912+0029	1.44	0.64	188.54	0.05	−89.96	1	s
SDSS J0935-0003	0.93	0.65	−134.92	0.19	−45.07	1	s
SDSS J0936+0913	1.09	0.94	−87.29	0.04	49.36	2	d
SDSS J0946+1006	1.40	0.88	−60.54	0.09	45.64	1	d
SDSS J0955+0101	0.78	0.62	97.02	···	···	2	s
SDSS J0956+5100	1.28	0.77	26.76	0.05	30.52	2	d
SDSS J0959+0410	0.98	0.84	−223.91	···	···	2	d
SDSS J0959+4416	0.97	0.93	−63.32	0.03	−8.76	2	d
SDSS J1020+1122	1.21	0.80	188.91	0.05	62.15	2	d
SDSS J1023+4230	1.40	0.80	55.95	0.02	−9.95	3	d
SDSS J1029+0420	0.91	0.64	−334.18	···	···	2	d
SDSS J1032+5322	0.99	0.76	142.07	0.05	−58.71	3	d
SDSS J1100+5329	1.40	0.64	96.22	0.09	−49.54	2	s
SDSS J1103+5322	0.97	0.59	90.06	0.07	49.67	2	d
SDSS J1106+5228	1.20	0.70	58.03	0.03	−29.08	1	s
SDSS J1112+0826	1.42	0.70	−30.03	0.05	78.81	2	s
SDSS J1134+6027	1.20	0.75	−156.77	0.01	51.23	1	s
SDSS J1142+1001	1.01	0.81	2.59	0.00	−45.39	1	d

Table 2 (cont'd)

System (1)	b_{SIE} ($''$) (2)	q (SIE) (3)	PA(SIE) (4)	γ_{ext} (5)	$PA(\gamma)$ (6)	$N_{sources}$ (7)	Image type (8)
SDSS J1143-0144	1.63	0.83	350.87	0.09	79.43	2	s
SDSS J1153+4612	1.03	0.88	−58.65	0.06	29.22	1	d
SDSS J1204+0358	1.28	0.95	235.39	0.04	62.87	2	s
SDSS J1205+4910	1.18	0.74	−104.39	0.06	−59.69	2	d
SDSS J1213+6708	1.34	0.70	255.33	0.09	−0.99	1	d
SDSS J1218+0830	1.46	0.79	100.56	0.05	−5.01	1	d
SDSS J1250+0523	1.13	0.96	29.85	···	···	5	d
SDSS J1251-0208	0.80	0.67	179.78	0.12	65.65	2	s
SDSS J1402+6321	1.33	0.77	−28.69	0.03	73.11	2	d
SDSS J1403+0006	0.90	0.89	−18.28	0.05	−80.61	3	s
SDSS J1416+5136	1.29	0.72	2.43	0.09	71.78	3	d
SDSS J1420+6019	1.06	0.95	−165.71	0.03	73.01	1	d
SDSS J1430+4105	1.45	0.67	−19.23	···	···	6	d
SDSS J1432+6317	1.23	0.89	69.74	0.04	−33.65	1	d
SDSS J1436-0000	1.10	0.74	27.70	0.13	−37.50	1	s
SDSS J1443+0304	0.93	0.93	226.71	0.12	36.31	1	s
SDSS J1451-0239	1.05	0.90	5.56	0.04	−88.16	1	d
SDSS J1525+3327	1.18	0.52	−14.55	0.11	46.11	1	d
SDSS J1531-0105	1.69	0.81	−44.52	0.02	−21.84	2	s
SDSS J1538+5817	0.99	0.93	−15.46	0.01	−43.89	2	s
SDSS J1621+3931	1.18	0.69	163.64	0.09	−76.39	1	s
SDSS J1627-0053	1.22	0.89	95.94	0.02	0.63	2	d
SDSS J1636+4707	1.05	0.83	100.66	0.04	75.78	2	s
SDSS J2238-0754	1.26	0.86	−113.37	···	···	2	d
SDSS J2300+0022	1.22	0.67	1.31	0.10	68.49	1	d
SDSS J2303+1422	1.50	0.58	−38.19	0.03	14.71	2	d
SDSS J2321-0939	1.52	0.75	−17.66	0.08	−81.58	1	s
SDSS J2341+0000	1.36	0.80	32.69	0.02	4.64	4	d

Note. — **Col. (1)**: The unique SDSS spectrum identifier for the lens system. **Col. (2)**: Einstein ring radius of the SIE mass model in arcseconds. **Col.(3)**: Ratio between the minor and major axis (q = b/a) of the SIE mass model. **Col.(4)**: Position angle of the major axis of the SIE mass model, measured E from N. **Col.(5)**: External shear field, induced by the tidal effects of interlopers along the LOS. **Col.(6)**: Position angle of the external shear, measured E from N. **Col.(7)**: Number of Sérsic components used to model the background source for the best-fit lens model. **Col (8)**: Type of F814W image used to as input for LENSFIT, where "d" denotes a deep image ($\sim 2000s$) and "s" denotes a shallow image ($\sim 420s$).

Table 3. Source galaxy parameters derived from LENSFIT

System (1)	z_{fg} (2)	z_{bg} (3)	m_I (AB) (4)	M_B (Vega) (5)	r_{hl} (kpc) (6)	n (7)
SDSS J0008-0004	0.4400	1.1924	22.60	-21.82	6.97 ± 1.87	0.85
SDSS J0029-0055	0.2270	0.9313	23.51	-19.80	2.72 ± 0.73	2.73
SDSS J0037-0942	0.1955	0.6322	23.03	-18.73	0.71 ± 0.19	2.86
SDSS J0044+0113	0.1196	0.1965	19.60	-19.60	2.36 ± 0.63	2.65
SDSS J0109+1500	0.2939	0.5248	23.25	-18.18	1.77 ± 0.47	0.93
SDSS J0157-0056	0.5132	0.9243	22.19	-21.09	8.61 ± 2.31	0.28
SDSS J0216-0813	0.3317	0.5253	21.94	-19.49	4.45 ± 1.19	0.61
SDSS J0252+0039	0.2803	0.9818	24.43	-19.10	0.98 ± 0.26	1.31
SDSS J0330-0020	0.3507	1.0709	22.00	-21.91	1.83 ± 0.49	2.32
SDSS J0405-0455	0.0753	0.8098	24.95	-17.83	1.33 ± 0.36	0.05
SDSS J0728+3835(a)	0.2058	0.6877	23.95	-18.28	2.87 ± 0.77	1.99
SDSS J0728+3835(b)	0.2058	0.6877	24.31	-17.92	7.39 ± 1.98	3.83
SDSS J0728+3835(c)	0.2058	0.6877	27.49	-14.74	0.11 ± 0.03	0.04
SDSS J0737+3216	0.3223	0.5812	22.21	-19.51	4.49 ± 1.20	3.58
SDSS J0822+2652(a)	0.2414	0.5941	25.36	-16.42	1.52 ± 0.41	0.25
SDSS J0822+2652(b)	0.2414	0.5941	23.96	-17.82	2.01 ± 0.54	0.72
SDSS J0841+3824	0.1159	0.6567	24.43	-17.66	0.66 ± 0.18	0.16
SDSS J0903+4116	0.4304	1.0645	23.51	-20.37	2.89 ± 0.78	0.55
SDSS J0912+0029	0.1642	0.3229	21.18	-18.91	9.83 ± 2.64	0.94
SDSS J0935-0003	0.3475	0.4670	22.76	-18.35	1.88 ± 0.50	1.51
SDSS J0936+0913(a)	0.1897	0.5880	23.95	-17.80	1.69 ± 0.45	0.48
SDSS J0936+0913(b)	0.1897	0.5880	26.93	-14.82	0.49 ± 0.13	0.01
SDSS J0946+1006	0.2219	0.6085	23.14	-18.71	0.97 ± 0.26	0.99
SDSS J0955+0101	0.1109	0.3159	19.94	-20.10	6.21 ± 1.67	1.99
SDSS J0956+5100	0.2405	0.4699	21.34	-19.78	2.31 ± 0.62	1.54
SDSS J0959+0410	0.1260	0.5350	19.83	-21.66	11.33 ± 3.00	5.73
SDSS J0959+4416(a)	0.2369	0.5315	26.52	-14.95	0.33 ± 0.09	0.92
SDSS J0959+4416(b)	0.2369	0.5315	26.02	-15.45	1.07 ± 0.29	0.11
SDSS J1020+1122(a)	0.2822	0.5530	23.99	-17.59	1.51 ± 0.41	1.14
SDSS J1020+1122(b)	0.2822	0.5530	25.87	-15.71	1.34 ± 0.36	0.30
SDSS J1023+4230	0.1912	0.6960	23.87	-18.40	2.95 ± 0.79	0.32
SDSS J1029+0420	0.1045	0.6154	21.69	-20.20	5.04 ± 1.35	2.13

Table 3 (cont'd)

System (1)	z_{fg} (2)	z_{bg} (3)	m_I (AB) (4)	M_B (Vega) (5)	r_{hl} (kpc) (6)	n (7)
SDSS J1032+5322	0.1334	0.3290	20.41	−19.73	2.71 ± 0.73	1.75
SDSS J1100+5329(a)	0.3171	0.8581	23.99	−19.00	2.67 ± 0.72	1.05
SDSS J1100+5329(b)	0.3171	0.8581	26.95	−16.04	0.34 ± 0.09	0.08
SDSS J1103+5322	0.1582	0.7353	22.18	−20.27	3.83 ± 1.03	2.18
SDSS J1106+5228	0.0955	0.4069	23.86	−16.87	0.69 ± 0.19	0.90
SDSS J1112+0826	0.2730	0.6295	23.04	−18.92	1.68 ± 0.45	1.62
SDSS J1134+6027	0.1528	0.4742	21.31	−19.81	0.93 ± 0.25	8.88
SDSS J1142+1001	0.2218	0.5039	23.62	−17.70	0.67 ± 0.18	1.16
SDSS J1143-0144	0.1060	0.4019	20.90	−19.79	3.64 ± 0.98	1.46
SDSS J1153+4612	0.1797	0.8751	24.49	−18.57	1.14 ± 0.31	0.51
SDSS J1204+0358	0.1644	0.6307	23.02	−18.94	2.62 ± 0.70	1.84
SDSS J1205+4910	0.2150	0.4808	23.61	−17.58	0.60 ± 0.16	4.78
SDSS J1213+6708	0.1229	0.6402	22.51	−19.50	4.60 ± 1.23	2.67
SDSS J1218+0830	0.1350	0.7171	22.97	−19.40	3.44 ± 0.92	3.71
SDSS J1250+0523(a)	0.2318	0.7953	25.71	−17.00	0.46 ± 0.12	0.06
SDSS J1250+0523(b)	0.2318	0.7953	19.19	−23.52	12.11 ± 3.25	0.68
SDSS J1250+0523(c)	0.2318	0.7953	23.71	−19.00	3.32 ± 0.89	0.05
SDSS J1250+0523(d)	0.2318	0.7953	24.15	−18.56	3.07 ± 0.82	1.59
SDSS J1250+0523(e)	0.2318	0.7953	24.65	−18.06	1.84 ± 0.49	0.29
SDSS J1251-0208	0.2243	0.7843	23.32	−19.34	0.83 ± 0.22	2.36
SDSS J1402+6321	0.2406	0.4818	25.74	−15.45	1.16 ± 0.31	1.09
SDSS J1403+0006(a)	0.1888	0.4730	23.38	−17.76	1.08 ± 0.29	0.73
SDSS J1403+0006(b)	0.1888	0.4730	23.62	−17.62	1.15 ± 0.31	0.31
SDSS J1403+0006(c)	0.1888	0.4730	22.74	−18.40	1.69 ± 0.45	0.86
SDSS J1416+5136(a)	0.2987	0.8111	21.84	−20.94	5.03 ± 1.35	0.36
SDSS J1416+5136(b)	0.2987	0.8111	24.79	−17.99	0.72 ± 0.19	0.61
SDSS J1416+5136(c)	0.2987	0.8111	24.04	−18.74	1.27 ± 0.34	0.50
SDSS J1420+6019	0.0629	0.5351	21.70	−19.79	6.84 ± 1.84	5.97
SDSS J1430+4105(a)	0.2850	0.5753	20.21	−21.48	7.85 ± 2.11	3.26
SDSS J1430+4105(b)	0.2850	0.5753	22.58	−19.11	1.83 ± 0.49	0.78
SDSS J1430+4105(c)	0.2850	0.5753	24.39	−17.30	1.02 ± 0.27	0.04
SDSS J1430+4105(d)	0.2850	0.5753	22.73	−18.96	3.18 ± 0.85	1.01
SDSS J1430+4105(e)	0.2850	0.5753	23.28	−18.41	3.39 ± 0.91	0.02

Table 3 (cont'd)

System (1)	z_{fg} (2)	z_{bg} (3)	m_I (AB) (4)	M_B (Vega) (5)	r_{hl} (kpc) (6)	n (7)
SDSS J1430+4105(f)	0.2850	0.5753	23.23	−18.46	1.82 ± 0.49	0.29
SDSS J1432+6317	0.1230	0.6643	22.63	−19.50	0.98 ± 0.26	2.76
SDSS J1436-0000	0.2852	0.8049	21.61	−21.14	12.45 ± 3.34	3.92
SDSS J1443+0304	0.1338	0.4187	25.47	−15.34	1.19 ± 0.32	0.05
SDSS J1451-0239	0.1254	0.5203	24.26	−17.15	0.62 ± 0.17	3.71
SDSS J1525+3327	0.3583	0.7173	21.68	−20.69	5.82 ± 1.56	0.91
SDSS J1531-0105(a)	0.1596	0.7439	24.33	−18.16	1.68 ± 0.45	5.11
SDSS J1531-0105(b)	0.1596	0.7439	25.38	−17.11	1.80 ± 0.48	0.47
SDSS J1538+5817(a)	0.1428	0.5312	24.93	−16.54	1.05 ± 0.28	2.43
SDSS J1538+5817(b)	0.1428	0.5312	23.35	−18.12	0.98 ± 0.26	1.17
SDSS J1621+3931	0.2449	0.6021	21.56	−20.26	10.92 ± 2.93	4.04
SDSS J1627-0053	0.2076	0.5241	23.66	−17.77	1.20 ± 0.32	1.00
SDSS J1630+4520(a)	0.2479	0.7933	24.18	−18.52	1.80 ± 0.48	1.19
SDSS J1630+4520(b)	0.2479	0.7933	26.66	−16.04	0.85 ± 0.23	0.21
SDSS J1630+4520(c)	0.2479	0.7933	25.69	−17.01	1.15 ± 0.31	0.05
SDSS J1636+4707(a)	0.2282	0.6745	24.74	−17.43	1.35 ± 0.36	0.16
SDSS J1636+4707(b)	0.2282	0.6745	26.42	−15.75	0.55 ± 0.15	0.14
SDSS J2238-0754	0.1371	0.7126	23.43	−18.92	1.34 ± 0.36	2.31
SDSS J2300+0022	0.2285	0.4635	24.34	−16.75	1.55 ± 0.42	1.10
SDSS J2303+1422	0.1553	0.5170	23.31	−18.08	1.46 ± 0.39	0.53
SDSS J2321-0939	0.0819	0.5324	22.41	−19.06	1.94 ± 0.52	0.19
SDSS J2341+0000(a)	0.1860	0.8070	22.86	−19.90	2.99 ± 0.80	0.14
SDSS J2341+0000(b)	0.1860	0.8070	24.63	−18.13	1.34 ± 0.36	3.21
SDSS J2341+0000(c)	0.1860	0.8070	26.47	−16.29	0.95 ± 0.25	0.09
SDSS J2341+0000(b)	0.1860	0.8070	24.16	−18.60	1.40 ± 0.38	0.20

Note. — **Col. (1)**: The unique SDSS spectrum identifier for the lens system. **Col.(2)**: The redshift of the foreground lens galaxy. **Col.(3)**: The redshift of the background source galaxy. **Col.(4)**: Apparent broad I-band magnitude of the source galaxy, quoted in the AB system. The total systematic error of the apparent magnitude is $\sigma_{m_I} \sim 0.38$ mag. **Col.(5)**: Rest-frame, B-band magnitude of the source galaxy, quoted in the Vega system. **Col.(6)**: The half-light radius of the source galaxy and its total systematic error, expressed as a linear size using the cosmology stated in §1. **Col.(7)**: Sérsic index (n) of the source galaxy. The total systematic error of the Sérsic index is $\sigma_n \sim 0.1$. For the 15 lenses that exhibit "group" morphology, we quote the properties of the individual subcomponents, denoted as **system(a)**, **system(b)** etc. For the subset of source galaxy components that have the lowest Sérsic indices ($n \sim 0.01 - 0.1$), typically indicative of irregular morphologies with strong truncation, $\sigma_n \sim 0.1$ corresponds to an upper bound placed on the total systematic error. In the $n \sim 0.01 - 0.5$ regime, differences between the half-light radii of various Sérsic profiles are nearly negligible. Therefore, a variation in the lower bound of n is not very significant (provided that the $n > 0$ condition is always preserved) for the components with the lowest Sérsic indices since it does not alter the inferred size.

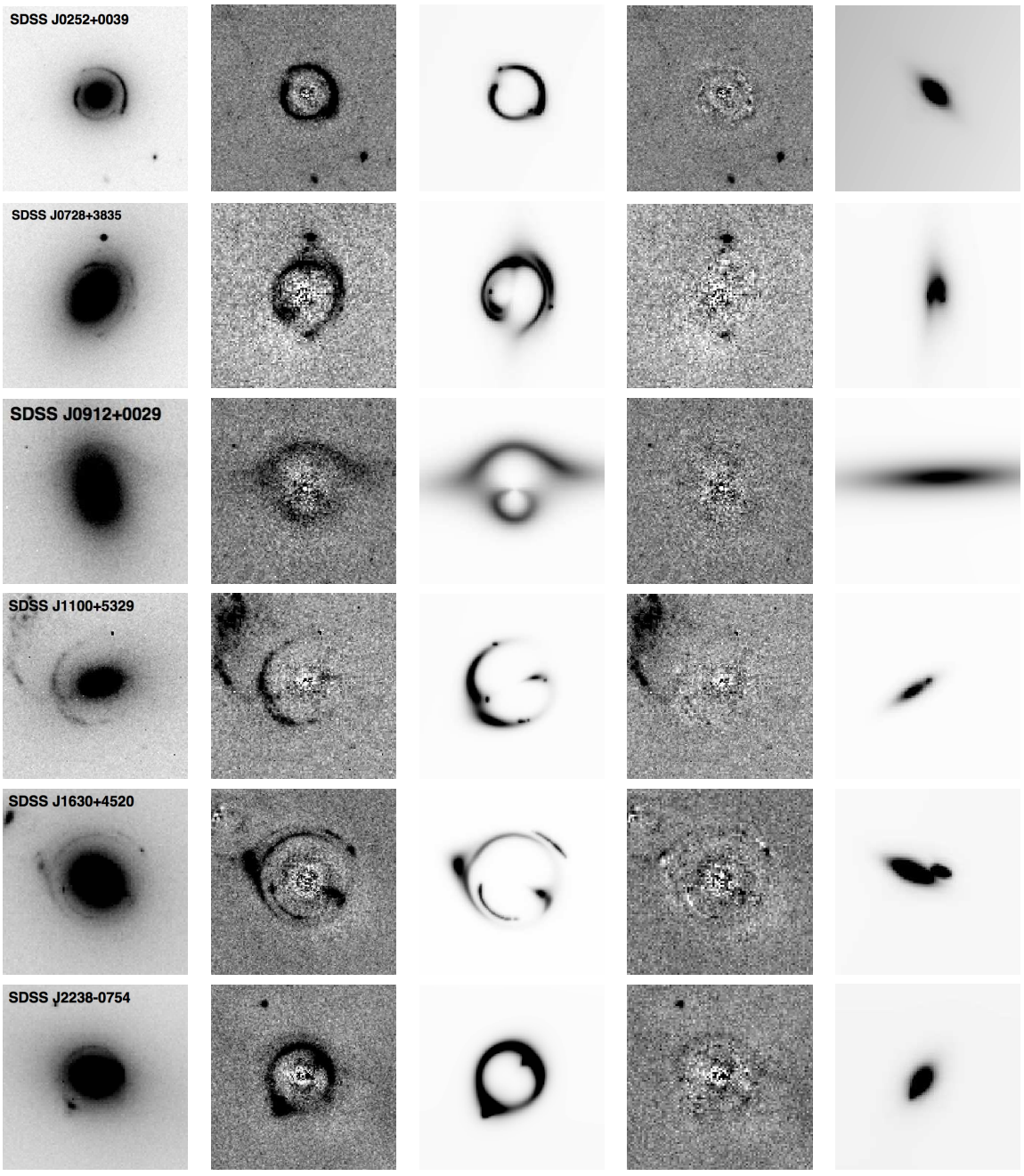

Figure 3.6 A subset of the SLACS lens models from LENSFIT. *From left to right*: ACS-F814W image of the SLACS lens; lens galaxy subtracted image showing the lensed features clearly; predictions of the lensed features from the best-fit SIE mass model and the "double-residual" image after subtracting the ACS PSF convolved lens model from the F814W image; reconstruction of the source components on the source plane. All images are $7\farcs5 \times 7\farcs5$ in size.

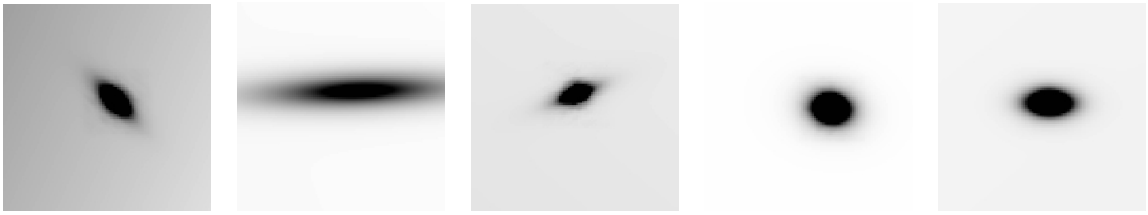

Figure 3.7 The reconstruction of 5 SLACS source galaxies that show "normal" morphology. A normal source refers to an object which can either be described by a single Sérsic component or by multiple concentric or nearly concentric components (for example, a bulge + disk galaxy). *Left to right:* SDSS J0252+0039; SDSS J0912+0029; SDSS J1205+4910; SDSS J1432+6317; SDSS J1627-0053.

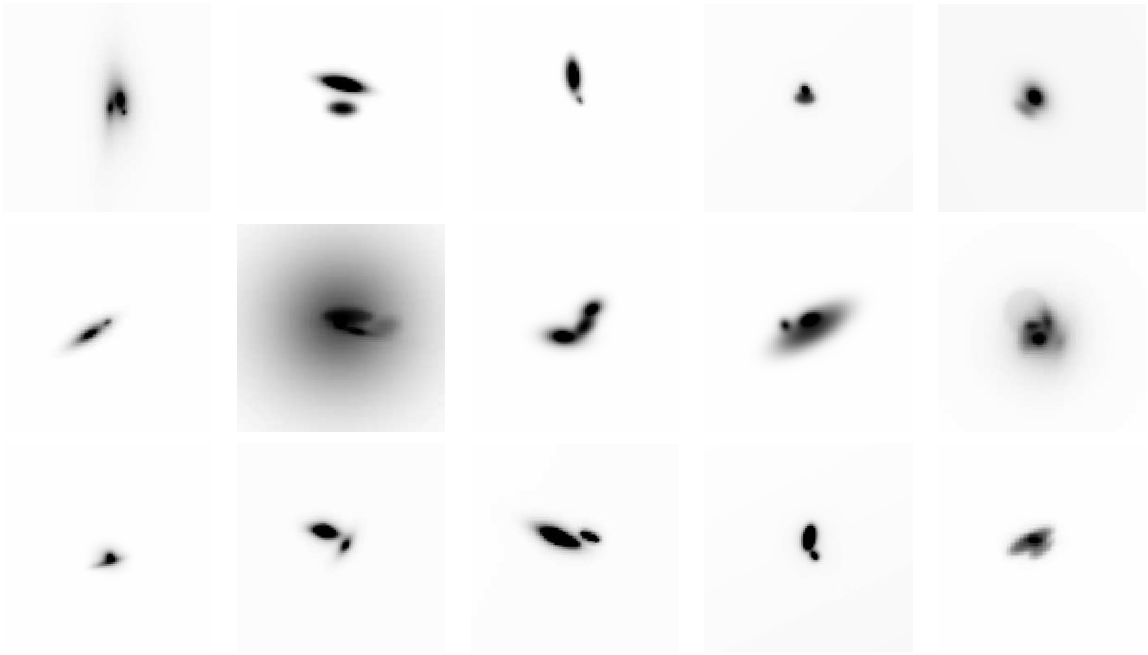

Figure 3.8 The source plane reconstruction of the 15 SLACS systems that show "group" morphology. *Top row, from left to right:* SDSS J0728+3835; SDSS J0822+2652; SDSS J0936+0913; SDSS J0959+4416 and SDSS J1020+1122 *Middle row, from left to right:* SDSS J1100+5329; SDSS J1250+0523; SDSS 1403+0006; SDSS J1416+5136 and SDSS J1430+4105 *Bottom row, from left to right:* SDSS J1531-0105; SDSS J1538+5817; SDSS J1630+4520; SDSS J1636+4704 and SDSS J2341+0000.

3.4.1 Mass Model Properties and Comparisons

In this section, we compare our mass model parameters to those obtained by B08. Although there are several differences in the lens modeling routines, such as the optimization procedure and the lens galaxy subtraction, the use of a common mass model allows a direct comparison between this study and B08. Figure 3.9 shows the fractional difference between Einstein ring radii and SIE axis ratios from the two studies. The root-mean-square (RMS) of the fractional difference between Einstein ring radii from the two studies correspond to $\sim 5\,\%$. With the exception of the lens SDSS J1057-0056 (the outlier in Figure 3.9(*right*)), the RMS of the fractional difference between SIE axis ratios from the two studies correspond to $\sim 12\,\%$. The apparent bias in Figure 3.9(*left*), where LENSFIT estimates of the Einstein radii are systematically lower than that of B08, is caused by the difference in lens galaxy subtraction methods utilized by the two studies. The B-spline fitting method of removing the lens galaxy light profile systematically truncates the lensed features, leading to a higher estimate of the Einstein radius. We believe that the LENSFIT estimates of the Einstein radii are more reliable since the simultaneous modeling of lens and source galaxy profiles minimizes the instances of over- or under-subtraction of the lensed features.

However, the apparent bias in Figure 3.9(*right*) is more complicated. It should also be noted that the SIE models of Bolton et al. (2008a) do not include an external shear component (γ_{ext}), which is coupled to the axis ratio of the mass model (q_{SIE}, Keeton (2001b)). A mass model with a lower axis ratio (for example, $q_{SIE} \sim 0.6$) may be an intrinsic property of the individual lens galaxy, equivalently, such an axis ratio can also be reproduced by a mass model with an intrinsically higher q_{SIE} subjected to an external shear field, which distorts the shape of the lens into an ellipse (i.e. lower the q_{SIE} value). However, the higher order perturbations of the mass model are also determined by the source galaxy light profile, since the lens modeling process has a circular feedback mechanism (i.e. mass model parameters feed to the determination of the source galaxy light profile and vice versa). Therefore, the trade-off between the q_{SIE} and γ_{ext} parameters may not strictly be a direct correlation[6], due to their dependence on the source galaxy light profile within the context of lens modeling.

[6]For example, we cannot make the assumption that all lenses with large external shear fields will have lower q_{SIE} values.

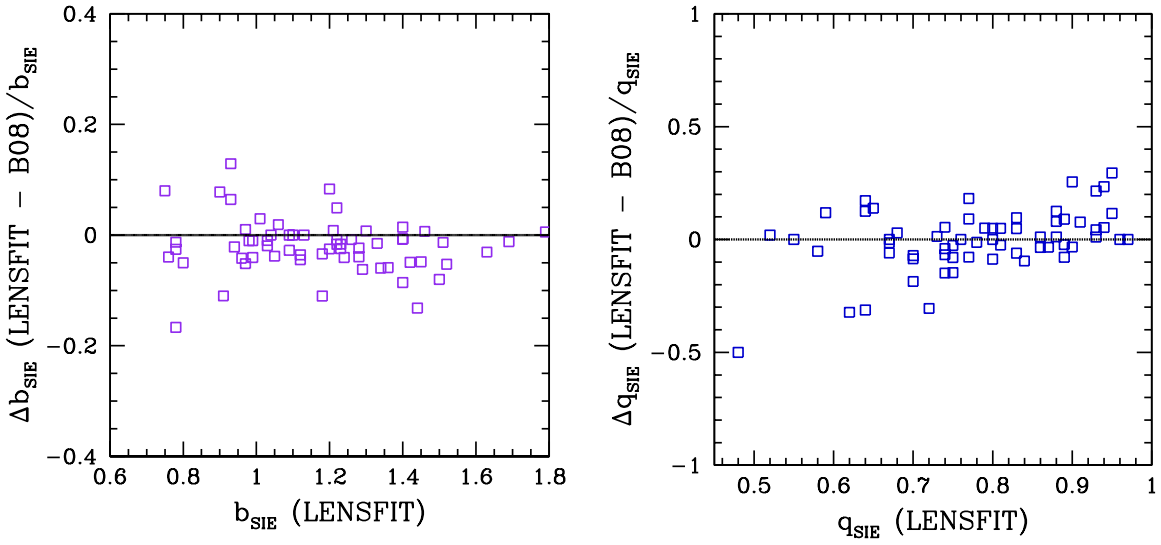

Figure 3.9 Comparison of the mass model parameters of the SLACS lenses from LENSFIT to those from Bolton et al. (2008a). (*Left:*) Fractional difference between the Einstein ring radii, b_{SIE}, from this study and Bolton et al. (2008a). (*Right:*) Fractional difference between the SIE axis-ratios, q_{SIE}, from this study and Bolton et al. (2008a).

3.4.2 Source Galaxy Properties

In the following section, we plot the distributions of the source galaxy half-light radius, Sérsic index, apparent I-band magnitude and rest-frame B-band absolute magnitude in Figure 3.10. Unless otherwise stated, Figures 3.10, 3.13 through 3.15 and 3.20 show the subcomponent properties of the 15 SLACS lenses whose source morphology resembles a "group" (as shown in Figure 3.8). For the remaining 47 lenses, we plot the *global* properties of the source galaxies derived using the method described in §3.2.1.

As evident from Figure 3.10(*top left*), SLACS source galaxies consist of a primarily compact population that peaks at $r_{hl} \sim 1.50$ kpc and drops off rapidly to $r_{hl} \geq 5.00$ kpc. The peak of the Sérsic index distribution correspond to $n \sim 1.0$, with a significant fraction at $n \leq 2.5$ ($\sim 80\%$). However, our lens modeling results indicate a non-negligible fraction of source galaxies with larger half light radii and Sérsic indices. The distribution of the I-band apparent magnitudes, shown in Figure 3.10(*bottom left*), demonstrates that a majority of the SLACS source galaxies correspond to $22 \leq m_I \leq 26$. We perform a standard k-correction procedure to

obtain the absolute magnitudes by assuming SBc- (source galaxies with $n \leq 2.5$) and E-type (source galaxies with $n > 2.5$) galaxy templates. The distribution of the rest-frame B-band magnitudes of our sample is shown in Figure 3.10(*bottom right*).

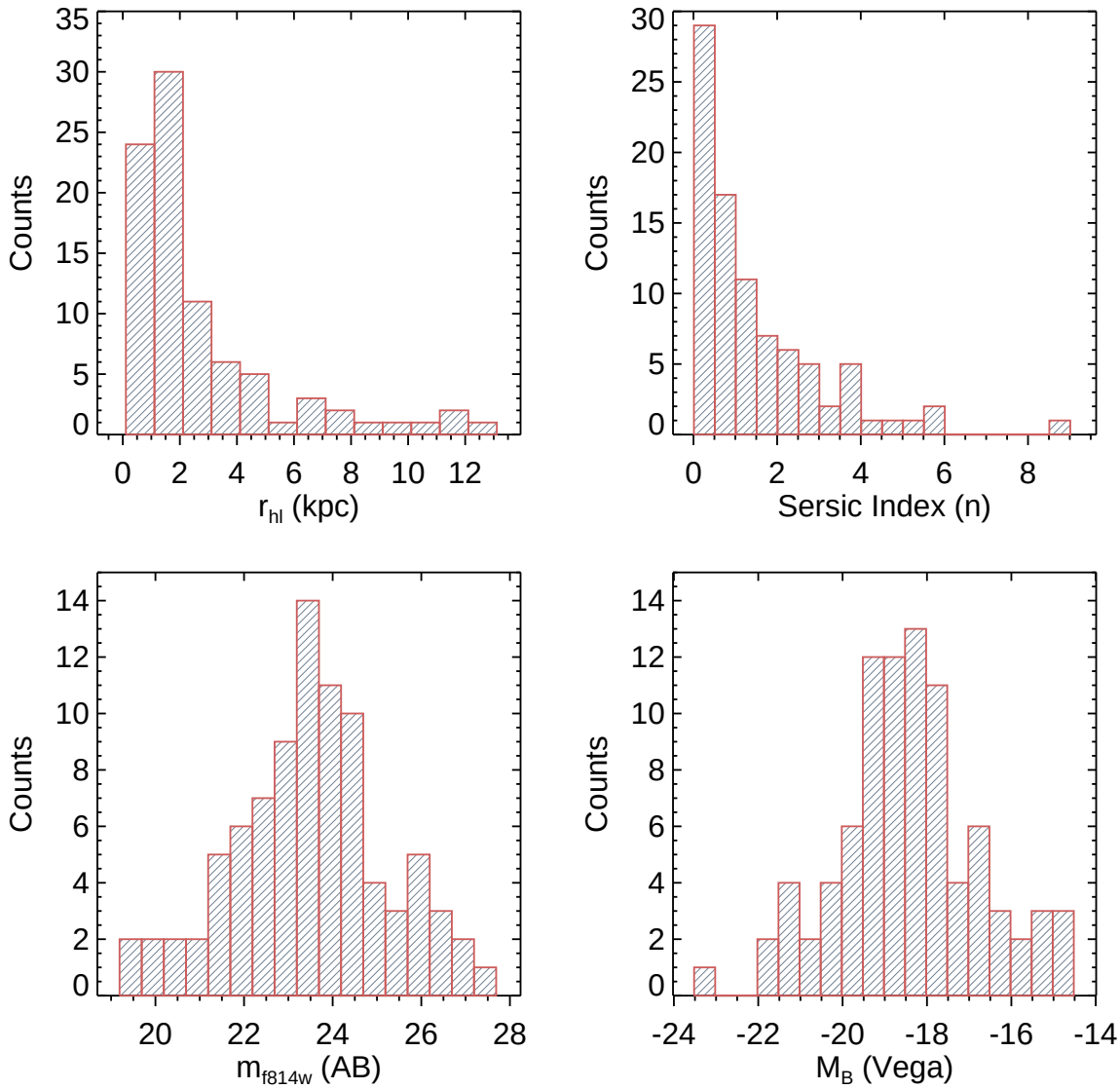

Figure 3.10 Distribution of the SLACS source galaxy structural parameters. For the 15 sources that show "group" morphology, the structural parameters of the individual subcomponents are plotted. For the remaining 47 sources, the structural parameters correspond to that of the single Sérsic component fit, as described in §3.3.2. *Top row, left to right:* Distribution of the half-light radii (kpc); Distribution of the Sérsic indices. *Bottom row, from left to right:* Distribution of the apparent I-band magnitudes (AB system); Distribution of the rest-frame B-band magnitudes (Vega system).

Comparison with the SLACS Series

Next, we compare our lens modeling results to another study of the SLACS source population. During the final stages of our analysis, we became aware of a new publication by Newton et al. (2011) (Paper XI of the SLACS series, referred to as N11) whose goals overlap with this project and allows a detailed comparison of the lens modeling results. The lens modeling procedure of N11, similar to that of Marshall et al. (2007) which analyzed the source galaxy of SDSS J0737+3216, differs from LENSFIT in the following ways: N11 uses the B-Spline method to remove the lens galaxy light profile prior to lens modeling and a single Sérsic component to model each source galaxy. There are 37 (out of 62 lenses) that are in common between this study and that of N11 and Figure 3.11 compares the angular sizes of the half-light radii, I-band apparent magnitudes, and Sérsic indices of the common sample. For comparison purposes, it is useful to keep the lens modeling steps between LENSFIT and N11 as close as possible, such that we can identify the key intrinsic differences between the two methods. Therefore, we reanalyze the common lens sample (37 out of 62 SLACS lenses) with the following changes such that our lens modeling steps follow those of N11 closely.

- We obtain the best-fit lens galaxy profile prior to the full lens modeling, by masking the lensed features, and hold it fixed throughout the remainder of the procedure (*vs.* simultaneously optimizing the mass model, source galaxy and lens galaxy light profiles).
- For the full lens modeling, we optimize the mass model and describe the source galaxy using only a single Sérsic profile (*vs.* using multiple Sérsic components to describe the source galaxy light profile).
- We use the best-fit parameters of the single, Sérsic source galaxy profile for comparison with N11 results.

It should be noted that making the above changes yield substantially poorer residuals in comparison to our original methodology; however, it is informative to visualize the differences between the two methods.

From Figure 3.11, it is evident that LENSFIT systematically measures brighter and larger source galaxies, with larger Sérsic indices, in comparison to N11. The

systematic offset between the LENSFIT and N11 results primarily stems from the methods of lens galaxy light subtraction. As discussed above, lens galaxy subtraction using Sérsic profiles can sometimes produce incomplete residuals that complicate the modeling of the source galaxy. This results in an additional "halo" around the source galaxy leading to an estimate of a higher luminosity, size and Sérsic index. Conversely, the use of a B-Spline model can result in an over-subtraction of the source galaxy flux, where tangentially magnified images are truncated, leading to an estimate of a lower luminosity, size and Sérsic index (Marshall et al. 2007). Therefore, the two methods might be expected to provide upper and lower limits to the source galaxy structural parameters.

To illustrate how the details of the source galaxy structures affect the lens model, which then feeds back to the inference of the global structure of the source galaxy itself, we perform the following test (on the original LENSFIT method, discussed in §3.3). During the first iterations to determine the complete lens model, we hold the best-fit lens galaxy light profile fixed and optimize the mass model and source galaxy light profile (described using multiple Sérsic components, if necessary). After LENSFIT converges to an initial solution, we free the parameters of the lens galaxy light profile and optimize all three components of the lens model. During this iteration, the source galaxy parameters for a majority of the SLACS lenses do not change significantly; however, the most deviant systems from the 1:1 relation shown in Figure 3.11 also undergo a significant changes in the source galaxy parameters. These systems typically correspond to lenses where foreground lens galaxy subtraction, even using multiple Sérsic components, leaves large residuals as shown in Figure 3.12.

Although the lenses shown in Figure 3.12 correspond to a small percentage of systems that are intrinsically difficult to model with Sérsic profiles, a *typical* lens from a SLACS-like survey can be modeled very accurately as shown in Figure 3.6. Thus, the solutions obtained by this study and that of N11 can be considered to bracket the true source galaxy morphology. As discussed above, the lens galaxy subtraction method of N11 yields *visually* clean residuals (which, in turn, results in a clean "double residual"); however, this should not purely be considered as a benchmark of lens modeling accuracy. When quantifying the advantages of a lensing survey or the evolution of disk galaxy scaling relations (the goals of this project that will be discussed in the following sections), the lens modeling methodology of N11 can lead to overly optimistic conclusions. In comparison, LENSFIT utilizes

a light profile that is commonly observed over a large range of redshifts to model both lens and source galaxies, a method that ultimately yields more conservative and reliable conclusions. The simultaneous decomposition of the lens galaxy light profile and lensed features ensures the reliability of the LENSFIT method since the lens galaxy profile shape is typically highly symmetric and monotonically declining, which is different from the radially and azimuthally varying source galaxy profile on the image plane (thus, simultaneity can be used to break the degeneracy between lens and source galaxy light profiles on the image plane). Although the method of N11 yields visually clean residuals, the high degrees of freedom of the B-spline models can truncate the lensed features, which coupled with non-simulataneous modeling of the source galaxy light profile systematically leads to inferences of a fainter and more compact source galaxy population. In other words, with the method of N11, the lens modeling software cannot break the degeneracy between the lens and source galaxy profiles on the image plane. Therefore, it would not be able to distinguish between lensed features stemming from an intrinsically faint and compact source galaxy vs. truncated lensed features due to the lens galaxy subtraction method, an issue that does not affect LENSFIT modeling.

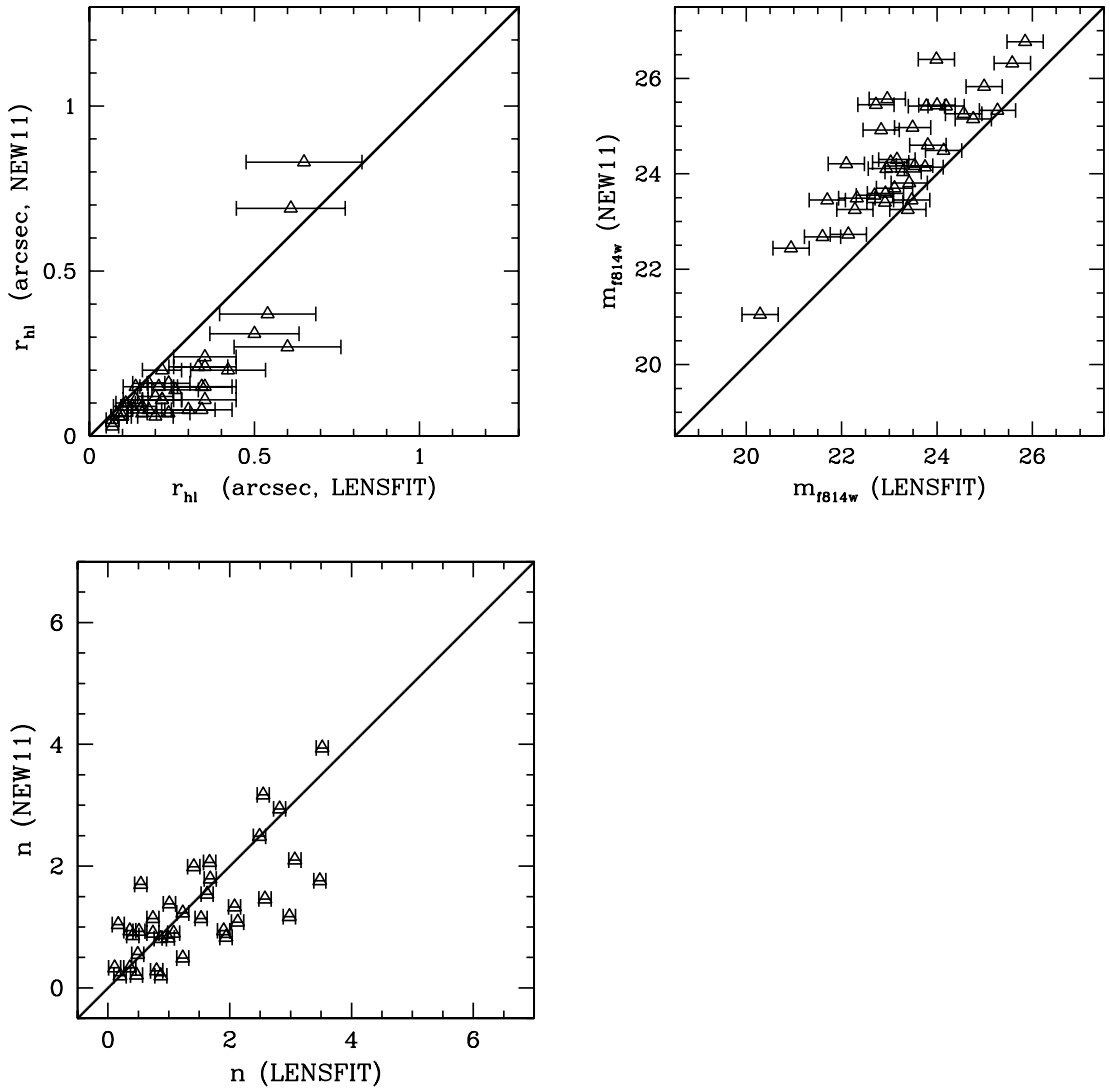

Figure 3.11 Comparison of our SLACS source galaxy parameters to those derived by Newton et al. (2011). *Top row, left to right:* Comparison of the half-light radii angular sizes (arcseconds); Comparison of the I-band apparent magnitudes (AB system). *Bottom row:* Comparison of the Sérsic indices.

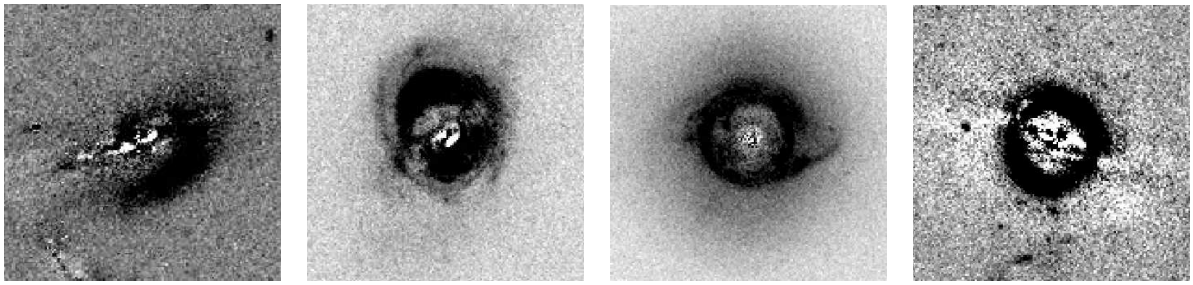

Figure 3.12 Lens galaxy subtracted ACS-F814W images showing the lensed features for a subset of lenses that are most deviant from the 1:1 relation in Figure 3.11. These systems show large residuals after the lens galaxy subtraction, which can result in an overestimate of the source galaxy luminosity, size and Sérsic index. *From left to right:* SDSS J0955+0101; SDSS J0959+0410; SDSS J1250+0523 and SDSS J1420+6019.

3.5 Quantifying the Advantages of a Lensing Survey

Since the first discovery of a gravitationally lensed quasar (Walsh et al. 1979), the advantages of strong gravitational lensing has been utilized for a variety of applications including (but not limited to) constraining the mass profiles of early-type galaxies, studying the properties of quasar-host galaxies and deriving detailed two-dimensional kinematics of high-redshift galaxies (Bolton et al. 2006; Inada et al. 2009; Johnston et al. 2003; Jones et al. 2010; McGreer et al. 2010; Peng et al. 2006; Riechers et al. 2011; Ross et al. 2009; Smith et al. 2009; Stark et al. 2008; Yuan et al. 2012). In the following section, we quantify the advantage of a galaxy-scale lensing survey such as SLACS which, in turn, will enable us to study the evolution of various scaling relations at the faint, compact and low-mass regime. To put the SLACS source galaxies within the context of the galaxy population at intermediate- and high-redshifts, we plot its luminosity-size relation as shown in Figure 3.13 (green filled circles).

The redshift ranges of the luminosity-size relation correspond to $0.40 \leq z < 0.75$ and $0.75 \leq z \leq 1.20$. The redshift cut excludes the following 3 systems from the sample: SDSS J0044+0113 ($z_{bg} = 0.20$); SDSS J0912+0029 ($z_{bg} = 0.32$) and SDSS J1032+5322 ($z_{bg} = 0.33$). We further group the source galaxies into disk-dominated ($n \leq 2.5$) and bulge-dominated ($n > 2.5$) samples. The majority of the source galaxies of the SLACS lenses presented in Bolton et al. (2008a) are located at z < 0.84 due

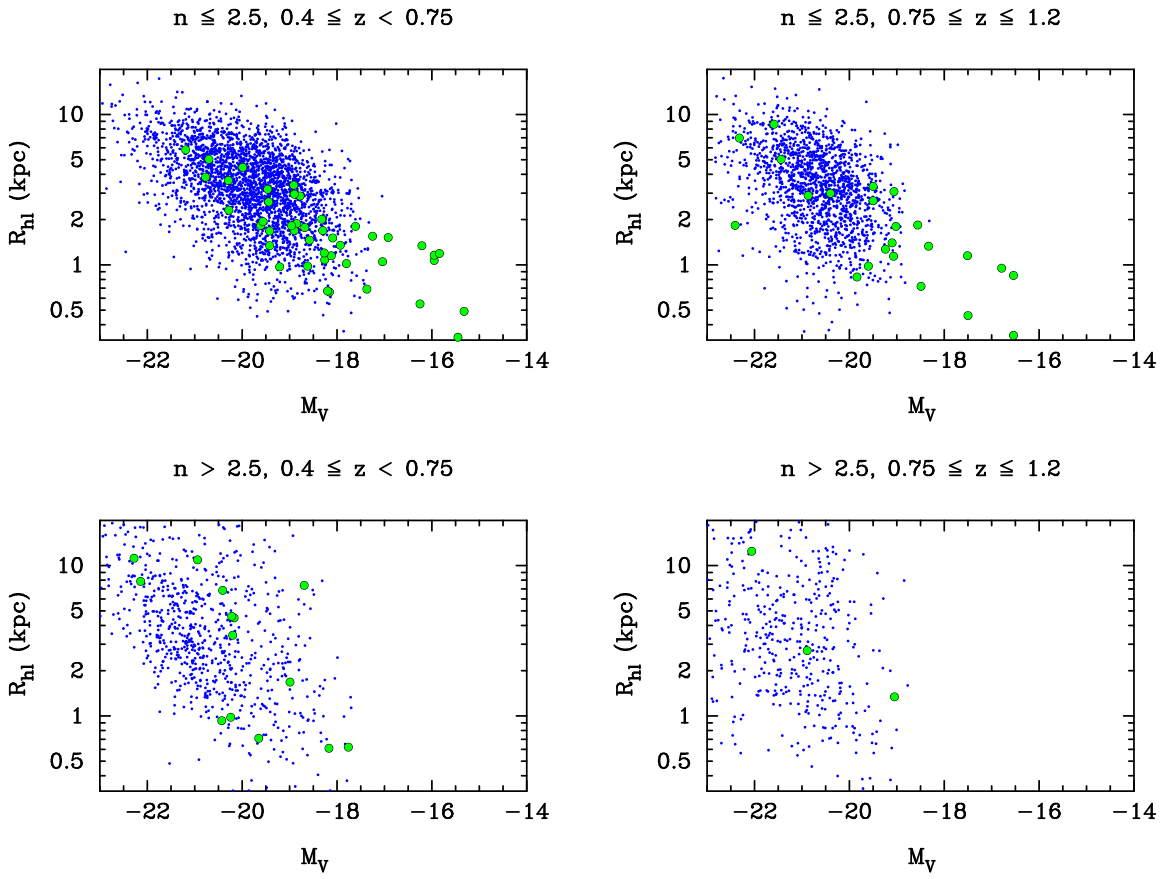

Figure 3.13 Comparison of the SLACS source galaxy population to the GEMS galaxy sample (Barden et al. 2005; Rix et al. 2004) on the luminosity-size plane. The green circles correspond to the SLACS source galaxy parameters and the blue points correspond to the GEMS galaxy parameters. Both samples are grouped in an identical manner in all the panels. **Top-left:** Luminosity-size relation of the disk-dominated galaxies ($n \leq 2.5$) at $0.4 \leq z < 0.75$. **Top-right:** Same as the top-left panel for $0.75 \leq z < 1.2$. **Bottom-left:** Luminosity-size relation of the bulge-dominated galaxies ($n > 2.5$) at $0.4 \leq z < 0.75$. **Bottom-right:** Same as the bottom-left panel for $0.75 \leq z < 1.2$. For the 15 SLACS sources that exhibit "group" morphology, the structural parameters are those of the individual components. For the remaining 47 SLACS sources, the structural parameters correspond to the results of the *global*, single Sérsic component fit, as described in §3.3.3. The systematic uncertainties of the sizes and luminosities of SLACS source galaxies are given in Table 3 and are not shown in the subplots for clarity.

to the spectroscopic selection criteria of the SLACS survey. Beyond the $z \sim 0.84$ limit, [OIII] 5007 Å emission line is shifted out of the SDSS spectral range; therefore, higher redshift lens candidates are less likely to be imaged initially in comparison to the intermediate redshift candidates, which have spectroscopic confirmation from all three emission lines. However, *HST* imaging of higher redshift lens candidates, which were confirmed using only two emission lines, were presented in the more recent

publications of the SLACS series (Auger et al. 2009, 2010).

The comparison galaxy sample of Figure 3.13, shown in blue, corresponds to the *HST* imaging survey GEMS (Rix et al. 2004), which has photometric redshift estimates from the COMBO-17 catalog (Barden et al. 2005). We select GEMS galaxies at $0.40 \leq z \leq 1.10$, which are indicated to have successful GALFIT structural fits and are matched to a COMBO-17 object with a successful photometric redshift estimate ($\leq 0\farcs5$ separation, Barden et al. (2005)). The advantages of a lensing survey are most apparent in the top-left and top-right panels of Figure 3.13[7], which show the comparison between the disk-dominated SLACS source galaxies and the corresponding GEMS sample at $0.40 \leq z < 0.75$ and $0.75 \leq z \leq 1.20$.

This comparison clearly shows a tail of compact, low-luminosity SLACS sources extending ~ 2 magnitudes beyond the GEMS sensitivity limit ($M_V \sim -18$ for the $0.40 \leq z < 0.75$ sample and $M_V \sim -19$ for the $0.75 \leq z \leq 1.20$ sample). Wide field galaxy surveys will often miss the more numerous, low-luminosity galaxy population at intermediate to high redshifts because of the luminosity cut-off, whereas most compact galaxies get misidentified as stars or else are too small to be fit accurately. However, by using an emission line based selection criterion, lensing surveys can probe ~ 2 magnitudes deeper into the intrinsically fainter, star forming galaxy population (Bolton et al. 2006, 2008a; Marshall et al. 2007).

3.6 Evolution of the Luminosity-Size Relation Since $z \sim 1$

The advantages of a lensing survey also enable us to investigate the evolution of the luminosity-size relation of SLACS source galaxies as shown in Figures 3.14, 3.15 and 3.20 (open circles and circles with a cross). In Figures 3.14, 3.15 and 3.20, the open circles correspond to the measurements of SLACS sources that exhibit "normal" galaxy morphology[8] on the source plane. The circles with crosses correspond to the

[7]Since the SLACS lenses were initially selected spectroscopically, from the presence of nebular emission lines, a majority of the source galaxies are most likely star forming, disk-like systems.

[8]Galaxies that can be best described by a single, Sérsic component or multiple, concentric or nearly concentric Sérsic components.

subcomponent measurements of SLACS sources that exhibit "group" morphology[9]. The luminosities are expressed in rest-frame V-band absolute magnitude and the SLACS source galaxies are grouped in an identical manner to Figure 3.13.

Similar to the previous observational studies of the luminosity-size relation (Barden et al. 2005; Melbourne et al. 2007; Trujillo et al. 2006), we use the SDSS galaxy sample as a local comparison. The structural parameters of the SDSS galaxies are provided by Simard et al. (2011), who perform two-dimensional Sérsic profile fits to $\sim 1,100,000$ galaxies in the g and r bandpasses. Simard et al. (2011) impose the following faint surface brightness limit on the imaging sample to match the completeness limit of the SDSS MAIN galaxy spectroscopic sample: $\mu_{50,r} = 23.0\,\mathrm{mag\,arcsec^{-2}}$ (Strauss et al. 2002). Furthermore, galaxies at $z < 0.005$ whose distances may be contaminated by peculiar velocities are also excluded from the sample. The redshift distribution of the final sample of $\sim 670,000$ SDSS galaxies peaks at $z \sim 0.1$ and declines rapidly to $z \sim 0.3$ (Simard et al. 2011).

The SDSS luminosity-size relation, shown as the greyscale in Figures 3.14, 3.15 and 3.20, represents the volume-corrected number density of SDSS galaxies on the luminosity-size plane (grouped into disk-dominated vs. bulge-dominated galaxies according their Sérsic indices). In the following sections, we will discuss various scenarios that will match the SLACS source galaxy population to the local galaxy population on the luminosity-size plane. We focus our discussion primarily on the disk-dominated source galaxies ($n \leq 2.5$), shown in the upper panels of Figure 3.14.

3.6.1 Observational Limits on the Size and Luminosity Evolution of Disk Galaxies Since $z \sim 1$

From the top-left and top-right panels of Figure 3.14, it is evident that the luminosity-size relation of disk-dominated SLACS source galaxies requires some evolution to migrate to the locus of the local disk galaxy population[10] Possible evolutionary paths for the surface brightness evolution of disk galaxies include: pure size evolution, pure luminosity evolution or a combination of both (Kanwar et al. 2008). Due to the limited sample size, we cannot test the number density evolution of the SLACS source

[9]Galaxies that are characterized by multiple, offset Sérsic components as shown in Figure 3.8.
[10]Provided that the local comparison (i.e. SDSS) is a representative sample.

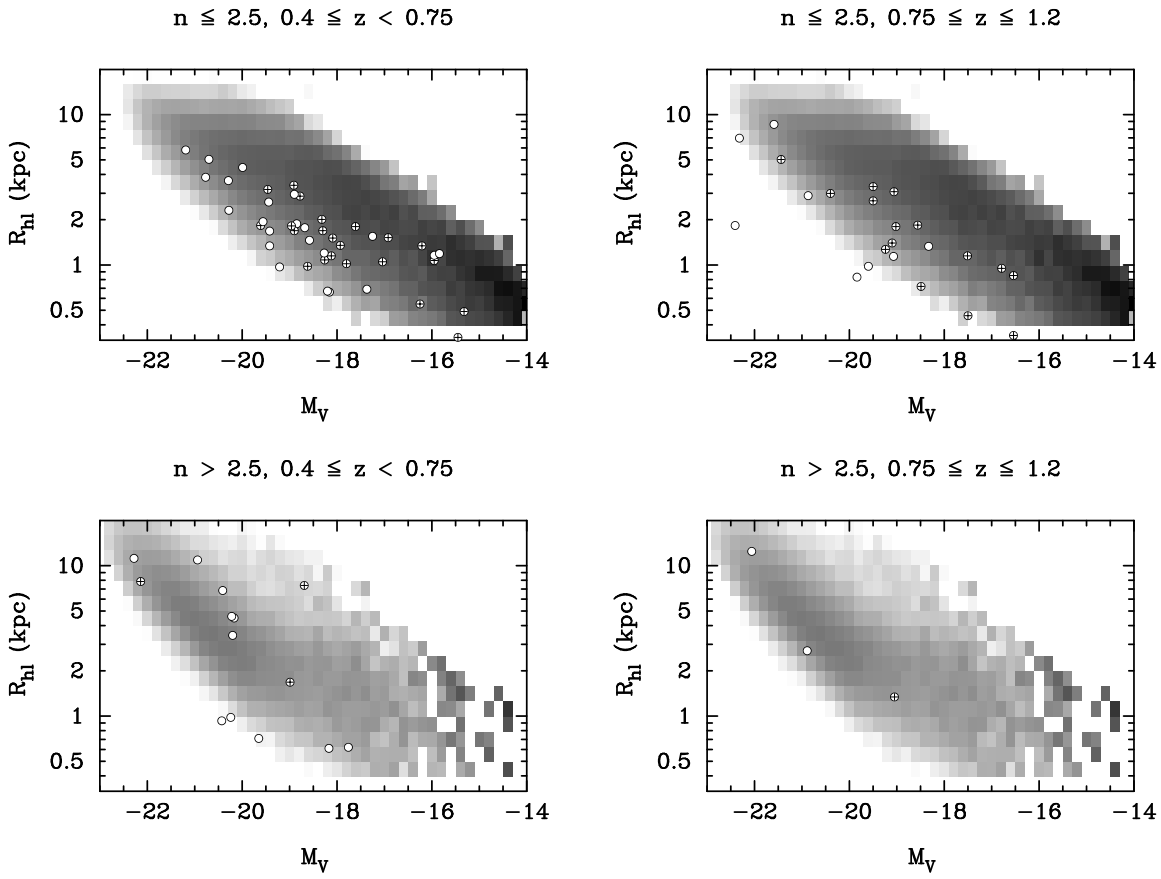

Figure 3.14 Comparison of the SLACS source galaxy luminosity-size relation to the SDSS luminosity-size relation (i.e. local luminosity-size relation), provided by Simard et al. (2011). In all panels, SLACS source galaxy measurements are shown as open circles or circles with a cross. The open circles correspond to the measurements of SLACS sources that show "normal" galaxy morphology and the circles with a cross correspond to the subcomponent measurements of SLACS sources that show "group" morphology. The systematic uncertainties of the sizes and luminosities of SLACS sources are given in Table 3 and are not shown in the subplots for clarity. The greyscale represents the volume-corrected number density of SDSS galaxies on the luminosity-size plane. The SDSS galaxy sample peaks at $z \sim 0.1$ and declines rapidly to $z \sim 0.3$. **Top-left:** Luminosity-size relation of the disk-dominated SLACS galaxies ($n \leq 2.5$) at $0.4 \leq z < 0.75$ and the luminosity-size relation of disk-dominated SDSS galaxies. **Top-right:** Same as the top-left panel for the $0.75 \leq z < 1.2$, disk-dominated SLACS source galaxies. **Bottom-left:** Luminosity-size relation of bulge-dominated galaxies ($n > 2.5$) at $0.4 \leq z < 0.75$ and the luminosity-size relation of bulge-dominated SDSS galaxies. **Bottom-right:** Same as the bottom-left panel for the $0.75 \leq z < 1.2$, bulge-dominated SLACS source galaxies.

galaxies up to $z \sim 1$, similar to the study of Sargent et al. (2007); however, we can test the remaining evolutionary trends. Therefore, we decompose the surface brightness evolution of SLACS disk galaxies into pure size or pure luminosity evolution and

determine the average observable evolution in each scenario, as shown in Figure 3.15.

To quantify these limits, we perform a V_{max}-weighted linear regression on the SDSS luminosity-size relation as shown below,

$$\log(R_{hl}) = -0.188\ (\pm 0.003)\ M_V - 2.95\ (\pm 0.06) \tag{3.3}$$

The top-left and bottom-left panels of Figure 3.15 show reproductions of the SLACS disk galaxy luminosity-size relation at $0.4 \leq z < 0.75$ and $0.75 \leq z \leq 1.20$. The long dashed lines in these panels correspond to equation 3.3. The short dashed lines correspond to the weighted linear regression to the $0.40 \leq z < 0.75$ and $0.75 \leq z \leq 1.20$ SLACS disk galaxy luminosity-size relations, with the slope fixed to that of equation 3.3. We test the y-axis weighting scheme (i.e. weighted by the errors of the size parameter) and the orthogonal distance regression (ODR, which takes errors on both size and luminosity parameters into account) for the linear regression and find that both weighting schemes yield the same results within their errors. Therefore, we adopt the y-axis weighting scheme for the linear regression to the SLACS sample. The $0.40 \leq z < 0.75$ SLACS disk galaxy sample is characterized by (short dashed line in the top-left panel of Figure 3.3),

$$\log(R_{hl}) = -0.188\ (\pm 0.003)\ M_V - 3.29\ (\pm 0.04) \tag{3.4}$$

and the $0.75 \leq z \leq 1.20$ disk galaxy sample is characterized by (short dashed line in the *bottom-left* panel of Figure 3.3),

$$\log(R_{hl}) = -0.188\ (\pm 0.003)\ M_V - 3.42\ (\pm 0.07) \tag{3.5}$$

The average observable pure-size and pure-luminosity evolution of the SLACS sample correspond to the offsets of equations 3.4 and 3.5 in the size and luminosity directions such that their intercepts match that of equation 3.3. The middle and right panels of Figure 3.15 show the positions of the SLACS disk galaxy samples at $0.40 \leq z < 0.75$ and $0.75 \leq z \leq 1.20$ after the average pure-size and pure-luminosity evolution are applied respectively. The top-middle and bottom-middle panels show the SLACS disk galaxy sample shifted by 0.29 dex and 0.46 dex in *size*, to match the SDSS sample, based on the intercepts of equations 3.3, 3.4 and 3.5. Equivalently, the top-right and bottom-right panels show the SLACS disk galaxy sample shifted in *luminosity* (rest-frame V-band) by 1.4 mag and 2.3 mag, to match the SDSS sample.

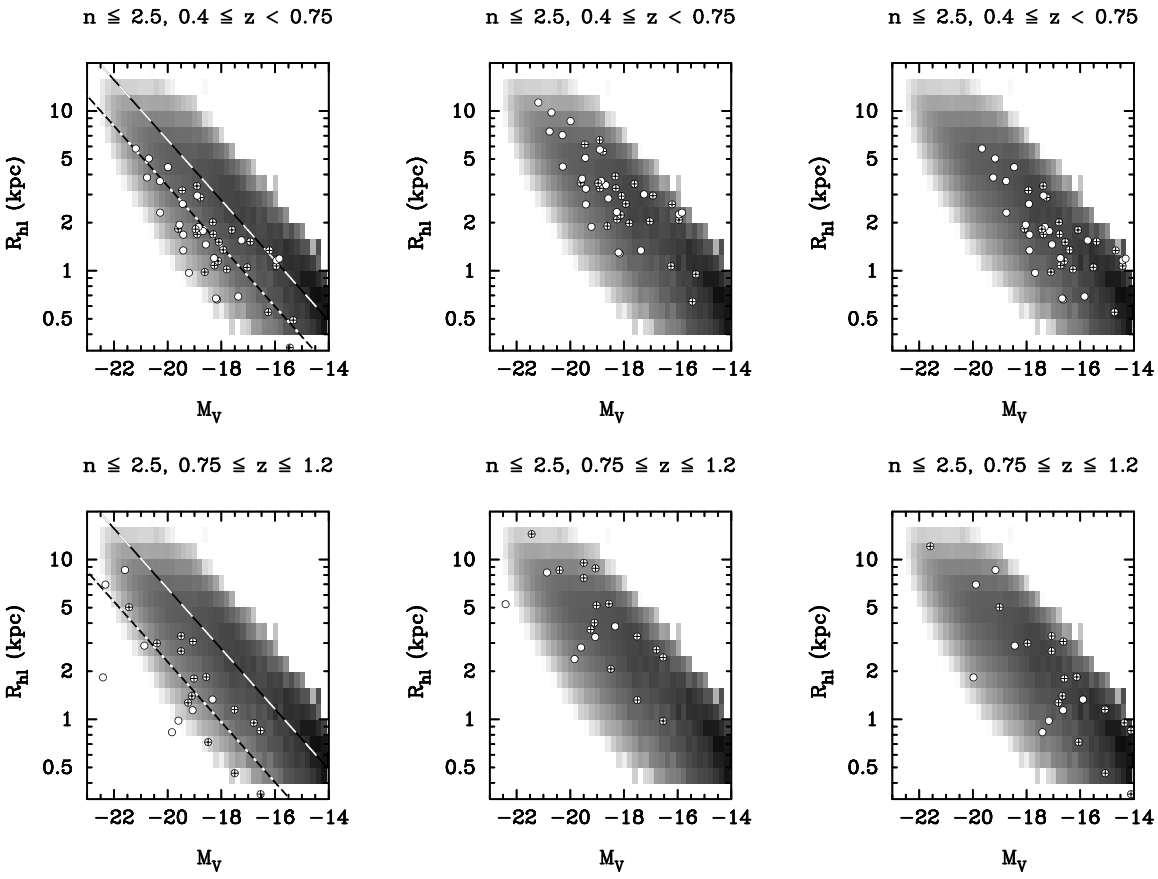

Figure 3.15 Quantifying the average observable size and luminosity evolution of disk-dominated SLACS source galaxies since $z \sim 1$. Similar to Figure 3.14, SLACS source galaxy measurements are shown as open circles (normal galaxies) and circles with a cross (groups). The greyscale represents the volume-corrected number density of SDSS galaxies on the luminosity-size plane. The systematic uncertainties of the sizes and luminosities of SLACS sources are given in Table 3 and are not shown in the subplots for clarity. *Top row, from left to right* → **Top-left:** Luminosity-size relation of SLACS disk-galaxies at $0.4 \leq z < 0.75$ and the comparison SDSS disk galaxy sample. The long dashed line corresponds to the V_{max}-weighted linear regression to the SDSS sample. The short dashed line corresponds to the y-axis weighted linear regression to the SLACS disk galaxy sample at $0.4 \leq z < 0.75$, with the slope fixed to that of the long dashed line. The error bars of the SLACS disk galaxy parameters (given in Table 2) are used for the linear regression but not shown in the subplots for clarity. **Top-middle:** The $0.4 \leq z < 0.75$ SLACS disk galaxy sample shifted in *size* by 0.29 dex, such that the intercept of the average surface brightness fit to the SLACS sample (i.e. the short dashed line in the top-left panel) now to matches the average surface brightness fit to the SDSS sample (i.e. the long dashed line in the top-panel). **Top-right:** Similar to the top-middle panel except the SLACS disk galaxy sample is now shifted in *luminosity* by 1.4 mag. *Bottom row, from left to right* → **Bottom-left:** Luminosity-size relation of SLACS disk-galaxies at $0.75 \leq z \leq 1.20$ and the SDSS disk galaxy sample. The long dashed line is identical to the top-left panel and the short dashed line corresponds to the y-axis weighted linear regression to the SLACS disk galaxy sample at $0.75 \leq z < 1.20$, with the slope fixed to that of the long dashed line. **Bottom-middle:** The $0.75 \leq z \leq 1.20$ SLACS disk galaxy sample shifted in *size* by 0.46 dex, such that the intercept of the average surface brightness fit to the SLACS sample now to matches the average surface brightness fit to the SDSS sample. **Bottom-right:** Similar to the method of the bottom-middle panel except the SLACS disk galaxy sample is now shifted in *luminosity* by 2.3 mag.

It should be noted that comparisons made between the SLACS source galaxies and the SDSS sample must be interpreted with caution due to the uncertainties in quantifying the SLACS selection function. The selection function of a SLACS-like lensing survey is completely different from that of a broad-band imaging survey since the source galaxies of lens systems are selected based on the presence of nebular emission lines[11]. Furthermore, unlike the statistical analyses of lensed quasars that address the probability of a given source being lensed, spectroscopic galaxy-scale lensing surveys address the statistical question of the probability of a given galaxy being a lens (Dobler et al. 2008). Quantifying the SLACS selection function is beyond the scope of this project; nevertheless, we can test the evolution of SLACS luminosity-size relation while considering the cautionary notes discussed above. We refer the reader to Dobler et al. (2008) for a detailed statistical analysis of a spectroscopic galaxy-scale lensing survey, which include the following components: the dominant selection effects (including the size of the spectroscopic fiber), the probability of detecting a source galaxy emission line (ex: [O II] 3727Å) for a given set of observational parameters, the probability of detecting a gravitational lens in a follow-up imaging survey and an estimate of the number of galaxy-scale lenses that are expected to be discovered using the spectroscopic selection criterion.

Since the SLACS sample was selected based on source emission lines, a reasonable assumption is that it is useful to compare it to a local, control sample with a similar [O II] 3727Å emission line equivalent width (EW) distribution. Figure 3.16 examines the g-band surface brightness offsets of SDSS disk galaxies (from the V_{max}-weighted linear regression to the SDSS sample, in Figure 3.15) as a function of the rest-frame [O II] 3727Å emission line EW. In Figure 3.16, galaxies with no [O II] 3727Å detection are assigned an EW of 0Å. The large open circles, which correspond to the median surface brightness offset in 10Å bins, indicate that there is indeed a systematic increase in g-band surface brightness of SDSS disk galaxies with increasing [O II] 3727Å line strength. Thus, the next step is to construct the local comparison sample by utilizing the subset of SDSS disk galaxies with [O II] 3727Å EWs similar to that of the SLACS sample. However, it is not possible to directly measure the [O II] 3727Å EW of

[11]Another factor that affects the selection function of a SLACS-like lensing survey is the magnification bias. Since the spectroscopic selection method yields lens candidates that are typically unresolved, SLACS-like surveys favour lenses with high total magnification. The magnification bias is strongest for compact sources (Marshall et al. 2007).

a SLACS source galaxy[12] since the SDSS continuum is entirely dominated by the contribution from the bright, typically early-type lens galaxy.

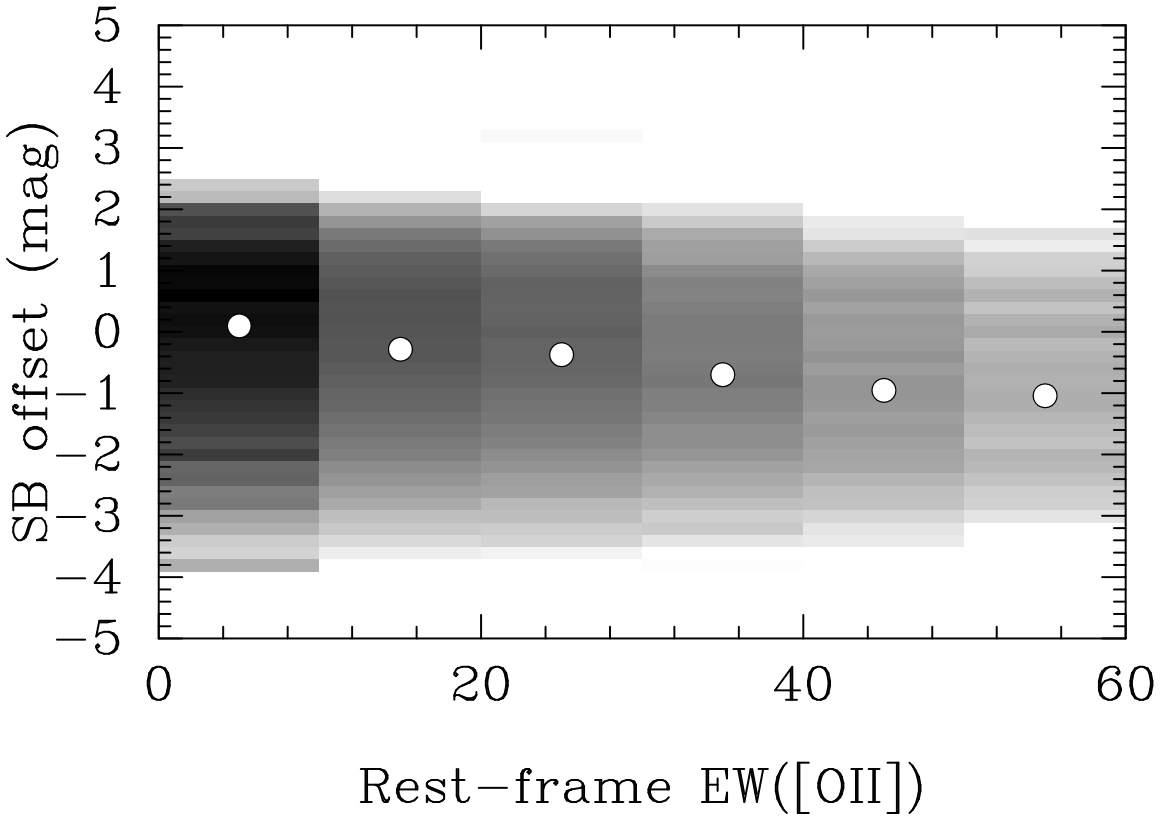

Figure 3.16 The g-band surface brightness trend of the SDSS disk galaxy population as a function of the rest-frame [O II] 3727Å equivalent width. SDSS disk galaxies with no [O II] 3727Å emission line detection are assigned an equivalent width of 0Å. The median g-band surface brightness offset of the SDSS galaxies is normalized to zero. The large, open circles correspond to the median surface brightness offset in 10Å bins. As evident from the median offsets (i.e. the open circles), there is a systematic increase in surface brightness with increasing [O II] 3727Å line strength.

An estimate of the [O II] 3727Å EW of a SLACS source can be derived by matching the spectral energy distribution (SED) of a star-forming galaxy to the available *HST* photometry, while accounting for the effects of SDSS spectroscopic fiber and seeing conditions. A suitable match between the SED and the *HST* photometry, in principle, yields an estimate of the continuum contribution from the source galaxy. In turn, the best-fit continuum of the source galaxy can be combined with the observed [O II] 3727Å emission line, from SDSS, to measure the corresponding EW. However, [O II]

[12]Examples of SDSS spectra showing the [O II] 3727Å emission line are shown in Figure 1.11. For the full set, please refer to Bolton et al. (2006).

3727Å EW estimates from the method described above can be highly uncertain and only a subset of the SLACS lenses have *HST* photometry in multiple filters to pursue this method (A. Bolton and the SLACS collaboration, private communication).

In the absence of reliable [O II] 3727Å EW measurements for SLACS source galaxies, we cannot impose a [O II] 3727Å EW cut on the local comparison sample. Therefore, offsets of the SLACS sources in size and luminosity, as shown in the middle and right panels of Figure 3.15, cannot be interpreted as being caused by only the surface brightness evolution of disk galaxies with redshift. For example, disk galaxies with extremely strong [O II] 3727 Å emission (ex: EW $\sim$ 55Å) only require a surface brightness evolution of ~ 1.0 mag to match the local comparison sample (for example, after accounting for a median surface brightness offset of ~ -1.0 mag at 55 Å as shown in Figure 3.16). Thus, the average pure-size and pure-luminosity evolution of disk galaxies we estimate from Figure 3.15 must be considered as upper limits. However, despite the fact that we can not derive reliable [O II] 3727Å EW estimates for the SLACS sources, Figure 3.16 shows that our overall conclusions from Figure 3.15 are likely unaltered since the maximum surface brightness offset for galaxies with strongest [O II] 3727Å emission is ~ -1.2 mag[13].

Since we cannot reliably impose a [O II] 3727Å cut on the SDSS sample, as a final measure, we attempt to weigh the SDSS disk galaxy sample by each galaxy's probability of being a SLACS-like source galaxy. According to Dobler et al. (2008), the detection of galaxy-scale lens in a SLACS-like survey is dependent on three parameters:

1. Total probability that a galaxy has a rogue emission line (P_R), such as [O II] 3727Å, where $P_R = P_L + P_N$. The parameter P_N corresponds to the probability that a galaxy has rogue emission line due to source that is not lensed.

2. Lensing probability (P_L) defined to be the probability that a galaxy has a emission line due to a source that is lensed.

3. False positive rate, $R_F = P_N/P_R$, defined as the fraction of lens candidates which do not show evidence of lensing after follow-up observations.

[13]A visual inspection of the SDSS spectra show that [O II] 3727Å EWs of SLACS source galaxies are typically on the order of ~ 10 Å.

The study by Dobler et al. (2008) examines each of these parameters as a function of *source* size, separated by the distributions of the lens redshift (z_l), lens velocity dispersion (σ) and seeing effects. For example, Figure 3.17 indicate how P_L, P_R and R_F varies as a function of source size (under $2''.0$ seeing), separated according to z_l as shown by the various curves. Thus, we can utilize these curves to estimate the probability of a galaxy, given its size, being the source for a galaxy-scale lens (located at an appropriate z_l).

We apply the same methodology to the SDSS disk galaxy sample. In other words, we weigh the SDSS disk galaxy sample by each galaxy's probability of being a source galaxy of a SLACS-like lens, if the lens galaxy was located at a redshift of $z_l = 0.20$ (which is similar to the median redshift of the SLACS lens galaxy sample). The volume-corrected number density of SDSS disk galaxies is then defined as,

$$\left(\frac{1}{V_{max}}\right)_{slacs-like\,sdss} = \left(\frac{1}{V_{max}}\right)_{sdss,original} \frac{P_L\,P_R}{1-R_F} \tag{3.6}$$

where P_L, P_R and R_F correspond to the probability curves at $z_l = 0.20$ shown in Figure 3.17. Figure 3.18 shows a reproduction of Figure 3.15 after the SDSS disk galaxy sample is weighted by each galaxy's probability of being a SLACS-like source galaxy as determined by equation 3.6. As evident in Figure 3.18, the volume-corrected number density of the SDSS disk galaxies on the luminosity-size plane is virtually indistinguishable from that of Figure 3.15; therefore, the weighting of the SDSS disk galaxy sample does not affect the overall conclusions of this study. The quantity $(P_L\,P_R)/(1-R_F)$ only changes by a factor of ~ 2 over the full range of source galaxy sizes (as shown in Figure 3.19), while the number density of SDSS disk galaxies changes by a factor of ~ 1000 on the logarithmic luminosity-size plane. Thus, we do not observe a significant change in the SDSS disk galaxy sample due to the weighting scheme discussed above.

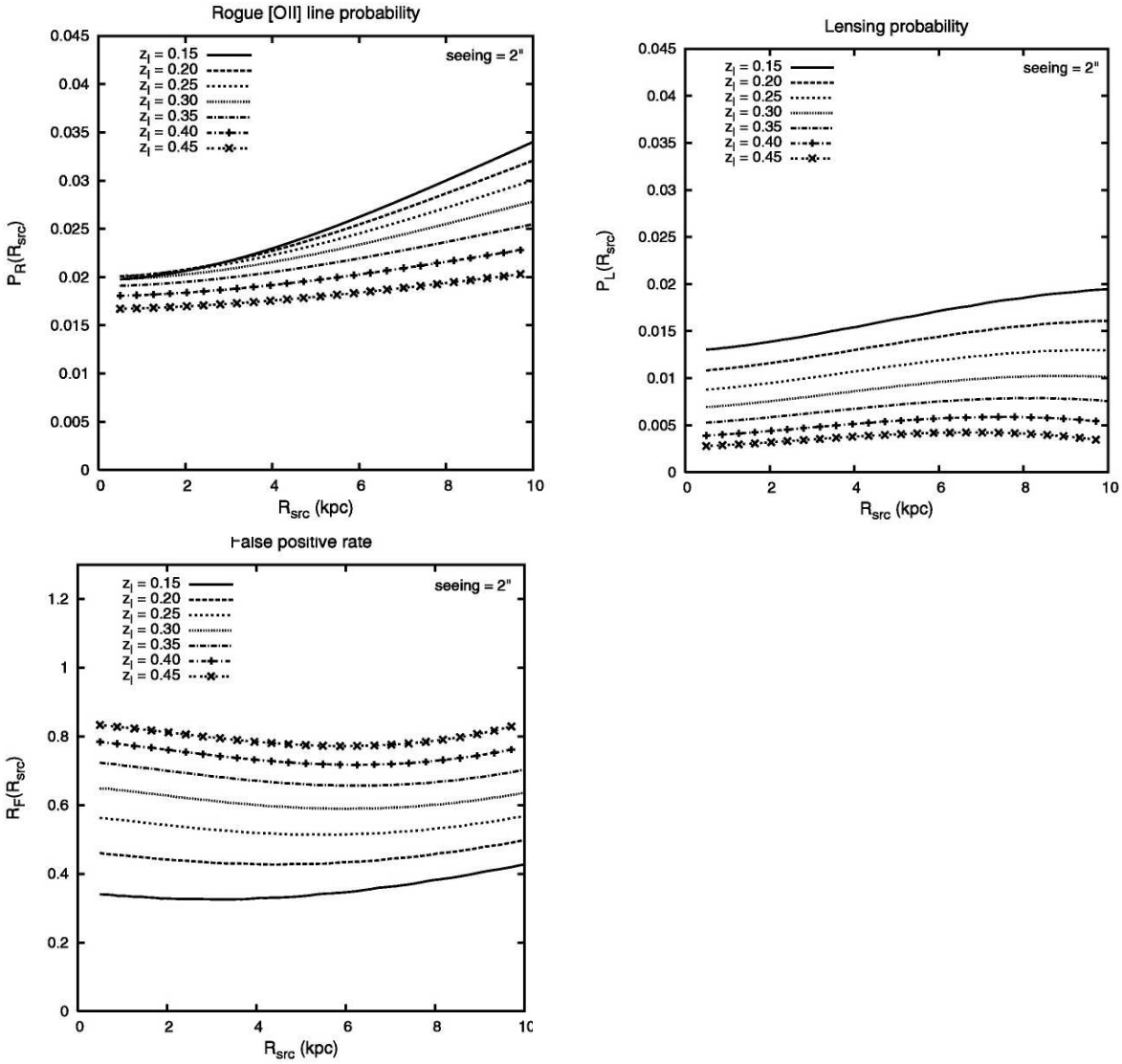

Figure 3.17 *Tow row, from left to right:* Total rogue line probability (P_R) and lensing probability P_L, as a function of source size under 2.″0 seeing. *Bottom row:* False positive rate, R_F, as a function of source size under 2.″0 seeing (Figure 4 of Dobler et al. (2008)).

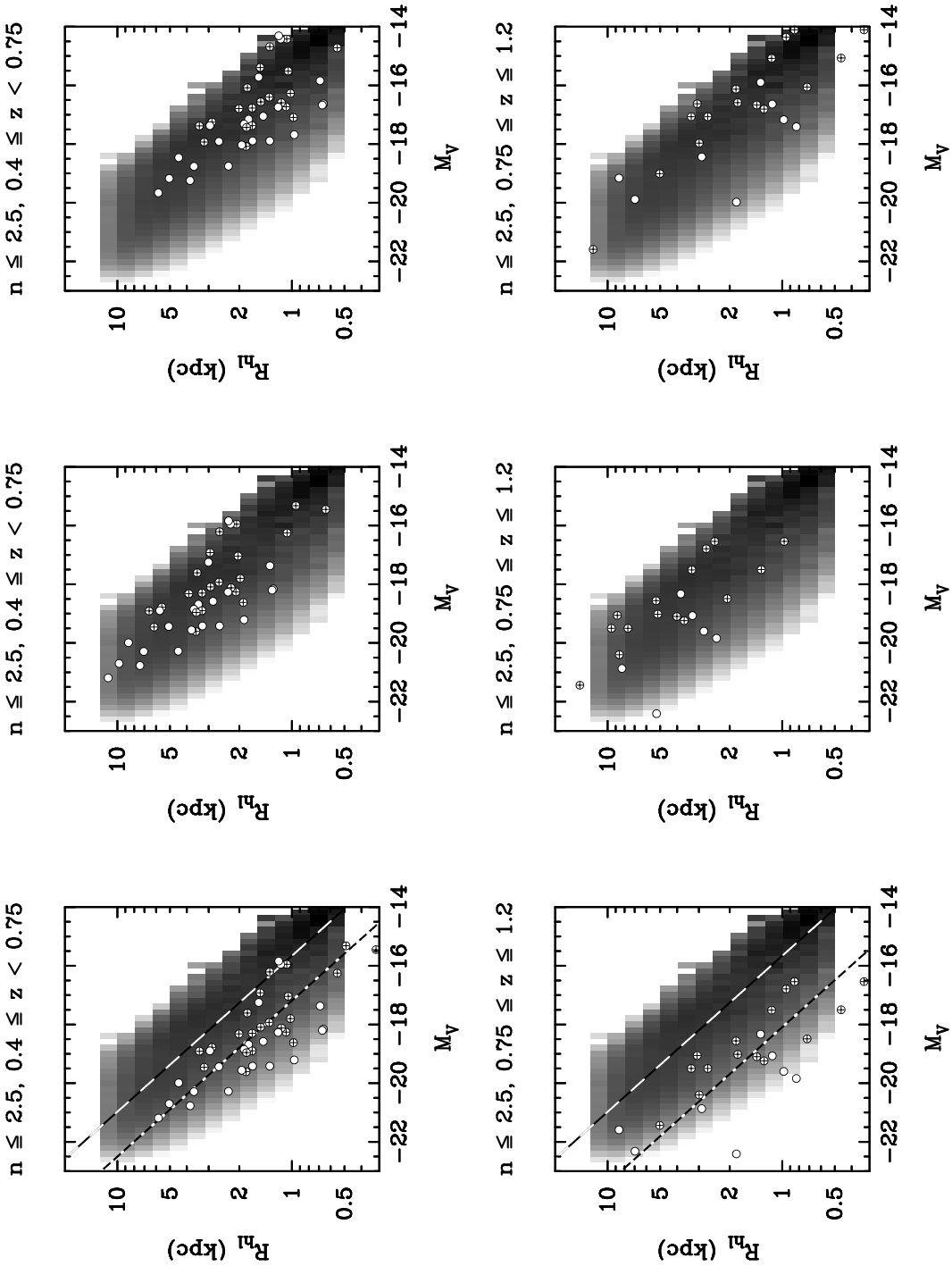

Figure 3.18 Same as Figure 3.15 after the volume-corrected number density of SDSS disk galaxy sample (on the luminosity-size plane) is weighted by each galaxy's probability of being a SLACS-like source galaxy. A comparison to Figure 3.15 indicates that the volume-corrected number density of SDSS disk galaxies is indistinguishable between the weighted vs. non-weighted scenarios.

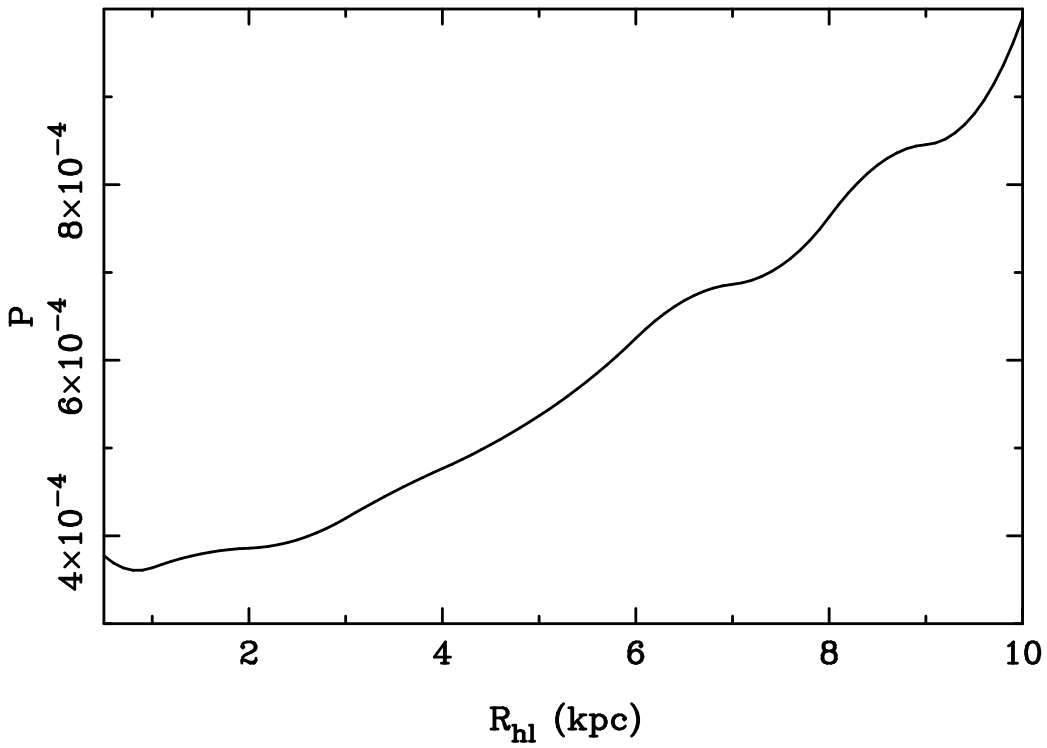

Figure 3.19 The total probability of a given emission line galaxy being the background source of a galaxy-scale lens, i.e. the quantity $(P_L\, P_R)/(1 - R_F)$ in equation 3.6, as a function of the galaxy's half-light radius. The functional forms of P_L, P_R and R_F are obtained from Dobler et al. (2008).

3.6.2 Comparison to Previous Observational Studies

When making comparisons between various studies of disk galaxy evolution, it should be noted that the selection criteria of a disk-dominated galaxy are not always uniform. For example, Barden et al. (2005) select disk galaxies based on the Sérsic index criterion, where a disk galaxy has $n \leq 2.5$, while Melbourne et al. (2007) select the blue galaxies within the GOODS-N field. Trujillo et al. (2006) also select disk galaxies using the $n \leq 2.5$ criterion and impose an additional constraint of $e \leq 0.5$[14] on the final sample. In contrast to the half-light radius utilized in most studies of the luminosity-size relation, Trujillo et al. (2006) use the truncation radius of the stellar disk as an estimator of galaxy size.

[14] $e = \sqrt{1 - (b/a)^2}$ for an ellipse, where a and b correspond to the semi-major and semi-minor axes respectively.

As evident from the middle and right panels of Figure 3.15, both pure-size and pure-luminosity evolution match the SLACS disk galaxies to the local disk galaxy population. Therefore, the surface brightness evolution of disk galaxies since $z \sim 1$ can be interpreted as an increase of the half-light radius at a fixed magnitude or a decrease in luminosity at a fixed size (Brooks et al. 2011; Trujillo & Aguerri 2004). Thus, quantifying the true evolution of the luminosity-size relation can be extremely difficult due to this degeneracy. Throughout the remainder of this chapter, we will compare the evolutionary trends observed in the SLACS disk galaxy sample to previous observational studies and theoretical expectations, which will enable us to place constraints on the size and luminosity evolution of disk galaxies.

It is accepted that some of the surface brightness evolution observed in disk galaxies must be caused by a dimming in luminosity due to the declining star formation rate since $z \sim 1$. However, it is equally important to determine how much disk galaxies fade since $z \sim 1$ and whether the luminosity evolution is also accompanied by changes in the sizes of disk galaxies. For example, previous observational studies have observed a surface brightness evolution of $M_V \sim 1$ mag in disk galaxies (Barden et al. 2005), which only corresponds to an upper limit of luminosity evolution if disk galaxies also undergo growth in size since $z \sim 1$.

Previous observational studies that examine the number density evolution of disk galaxies, such as Kanwar et al. (2008), show that the size function of disk galaxies does not change significantly since $z \sim 1$. These observations can be interpreted in the following ways: disk galaxies have completed growing by $z \sim 1$ and the observed change in surface brightness corresponds to pure luminosity evolution or the rate of disk galaxies moving out of a given size bin is equal to the rate of disk galaxies moving into that size bin. If we assume that disk galaxies are fully in place by $z \sim 1$, then the observed $M_V \sim 2.3$ mag luminosity evolution since $z \sim 1$ of the SLACS disk sample, as shown in the right panels of Figure 3.15, is significantly larger than the $M_V \sim 1$ mag luminosity evolution observed in previous studies (Barden et al. 2005). However, the large luminosity evolution we observe is not unexpected since the observational bias between SLACS and SDSS samples, as discussed in §3.6.1, only allows us to derive an *upper* limit to the surface brightness evolution of disk galaxies. If we are considering galaxies with extremely strong [O II] 3727Å emission (for example, emission line galaxies with $\mathrm{EW_{[OII]}} \gtrsim 40$Å as shown in Figure 3.16), then the observed luminosity evolution will be reduced to $\mathrm{M_V} \sim 1.3$ mag, which is

comparable to the results of Barden et al. (2005).

Another key factor in this comparison is that the SLACS sample extends ~ 2 magnitudes beyond the GEMS sensitivity limit (the sample used in the study of Barden et al. (2005), as shown in the top panels of Figure 3.13). Thus, our average surface brightness fit to the luminosity-size relation of intermediate- and high-redshift disk galaxy population is also affected by the previously unaccounted, faint and compact regime. Under the assumption of pure luminosity evolution and modest observational bias due to the correlation between surface brightness and [O II] 3727Å emission[15], our results are similar to those of Melbourne et al. (2007), which find evidence for differential luminosity evolution of disk galaxies since $z \sim 1$, in the TKRS sample of the GOODS-N field as follows: $M_B = 1.53$ mag for large galaxies ($r_{hl} > 5$ kpc); $M_B = 1.65$ mag for intermediate galaxies (2.5 kpc $\leq r_{hl} \leq 5$ kpc) and $M_B = 2.55$ mag for small galaxies ($r_{hl} < 2.5$ kpc).

Due to the degeneracy of the luminosity-size plane, potential growth in size since $z \sim 1$ (combined with luminosity evolution) is yet a possible explanation for the surface brightness evolution of disk galaxies. This expectation is also in agreement with various analytical predictions of disk galaxies. For example, the disk scale length (R_d) of a galaxy embedded in a halo that is described by a simple, singular isothermal sphere model (Mo et al. 1998) scale with $H(z)^{-1}$, which corresponds to a $\sim 2\times$ growth of disk sizes since $z \sim 1$ (Brooks et al. 2011). Although theoretical models predict $\sim 2\times$ growth in disk sizes, observational studies typically observe a more modest growth. For example, Trujillo & Pohlen (2005) find that a moderate growth in disk size (i.e. $\sim 25\,\%$) combined with the $M_V \sim 1$ mag luminosity evolution can account for the surface brightness evolution of disk galaxies in Hubble Ultra Deep Field (HUDF).

The results of Trujillo & Pohlen (2005) are also consistent with the studies that examine the evolution of the stellar mass-size relation of disk galaxies. For example, the results of Barden et al. (2005) indicate that, unlike the luminosity-size relation, the stellar mass-size relation does not undergo significant evolution since $z \sim 1$. This scenario correspond to the "inside-out" growth of disk galaxies (i.e. where growth occurs in the outer regions of disk galaxies via minor mergers and accretion events

[15]A visual inspection of the residual SDSS spectra, which show the emission lines used to spectroscopically identify SLACS lens candidates, show that most sources have moderate [O II] 3737Å emission.

while still remaining on the same stellar mass-size relation) and is also in agreement with further observational evidence and theoretical predictions which find that the stellar mass-size relation does not show significant evolution since $z \sim 3$ (Trujillo et al. 2004; Brooks et al. 2011; Dutton et al. 2011).

3.6.3 Comparison to Theoretical Predictions of Disk Galaxy Evolution

Observational studies of the luminosity-size relation (Shen et al. 2003; Barden et al. 2005; Melbourne et al. 2007; Trujillo & Pohlen 2005; Trujillo et al. 2006) can only examine instantaneous populations of disk galaxies at a given redshift. In order to fully understand the physical processes that affect the surface brightness evolution of disk galaxies, it is useful to track individual objects from $z = 1$ to $z = 0$, which cannot be accomplished with observations. Therefore, it is important to compare the observations of the luminosity-size relation to semi-analytical models (SAMs) of disk galaxy formation and evolution. In this section, we apply the theoretical predictions of Brooks et al. (2011), whose high resolution cosmological simulations track the evolution of individual disk galaxies on the luminosity-size and stellar mass-size plane since $z \sim 1$, to the SLACS disk galaxy sample and discuss the implications.

Brooks et al. (2011) use the N-body + Smooth Particle Hydrodynamics (SPH) code GASOLINE, within the ΛCDM context, to simulate the formation and evolution of disk galaxies from $z = 1$ to $z = 0$. The disk galaxies are selected from 25 Mpc or 50 Mpc volumes, with uniform mass resolution, and are re-simulated at higher resolution with baryons. The star formation and supernovae feedback (SN) feedback prescription used in these SAMs overcome the "angular momentum catastrophe", which refers to the phenomenon where ΛCDM simulations produce disks that are too compact and rotate too fast at a given radius (Steinmetz & Navarro 1999), and produce disk galaxies whose properties[16] are in excellent agreement with the observed population (Brooks et al. 2011). All galaxies in these simulations do not undergo major mergers after $z \sim 0.5$, thus, are disk-dominated at $z = 0$. Artificial surface brightness images of the simulated disk galaxies, at a given redshift, are produced using the code SUNRISE and the luminosities and half-light radii are measured using

[16]For example, the stellar mass-metallicity relation.

Table 4. Evolution of disk galaxy properties from the SAMs of Brooks et al. (2011)

Galaxy	M_B	$\Delta\, M_B$	h_B	$\Delta\, h_B$	$M_\star$	$\Delta\, M_\star$
⋯	mag	Δ mag	kpc	$z = 0/z = 1$	$M_\odot$	$z = 0/z = 1$
⋯	$z = 0$	to $z = 1$	$z = 0$	⋯	$z = 0$	⋯
(1)	(2)	(3)	(4)	(5)	(6)	(7)
h258	-21.2	-0.2	6.3	2.7	3.2×10^{10}	2.53
h516	-15.7	2.0	0.95	1.0	4.3×10^{8}	1.69

Note. — Modified version of Table 3 from Brooks et al. (2011), summarizing the properties of simulated disk galaxies used for the comparison with the SLACS disk galaxy population. **Col. (1)**: Simulated galaxy name. **Col. (2)** Absolute B-band magnitude of the simulated disk galaxy at $z = 0$. **Col. (3)** Luminosity evolution from $z = 1$ to $z = 0$, where a negative ΔM_B means that the disk of the simulated galaxy is brighter at $z = 0$ in comparison to $z = 1$. **Col. (4)** Half-light radius of the disk component at $z = 0$. **Col. (5)** Growth of the half-light radius of the disk component from $z = 1$ to $z = 0$. **Col. (6)** Stellar mass of the disk component at $z = 0$. **Col. (6)** Growth of the stellar mass of the disk component from $z = 1$ to $z = 0$.

the Sérsic bulge and exponential disk decomposition of GALFIT (Peng et al. 2002).

In this study, we analyze the evolutionary tracks of a large and bright disk galaxy, i.e. galaxy h258 in Brooks et al. (2011), and a faint and compact disk galaxy, i.e. galaxy h516 in Brooks et al. (2011), on the luminosity-size plane. Table 4 (a modified version of Table 3 in Brooks et al. (2011)) summarizes the properties of h258 and h516. The evolution of h258 and h516 on the luminosity-size plane are shown as red and blue arrows in Figure 3.20(*left*) and 3.20(*right*). The blue arrows show the evolution of h258 from $z = 0.5$ to $z = 0.0$, in Figure 3.20(*left*), and from $z = 1.0$ to $z = 0.0$, in Figure 3.20(*right*). The red arrows show the evolution of h516 from $z = 0.5$ to $z = 0.0$, in Figure 3.20(*left*), and from $z = 1.0$ to $z = 0.0$, in Figure 3.20(*right*).

As evident from Figure 3.20, applying the evolutionary tracks of Brooks et al. (2011) at the appropriate regimes, provides an excellent match to bring the SLACS disk galaxies to the locus of the two-dimensional, SDSS luminosity-size distribution. Thus, a comparison between theoretical predictions and our observations allows us to place further constraints on the dominant physical processes of disk galaxy evolution. Given that the star formation rate and the growth of a galaxy can change simultaneously, the most likely explanation for the evolution of disk galaxy luminosity-size

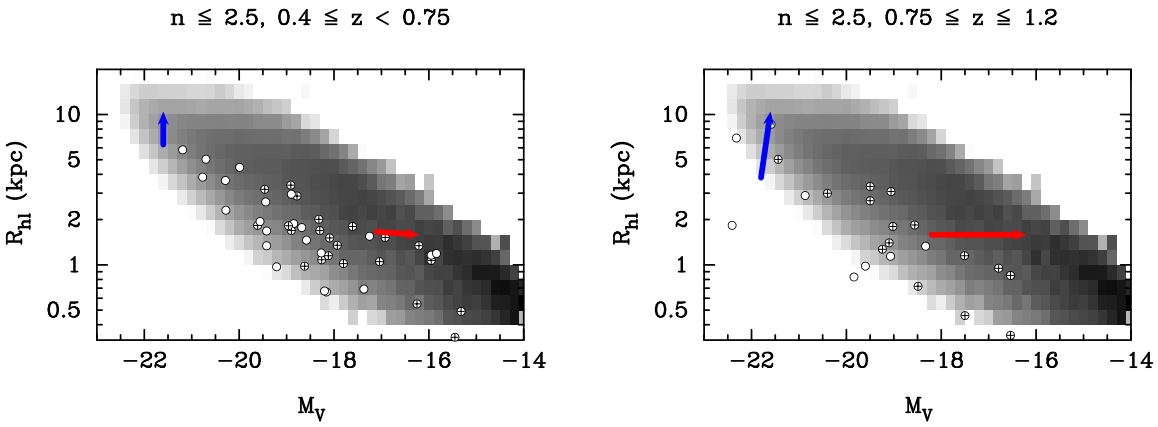

Figure 3.20 Comparison of our results to the theoretical predictions of disk galaxy evolution by Brooks et al. (2011). In all panels, SLACS source galaxy measurements are shown as open circles and circles with a cross. The open circles correspond to the measurements of SLACS sources that show "normal" galaxy morphology and the circles with a cross correspond to the subcomponent measurements of SLACS sources that show "group" morphology. The greyscale represents the volume-corrected number density of SDSS galaxies on the luminosity-size plane. **Left:** The luminosity-size relation of SLACS disk galaxies at $0.4 \leq z < 0.75$ and the local disk galaxy luminosity-size relation. The red and blue arrows show the predicted evolutionary paths of a faint, compact disk galaxy and a bright, massive disk galaxy from $z = 0.5$ to 0.0 respectively (Brooks et al. 2011). **Right:** Same as the left panel for the $0.75 \leq z < 1.2$ SLACS disk galaxy sample. The red and blue arrows show the predicted evolutionary path of a faint, compact disk galaxy and a bright, massive disk galaxy from $z = 1.0$ to 0.0 respectively (Brooks et al. 2011).

relation may be a combination of luminosity and size evolution. In particular, the results of Brooks et al. (2011) are strongly indicative of the *mass-dependent* evolution of disk galaxy luminosity-size relation, where dwarf galaxies (such as h516) undergo a larger evolution in luminosity than size while massive galaxies (such as h258) undergo a larger evolution in size than luminosity.

The evolution of massive galaxies (i.e. blue arrows), as predicted by the SAMs of Brooks et al. (2011), is consistent with the "inside-out" growth of disk galaxies which is also evident in previous observational studies as discussed above. Furthermore, Brooks et al. (2011) examine the evolution of the individual galaxies on the stellar mass-size plane and find that the growth of massive simulated disk galaxies occur such that they stay approximately on the same stellar mass-size relation since $z \sim 1$ (Figure 7 of Brooks et al. (2011)). However, the evolution of less massive disk galaxies ($M_\star \leq 10^9\,M_\odot$), which undergo very little changes in disk size yet significant dimming since $z \sim 1$, poses an interesting challenge. The rapid dimming of low-mass disk galaxies ($M_V \sim 2$ mag) is at odds with the expectation that they should be undergoing

more star formation since $z \sim 1$, in comparison to massive disk galaxies whose star formation peaked at earlier epochs (Brooks et al. 2011).

A simple model that explains the dimming of a disk galaxy is an exponential decay in the star formation rate. An exponential decay model with an e-folding timescale (τ) of 3 Gyr results in the dimming of a disk galaxy by $M_V \sim 1$ mag since $z \sim 1$ (Melbourne et al. 2007), which is consistent with the previous observations of large and intermediate size disk galaxies. However, the large luminosity evolution predicted for the previously inaccessible, faint and compact galaxies requires a very rapid decline in the star formation rate since $z \sim 1$, which may be indicative of a more complicated scenario of star formation. For example, Melbourne et al. (2007) find that an exponential decay model of $\tau = 1$ Gyr results in the decline of the star formation by a factor of ~ 1000. In the SAMs of Brooks et al. (2011), the surface brightness evolution of low-mass disk galaxies are closely coupled to their bursty star formation history, which can result in a rapid increase in luminosity due to the starburst followed by significant fading of the disk galaxy from $z \sim 1$ to $z \sim 0$. Thus, with the advantages of a lensing survey, we may be observing in detail a compact starbursting disk galaxy population that is typically overlooked by broad-band imaging surveys.

The conclusions drawn from the comparison between high-resolution cosmological simulations and our observations further strengthens the advantages of lensing surveys. The *mass-dependent* evolution of disk galaxies on the luminosity-size plane can only be fully confirmed with detailed observations of faint and compact galaxies, which approach the resolution limit of *HST*. Thus, the lensing magnification provides a unique advantage to explore the faint and compact regime at greater sensitivity and detail, two requirements that are difficult to attain simultaneously with the capabilities of current broad-band imaging surveys.

3.7 Summary

We analyze 62 *HST*-ACS I-band observations of gravitationally lensed galaxies from the SLACS Survey. The sample of gravitationally lensed galaxies span a redshift range of $0.20 \leq z \leq 1.20$ with a median redshift of $z = 0.61$. This sample is selected spectroscopically based on the presence of multiple nebular emission lines; therefore, it is not subjected to magnitude-cutoffs similar to those imposed on broad-

band imaging surveys at similar redshifts. Furthermore, the magnification in size and flux of the background source provided by strong gravitational lensing allows accurate measurements of galaxies (provided that the mass model of the deflector is well constrained), which are otherwise too faint and compact to be measured reliably.

We exploit the magnification advantage to measure the luminosities, sizes and Sérsic indices of the SLACS lensed galaxies using the lens modeling software LENSFIT (Peng et al. 2006). The results of lens modeling show that the SLACS source galaxy sample consists of a primarily compact, disk-dominated population with the peaks of the size and Sérsic index distributions corresponding to $r_{hl} \sim 1.50\,\mathrm{kpc}$ and $n \sim 1.0$ respectively. A comparison of the SLACS luminosity-size relation to that of a non-lensed comparison sample (i.e. GEMS) shows a tail of low-luminosity, compact lensed galaxies extending ~ 2 magnitudes fainter than the sensitivity limits of a typical broad-band imaging survey. We also compare the luminosity-size relation of our sample to that of the local population, which consists of $\sim 670,000$ SDSS galaxies (Simard et al. 2011).

A comparison of our observations to theoretical predictions shows that the surface brightness evolution of disk galaxies since $z \sim 1$, which matches the SLACS disk galaxy population to the local disk galaxy population, is most likely caused by changes in both luminosity and size. The comparison between the SLACS sample and detailed semi-analytical models of Brooks et al. (2011), which track the evolution of individual disk galaxies on the luminosity-size and size-stellar mass planes from $z \sim 1$ to $z \sim 0$, is consistent with mass-dependent evolution. The mass-dependent evolution of disk galaxies on the luminosity-size relation indicates that high-mass ($\mathrm{M}_\star > 10^9 \mathrm{M}_\odot$) galaxies evolve more in size, than luminosity, and the low-mass disk galaxies ($\mathrm{M}_\star \leq 10^9 \mathrm{M}_\odot$) evolve more in luminosity, than size. Within this context, the evolution of bright and massive disk galaxies can be explained as "inside-out" growth, where the size of a disk galaxy increases through minor mergers and accretion events while moving along the stellar mass-size relation since $z \sim 1$. Further observational confirmation of the "inside-out" growth scenario requires comparison of the intermediate- to high-redshift stellar mass-size relation (for example, of the SLACS source galaxies) to that observed locally. However, the large decrease in luminosity of faint and compact disk galaxies, since $z \sim 1$, cannot be explained through a simple, exponential decaying of the stellar populations but may require a complex and bursty star formation history.

Chapter 4

Beyond the Biggest and the Brightest: Integral Field Spectroscopy of Gravitationally Lensed Galaxies with Laser Guide Star Adaptive Optics

4.1 Introduction

In the local universe, galaxy morphologies follow the well known Hubble Sequence as shown in Figure 1.1. Both photometric and kinematic properties of galaxies vary systematically within the Hubble Sequence (Neichel et al. 2008) and, as discussed previously, the early-type galaxies in the local universe are typically dispersion dominated systems while the late-type galaxies are rotation dominated systems. Large-scale *HST* imaging surveys of galaxy morphology show that a significant fraction of galaxies at increasingly larger look-back times have morphologies that do not fit the classifications of the locally observed Hubble Sequence (Abraham et al. 1996). For example, $\sim 30\%$ of the intermediate-mass galaxies at $z \sim 0.4-1$ show peculiar morphologies in broad-band images and out of these peculiar galaxies, a significant fraction ($\sim 60\%$) are also compact, a class that is nearly non-existent in the local universe (Neichel

et al. 2008; Rawat et al. 2007; Zheng et al. 2004). A variety of observational evidence indicates that massive early-type galaxies were assembled prior to $z = 1$ (Bernardi et al. 2006); however, our understanding of the processes[1] involved in the evolution of late-type galaxies from high redshift to the locally observed population is still highly uncertain. While the photometric properties of galaxies offer a wealth of information about merger rates, accretion events and star formation (amongst others), it is equally important to combine imaging and spectroscopy to fully understand these processes, especially those dominant in emission line galaxies at intermediate and high redshifts.

Spectroscopic properties of galaxies such as their dynamical states, star formation rates (SFR) and chemical abundances are some of the key elements to understanding the fundamental physical processes that give rise to the diverse galaxy populations observed at various look-back times. These properties are best measured using optical nebular emission lines such as Hα, Hβ, [O III] 5007Å and [N II] 6583Å (redshifted to the near-infrared regime at intermediate and high redshifts), which are very sensitive probes of the underlying gravitational potential and active star forming regions (Law et al. 2007). Therefore, emission line morphology is also a valuable indicator of the dynamical mass, a probe of the total matter content, of star forming galaxies. A comparison between the stellar mass and the dynamical mass allows one to estimate the contribution of the dark matter component to a galaxy. Furthermore, the stellar mass-to-light ratios ($M/L_\star$) of star forming galaxies, derived using broad-band photometry, are sensitive to factors such as varying stellar populations, reddening and a non-universal Initial-Mass Function (IMF).

Integral Field Spectroscopy (IFS) provides a two-dimensional spectral map of a galaxy that can, for example, distinguish between rotation or merger induced effects and also overcomes the complications associated with long slit spectroscopy such as slit placement and misalignment with the kinematic major axis (Förster Schreiber et al. 2006; Nesvadba et al. 2008). In the recent years, AO-assisted IFS has significantly enhanced the dynamical studies of intermediate- to high-redshift galaxies (Cresci et al. 2009; Epinat et al. 2009; Förster Schreiber et al. 2006, 2009; Genzel et al. 2011; Lemoine-Busserolle & Lamareille 2010; Wisnioski et al. 2011, 2012; Wright et al. 2007). Current IFS studies of star forming galaxies at the peak epoch of star formation and AGN activity (i.e. $z \sim 1.5 - 3$) are being revolutionized by large scale surveys such as the Spectroscopic Imaging survey in the Near-Infrared with

[1]For example, secular evolution, minor mergers, accretion events or violent major mergers.

SINFONI, SINS (Förster Schreiber et al. 2006, 2009; Cresci et al. 2009; Genzel et al. 2011), which show evidence for an approximately equal mix of subsamples based on kinematic properties including dispersion dominated systems, rotationally supported systems and non-negligable random motions that may be induced by merger events (Figure 4.1). However, these surveys are typically limited to bright and massive galaxies ($M_\star \geq 10^{10}\,M_\odot$) and the studies of compact star forming galaxies ($r_{hl} \sim 1-5\,kpc$) are restricted by poor spatial resolution. Even near-diffraction limited observations of compact galaxies, using 8-10m class telescopes, can only yield a handful of resolution elements which cannot be used to clearly distinguish the processes that resulted in the observed morphology (Jones et al. 2010).

The lensing magnification of the observed angular size and flux of a distant galaxy also enables the detailed study of its kinematic properties since the velocity field is conserved in gravitational lensing, in addition to its surface brightness. Furthermore, the details of a lensed galaxy's kinematic properties can be further enhanced by combining the magnification advantage with the increased spatial resolution provided by AO, which is now routinely used by IFS studies of non-lensed galaxies (Förster Schreiber et al. 2009; Wisnioski et al. 2012). Under favourable AO corrections, magnification factors of $\sim 10\times$ allow us to probe lensed galaxies at physical scales of $\sim 200\,pc$, which typically corresponds to a sampling of ~ 100 resolution elements of an average galaxy. Since the advent of AO as an essential aspect of 8-10m class telescopes, various studies have begun to combine diffraction-limited IFS with the magnification advantage to study the kinematic properties of gravitationally lensed galaxies at increasingly higher redshifts (Salucci et al. 2007; Smail et al. 2007; Stark et al. 2008; Jones et al. 2010); however, most of the galaxies that were initially observed in these studies have not been typical of the high-redshift population. Since gravitational lensing is a relatively rare phenomenon, compiling diffraction-limited IFS observations of a large sample of lensed galaxies, representative of the high redshift galaxy population, is a difficult task.

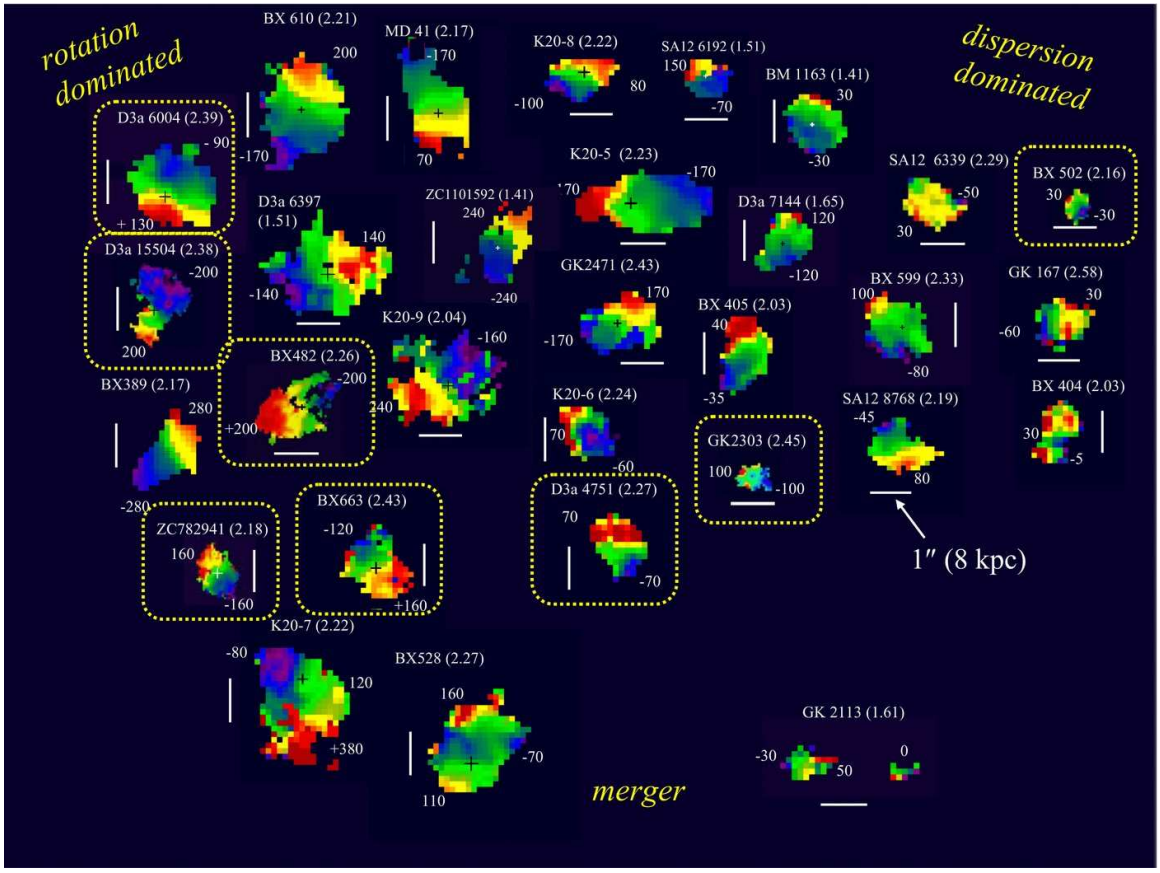

Figure 4.1 Velocity fields of 30 (out of 62) galaxies observed in the SINS survey (Figure 17 of Förster Schreiber et al. (2009)). SINS galaxy sample consist of massive ($M_\star \geq 10^{10}\,M_\odot$), emission line galaxies at $z \sim 1.5 - 3$. All velocity fields, with the exception of K20-ID5, are derived using the Hα emission line. The blue colours of the velocity field correspond to the blueshifted emission and the red colours correspond to the redshifted emission with respect to the systemic velocity of Hα. The galaxies are grouped according to their kinematics (rotation vs. dispersion dominated) and kinemetry (disk-like vs. merger-like) and the subset of galaxies that was observed with adaptive optics are indicated in yellow boxes.

However, a pioneering study by Jones et al. (2010) (following the study of a gravitationally lensed, L* Lyman-break galaxy at $z = 3.07$ by Stark et al. (2008)) successfully utilize the lensing magnification and diffraction-limited IFS to derive detailed kinematics of a sample of sub-luminous galaxies at $z = 1.7 - 3.1$ as shown in Figure 4.2. The sample of strongly lensed galaxies observed by Jones et al. (2010) consists of six objects[2] with sizes of 1-7 kpc and dynamical masses of $10^{9.7-10.3}\,M_\odot$, which are sampled at spatial resolutions as high as ~ 100 pc using the AO-fed OSIRIS

[2]Gravitationally lensed objects observed by Jones et al. (2010) and Stark et al. (2008) reside within cluster scale lenses in contrast to the galaxy-scale lenses of the SLACS survey.

integral field spectrograph at the Keck Observatory. Detailed observations of the Hα emission line morphology of these galaxies show that they contain giant star-forming H II regions whose dynamical masses ($10^{8.8-9.5}\,M_{\odot}$) are comparable with those of spiral galaxies in the local universe, but with star formation densities that are $\sim 100\times$ higher (Jones et al. 2010).

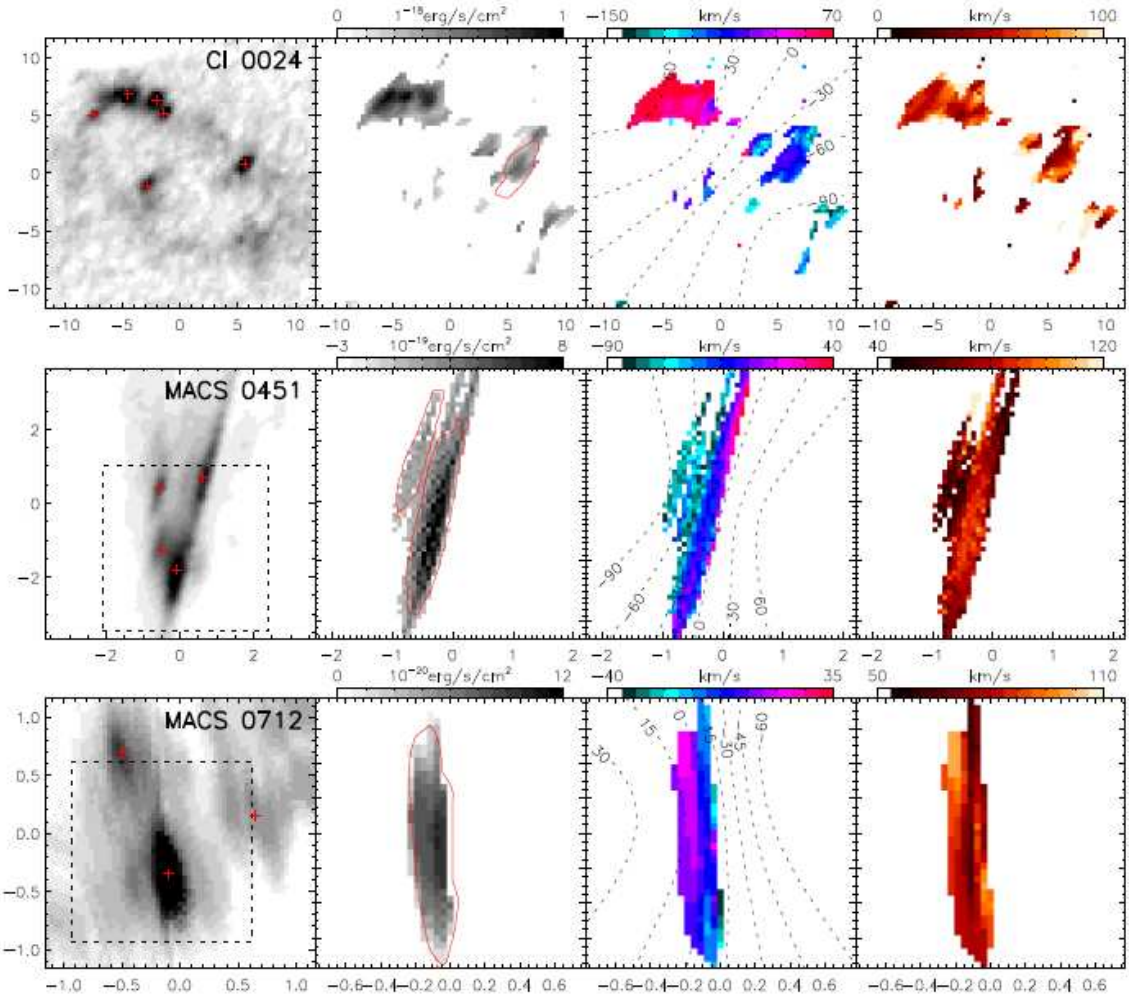

Figure 4.2 Two-dimensional Hα emission line properties of 3 gravitationally lensed galaxies (out of 6) presented in Jones et al. (2010), reconstructed on the source plane. *From left to right in each row:* ACS broad-band imaging reconstruction of the lensed galaxy, Hα emission line intensity, velocity and velocity dispersion maps (from the AO-assisted OSIRIS observations). Dashed boxes on the first panels of MACS 0451 and MACS 0712 show the smaller FOV of OSIRIS.

Following the pioneering IFS studies of gravitationally lensed galaxies discussed above, the primary goal of this project is to obtain detailed kinematic and star for-

mation rate information of a sample of galaxies that is representative of the galaxy population at $z > 0.75$. The primary instruments that we aim to utilize for this study, to observe Hα and [N II] 6583Å nebular emission lines, are the near-infrared integral field spectrographs of Gemini-North observatory and ESO Very Large Telescope (ESO-VLT), NIFS and SINFONI. The lensed targets for this project are derived from the SLACS survey (Bolton et al. 2006, 2008a), whose selection method has already provided the following pre-requisities: an estimate of the [O II] 3727Å emission line flux through SDSS spectroscopy which can be used to infer the Hα emission line flux; spectroscopic redshifts of both lens and source galaxies and high-resolution *HST* imaging to derive an accurate mass-model (if available, multi-wavelength *HST* imaging can also be used to estimate the stellar mass of the lensed galaxy).

This chapter discusses the observational setup, data analysis and the preliminary results of the feasibility study of this project, which observed the gravitationally lensed galaxy SDSS J0252+0039 (Bolton et al. 2008a) using NIFS + ALTAIR on Gemini-North[3]. This chapter is structured as follows. In §4.2, we present a description of the target selection for an IFS study of SLACS lensed galaxies and the target of the feasibility study. In §4.3, we describe the observational procedure of the feasibility study and subsequent data analysis. In §4.4, we present some of the preliminary results and discuss the future work to be done within this project.

4.2 Target Selection and Feasibility Study

The subset of gravitationally lensed galaxies selected for IFS follow-up with NIFS (and SINFONI for future follow-up) are derived from the 63 lens systems discussed in Bolton et al. (2008a), which also have extensive gravitational lens modeling using LENSFIT[4]. We first impose a $z_{bg} > 0.75$ cut such that Hα and [N II] 6583Å emission lines of the lensed galaxies fall within J, H or K bands, the wavelength regime where AO corrections are currently optimized. We further eliminate targets where the redshifted nebular emission lines fall within 10Å from strong OH sky lines. Finally, we construct the lensed galaxy sample that meets the reference star requirements of each

[3]This object is located at the sensitivity limit of a typical non-lensing surveys such as GEMS (Barden et al. 2005), as shown in Figure 3.13.

[4]As discussed in Chapter 3.

Table 5. A summary of SLACS lensed galaxies for IFS follow-up

SDSS J+	z_{bg}	TT Star Magnitude (R band)	TT Star Radius (arcsec)	Follow-up Instrument (NIFS/SINFONI)
1251-0208	0.7843	14.8	$56\farcs1$	SINFONI
0252+0039	0.9818	14.4	$19\farcs9$	**NIFS***
0808+4706	1.0251	11.8	$18\farcs2$	NIFS
2341+0000	0.8070	16.3	$36\farcs4$	SINFONI
0008-0004	1.1924	18.2	$39\farcs1$	SINFONI
0157-0056	0.9243	13.8	$19\farcs8$	NIFS & SINFONI

Note. — A summary of the SLACS lensed galaxies suitable for a IFS follow-up study, arranged by the ascending order of half-light radii. *From left to right in each row:* SDSS identifier of the lens system, spectroscopic redshift of the lensed galaxy of interest, tip-tilt star magnitude in the R band, tip-tilt star separation from the science target and the follow-up integral field spectrograph. The bold text indicate that SDSS J0252+0039 was observed with NIFS + ALTAIR.

observing facility's AO system. Both NIFS and SINFONI operate in the laser guide star AO (LGSAO) mode, where an artificial sodium laser guide star is generated on sky near the science target for higher-order AO corrections. However, the LGSAO mode still requires a natural guide star to correct the tip-tilt motions, which are not detected by the LGS. Gemini-North LGSAO system requires a tip-tilt star of $R < 17.5$ mag within a $25\farcs0$ radius of the science object (the tip-tilt star magnitude limit can be extended down to $18 < R < 18.5$ for dark time) and the VLT AO module requires a tip-tilt star of $V = 12 - 17$ mag within a $60\farcs0$ radius from the science target. These collective requirements yield a sample of 6 lensed candidates suitable for an IFS study, whose properties are summarized in Table 5.

4.2.1 SDSS J0252+0039

From the three candidates that meet the LGSAO requirements of Gemini-North, as shown in Table 5, we select SDSS J0252+0039 to test the feasibility of this project. The lensed galaxy of SDSS J0252+0039, located at $z_{bg} = 0.9818$, is magnified $\sim 11\times$ by the gravitational potential of an early-type galaxy at $z_{fg} = 0.2803$. The lensed galaxy of interest in SDSS J0252+0039 shows strong [O II] 3727Å nebular emission

in its residual SDSS spectra[5], which was used to estimate the expected Hα flux using the observed flux ratios, f(Hα)/f([OII]) $\sim 2.2 - 4.35$ (Kennicutt 1992; Hopkins et al. 2003). *HST* lens modeling of SDSS J0252+0039, in the ACS-F814W filter, shows that the lensed galaxy's *global* broad-band morphology corresponds to a compact, disk galaxy ($r_{hl} = 0.98$ kpc and $n = 1.31$). Furthermore, the B-band luminosity of the reconstructed lensed galaxy ($M_B = -19.10$) indicates that it is a $\sim 0.11\ L^{\star}$ galaxy[6]. At its respective redshift, the lensed galaxy of SDSS J0252+0039 not only corresponds to a more representative target from the most numerous population but also pushes the lower limit of the sub-luminous galaxies examined by previous IFS studies (Stark et al. 2008; Jones et al. 2010). Thus, the lensed galaxy of SDSS J0252+0039 is an ideal target to test whether it is technically feasible to combine the lensing magnification in the galaxy-scale regime (the studies by Stark et al. (2008) and Jones et al. (2010) examine cluster-scale lenses) with the diffraction-limited IFS to derive detailed kinematic information of sub-luminous galaxies at $z > 0.75$.

Figure 4.3 SLACS lens model of SDSS J0252+0039. *From left to right*: ACS-F814W image of the SLACS lens; lens galaxy subtracted image showing the lensed features clearly; predictions of the lensed features from the best-fit SIE mass model; the "double-residual" image and the reconstruction of the lensed galaxy on the source plane. All images are $7\farcs5 \times 7\farcs5$ in size.

[5]It should be noted that the continuum of the SDSS spectrum is primarily dominated by the lens galaxy. Therefore, an estimate of the [O II] 3727Å flux (f([O II] 3727) $\sim 5 \times 10^{-16}$ erg s^{-1} cm^{-2}) is only approximate. However, it is sufficient to estimate the expected Hα flux using Hα/[O II] line ratios, which was then used in the exposure time calculator of NIFS.

[6]Given the characteristic B-band luminosity of all galaxy types, $M_B{}^{\star} \sim -21.45$, at $z \sim 1$ (Faber et al. 2007).

4.3 NIFS Observations and Data Reduction of SDSS J0252+0039

Observations of SDSS J0252+0039 were made with the LGSAO mode of NIFS on Gemini-North as a part of the program GN-2009B-Q-38. The integral field unit (IFU) of NIFS is an image slicer which splits a $3\farcs0 \times 3\farcs0$ FOV into 29 slices of $0\farcs103$ width. The dispersed spectra from the 29 slices are then reformatted on the detector to provide two-dimensional spectro-imaging, in a wavelength range of interest. The lensed galaxy redshift of SDSS J0252+0039 places Hα and [N II] 6583Å in the NIFS J grating, which has a spectral resolution of 6040 and a range of 1.15 - 1.33 μm. All observations were performed using the standard ABBA configuration, where we switched to a blank sky $8\farcs0$ away from the target to achieve sky subtraction since the lens system fills the NIFS FOV. Individual exposures (both target and sky fields) were $600s$ long and the total on-target exposure time was $21ks$. The entire observing program, including sky exposures and associated overheads, was 12.5 hours in length. Before each observing block, we took short exposures ($\sim 22s$) of the tip-tilt star to center the IFU pointing and then chopped on to the position of SDSS J0252+0039, a process known as "blind acquisition". Furthermore, we use the observations of the tip-tilt star to compute the FWHM of the AO-corrected PSF (both before and after each observing block).

We reduce the NIFS data using the standard Gemini IRAF NIFS pipeline, which includes the processing of baseline calibration, telluric and science data. We use the NIFS processing scripts to perform extraction, flat-fielding, sky-subtraction, wavelength calibration and telluric calibration (to remove OH sky lines), which yield individual data cubes of $600s$ exposure time. We then use the coordinates of the central spatial pixel of the first data cube to align and co-add the remaining data, to produce a single $21ks$ data cube of SDSS J0252+0039. We reduce the observations of the tip-tilt star in a similar manner to that of the science target. We then construct white light (i.e. wavelength collapsed) images of the tip-tilt star and perform Gaussian profile fits, which yield FWHM $\sim 0\farcs2 - 0\farcs25$ for the AO-corrected PSF. The FWHM of the AO-corrected PSF corresponds to $\sim 1.6 - 2.0$ kpc at $z_{bg} = 0.9818$. Moreover, accounting for the total magnification factor of $11\times$, the exceptional spatial scales probed by AO-assisted IFS of SDSS J0252+0039 correspond to $\sim 145 - 180$ pc, on

the source plane. The spectral resolution of the data, measured from argon arc lines in the 1.15 - 1.33 μm wavelength range, is 1.9 Å ($\sim 45\,\mathrm{km\,s^{-1}}$). In the following section, the quoted widths of nebular emission lines (σ_{corr}) are corrected for the instrumental resolution where, $\sigma_{\mathrm{corr}} = \sqrt{{\sigma_{\mathrm{obs}}}^2 - {\sigma_{\mathrm{arc}}}^2}$.

4.4 Preliminary Results and Future Work

4.4.1 Spatially Resolved Spectroscopy of Hα

During the preliminary analysis, we focus on deriving the spatially resolved kinematics and star formation rates of the lensed galaxy of SDSS J0252+0039 using Hα, the brightest kinematic tracer of star-forming galaxies. We first examine the wavelength calibrated NIFS data cube of SDSS J0252+0039, using the data cube visualization software Qfitsview. As shown in Figure 4.4, we observe strong emission in multiple velocity channels that are centered on the systemic velocity of Hα. Furthermore, the distribution of Hα emission within the NIFS data cube follow the observed broad I-band morphology of the Einstein ring closely.

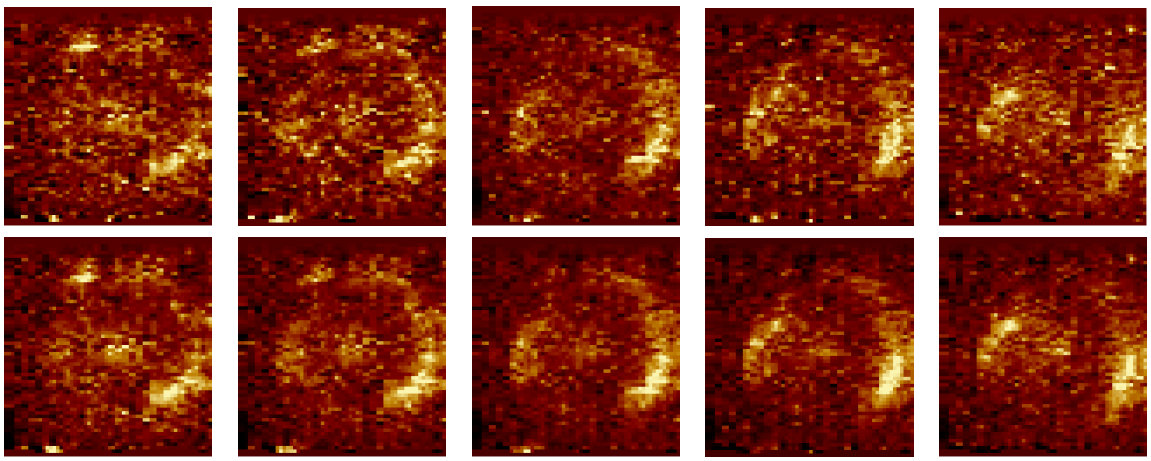

Figure 4.4 Spectro-imaging of SDSS J0252+0039 (visualized via Qfitsview) in 5 velocity channels, centered on the systemic velocity of Hα emission line. The velocity interval between the channels correspond to ~ 25 km/s. The top row shows spectro-imaging from the original data cube and the bottom row shows the same velocity channels after the data cube was convolved with a Gaussian kernel of FWHM = 2 Å, to boost the signal-to-noise in each spaxel. As evident in both rows, we observe Hα emission along the Einstein ring, whose distribution resembles the *HST* broad-band imaging (shown in Figure 4.3). All images are $3\farcs0 \times 3\farcs0$ in size.

To estimate the kinematics and star formation rates of the lensed galaxy, we construct emission line maps by fitting a Gaussian profile to the Hα line at each spatial pixel. Before performing emission line fits, we subtract the median value at each spatial pixel to remove the source continuum and any residual background from the reduction procedure (similar to the methodology of Jones et al. (2010)). We then perform a weighted χ^2 minimization (based on the IDL minimization procedure MPFIT by Craig B. Markwardt) to determine the two-dimensional line intensity, velocity and dispersion fields. We also subtract the instrumental resolution in quadrature from the best-fit Gaussian σ at each spatial pixel. The fitting region of each spectrum, centered on the systemic velocity of Hα, is weighted by the continuum scatter in the spectral window. Furthermore, we perform an emission line fitting procedure after the data cube is convolved with a Gaussian kernel of FWHM = 2 Å along the spectral direction, to boost the signal-to-noise in each spaxel.

Figures 4.5 shows the Hα line flux (measured in instrumental units), velocity and velocity dispersion of the lensed galaxy, on the image plane. Only emission line detections at the $\geq 3\sigma$ level are shown in Figures 4.5 (from the smoothed data cube) and Figure 4.6 illustrates the Gaussian profile fit to an individual spectrum in the NIFS data cube. Figure 4.5(*Bottom-left*) shows evidence of a velocity gradient along the Einstein ring feature (potentially consistent with the disk-like morphology inferred in the rest-frame B-band reconstruction), with counter-imaging of the velocity field that is also consistent with the broad-band lens model. We estimate the global average velocity dispersion of the lensed galaxy, which is representative of the internal motions of the gas (Law et al. 2007), as a flux-weighted mean of the spaxels ($\sigma_{\rm mean} = \sum \sigma_{\rm pix} {\rm I}_{\rm pix} / \sum {\rm I}_{\rm pix}$) with H$\alpha$ line detections at the $\geq 3\sigma$ level. We obtain an average velocity dispersion of $\sigma_{\rm mean} \sim 40\,{\rm km\,s^{-1}}$ from the emission line fitting procedure to the non-smoothed data cube. Furthermore, we find that the 2 Å smoothing process utilized above produces a $+14\,{\rm km\,s^{-1}}$ boost in the σ_{mean} estimate in comparison to the non-smoothed case.

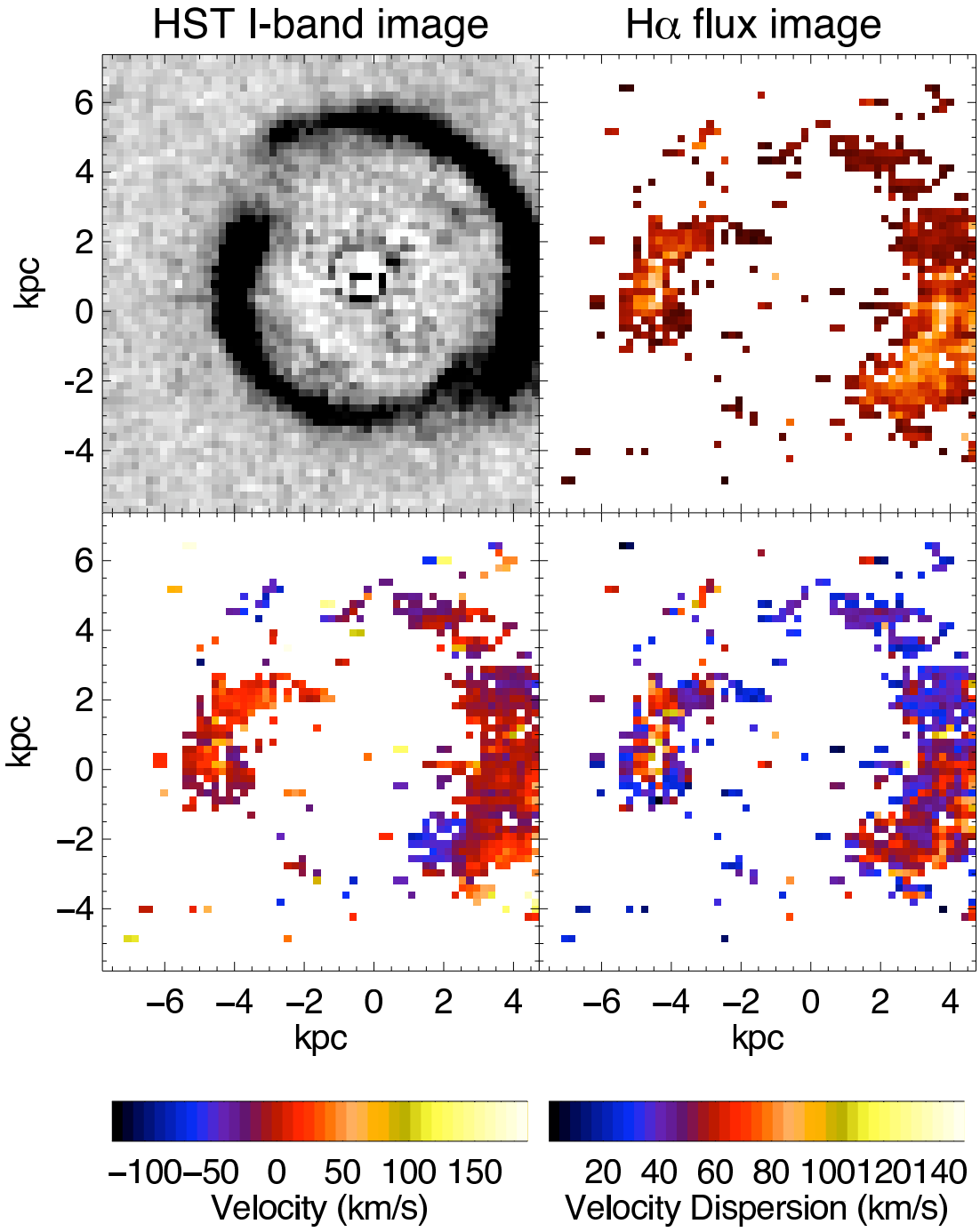

Figure 4.5 **Top-left**: *HST* I-band image of the gravitationally lensed galaxy of SDSS J0252+0039, with the lens galaxy subtracted for clarity. **Top-right**: Image plane emission line properties of the lensed galaxy of SDSS J0252+0039. $H\alpha$ emission line flux is estimated in instrumental units and only the detections at the $\geq 3\sigma$ level are plotted. **Bottom-left**: The velocity field of the lensed galaxy of SDSS J0252+0039, measured relative to the systemic velocity of Hα. **Bottom-right**: Velocity dispersion map of the lensed galaxy of SDSS J0252+0039. The instrumental resolution of NIFS J-band data is subtracted in quadrature from the velocity width measurements.

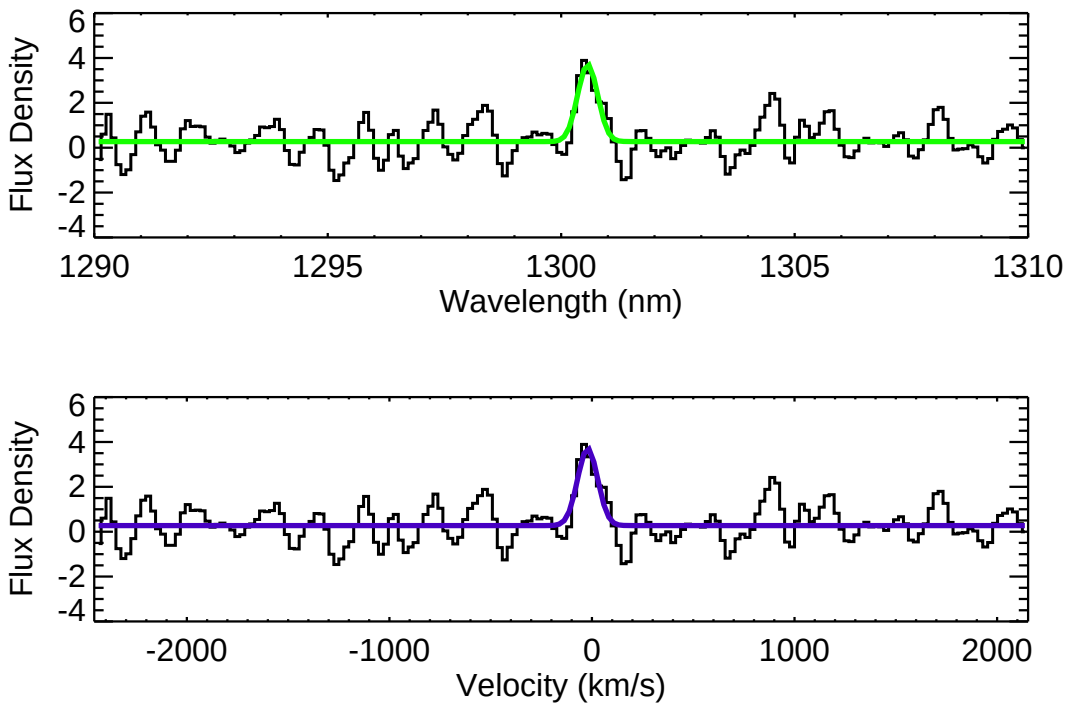

Figure 4.6 Gaussian profile fit to the Hα emission line in an individual spaxel in the NIFS data cube, in wavelength (top row) and velocity (bottom row) channels. The flux density is expressed in instrumental units.

4.4.2 Remaining Work and Future Follow-up

Further steps needed to be taken to derive spatially resolved kinematics and star formation rate information of the lensed galaxy of SDSS J0252+0039 are summarized below. The flux calibration of NIFS data cubes is not supported by the standard reduction scripts discussed above. The A0V telluric standard star was observed both before and after each observing block, at a similar airmass to that of SDSS J0252+0039. Therefore, we will compare the integrated NIFS telluric spectrum to previous long-slit spectra in the J-band to derive the flux calibration, and compute the Hα flux in each spaxel in physical units[7]. The Hα luminosity is a direct probe of the instantaneous SFR of a galaxy, since it traces the ionizing radiation produced by young, massive stars (Law et al. 2007). After the flux calibration of the NIFS data

[7]Figure 4.5 expresses the Hα flux in instrumental units.

cube, we will derive the SFR at each spaxel, with a reliable Hα line detection, using the prescription of Kennicutt (1998) to convert between the Hα luminosity and SFR.

One of the crucial aspects of deriving spatially resolved kinematics of the lensed target is reconstructing the Hα emission line properties on the source plane. The "de-lensing" process of the velocity field can be achieved in two ways: parametric model based reconstruction, where the velocity profile of the lensed galaxy is assumed on the source plane and then mapped on to the image plane through forward-ray tracing for a given gravitational lens potential. The predicted lensed features of the velocity field are then compared to the emission line maps measured on the image plane and the parameters are optimized until the best-fit solution is reached (based on a merit function such as the χ^2 statistic). This method is similar to the surface brightness profile modeling of lensed galaxies, with the exception that it now utilizes the conservation of the velocity field. Since gravitational lensing is an achromatic phenomenon, the mass-model can be constrained to that obtained by lens modeling of broad-band images, if available. Furthermore, observations of resolved velocity structure improves the gravitational lens modeling process by doubling the constraints on a pixel on the image plane. Pixels that are counter images of each other, in theory, have the same surface brightness and velocity; therefore, one can trace multiply imaged points to the same location on the source plane. For example, if the lens model of a system can be derived from high-resolution broad-band imaging, one can then apply the coordinate transformation to the measured emission line maps to reconstruct its morphology on the source plane (after accounting for differences between the offset and rotation of the FOV between the broad-band image and the spectro-image, if any).

We will fit the following parametric rotation curve model, described in Courteau (1997), to test whether the source plane kinematics of SDSS J0252+0039 are consistent with that of a rotating system.

$$V(R) \; = \; V_0 + \frac{2}{\pi} \, V_c \, arctan \frac{R}{R_t} \tag{4.1}$$

The parameters of the disk model include the systemic velocity (V_0), asymptotic velocity (V_c), scale radius (R_t), coordinates of the disk center (x_d, y_d), position angle (θ) and the disk inclination (i). We will use the best-fit rotation curve model to estimate the maximum rotational speed (V_{max}) of the lensed galaxy, which can then be used

to estimate its dynamical mass[8]. Furthermore, the extent of the Hα emission on the source plane, measured from the reconstructed flux map, and σ_{mean} can also be used to estimate the dynamical mass[9] for comparison. The kinematic information derived using the method above can be used to determine where SDSS J0252+0039 lies relative to the local Tully-Fisher relation (Tully & Fisher 1977). Another important outcome of near-infrared observations is the ability to derive line ratios such as [N II] 6583Å/Hα, which is highly sensitive to the metallicity since it is directly related to the oxygen abundance (O/H, Pettini & Pagel (2004)). An examination of the velocity channels centered on the systemic velocity of [N II] 6563Å does not show strong emission along the Einstein ring. Therefore, we cannot use the NIFS observations to derive spatially resolved metallicity gradients; however, we can obtain an upper limit to the global metallicity of SDSS J0252+0039 by deriving the [N II] 6563Å/Hα index of the spatially integrated spectrum of SDSS J0252+0039 (by co-adding the spaxels that have reliable Hα detections).

The preliminary results from the IFS observations of SDSS J0252+0039 show the remarkable potential of combining the lensing magnification with the advantages of diffraction-limited IFS, even at the regime of galaxy-scale gravitational lensing. If SDSS J0252+0039 is an unlensed galaxy at $z = 0.9818$ that is observed under very favourable seeing-limited conditions (for example, FWHM $\sim 0\farcs6$ in the J band), the spatial scales achieved by such IFS observations only correspond to $\sim 5\ kpc$ which is not sufficient to probe the kinematics of compact galaxies. After the complete analysis of SDSS J0252+0039, we aim to extend the feasibility study of this project to the SLACS source galaxies shown in Table 5 using NIFS and SINFONI. The next chapter discusses the prospects of obtaining more LGSAO-assisted IFS observations of gravitationally lensed galaxies with the advent of the successor to SLACS survey, whose selection method enables the discovery of SLACS-like lenses at progressively higher source redshifts. Ultimately, AO-assisted IFS studies of gravitationally lensed galaxies[10] pave the path to make observations of the compact and sub-luminous galaxy population (at intermediate to high redshifts) a common practice rather than a novelty when examining galaxy evolution.

[8] $M_{dyn}\ sin^2\ i\ =\ R\,(V_{max}\ sin\ i)^2/G$

[9] $M_{dyn}(R)\ =\ C\ R\ {\sigma_{mean}}^2/G$

[10] For example, the observations of SDSS J0252+0039 in this study and studies by Stark et al. (2008), Jones et al. (2010) and Yuan et al. (2012) etc.

Chapter 5

Conclusions

In this dissertation, we have presented the results of a study that systematically examines the individual components of galaxy-scale gravitational lenses discovered in the SLACS survey, one of the largest and most comprehensive discovery programs conducted to date. This study investigates key scaling relations of the lens and source galaxy populations of SLACS lenses to determine the effect of various baryonic and non-baryonic processes that are involved in the evolution of galaxies. This chapter summarizes the results from the individual projects of this thesis, discusses the implications of utilizing gravitational lensing to study galaxy evolution and the future prospects for this field.

5.1 Chapter Summaries

First, we investigate the correlation between the mass of a central supermassive black hole and the total gravitational mass of the host galaxy. The results are based on 43 gravitational lenses from the SLACS survey whose black hole masses were estimated through two scaling relations: the relation between black hole mass and Sérsic index (M_{bh} - n relation) and the relation between black hole mass and stellar velocity dispersion ($M_{bh} - \sigma_\star$ relation). We use the enclosed mass within R_{200} (i.e. the radius within which the density profile of a lens galaxy exceeds the critical density of the universe by a factor of 200), determined by gravitational lens modeling of *HST* imaging (Bolton et al. 2008a), as a tracer of the total gravitational mass. The best fit

correlation, where M_{bh} is determined from $M_{bh} - \sigma_\star$ relation, is

$$\log(M_{bh}) = (8.17 \pm 0.13) + (1.57 \pm 0.39)(\log(M_{tot}) - 13.0) \quad (5.1)$$

over 3 orders of magnitude in M_{bh} and the scatter in $\log(M_{bh})$ for a fixed $\log(M_{tot})$ is 0.10 dex. From a variety of tests, we find that we cannot reliably estimate black hole mass from the M_{bh} - n relation for the SLACS lens galaxy sample. The observed $M_{bh} - M_{tot}$ relation provides some of the first observational evidence to test the prediction that supermassive black hole properties are fundamentally determined by the halo properties of the host galaxy.

After examining the lens galaxy population of the SLACS survey, we focus our attention on its source galaxy population. We take advantage of the magnification in size and flux of a galaxy, provided by strong gravitational lensing, to analyze the properties of 62 source galaxies from Bolton et al. (2008a). The sample of gravitationally lensed galaxies span a redshift range of $0.20 < z < 1.20$ with a median redshift of $z = 0.61$. We use the lens modeling code LENSFIT to derive the luminosities, sizes and Sérsic indices of the lensed galaxies. The measured properties of the lensed galaxies show a primarily compact, "disk"-like ($n \leq 2.5$) population with the peaks of the size and Sérsic index distributions corresponding to $\sim 1.50\,kpc$ and $n \sim 1$ respectively. Comparison of the SLACS galaxies to a non-lensing, broad-band imaging survey shows that a lensing survey allows us to probe a galaxy population that reaches ~ 2 magnitudes fainter. Our analysis allows us to compare the $\langle z \rangle = 0.61$ disk galaxy sample to an unprecedented local galaxy sample of $\sim 670,000$ SDSS galaxies at $z \sim 0.1$, which indicates that the evolution of the luminosity-size relation since $z \sim 1$ may not be fully explained in terms of pure-size or pure-luminosity evolution but by a combination of both. Our observations are also in agreement with recent numerical simulations of disk galaxies that show evidence of *mass-dependent* evolution since $z \sim 1$, where high-mass disk galaxies ($M_\star > 10^9\,M_\odot$) evolve more in size and low-mass disk galaxies ($M_\star \leq 10^9\,M_\odot$) evolve more in luminosity.

A natural extension of *HST* imaging based lens modeling of the SLACS source galaxy population (from the previous project), is to derive its spectroscopic properties. The study of spectroscopic properties of the intermediate and high redshift galaxy population is being revolutionized by the development of laser guide star adaptive optics and integral field spectroscopy; however, until recently, such studies have been

limited to the largest and most luminous galaxies at higher redshift, even with 8 - 10 m class telescopes. Lensing magnification, when combined with adaptive optics, allows detailed nebular emission line measurements of galaxies that are much more typical of the population at high redshifts. Thus, the goal of this project is to obtain detailed kinematic and star formation rate information of a sample of SLACS lensed galaxies, at $z > 0.78$, using the near-infrared integral field spectrographs on Gemini-North and VLT (NIFS and SINFONI). The feasibility study for this project was undertaken at Gemini-North using the LGSAO mode of NIFS in the J band. The observations of the gravitationally lensed galaxy at $z = 0.9818$, SDSS J0252+0039, demonstrate that high signal-to-noise emission line maps of a compact, sub-L* galaxy can be obtained by combining the advantages of gravitational lensing and adaptive optics. The effective angular resolution of the pilot observations (FWHM $\sim 0\farcs2$) correspond to a physical scale of $\sim 145\,pc$ on the source plane. The average velocity dispersion of the lensed galaxy, $\sigma_{mean} \sim 13\,km\,s^{-1}$, and the velocity field on the image plane is indicative of a potentially rotation-dominated system.

5.2 Future Outlook

The projects of this thesis show the great potential behind utilizing the advantages of strong gravitational lensing to study galaxy evolution. For example, utilizing the constraints on the inner mass density profiles of early-type, lens galaxies allows us to make the fundamental connection between the dark matter halo and the central SMBH that ultimately affects the global properties of the host galaxy. By reconstructing the source galaxy population of a SLACS-like survey, through lens modeling, we can extend our understanding of the evolution of scaling relations[1] to the faint, compact and ultra-low mass regime.

Alternatively, one can detect faint, non-lensed galaxies at increasingly higher redshifts by using exceptionally long exposure times. An example of such a deep survey is the Hubble Ultra Deep Field (HUDF), a 1 million seconds exposure of an 11 arcmin^2 region in the southern sky with *HST*-ACS using four filters (Beckwith et al. 2006). However, when constructing various scaling relations, these surveys typically impose a cut to eliminate foreground stars from the galaxy samples. This procedure, in turn,

[1]For example, scaling relations such as the luminosity-size or size-stellar mass relation.

also eliminates most of the compact galaxies from a sample. Even without imposing this cut, it can be difficult to accurately measure the properties of compact galaxies at intermediate to high redshifts. For example, at its median redshift ($\langle z \rangle = 0.61$), the peak of the unlensed SLACS source galaxy size distribution is only $\sim 0\farcs22$, which corresponds to < 3 *HST* resolution elements. The exceptional sensitivity and spatial resolution required to obtain imaging observations with wider sky coverage[2] and to attain accurate measurements of galaxy properties can be achieved using the next generation of space-based telescopes (such as the James Webb Space Telescope, JWST) and ground-based Extremely Large Telescopes (ELTs) equipped with AO technology (such as the Thirty Meter Telescope, TMT (Crampton & Simard 2006; Crampton et al. 2008)). However, until the next generation of observatories are fully operational towards the next decade, gravitational lensing provides the best means to study faint and compact galaxies, the most numerous component of high-redshift galaxy population.

As discussed before, the applications of gravitational lensing are typically limited by sample size. Table 1, an updated version of Table 2 from More et al. (2011), provides a recent summary of lensing surveys. However, an increase of the sample size by at least an order of magnitude is required for further progress of the applications gravitational lensing. Considering the typical yields of strong gravitational lens searches, collecting a strong lens sample on the order of ~ 1000 can be a feasible goal over the next few years. For example, the typical yields of lens surveys are $\sim 10\,\mathrm{deg}^{-2}$ for imaging searches at *HST* depth and resolution; $\sim 1\,\mathrm{deg}^{-2}$ for ground-based surveys; $\sim 1\,\mathrm{deg}^{-2}$ at the expected $0\farcs25$ resolution for the Square Kilometer Array (SKA) and $\sim 10^{-3}$ per spectrum for spectroscopic searches such as SLACS (Treu 2010). Therefore, with the advent of galaxy redshift surveys that will obtain spectra of millions of galaxies and the next generation of ground-based all sky surveys within the next decade, we can expect to collect on the order of $\sim 10,000$ gravitational lenses albeit with different properties due to their selection methods. For example, spectroscopic searches will yield the velocity dispersion profile of the lens and both lens and source redshifts. Imaging searches at *HST*-like spatial resolution and sensitivity is ideally suited to discover lenses with small angular separation, thus, enabling the study of smaller mass deflectors.

[2]While aiming to attain similar depths to HUDF-like surveys using much shorter exposure times.

Table 6. A summary of recent optical lensing surveys

Survey Name	Reference	Telescope	Bands	Area (deg^2)	Depth (mag)	Lens Candidates	Confirmed/ Followed-up
AEGIS	Moustakas et al. (2007)	*HST*	V, I	0.18	$V = 28.75$	7	3/0
GEMS	More et al. (2011)	*HST*	V, z	0.22	$V = 28.25$	10	1/0
COSMOS	Faure et al. (2011)	*HST*	I	1.80	$I = 25.00$	88	4/18
CFHTLS-SL2S	Gavazzi et al. (2012)	CFHT	u, g, r, i, z	170	$g = 25.47$	330	40/65
SDSS-SLACS	Bolton et al. (2006)	Sloan	spectroscopy	3732	$r = 17.77$	131	85/131
BOSS-BELLS	Brownstein et al. (2012)	Sloan	spectroscopy	10000	$r = 22.20$	44	25/44

Note. — A summary of recent lensing surveys, based on an updated version of Table 2 from More et al. (2011). The number of lens candidates discovered from BELLS only reflect the results from 6 months of observations. After its five-year span (2009-2014) obtaining spectra of $\sim 1.5 \times 10^6$ luminous red galaxies, BOSS is expected to yield several hundreds of lens candidates.

The work done by this thesis can be extended to a larger sample of galaxies with the successor to SLACS, the BOSS Emission-Line Lens Survey (BELLS, Brownstein et al. (2012)). The BELLS survey applies the selection method of SLACS to SDSS-III's Baryon Oscillation Spectroscopic Survey (BOSS), which will obtain redshifts of 1.5 million luminous red galaxies within the 2009-2014 survey span (Dawson et al. 2012). Brownstein et al. (2012) presents *HST* followup of 44 lens candidates, which were selected from the first 6 months of spectroscopic data from BOSS. Out of the 44 lens candidates, 25 systems are definite lenses and 11 systems are probable lenses (Brownstein et al. 2012). Given the yield of a spectroscopic lens search as discussed above, we can expect BELLS to discover ~ 1500 gravitational lenses by 2014. The wavelength coverage of BOSS is $360 - 1000\,nm$; thus, BELLS lens systems have lens redshifts of $0.4 \leq z \leq 0.7$. Furthermore, due to the extended wavelength coverage of SDSS-III compared to SDSS-I, the maximum source redshift of BELLS is $z_{source} = 1.63$ (by using the [OII]$\lambda\lambda$3727 emission line). Figures 5.1 and 5.2 show examples of the BELLS spectroscopic selection and *HST* imaging follow-up.

The variety of strong gravitational lenses that are expected to be discovered from surveys such as BELLS are also potential candidates for integral field spectroscopic, follow-up studies that allow us to examine the two-dimensional distribution of kinematics, star-formation rates and metallicities of both lens and source galaxies. As we examine source galaxy populations at increasingly higher redshifts ($z > 1$), bright kinematic tracers of emission line galaxies, such as Hα, shift into the infrared wavelengths. As discussed above, integral field spectroscopy of both lensed and non-lensed

galaxies at high redshift is becoming more reliant on the spatial resolution improvement provided by AO, whose performance is currently optimized in the near-infrared regime. Some of the AO-assisted integral field spectrographs, currently available on 8-10 m class telescopes, that are suitable for 2D spectroscopic follow-up include SINFONI (VLT), NIFS (Gemini-North) and OSIRIS (Keck observatory).

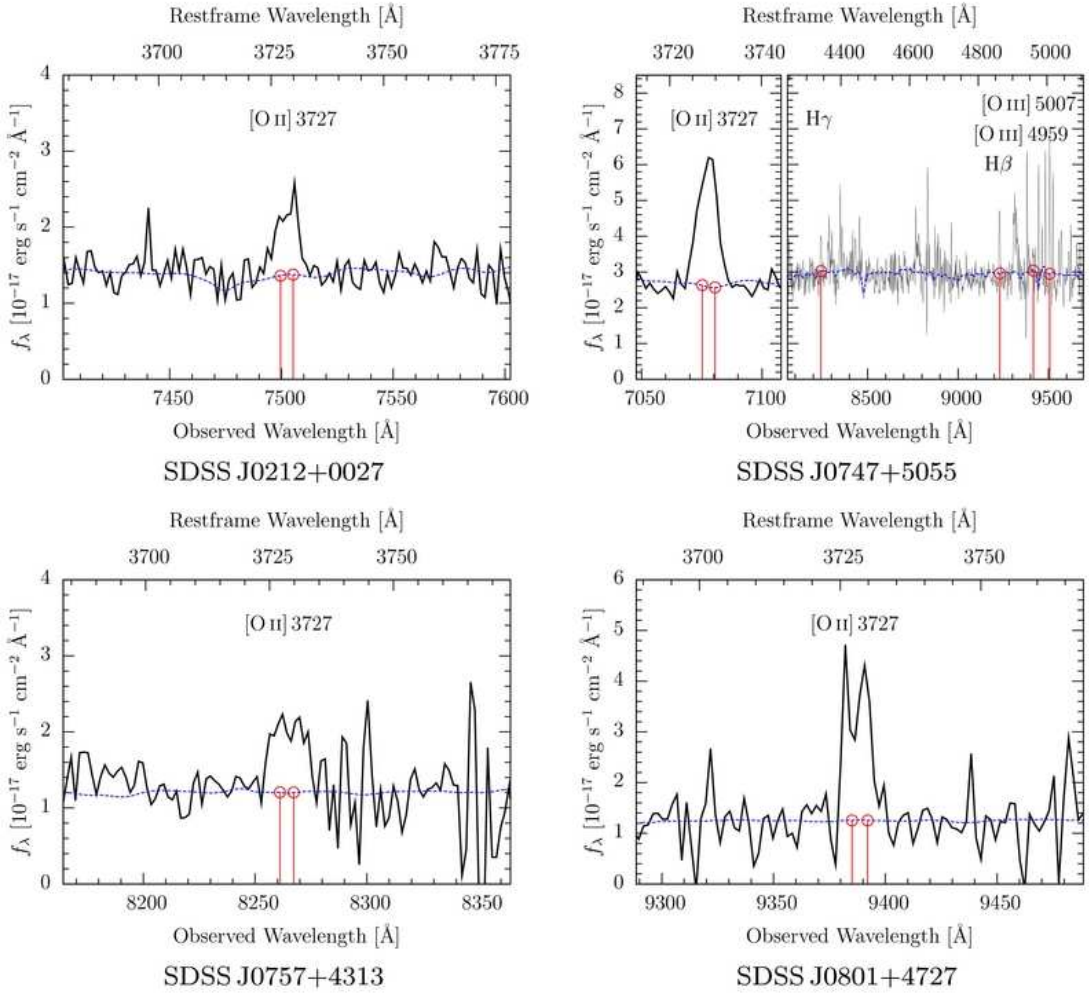

Figure 5.1 Examples of the spectroscopic selection of BELLS lenses, which is similar to the selection method of the SLACS survey (Bolton et al. 2006) at higher lens and source redshifts. In each spectrum, the black and blue dashed lines correspond to the composite BOSS spectrum and the BOSS template fit to the foreground galaxy continuum respectively. The red vertical lines show the emission lines from the source galaxy (Brownstein et al. 2012).

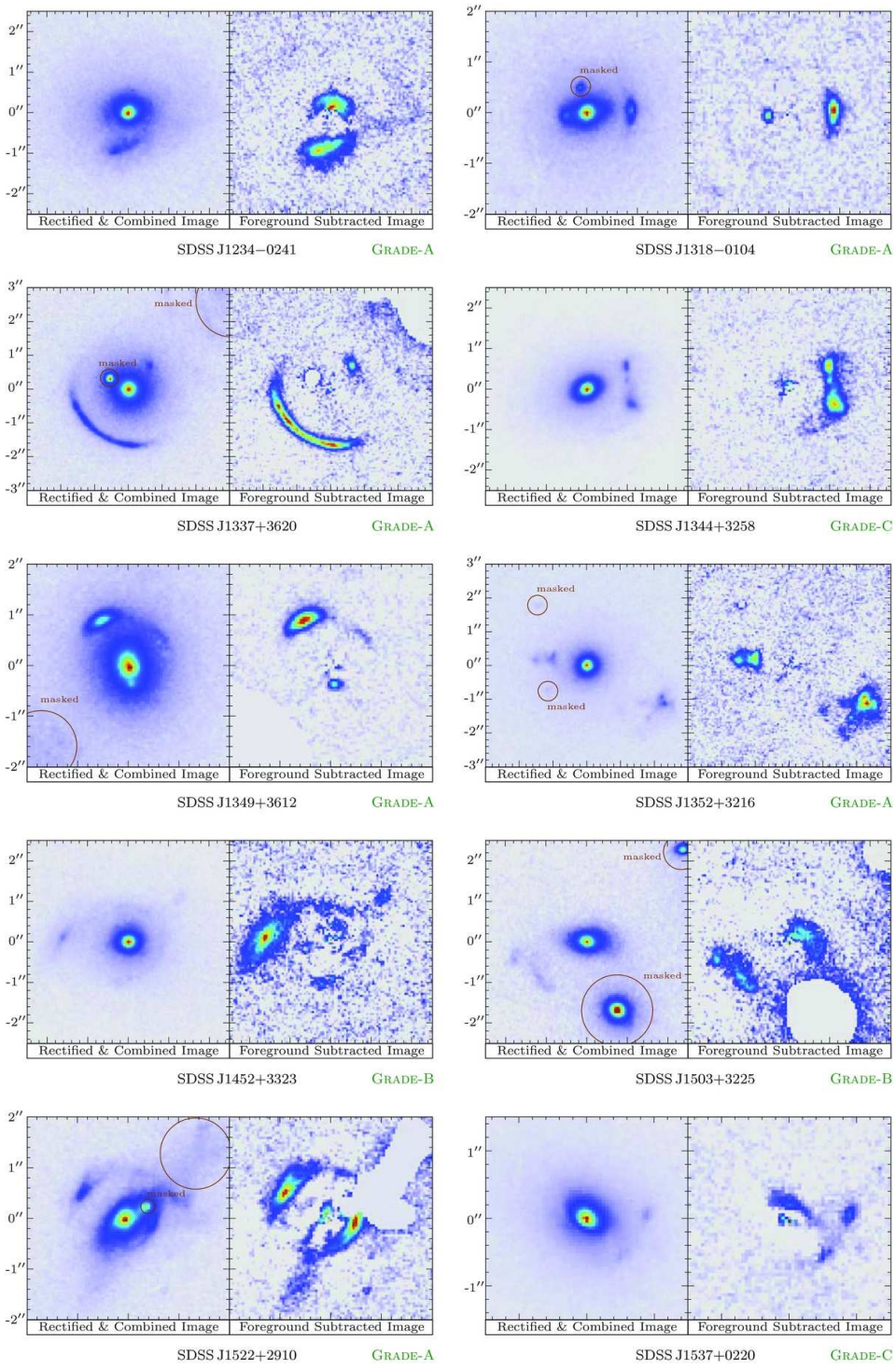

Figure 5.2 *HST*-ACS images of a subset of galaxy-scale gravitational lenses from the BELLS survey, observed using the F814W filter (Brownstein et al. 2012). In each panel, the left thumbnail corresponds to the F814W image of a BELLS lens and the right thumbnail corresponds to the lens galaxy subtracted image, which shows the lensed features clearly. Filled white areas correspond to the masks of the extraneous non-lensed features.

Moreover, multi-wavelength spectrographs are ideal instruments for the spectroscopic follow-up of gravitational lenses discovered through imaging searches. For example, the X-SHOOTER spectrograph on the VLT, which has a wavelength coverage of $300 - 2500\,nm$, can be used to confirm the spectroscopic redshifts of the lens and the source. Furthermore, nearby prospects for the near-infrared spectroscopy of gravitational lenses include utilizing the multiplexing capabilities of upcoming multi-object spectrographs such as KMOS (VLT), FLAMINGOS-2 (Gemini-South) and MOSFIRE (Keck). A natural extension of the near-infrared 2D spectroscopic studies discussed above is mapping the molecular gas distribution of the high redshift lensed galaxy population, in the mm/submm wavelengths, especially by utilizing the sensitivity and spatial resolution provided by the Atacama Large Millimeter/submillimeter Array (ALMA). This approach is similar to the studies in the recent years that map the molecular gas distribution (using millimeter CO interferometry) of massive star-forming galaxies at $z \sim 1.5 - 3$, utilizing facilities such as IRAM Plateau de Bure Interferometer (Tacconi et al. 2006, 2008, 2010). When observing emission line galaxies at the peak epoch of star formation, i.e. $z \sim 1.5{-}3$, the commonly utilized CO(3-2) tracer shifts into the ALMA frequency bands 3 and 4 (84 - 116 GHz and 125 - 163 GHz respectively). At its maximum baseline upon array completion, ALMA is expected to yield spatial resolutions of $\sim 0\farcs03 - 0\farcs05$ in Bands 3 and 4, ideal for the follow-up of gravitationally lensed galaxies.

With the advent of next generation all-sky surveys, which will potentially yield $\sim 10,000\times$ of gravitational lenses, the future of this field is even more promising over the next decade. One of the most exciting prospects for collecting a large sample of gravitational lenses is the Large Synoptic Survey Telescope (LSST), a wide-field deep survey of a $20,000\,\mathrm{deg}^2$ area of the southern sky using a ground-based 8.4 m telescope. Over the LSST time span of 10 years, each area of the sky will be visited ~ 1000 times to produce 6-band images in the $0.3 - 1.1\,\mu m$ regime. Given the typical lens yield by a ground-based imaging search ($1\,\mathrm{deg}^{-2}$ at best), we can expect to collect a lens sample on the order of $\sim 20,000$ from an all-sky survey such as the LSST. Gravitational lenses discovered from a LSST-like imaging search will require further high resolution angular imaging and spectroscopic follow-up and will be ideal targets for future space-based and ground-based facilities such as JWST and the ELTs. Therefore, within the next decade, we can look forward to great progress in combining our own innovations with the advantages nature's own telescope have provided us.

Appendix A

The Anatomy of a Gravitational Lens

The modeling of a gravitational lens, such as the LENSFIT methodology discussed in chapter 3, can often be a complex and time-consuming process that requires extensive user input. Although this thesis will not delve into a step-by-step account of the lens modeling process for all gravitational lenses examined in this thesis, the following section will discuss the overall lens modeling of SDSS J1137+4936, which was done at the request of Saintonge et al. (2013, in prep).

SDSS J1137+4936 was initially discovered by Kubo et al. (2009) during a systematic search for strong lenses in SDSS imaging data. Kubo et al. (2009) present the discovery of six strong gravitational lenses whose deflectors (5 galaxy groups and 1 LRG) are located at $z = 0.17 - 0.45$ and the source galaxies are located at $z = 0.4 - 1.4$. SDSS J1137+4936 is a galaxy-scale gravitational lens, where a single LRG at $z = 0.45$ is forming a bright lensed arc. Further imaging using the SPICAM imager at the Apache Point Observatory (APO) 3.5 m telescope shows the blue arc as two split knots due to poor angular resolution (Figure A.1); however, *HST*-WFPC2 imaging[1] show that the arc is comprised of two images as shown in Figure A.2. Figure A.2 (*Right*) shows SDSS J1137+4936 after the light profile of the foreground LRG is subtracted, showing the lensed features clearly. The images of the lens are marked **A** through **E** in Figure A.2.

[1]Using F814W, F606W and F450W filters.

The follow-up spectroscopy of the bright arc (i.e. image E) by Kubo et al. (2009) confirms a source redshift of $z = 1.41$ and show evidence of a secondary source at $z = 1.38$. Images A, B and C, which resemble three, small knots merging together in a faint secondary arc, most likely result from the second source at $z = 1.38$. Image D corresponds to an extraneous feature that is commonly mistaken for a counter-image of the lensed arc and must be masked during the initial lens modeling process. The lens modeling process of SDSS J1137+4936 is given as a condensed summary below.

1. SDSS J1137+4936 is an unusual system, due to the two background sources that are very close in redshift forming nearly overlapping multiple images. As discussed in chapter 3, the first step in lens modeling involves subtracting the lens galaxy light profile which enables the lens modeling software to "see" the lensed features more clearly. We start the lens modeling process with the F814W image, since it has high S/N.

2. Similar to SLACS lenses, we use a SIE mass-model for the foreground LRG and single or multiple Sérsic components to model the source galaxy light profile.

3. During the very first stages of lens modeling, it is important to realize that image D is *not* a component of the SDSS J1137+4936 system. If left unmasked, lens modeling software can "lock on" to image D and attempt to reproduce images A, B, C, D and sections of arc E simultaneously. This results in significantly deviant predicted positions of images A, B and C, which, in turn, yields an incorrect SIE mass-model. The incorrect astrometry of images A through C hint at the fact that image D may not be a lensed image.

4. We mask the bright arc (E) and image D and run LENSFIT such that it can first predict the correct positions of images A, B and C. This run provides an initial estimate of the SIE mass-model parameters, which can be refined during later runs.

5. We then mask images A through C, unmask the bright arc E and allow LENSFIT to predict its position and brightness using a single Sérsic component. We use the SIE mass-model from the previous step as an initial estimate. We use additional Sérsic components as required to model the bright arc E, which results from the $z = 1.41$ galaxy.

6. When the LENSFIT model of the bright arc E yields satisfactory residuals, we unmask images A through C and perform another LENSFIT iteration. This iteration allows LENSFIT to simultaneously predict images A, B, C and E and converge towards the best-fit solution. Image D is masked and the best-fit estimate for the lens galaxy light profile is held fixed throughout these iterations.

7. We finally unmask image D and perform a full iteration, where LENSFIT is allowed to predict images A through E. If the correct SIE mass-model (and source galaxy light profiles) is predicted from the previous runs, LENSFIT should predict images A, B, C and E but not D.

8. For a full iteration, we free the parameters from both lens and source galaxy light profiles and the SIE mass-model. The best-fit solution is determined by the reduced χ^2 value and a visual inspection of the "double-residual" image.

9. Since the gravitational lensing phenomenon is achromatic, the mass-model should be identical across all filters within the systematic uncertainties. Therefore, when modeling a gravitational lens in multiple filters, it is customary to fix the mass-model parameters to those determined by the highest S/N filter (F814W and F606W imaging for SDSS J1137+4936).

10. When modeling the F606W image of SDSS J1137+4936, we follow a similar procedure to the one described above. However, we do not fix the SIE mass-model parameters to those from the F814W run, rather, we allow them to vary freely during the entire process. Furthermore, we do not use the F814W mass-model parameters as initial estimates, such that we can test whether the lens modeling process is sufficiently robust to converge to the same mass-model parameters for different filters.

11. The SIE mass-model parameters from the F814W and F606W images are virtually indistinguishable, thus confirming that the lens model solution is robust. Since the F450W image has a lower S/N, we initially fix the mass-model parameters to those constrained by the F814W and F606W images. However, during the final iterations we allow the mass-model parameters to vary freely and find that the fractional difference between the F450W mass-model and the F814W/F606W mass-model is less than $\sim 2\%$.

12. In the F814W and F606W filters, the morphology of the background source at $z = 1.41$ is best described by three Sérsic components (only two components in the F450W filter), while the morphology of the source at $z = 1.38$ is best described by a single Sérsic component. Figures A.3 through A.8 show the results of lens modeling of SDSS J1137+4936 in all three filters.

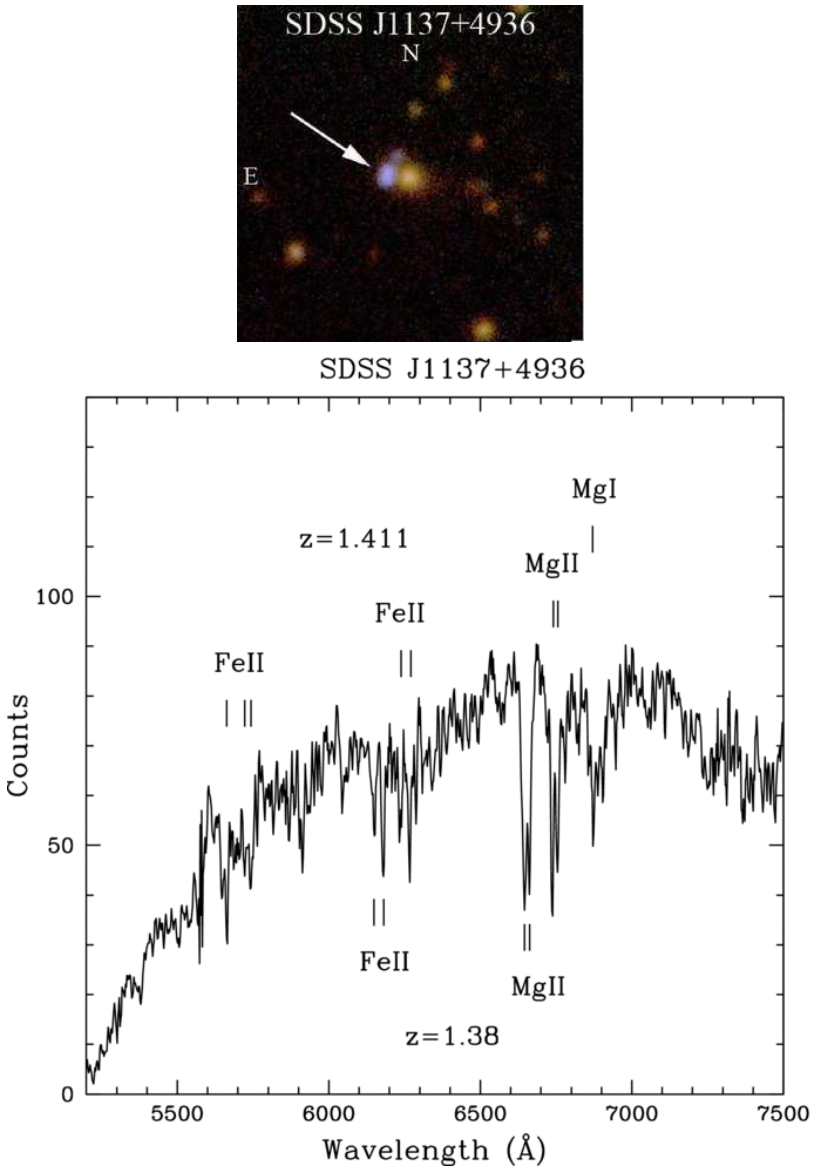

Figure A.1 *Top:* Colour image of the galaxy-scale gravitational lens SDSS J1137+4936, from *g*, *r* and *i* imaging, using the SPICAM imager at the APO 3.5 m telescope. This system consists of a luminous red galaxy at $z = 0.45$, forming a blue arc located to the east as shown by the arrow. *Bottom:* The spectrum of the background source of SDSS J1137+4936, which shows evidence for two galaxies located at $z = 1.38$ and $z = 1.41$ (Kubo et al. 2009).

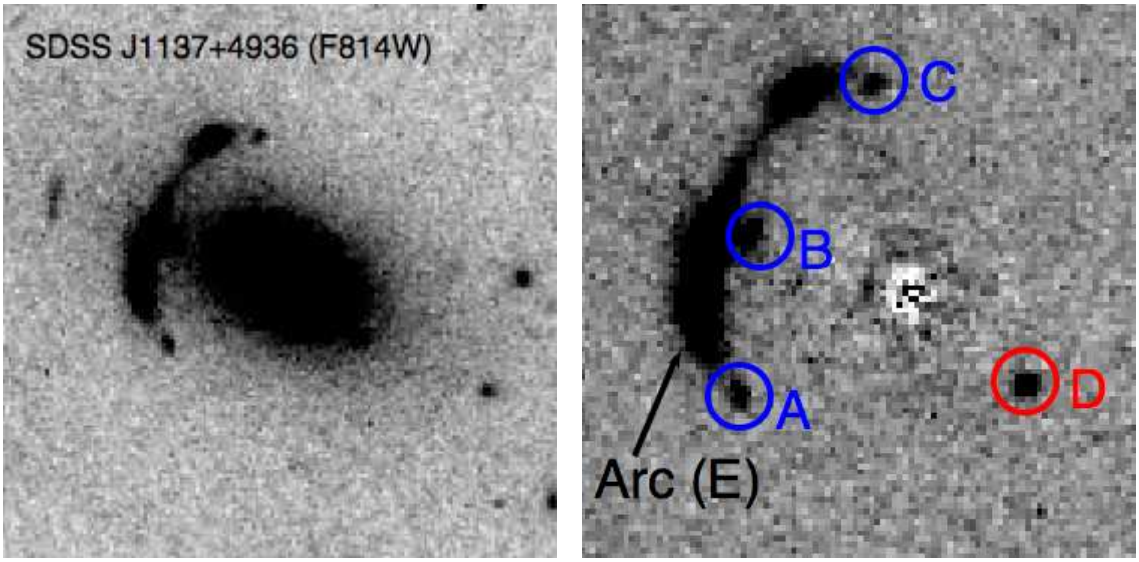

Figure A.2 *HST*-WFPC2 observations of SDSS J1137+4936. *Left: HST*-WFPC2 image of SDSS J1137+4936 taken in the F814W filter ($7\farcs5 \times 7\farcs5$). *Right:* The lens galaxy subtracted F814W image ($5\farcs0 \times 5\farcs0$) showing the lensed features. Images A, B and C correspond to a single source on the source plane (at $z = 1.38$). Image D corresponds to an extraneous feature that is commonly mistaken as a counter-image of the lensed arc. This feature was masked during the lens modeling process. Arc E corresponds to another source at $z = 1.41$.

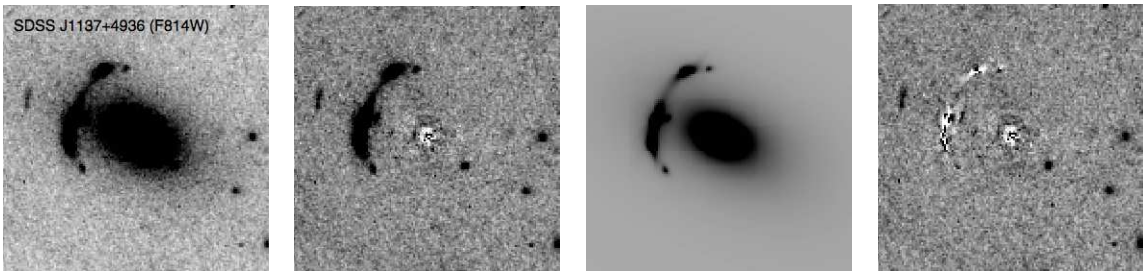

Figure A.3 LENSFIT model of SDSS J1137+4936 in the F814W filter. *From left to right: HST*-WFPC2 image of SDSS J1137+4936; The lens galaxy subtracted image showing the lensed features; The complete lens model on the image plane including the light profile of the lens galaxy and the lensed features from the best-fit SIE mass-model; The "double residual" image after subtracting the PSF convolved lens model from the F814W image. All images are $7\farcs5 \times 7\farcs5$ in size.

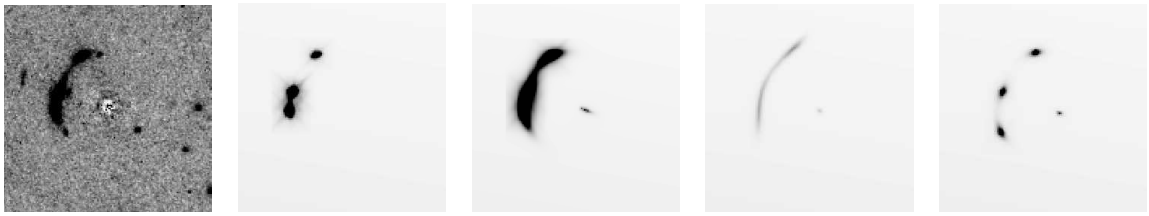

Figure A.4 As discussed in Kubo et al. (2009), the lensed features of SDSS J1137+4936 are caused by two, spectroscopically-confirmed sources at $z = 1.41$ and $z = 1.38$. The bright arc is caused by the galaxy at $z = 1.41$, which can be best described by three Sérsic components in the F814W filter. The $z = 1.38$ galaxy, that results in the image of three small, merging knots, is best described by a single Sérsic component. The following panels provide a breakdown of the two source galaxies into their constituent components and examine the resulting lensed features, as determined by LENSFIT. *From left to right:* Lens galaxy subtracted F814W image of SDSS J1137+4936; Sérsic components 1 through 3 of the $z = 1.41$ source galaxy, and the resulting lensed features; The $z = 1.38$ galaxy, which is described by a single, Sérsic component. Panels 2 through 5 have identical greyscales and all images are $7\farcs5 \times 7\farcs5$ in size.

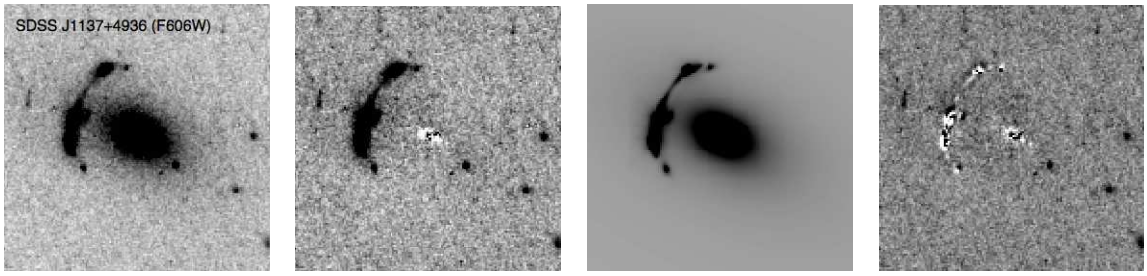

Figure A.5 Same as Figure A.3, except the lens model is now based on F606W imaging. The best-fit SIE mass-model in the F606W filter, which was allowed to vary during all LENSFIT runs, is virtually indistinguishable from that of the F814W filter. Since the gravitational lensing phenomenon is achromatic, the agreement between SIE mass-models from several filters is a good test of the robustness of the LENSFIT modeling procedure.

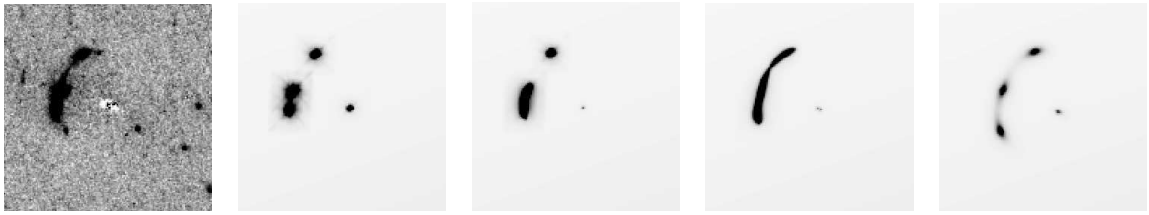

Figure A.6 Same as Figure A.4, except in the F606W filter. Similar to the F814W filter, the $z = 1.41$ source galaxy can be best described by three Sérsic components and the $z = 1.38$ source galaxy can be best described by a single, Sérsic component. Panels 2 through 5 have identical greyscales and all images are $7\farcs5 \times 7\farcs5$ in size.

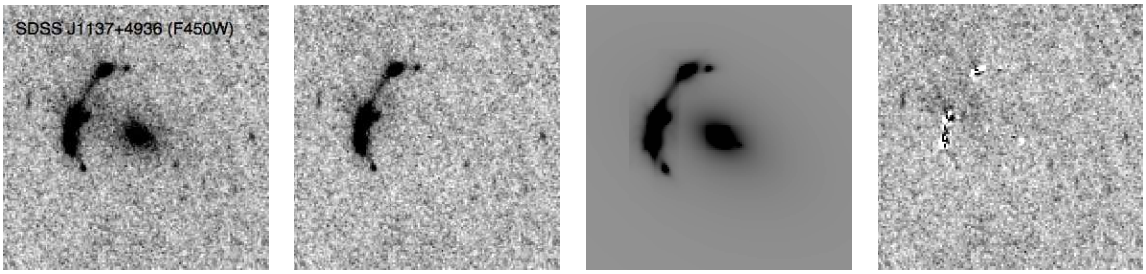

Figure A.7 Same as Figures A.3 and A.5, except the lens model is based on F450W imaging. The fractional difference between the SIE mass-model parameters in the F450W filter (which was allowed to vary freely) and those of F606W/F814W filters is less than $\sim 2\%$. This difference can be caused by varying S/N between filters (F450W image has a lower S/N in comparison to the F814W and F606W images).

Figure A.8 Same as Figures A.4 and A.6, except in the F450W filter. The $z = 1.41$ source galaxy can be best described by two Sérsic components in the F450W filter and the $z = 1.38$ source galaxy can be best described by a single, Sérsic component. Panels 2 through 5 have identical greyscales and all images are $7\farcs5 \times 7\farcs5$.

Appendix B

LENSFIT Models of SLACS Galaxy-Scale Gravitational Lenses

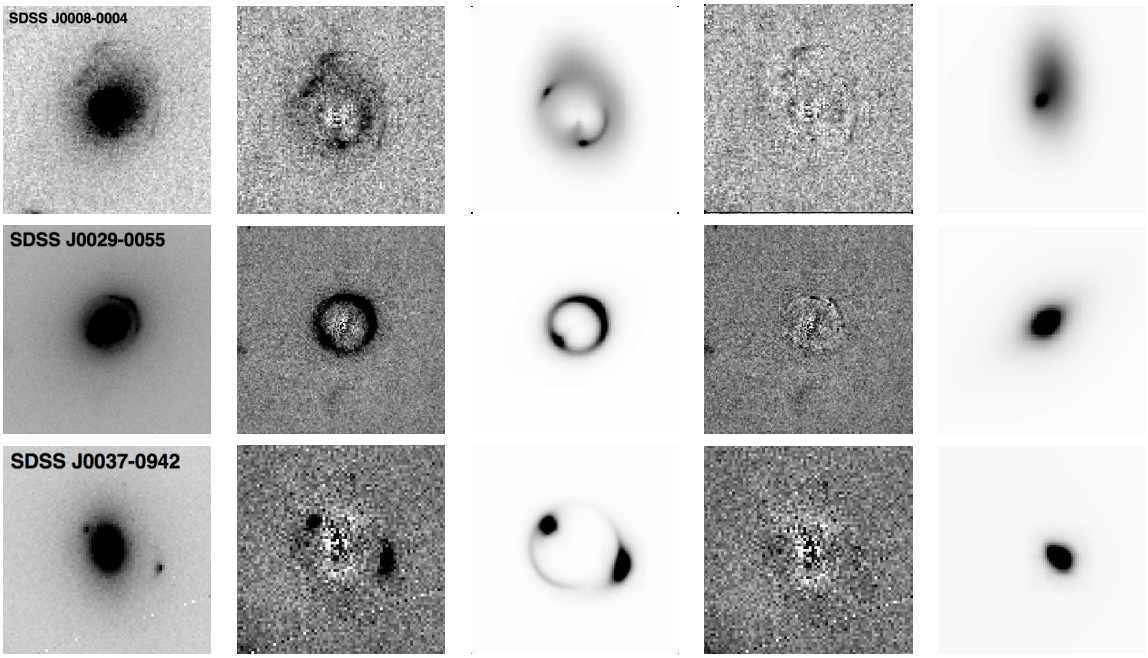

Figure B.1 LENSFIT models of SLACS galaxy-scale gravitational lenses. *From left to right*: ACS-F814W image of the SLACS lens; ACS PSF lens galaxy model subtracted F814W image showing the lensed features; predictions of the lensed features from the best-fit SIE mass model; complete lens-model on the image plane including the light profile of the lens galaxy and the "double-residual" image after subtracting the ACS PSF convolved lens model from the F814W image. All images are $7\farcs5 \times 7\farcs5$.

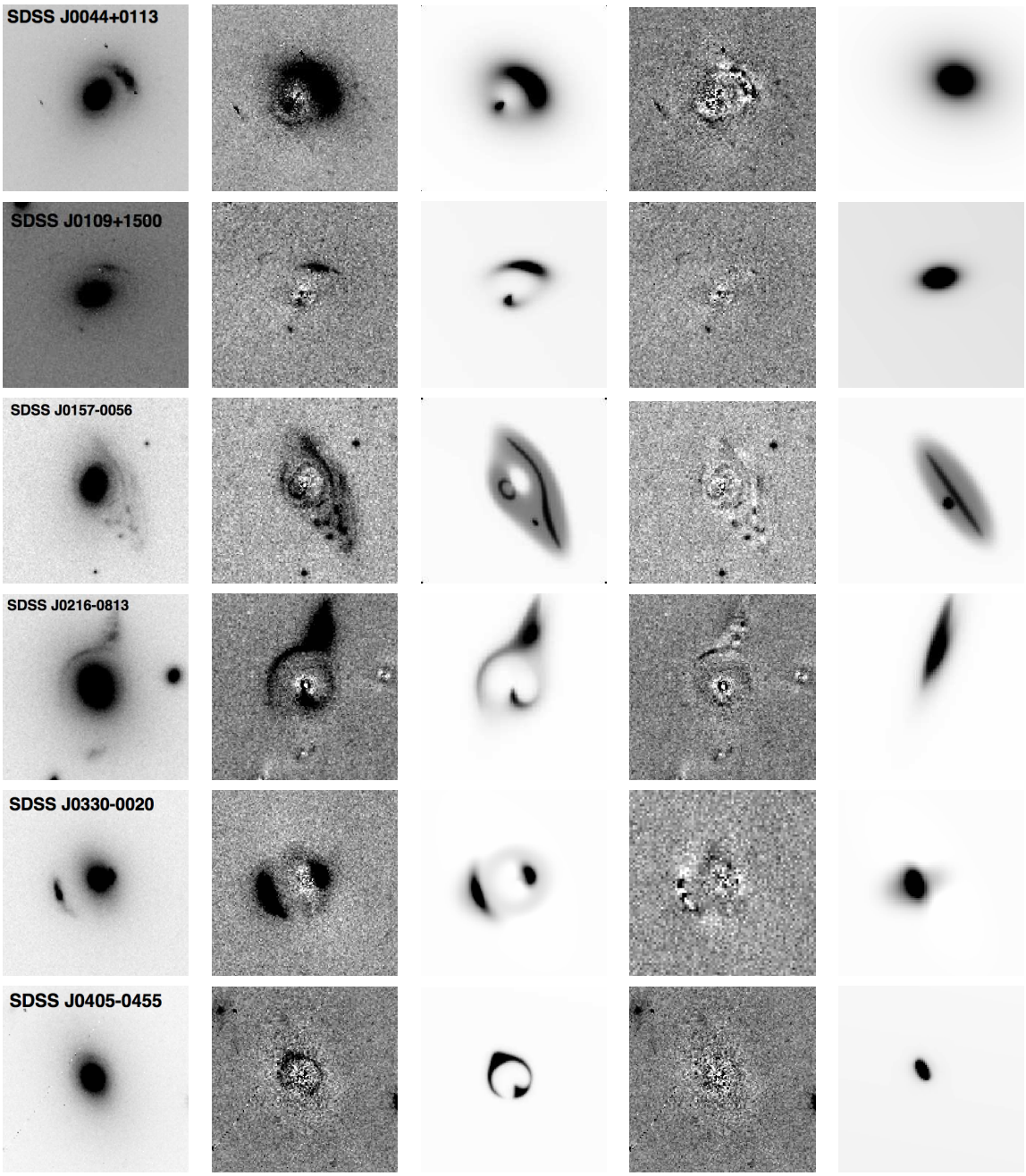

Figure B.2 LENSFIT models of SLACS galaxy-scale gravitational lenses. *From left to right*: ACS-F814W image of the SLACS lens; ACS PSF lens galaxy model subtracted F814W image showing the lensed features; predictions of the lensed features from the best-fit SIE mass model; complete lens-model on the image plane including the light profile of the lens galaxy and the "double-residual" image after subtracting the ACS PSF convolved lens model from the F814W image. All images are $7\farcs5 \times 7\farcs5$.

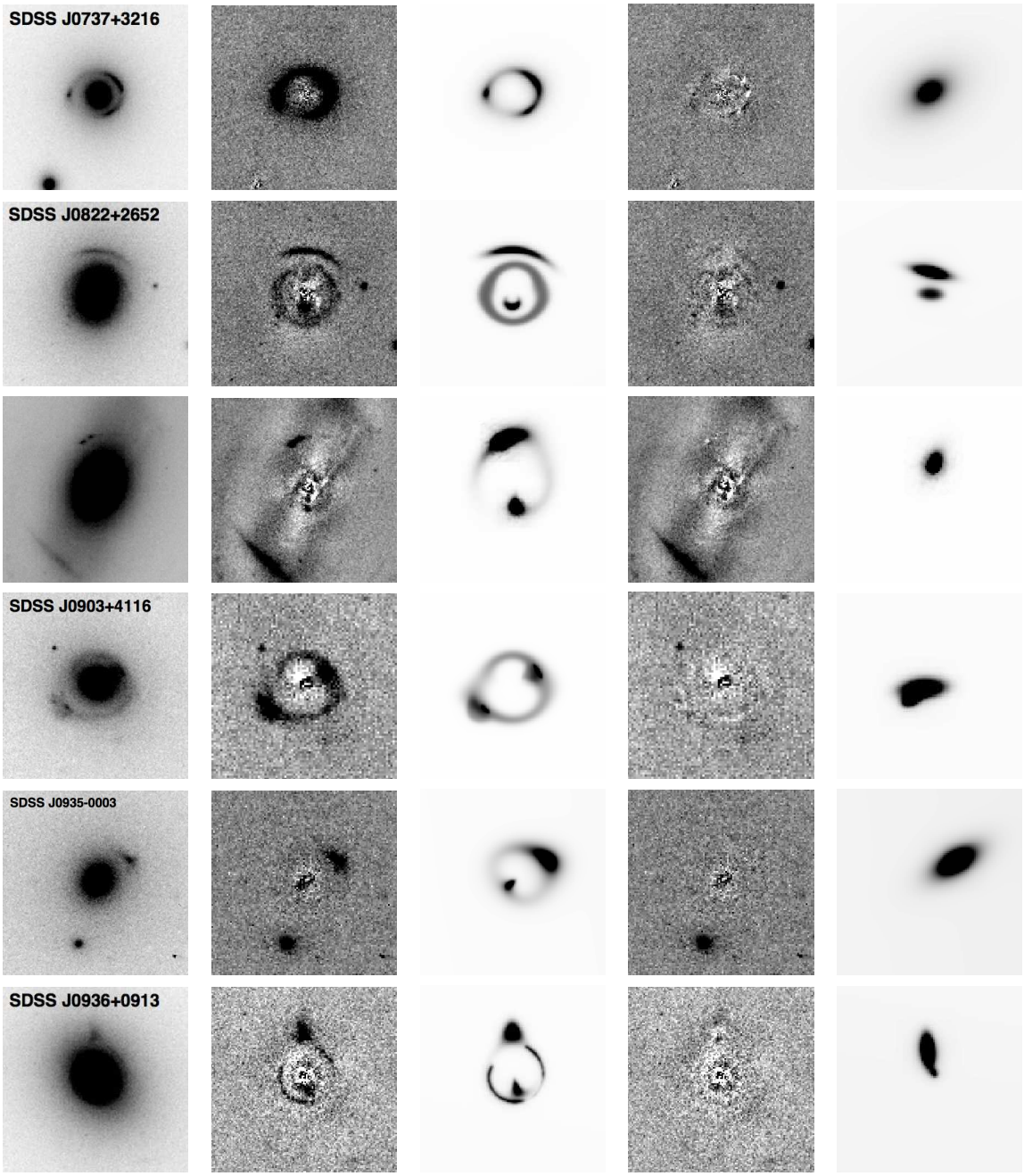

Figure B.3 LENSFIT models of SLACS galaxy-scale gravitational lenses. *From left to right*: ACS-F814W image of the SLACS lens; ACS PSF lens galaxy model subtracted F814W image showing the lensed features; predictions of the lensed features from the best-fit SIE mass model; complete lens-model on the image plane including the light profile of the lens galaxy and the "double-residual" image after subtracting the ACS PSF convolved lens model from the F814W image. All images are $7\farcs5 \times 7\farcs5$.

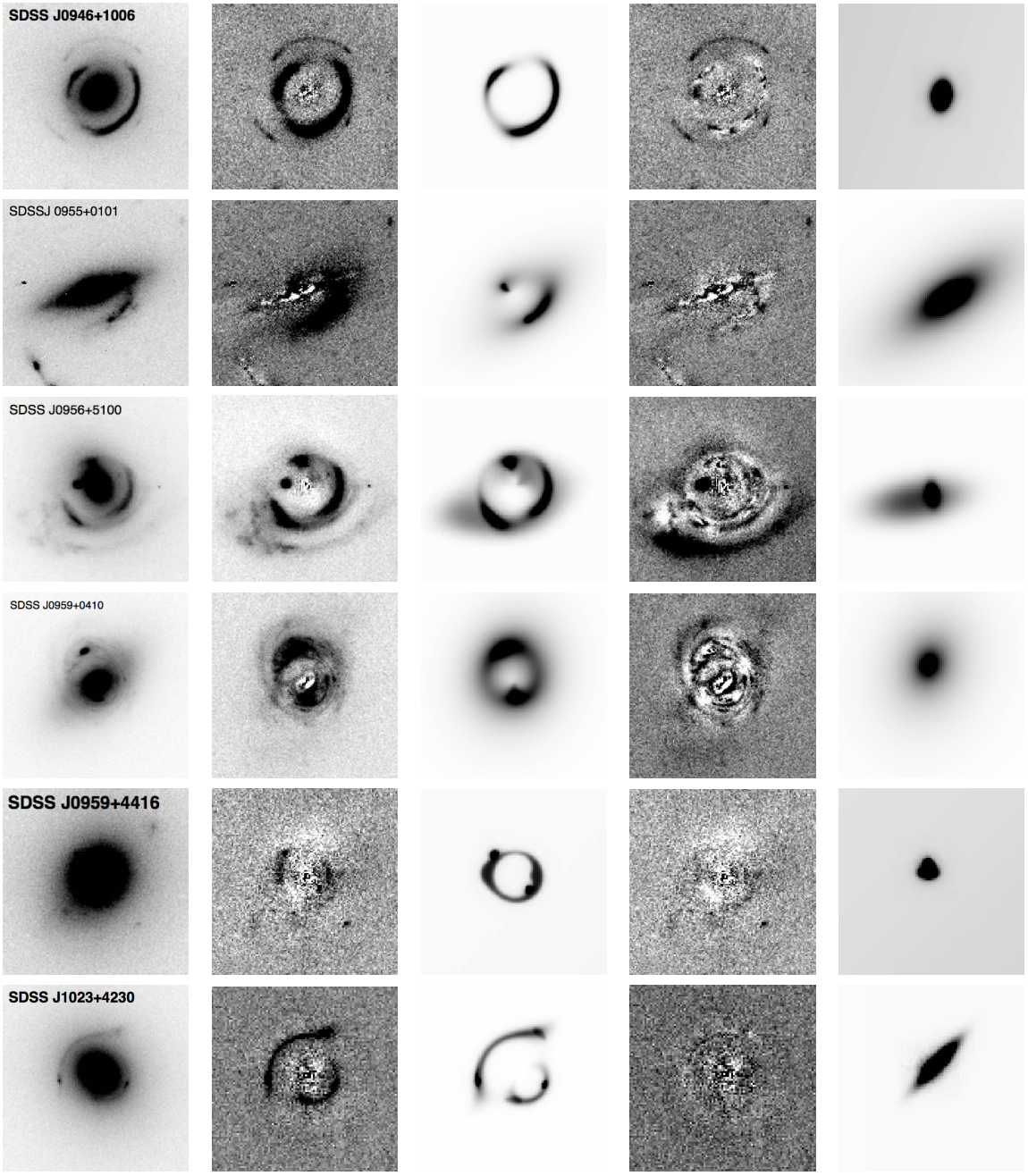

Figure B.4 LENSFIT models of SLACS galaxy-scale gravitational lenses. *From left to right*: ACS-F814W image of the SLACS lens; ACS PSF lens galaxy model subtracted F814W image showing the lensed features; predictions of the lensed features from the best-fit SIE mass model; complete lens-model on the image plane including the light profile of the lens galaxy and the "double-residual" image after subtracting the ACS PSF convolved lens model from the F814W image. All images are $7\farcs5 \times 7\farcs5$.

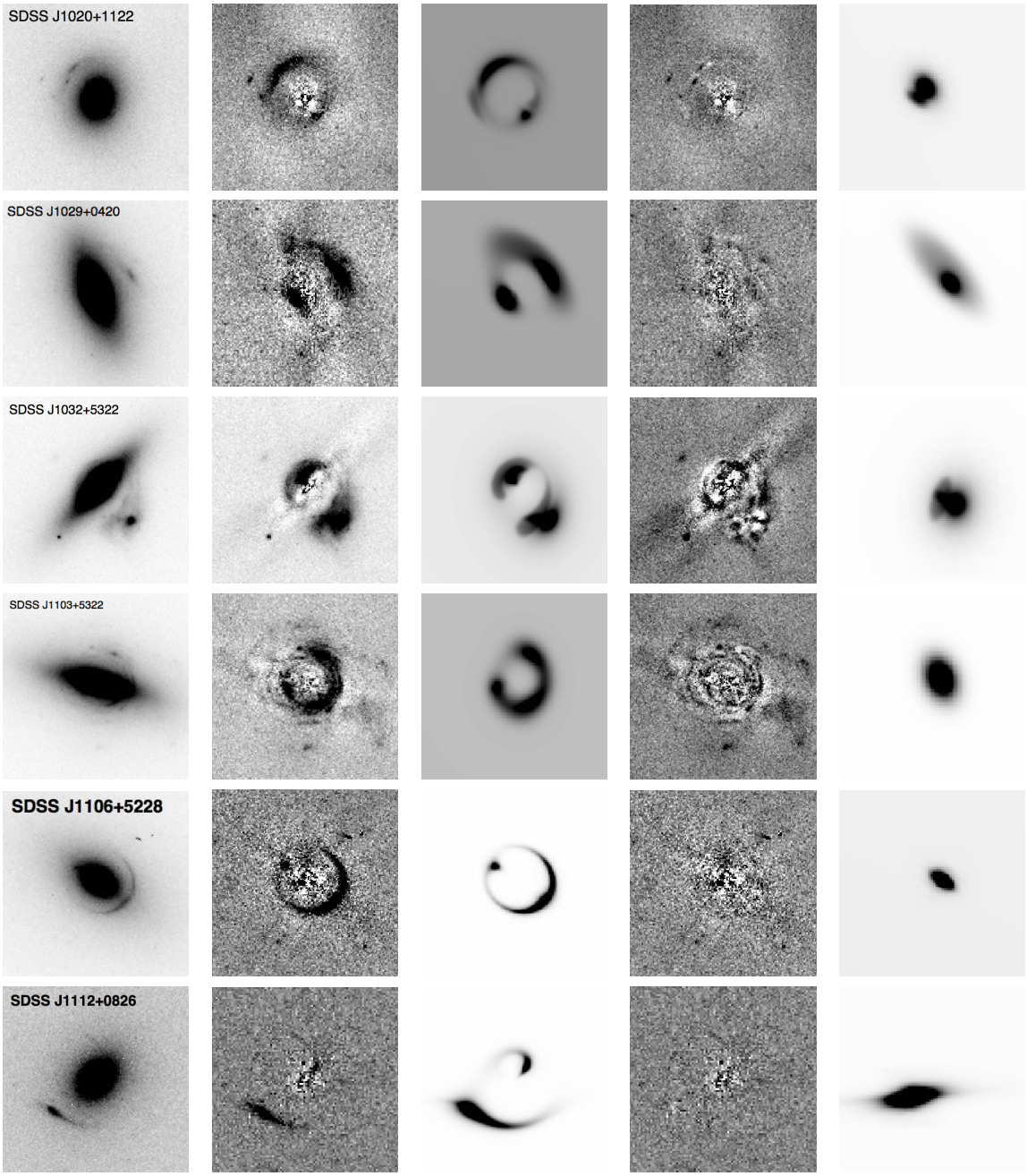

Figure B.5 LENSFIT models of SLACS galaxy-scale gravitational lenses. *From left to right*: ACS-F814W image of the SLACS lens; ACS PSF lens galaxy model subtracted F814W image showing the lensed features; predictions of the lensed features from the best-fit SIE mass model; complete lens-model on the image plane including the light profile of the lens galaxy and the "double-residual" image after subtracting the ACS PSF convolved lens model from the F814W image. All images are $7\farcs5 \times 7\farcs5$.

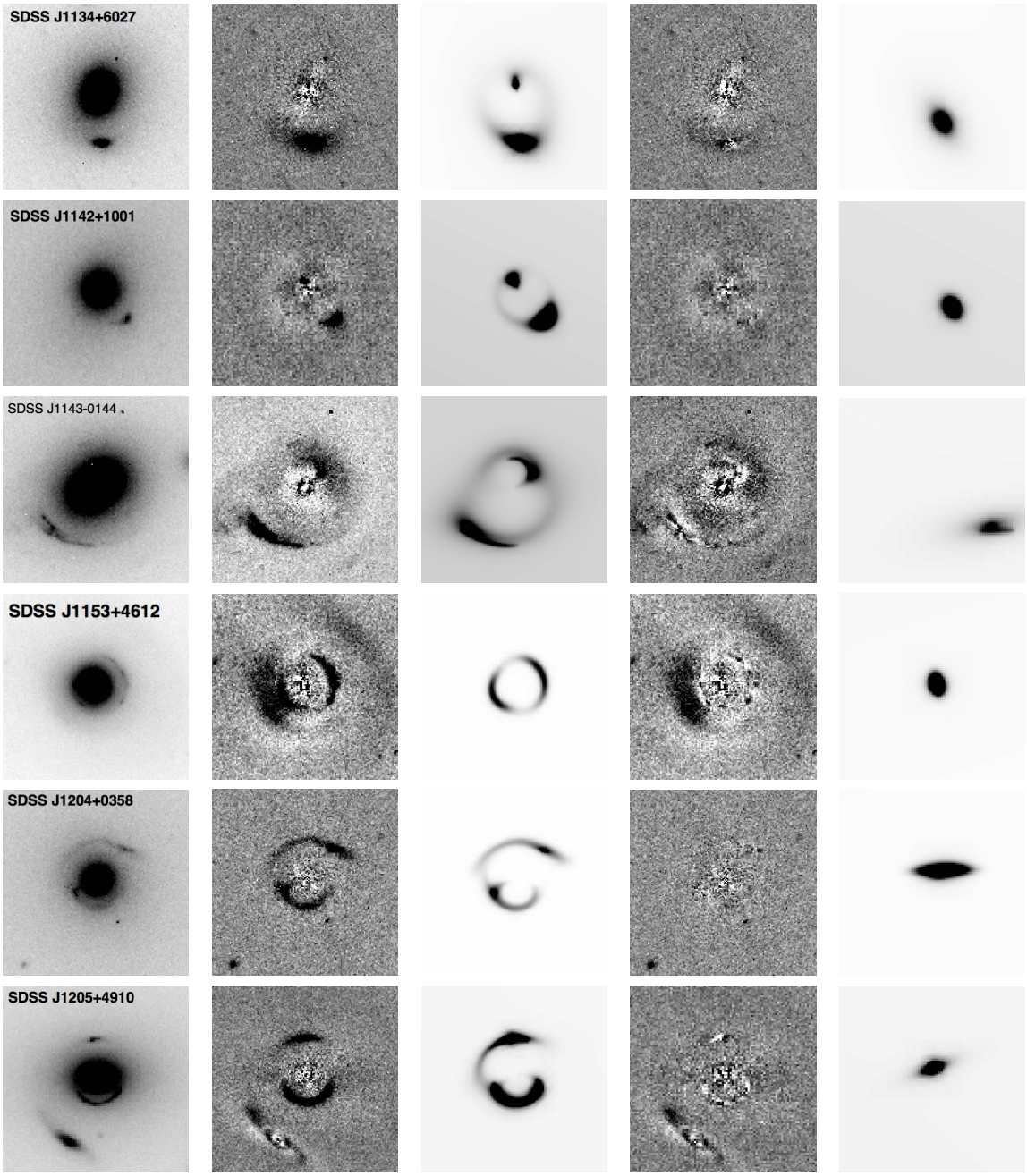

Figure B.6 LENSFIT models of SLACS galaxy-scale gravitational lenses. *From left to right*: ACS-F814W image of the SLACS lens; ACS PSF lens galaxy model subtracted F814W image showing the lensed features; predictions of the lensed features from the best-fit SIE mass model; complete lens-model on the image plane including the light profile of the lens galaxy and the "double-residual" image after subtracting the ACS PSF convolved lens model from the F814W image. All images are $7\farcs5 \times 7\farcs5$.

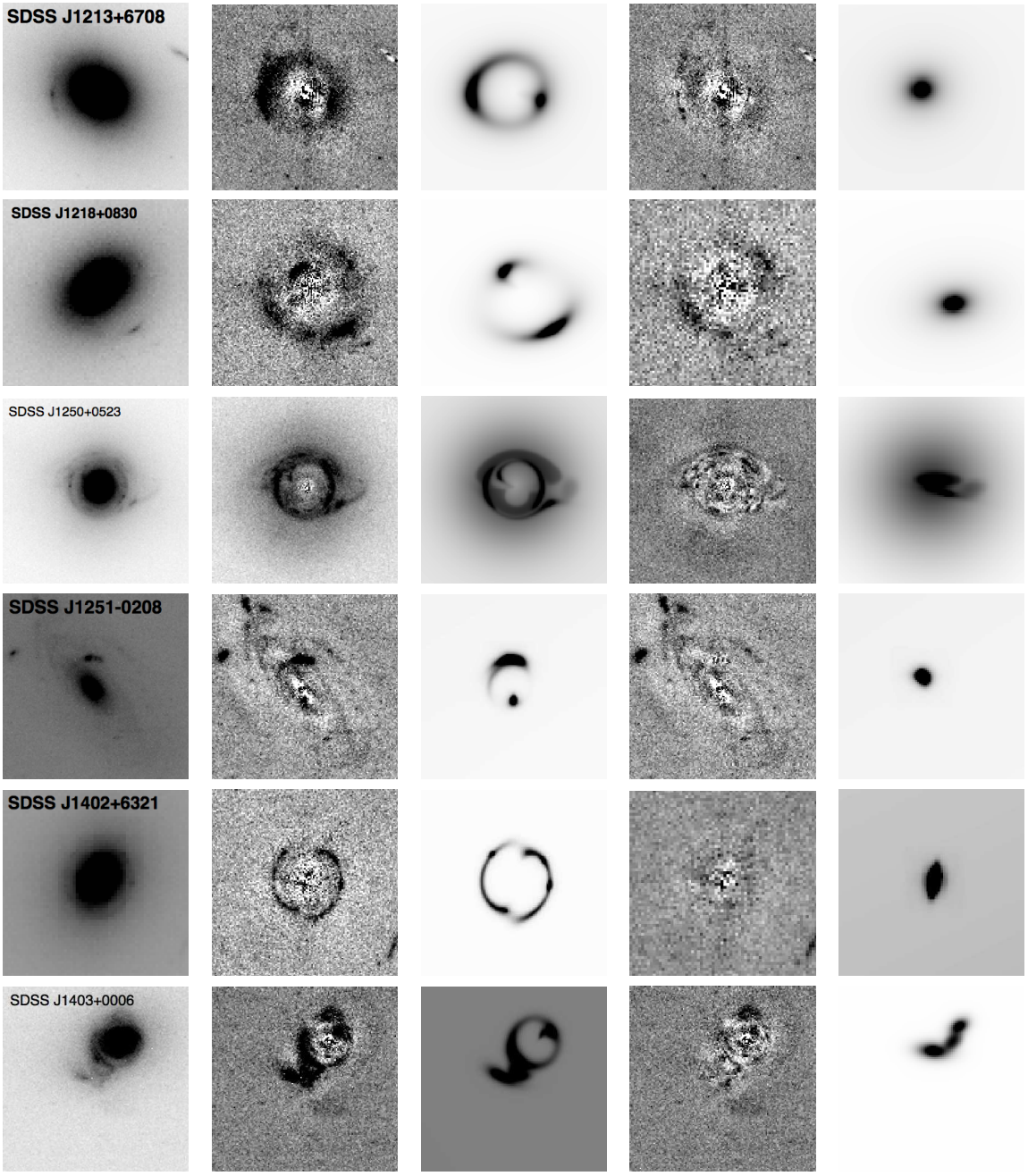

Figure B.7 LENSFIT models of SLACS galaxy-scale gravitational lenses. *From left to right*: ACS-F814W image of the SLACS lens; ACS PSF lens galaxy model subtracted F814W image showing the lensed features; predictions of the lensed features from the best-fit SIE mass model; complete lens-model on the image plane including the light profile of the lens galaxy and the "double-residual" image after subtracting the ACS PSF convolved lens model from the F814W image. All images are $7\farcs5 \times 7\farcs5$.

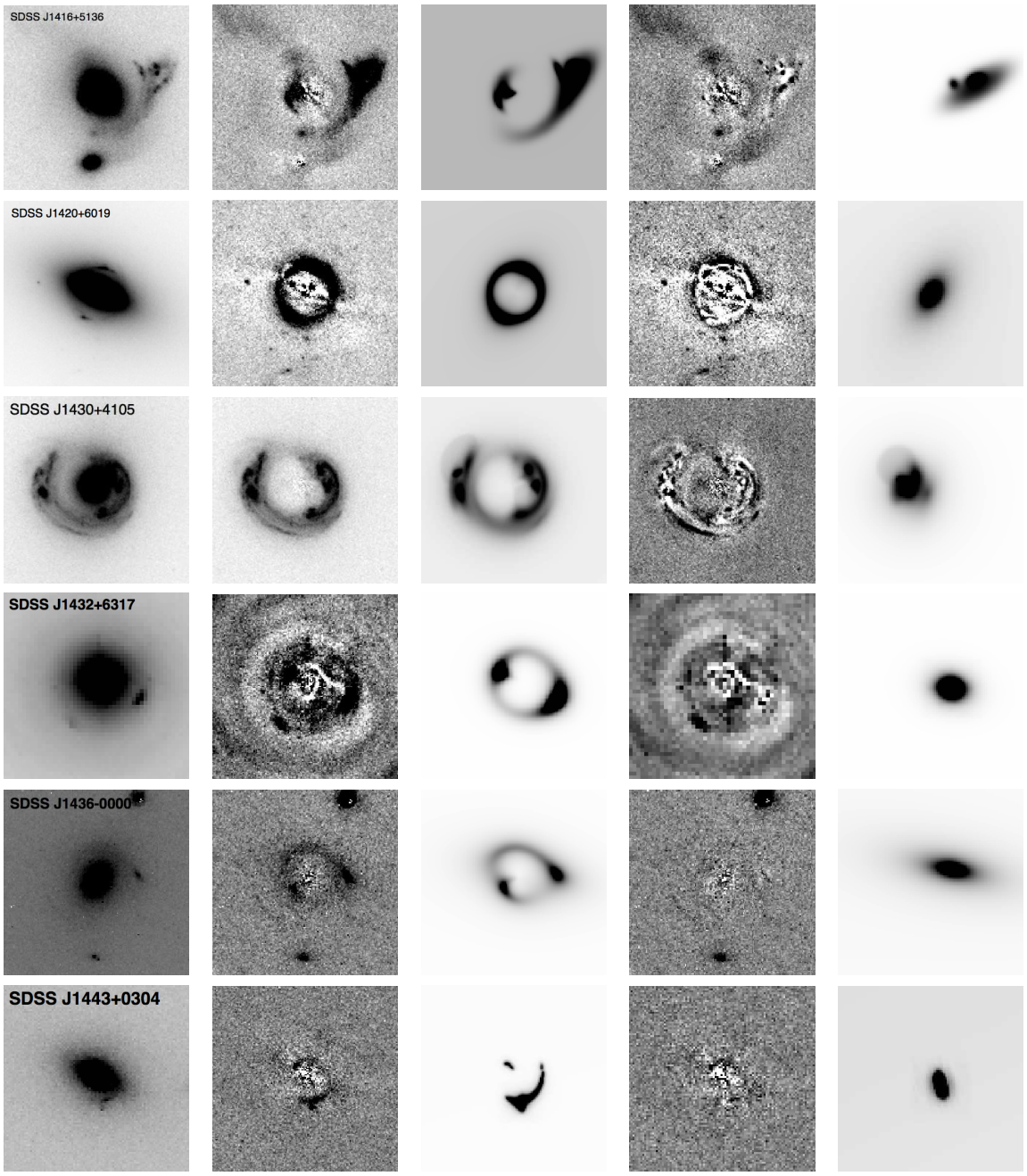

Figure B.8 LENSFIT models of SLACS galaxy-scale gravitational lenses. *From left to right*: ACS-F814W image of the SLACS lens; ACS PSF lens galaxy model subtracted F814W image showing the lensed features; predictions of the lensed features from the best-fit SIE mass model; complete lens-model on the image plane including the light profile of the lens galaxy and the "double-residual" image after subtracting the ACS PSF convolved lens model from the F814W image. All images are $7\farcs5 \times 7\farcs5$.

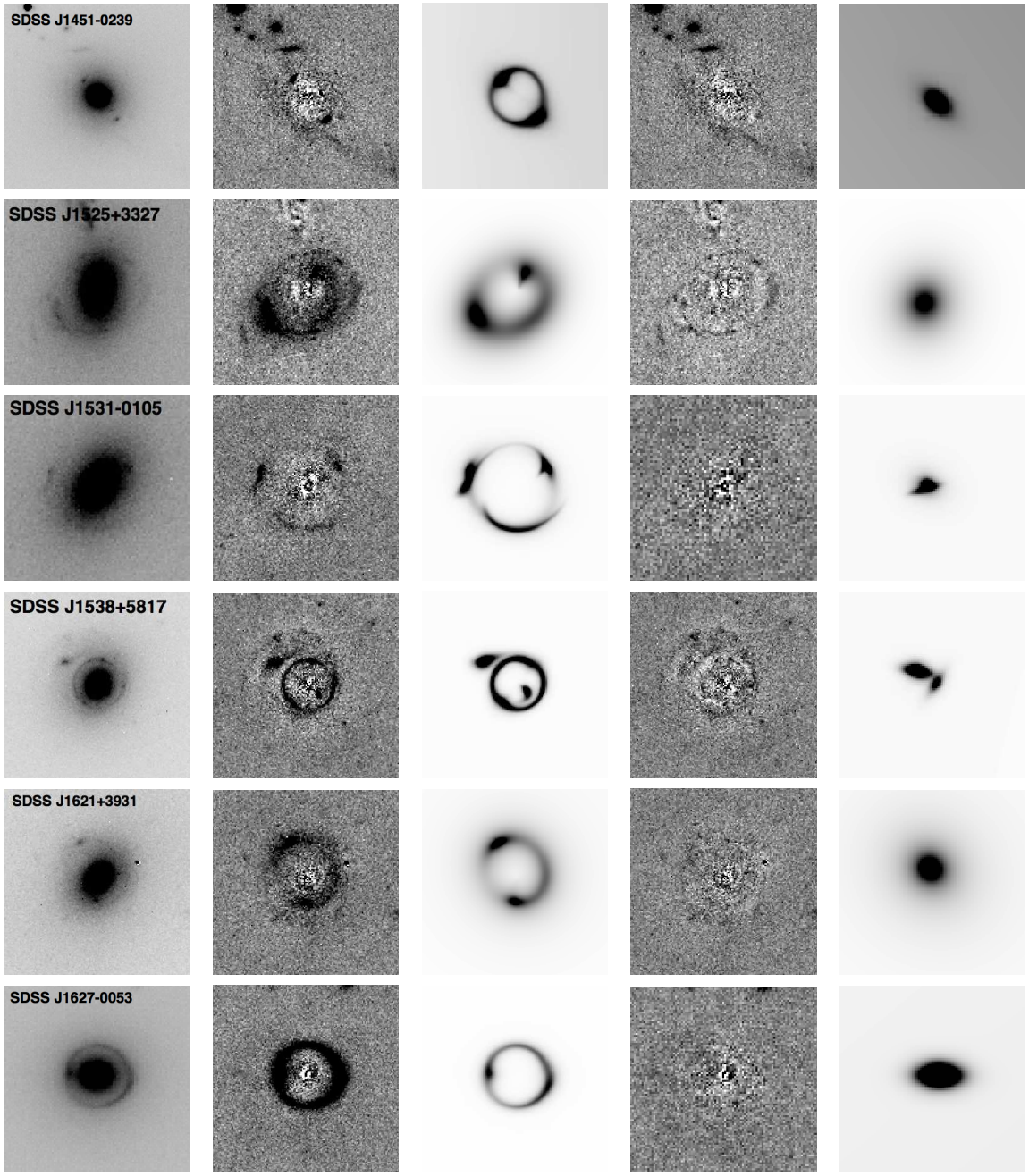

Figure B.9 LENSFIT models of SLACS galaxy-scale gravitational lenses. *From left to right*: ACS-F814W image of the SLACS lens; ACS PSF lens galaxy model subtracted F814W image showing the lensed features; predictions of the lensed features from the best-fit SIE mass model; complete lens-model on the image plane including the light profile of the lens galaxy and the "double-residual" image after subtracting the ACS PSF convolved lens model from the F814W image. All images are $7\farcs5 \times 7\farcs5$.

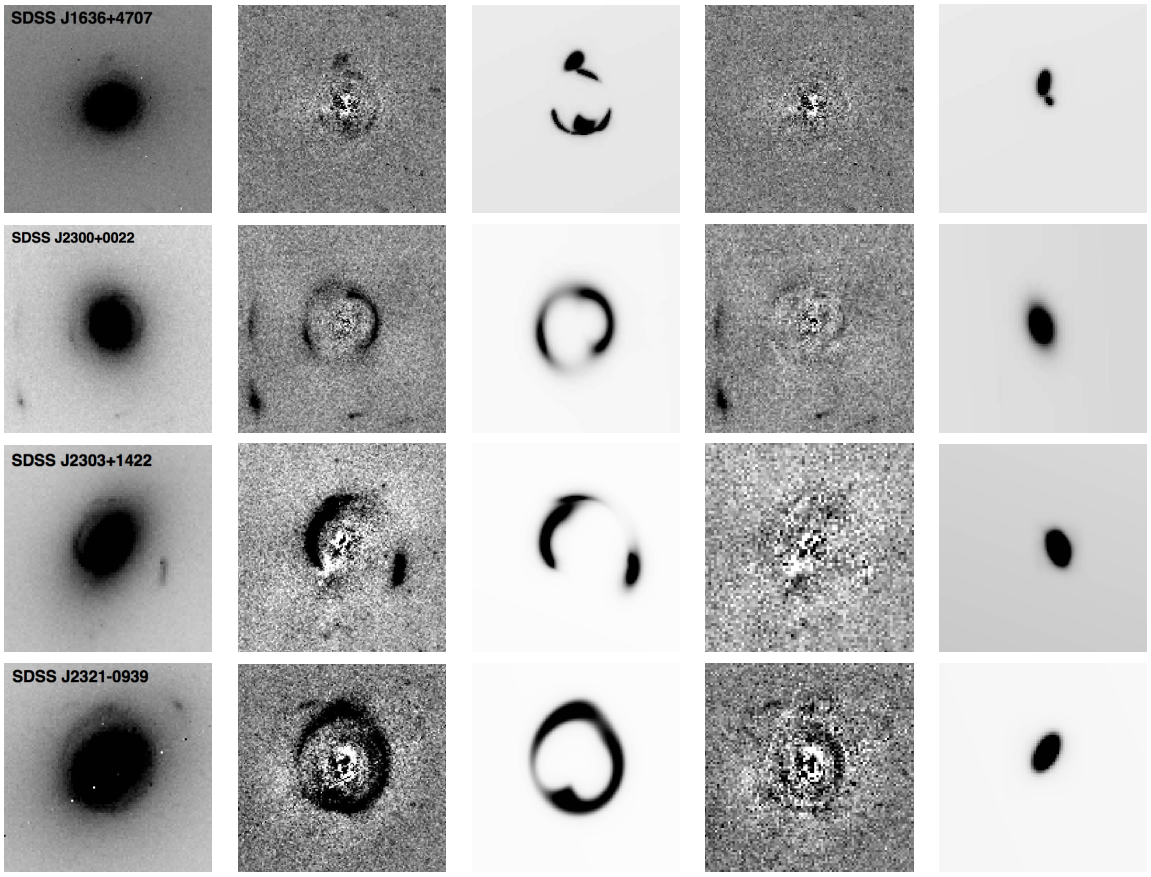

Figure B.10 LENSFIT models of SLACS galaxy-scale gravitational lenses. *From left to right*: ACS-F814W image of the SLACS lens; ACS PSF lens galaxy model subtracted F814W image showing the lensed features; predictions of the lensed features from the best-fit SIE mass model; complete lens-model on the image plane including the light profile of the lens galaxy and the "double-residual" image after subtracting the ACS PSF convolved lens model from the F814W image. All images are $7\farcs5 \times 7\farcs5$.

Bibliography

Abraham, R. G., Tanvir, N. R., Santiago, B. X., Ellis, R. S., Glazebrook, K., & van den Bergh, S. 1996, MNRAS, 279, L47

Adams, F. C., Graff, D. S., Mbonye, M., & Richstone, D. O. 2003, ApJ, 591, 125

Adams, F. C., Graff, D. S., & Richstone, D. O. 2001, ApJ, 551, L31

Allam, S. S., Tucker, D. L., Lin, H., Diehl, H. T., Annis, J., Buckley-Geer, E. J., & Frieman, J. A. 2007, ApJ, 662, L51

Auger, M. W., Treu, T., Bolton, A. S., Gavazzi, R., Koopmans, L. V. E., Marshall, P. J., Bundy, K., & Moustakas, L. A. 2009, ApJ, 705, 1099

Auger, M. W., Treu, T., Bolton, A. S., Gavazzi, R., Koopmans, L. V. E., Marshall, P. J., Moustakas, L. A., & Burles, S. 2010, ApJ, 724, 511

Baes, M., Buyle, P., Hau, G. K. T., & Dejonghe, H. 2003, MNRAS, 341, L44

Bandara, K., Crampton, D., & Simard, L. 2009, ApJ, 704, 1135

Barden, M., Rix, H.-W., Somerville, R. S., Bell, E. F., Häußler, B., Peng, C. Y., Borch, A., Beckwith, S. V. W., Caldwell, J. A. R., Heymans, C., Jahnke, K., Jogee, S., McIntosh, D. H., Meisenheimer, K., Sánchez, S. F., Wisotzki, L., & Wolf, C. 2005, ApJ, 635, 959

Beckwith, S. V. W., Stiavelli, M., Koekemoer, A. M., Caldwell, J. A. R., Ferguson, H. C., Hook, R., Lucas, R. A., Bergeron, L. E., Corbin, M., Jogee, S., Panagia, N., Robberto, M., Royle, P., Somerville, R. S., & Sosey, M. 2006, AJ, 132, 1729

Belokurov, V., Evans, N. W., Moiseev, A., King, L. J., Hewett, P. C., Pettini, M., Wyrzykowski, L., McMahon, R. G., Smith, M. C., Gilmore, G., Sanchez, S. F., Udalski, A., Koposov, S., Zucker, D. B., & Walcher, C. J. 2007, ApJ, 671, L9

Bernardi, M., Nichol, R. C., Sheth, R. K., Miller, C. J., & Brinkmann, J. 2006, AJ, 131, 1288

Bertin, E. & Arnouts, S. 1996, A&AS, 117, 393

Bian, F., Fan, X., Bechtold, J., McGreer, I. D., Just, D. W., Sand, D. J., Green, R. F., Thompson, D., Peng, C. Y., Seifert, W., Ageorges, N., Juette, M., Knierim, V., & Buschkamp, P. 2010, ApJ, 725, 1877

Bolton, A. S., Burles, S., Koopmans, L. V. E., Treu, T., Gavazzi, R., Moustakas, L. A., Wayth, R., & Schlegel, D. J. 2008a, ApJ, 682, 964

Bolton, A. S., Burles, S., Koopmans, L. V. E., Treu, T., & Moustakas, L. A. 2006, ApJ, 638, 703

Bolton, A. S., Burles, S., Schlegel, D. J., Eisenstein, D. J., & Brinkmann, J. 2004, AJ, 127, 1860

Bolton, A. S., Treu, T., Koopmans, L. V. E., Gavazzi, R., Moustakas, L. A., Burles, S., Schlegel, D. J., & Wayth, R. 2008b, ApJ, 684, 248

Bradley, L. D., Bouwens, R. J., Ford, H. C., Illingworth, G. D., Jee, M. J., Benítez, N., Broadhurst, T. J., Franx, M., Frye, B. L., Infante, L., Motta, V., Rosati, P., White, R. L., & Zheng, W. 2008, ApJ, 678, 647

Brooks, A. M., Solomon, A. R., Governato, F., McCleary, J., MacArthur, L. A., Brook, C. B. A., Jonsson, P., Quinn, T. R., & Wadsley, J. 2011, ApJ, 728, 51

Brownstein, J. R., Bolton, A. S., Schlegel, D. J., Eisenstein, D. J., Kochanek, C. S., Connolly, N., Maraston, C., Pandey, P., Seitz, S., Wake, D. A., Wood-Vasey, W. M., Brinkmann, J., Schneider, D. P., & Weaver, B. A. 2012, ApJ, 744, 41

Bullock, J. S., Kolatt, T. S., Sigad, Y., Somerville, R. S., Kravtsov, A. V., Klypin, A. A., Primack, J. R., & Dekel, A. 2001, MNRAS, 321, 559

Buyle, P., Ferrarese, L., Gentile, G., Dejonghe, H., Baes, M., & Klein, U. 2006, MNRAS, 373, 700

Cabanac, R. A., Alard, C., Dantel-Fort, M., Fort, B., Gavazzi, R., Gomez, P., Kneib, J. P., Le Fèvre, O., Mellier, Y., Pello, R., Soucail, G., Sygnet, J. F., & Valls-Gabaud, D. 2007, A&A, 461, 813

Cattaneo, A. 2001, MNRAS, 324, 128

Cattaneo, A., Haehnelt, M. G., & Rees, M. J. 1999, MNRAS, 308, 77

Courteau, S. 1997, AJ, 114, 2402

Courteau, S., McDonald, M., Widrow, L. M., & Holtzman, J. 2007, ApJ, 655, L21

Crampton, D. & Simard, L. 2006, in Society of Photo-Optical Instrumentation Engineers (SPIE) Conference Series, Vol. 6269, Society of Photo-Optical Instrumentation Engineers (SPIE) Conference Series

Crampton, D., Simard, L., & Silva, D. 2008, in Society of Photo-Optical Instrumentation Engineers (SPIE) Conference Series, Vol. 7014, Society of Photo-Optical Instrumentation Engineers (SPIE) Conference Series

Cresci, G., Hicks, E. K. S., Genzel, R., Schreiber, N. M. F., Davies, R., Bouché, N., Buschkamp, P., Genel, S., Shapiro, K., Tacconi, L., Sommer-Larsen, J., Burkert, A., Eisenhauer, F., Gerhard, O., Lutz, D., Naab, T., Sternberg, A., Cimatti, A., Daddi, E., Erb, D. K., Kurk, J., Lilly, S. L., Renzini, A., Shapley, A., Steidel, C. C., & Caputi, K. 2009, ApJ, 697, 115

Croton, D. J. 2009, MNRAS, 394, 1109

Croton, D. J., Springel, V., White, S. D. M., De Lucia, G., Frenk, C. S., Gao, L., Jenkins, A., Kauffmann, G., Navarro, J. F., & Yoshida, N. 2006, MNRAS, 365, 11

Dawson, K. S., Schlegel, D. J., Ahn, C. P., Anderson, S. F., Aubourg, E., Bailey, S., Barkhouser, R. H., Bautista, J. E., Beifiori, A., Berlind, A. A., Bhardwaj, V., Bizyaev, D., Blake, C. H., Blanton, M. R., Blomqvist, M., Bolton, A. S., Borde, A., Bovy, J., Brandt, W. N., Brewington, H., Brinkmann, J., Brown, P. J., Brownstein, J. R., Bundy, K., Busca, N. G., Carithers, W., Carnero, A. R., Carr, M. A., Chen, Y., Comparat, J., Connolly, N., Cope, F., Croft, R. A. C., Cuesta, A. J., da Costa, L. N., Davenport, J. R. A., Delubac, T., de Putter, R., Dhital, S., Ealet, A., Ebelke, G. L., Eisenstein, D. J., Escoffier, S., Fan, X., Filiz Ak, N., Finley, H., Font-Ribera, A., Genova-Santos, R., Gunn, J. E., Guo, H., Haggard, D., Hall, P. B., Hamilton, J.-C., Harris, B., Harris, D. W., Ho, S., Hogg, D. W., Holder, D., Honscheid, K., Huehnerhoff, J., Jordan, B., Jordan, W. P., Kauffmann, G., Kazin, E. A., Kirkby, D., Klaene, M. A., Kneib, J.-P., Le Goff, J.-M., Lee, K.-G., Long,

D. C., Loomis, C. P., Lundgren, B., Lupton, R. H., Maia, M. A. G., Makler, M., Malanushenko, E., Malanushenko, V., Mandelbaum, R., Manera, M., Maraston, C., Margala, D., Masters, K. L., McBride, C. K., McDonald, P., McGreer, I. D., Mena, O., Miralda-Escude, J., Montero-Dorta, A. D., Montesano, F., Muna, D., Myers, A. D., Naugle, T., Nichol, R. C., Noterdaeme, P., Olmstead, M. D., Oravetz, A., Oravetz, D. J., Owen, R., Padmanabhan, N., Palanque-Delabrouille, N., Pan, K., Parejko, J. K., Paris, I., Percival, W. J., Perez-Fournon, I., Perez-Rafols, I., Petitjean, P., Pfaffenberger, R., Pforr, J., Pieri, M. M., Prada, F., Price-Whelan, A. M., Raddick, M. J., Rebolo, R., Rich, J., Richards, G. T., Rockosi, C. M., Roe, N. A., Ross, A. J., Ross, N. P., Rossi, G., Rubino-Martin, J. A., Samushia, L., Sanchez, A. G., Sayres, C., Schmidt, S. J., Schneider, D. P., Scoccola, C. G., Seo, H.-J., Shelden, A., Sheldon, E., Shen, Y., Shu, Y., Slosar, A., Smee, S. A., Snedden, S. A., Stauffer, F., Steele, O., Strauss, M. A., Suzuki, N., Swanson, M. E. C., Tal, T., Tanaka, M., Thomas, D., Tinker, J. L., Tojeiro, R., Tremonti, C. A., Vargas Magana, M., Verde, L., Viel, M., Wake, D. A., Watson, M., Weaver, B. A., Weinberg, D. H., Weiner, B. J., West, A. A., White, M., Wood-Vasey, W. M., Yeche, C., Zehavi, I., Zhao, G.-B., & Zheng, Z. 2012, ArXiv e-prints

Di Matteo, T., Croft, R. A. C., Springel, V., & Hernquist, L. 2003, ApJ, 593, 56

Di Matteo, T., Springel, V., & Hernquist, L. 2005, Nature, 433, 604

Djorgovski, S. & Davis, M. 1987, ApJ, 313, 59

Dobler, G., Keeton, C. R., Bolton, A. S., & Burles, S. 2008, ApJ, 685, 57

Dressler, A., Lynden-Bell, D., Burstein, D., Davies, R. L., Faber, S. M., Terlevich, R., & Wegner, G. 1987, ApJ, 313, 42

Dutton, A. A., van den Bosch, F. C., Dekel, A., & Courteau, S. 2007, ApJ, 654, 27

Dutton, A. A., van den Bosch, F. C., Faber, S. M., Simard, L., Kassin, S. A., Koo, D. C., Bundy, K., Huang, J., Weiner, B. J., Cooper, M. C., Newman, J. A., Mozena, M., & Koekemoer, A. M. 2011, MNRAS, 410, 1660

Dye, S. & Warren, S. 2008, in IAU Symposium, Vol. 244, IAU Symposium, ed. J. Davies & M. Disney, 26–34

Dye, S. & Warren, S. J. 2005, ApJ, 623, 31

Eisenstein, D. J., Annis, J., Gunn, J. E., Szalay, A. S., Connolly, A. J., Nichol, R. C., Bahcall, N. A., Bernardi, M., Burles, S., Castander, F. J., Fukugita, M., Hogg, D. W., Ivezić, Ž., Knapp, G. R., Lupton, R. H., Narayanan, V., Postman, M., Reichart, D. E., Richmond, M., Schneider, D. P., Schlegel, D. J., Strauss, M. A., SubbaRao, M., Tucker, D. L., Vanden Berk, D., Vogeley, M. S., Weinberg, D. H., & Yanny, B. 2001, AJ, 122, 2267

El-Zant, A. A., Shlosman, I., Begelman, M. C., & Frank, J. 2003, ApJ, 590, 641

Epinat, B., Contini, T., Le Fèvre, O., Vergani, D., Garilli, B., Amram, P., Queyrel, J., Tasca, L., & Tresse, L. 2009, A&A, 504, 789

Faber, S. M., Willmer, C. N. A., Wolf, C., Koo, D. C., Weiner, B. J., Newman, J. A., Im, M., Coil, A. L., Conroy, C., Cooper, M. C., Davis, M., Finkbeiner, D. P., Gerke, B. F., Gebhardt, K., Groth, E. J., Guhathakurta, P., Harker, J., Kaiser, N., Kassin, S., Kleinheinrich, M., Konidaris, N. P., Kron, R. G., Lin, L., Luppino, G., Madgwick, D. S., Meisenheimer, K., Noeske, K. G., Phillips, A. C., Sarajedini, V. L., Schiavon, R. P., Simard, L., Szalay, A. S., Vogt, N. P., & Yan, R. 2007, ApJ, 665, 265

Fall, S. M. & Efstathiou, G. 1980, MNRAS, 193, 189

Fassnacht, C. D., Pearson, T. J., Readhead, A. C. S., Browne, I. W. A., Koopmans, L. V. E., Myers, S. T., & Wilkinson, P. N. 1999, ApJ, 527, 498

Faure, C., Anguita, T., Alloin, D., Bundy, K., Finoguenov, A., Leauthaud, A., Knobel, C., Kneib, J.-P., Jullo, E., Ilbert, O., Koekemoer, A. M., Capak, P., Scoville, N., & Tasca, L. A. M. 2011, A&A, 529, A72

Ferrarese, L. 2002, ApJ, 578, 90

Ferrarese, L., Côté, P., Jordán, A., Peng, E. W., Blakeslee, J. P., Piatek, S., Mei, S., Merritt, D., Milosavljević, M., Tonry, J. L., & West, M. J. 2006, ApJS, 164, 334

Ferrarese, L. & Ford, H. 2005, Space Sci. Rev., 116, 523

Ferrarese, L. & Merritt, D. 2000, ApJ, 539, L9

Fisher, D. B. & Drory, N. 2008, AJ, 136, 773

Förster Schreiber, N. M., Genzel, R., Bouché, N., Cresci, G., Davies, R., Buschkamp, P., Shapiro, K., Tacconi, L. J., Hicks, E. K. S., Genel, S., Shapley, A. E., Erb, D. K., Steidel, C. C., Lutz, D., Eisenhauer, F., Gillessen, S., Sternberg, A., Renzini, A., Cimatti, A., Daddi, E., Kurk, J., Lilly, S., Kong, X., Lehnert, M. D., Nesvadba, N., Verma, A., McCracken, H., Arimoto, N., Mignoli, M., & Onodera, M. 2009, ApJ, 706, 1364

Förster Schreiber, N. M., Genzel, R., Lehnert, M. D., Bouché, N., Verma, A., Erb, D. K., Shapley, A. E., Steidel, C. C., Davies, R., Lutz, D., Nesvadba, N., Tacconi, L. J., Eisenhauer, F., Abuter, R., Gilbert, A., Gillessen, S., & Sternberg, A. 2006, ApJ, 645, 1062

Gavazzi, R., Treu, T., Koopmans, L. V. E., Bolton, A. S., Moustakas, L. A., Burles, S., & Marshall, P. J. 2008, ApJ, 677, 1046

Gavazzi, R., Treu, T., Marshall, P. J., Brault, F., & Ruff, A. 2012, ArXiv e-prints

Gavazzi, R., Treu, T., Rhodes, J. D., Koopmans, L. V. E., Bolton, A. S., Burles, S., Massey, R. J., & Moustakas, L. A. 2007, ApJ, 667, 176

Gebhardt, K., Bender, R., Bower, G., Dressler, A., Faber, S. M., Filippenko, A. V., Green, R., Grillmair, C., Ho, L. C., Kormendy, J., Lauer, T. R., Magorrian, J., Pinkney, J., Richstone, D., & Tremaine, S. 2000, ApJ, 539, L13

Genzel, R., Newman, S., Jones, T., Förster Schreiber, N. M., Shapiro, K., Genel, S., Lilly, S. J., Renzini, A., Tacconi, L. J., Bouché, N., Burkert, A., Cresci, G., Buschkamp, P., Carollo, C. M., Ceverino, D., Davies, R., Dekel, A., Eisenhauer, F., Hicks, E., Kurk, J., Lutz, D., Mancini, C., Naab, T., Peng, Y., Sternberg, A., Vergani, D., & Zamorani, G. 2011, ApJ, 733, 101

Giavalisco, M., Ferguson, H. C., Koekemoer, A. M., Dickinson, M., Alexander, D. M., Bauer, F. E., Bergeron, J., Biagetti, C., Brandt, W. N., Casertano, S., Cesarsky, C., Chatzichristou, E., Conselice, C., Cristiani, S., Da Costa, L., Dahlen, T., de Mello, D., Eisenhardt, P., Erben, T., Fall, S. M., Fassnacht, C., Fosbury, R., Fruchter, A., Gardner, J. P., Grogin, N., Hook, R. N., Hornschemeier, A. E., Idzi, R., Jogee, S., Kretchmer, C., Laidler, V., Lee, K. S., Livio, M., Lucas, R., Madau, P., Mobasher, B., Moustakas, L. A., Nonino, M., Padovani, P., Papovich, C., Park, Y., Ravindranath, S., Renzini, A., Richardson, M., Riess, A., Rosati, P., Schirmer,

M., Schreier, E., Somerville, R. S., Spinrad, H., Stern, D., Stiavelli, M., Strolger, L., Urry, C. M., Vandame, B., Williams, R., & Wolf, C. 2004, ApJ, 600, L93

Gnedin, O. Y., Kravtsov, A. V., Klypin, A. A., & Nagai, D. 2004, ApJ, 616, 16

Graham, A. W. & Driver, S. P. 2007, ApJ, 655, 77

Graham, A. W., Erwin, P., Caon, N., & Trujillo, I. 2001, ApJ, 563, L11

Graham, A. W. & Guzmán, R. 2003, AJ, 125, 2936

Gültekin, K., Richstone, D. O., Gebhardt, K., Lauer, T. R., Tremaine, S., Aller, M. C., Bender, R., Dressler, A., Faber, S. M., Filippenko, A. V., Green, R., Ho, L. C., Kormendy, J., Magorrian, J., Pinkney, J., & Siopis, C. 2009, ApJ, 698, 198

Haehnelt, M. G. & Kauffmann, G. 2000, MNRAS, 318, L35

Haehnelt, M. G., Natarajan, P., & Rees, M. J. 1998, MNRAS, 300, 817

Halkola, A., Hildebrandt, H., Schrabback, T., Lombardi, M., Bradač, M., Erben, T., Schneider, P., & Wuttke, D. 2008, A&A, 481, 65

Hall, P. B., Yee, H. K. C., Lin, H., Morris, S. L., Gladders, M. D., Carlberg, R. G., Patton, D. R., Sawicki, M., Shepherd, C. W., & Wirth, G. D. 2000, AJ, 120, 1660

Häussler, B., McIntosh, D. H., Barden, M., Bell, E. F., Rix, H.-W., Borch, A., Beckwith, S. V. W., Caldwell, J. A. R., Heymans, C., Jahnke, K., Jogee, S., Koposov, S. E., Meisenheimer, K., Sánchez, S. F., Somerville, R. S., Wisotzki, L., & Wolf, C. 2007, ApJS, 172, 615

Hewett, P. C., Warren, S. J., Willis, J. P., Bland-Hawthorn, J., & Lewis, G. F. 2000, in Astronomical Society of the Pacific Conference Series, Vol. 195, Imaging the Universe in Three Dimensions, ed. W. van Breugel & J. Bland-Hawthorn, 94

Hewitt, J. N., Turner, E. L., Schneider, D. P., Burke, B. F., & Langston, G. I. 1988, Nature, 333, 537

Hopkins, A. M., Miller, C. J., Nichol, R. C., Connolly, A. J., Bernardi, M., Gómez, P. L., Goto, T., Tremonti, C. A., Brinkmann, J., Ivezić, Ž., & Lamb, D. Q. 2003, ApJ, 599, 971

Hopkins, P. F., Hernquist, L., Cox, T. J., Di Matteo, T., Martini, P., Robertson, B., & Springel, V. 2005a, ApJ, 630, 705

Hopkins, P. F., Hernquist, L., Cox, T. J., Di Matteo, T., Robertson, B., & Springel, V. 2005b, ApJ, 630, 716

Huchra, J., Gorenstein, M., Kent, S., Shapiro, I., Smith, G., Horine, E., & Perley, R. 1985, AJ, 90, 691

Inada, N., Oguri, M., Shin, M.-S., Kayo, I., Strauss, M. A., Morokuma, T., Schneider, D. P., Becker, R. H., Bahcall, N. A., & York, D. G. 2009, AJ, 137, 4118

Jee, M. J., Blakeslee, J. P., Sirianni, M., Martel, A. R., White, R. L., & Ford, H. C. 2007, PASP, 119, 1403

Jerjen, H., Binggeli, B., & Freeman, K. C. 2000, AJ, 119, 593

Johnston, D. E., Richards, G. T., Frieman, J. A., Keeton, C. R., Strauss, M. A., Knapp, G. R., Becker, R. H., White, R. L., Johnson, E. T., Ma, Z., SubbaRao, M., Bahcall, N. A., Bernardi, M., Brinkmann, J., Eisenstein, D. J., Fukugita, M., Hall, P. B., Inada, N., Pindor, B., Schlegel, D. J., Scranton, R., Sheldon, E. S., Schneider, D. P., Szalay, A. S., & York, D. G. 2003, AJ, 126, 2281

Jones, T. A., Swinbank, A. M., Ellis, R. S., Richard, J., & Stark, D. P. 2010, MNRAS, 404, 1247

Jorgensen, I., Franx, M., & Kjaergaard, P. 1995, MNRAS, 276, 1341

Kanwar, A., Simard, L., Schade, D., & Gwyn, S. D. J. 2008, ApJ, 682, 907

Keeton, C. R. 2001a, ArXiv Astrophysics e-prints

—. 2001b, ArXiv Astrophysics e-prints

Keeton, C. R. & Kochanek, C. S. 1998, ApJ, 495, 157

Kennicutt, Jr., R. C. 1992, ApJ, 388, 310

—. 1998, ApJ, 498, 541

King, L. J., Jackson, N., Blandford, R. D., Bremer, M. N., Browne, I. W. A., de Bruyn, A. G., Fassnacht, C., Koopmans, L., Marlow, D., & Wilkinson, P. N. 1998, MNRAS, 295, L41

Kochanek, C. S., Keeton, C. R., & McLeod, B. A. 2001, ApJ, 547, 50

Koekemoer, A. M., Fruchter, A. S., Hook, R. N., & Hack, W. 2003, in The 2002 HST Calibration Workshop : Hubble after the Installation of the ACS and the NICMOS Cooling System, Proceedings of a Workshop held at the Space Telescope Science Institute, Baltimore, Maryland, October 17 and 18, 2002. Edited by Santiago Arribas, Anton Koekemoer, and Brad Whitmore. Baltimore, MD: Space Telescope Science Institute, 2003., p.337, ed. S. Arribas, A. Koekemoer, & B. Whitmore, 337

Koester, B. P., Gladders, M. D., Hennawi, J. F., Sharon, K., Wuyts, E., Rigby, J. R., Bayliss, M. B., & Dahle, H. 2010, ApJ, 723, L73

Koopmans, L. V. E. 2005, MNRAS, 363, 1136

Koopmans, L. V. E., Treu, T., Bolton, A. S., Burles, S., & Moustakas, L. A. 2006, ApJ, 649, 599

Kormann, R., Schneider, P., & Bartelmann, M. 1994, A&A, 284, 285

Kormendy, J. & Richstone, D. 1995, ARA&A, 33, 581

Krist, J. 1993, in Astronomical Society of the Pacific Conference Series, Vol. 52, Astronomical Data Analysis Software and Systems II, ed. R. J. Hanisch, R. J. V. Brissenden, & J. Barnes, 536

Kubo, J. M., Allam, S. S., Annis, J., Buckley-Geer, E. J., Diehl, H. T., Kubik, D., Lin, H., & Tucker, D. 2009, ApJ, 696, L61

Kubo, J. M., Allam, S. S., Drabek, E., Lin, H., Tucker, D., Buckley-Geer, E. J., Diehl, H. T., Soares-Santos, M., Hao, J., Wiesner, M., West, A., Kubik, D., Annis, J., & Frieman, J. A. 2010, ApJ, 724, L137

Lagattuta, D. J., Vegetti, S., Fassnacht, C. D., Auger, M. W., Koopmans, L. V. E., & McKean, J. P. 2012, MNRAS, 424, 2800

Law, D. R., Steidel, C. C., Erb, D. K., Larkin, J. E., Pettini, M., Shapley, A. E., & Wright, S. A. 2007, ApJ, 669, 929

Lemoine-Busserolle, M. & Lamareille, F. 2010, MNRAS, 402, 2291

Lin, H., Buckley-Geer, E., Allam, S. S., Tucker, D. L., Diehl, H. T., Kubik, D., Kubo, J. M., Annis, J., Frieman, J. A., Oguri, M., & Inada, N. 2009, ApJ, 699, 1242

Lynds, R. & Petrosian, V. 1986, in Bulletin of the American Astronomical Society, Vol. 18, Bulletin of the American Astronomical Society, 1014

Marconi, A. & Hunt, L. K. 2003, ApJ, 589, L21

Marshall, P. J., Treu, T., Melbourne, J., Gavazzi, R., Bundy, K., Ammons, S. M., Bolton, A. S., Burles, S., Larkin, J. E., Le Mignant, D., Koo, D. C., Koopmans, L. V. E., Max, C. E., Moustakas, L. A., Steinbring, E., & Wright, S. A. 2007, ApJ, 671, 1196

McGreer, I. D., Hall, P. B., Fan, X., Bian, F., Inada, N., Oguri, M., Strauss, M. A., Schneider, D. P., & Farnsworth, K. 2010, AJ, 140, 370

McLure, R. J., Jarvis, M. J., Targett, T. A., Dunlop, J. S., & Best, P. N. 2006, MNRAS, 368, 1395

Melbourne, J., Phillips, A. C., Harker, J., Novak, G., Koo, D. C., & Faber, S. M. 2007, ApJ, 660, 81

Mo, H. J., Mao, S., & White, S. D. M. 1998, MNRAS, 295, 319

Monaco, P., Salucci, P., & Danese, L. 2000, MNRAS, 311, 279

More, A., Jahnke, K., More, S., Gallazzi, A., Bell, E. F., Barden, M., & Häußler, B. 2011, ApJ, 734, 69

Moustakas, L. A., Marshall, P., Newman, J. A., Coil, A. L., Cooper, M. C., Davis, M., Fassnacht, C. D., Guhathakurta, P., Hopkins, A., Koekemoer, A., Konidaris, N. P., Lotz, J. M., & Willmer, C. N. A. 2007, ApJ, 660, L31

Narayan, R. & Bartelmann, M. 1999, in Formation of Structure in the Universe, ed. A. Dekel & J. P. Ostriker, 360

Navarro, J. F., Frenk, C. S., & White, S. D. M. 1996, ApJ, 462, 563

Neichel, B., Hammer, F., Puech, M., Flores, H., Lehnert, M., Rawat, A., Yang, Y., Delgado, R., Amram, P., Balkowski, C., Cesarsky, C., Dannerbauer, H., Fuentes-Carrera, I., Guiderdoni, B., Kembhavi, A., Liang, Y. C., Nesvadba, N., Östlin, G.,

Pozzetti, L., Ravikumar, C. D., di Serego Alighieri, S., Vergani, D., Vernet, J., & Wozniak, H. 2008, A&A, 484, 159

Nesvadba, N. P. H., Lehnert, M. D., Davies, R. I., Verma, A., & Eisenhauer, F. 2008, A&A, 479, 67

Newton, E. R., Marshall, P. J., Treu, T., Auger, M. W., Gavazzi, R., Bolton, A. S., Koopmans, L. V. E., & Moustakas, L. A. 2011, ApJ, 734, 104

Peng, C. Y., Ho, L. C., Impey, C. D., & Rix, H.-W. 2002, AJ, 124, 266

—. 2010, AJ, 139, 2097

Peng, C. Y., Impey, C. D., Rix, H.-W., Kochanek, C. S., Keeton, C. R., Falco, E. E., Lehár, J., & McLeod, B. A. 2006, ApJ, 649, 616

Pettini, M. & Pagel, B. E. J. 2004, MNRAS, 348, L59

Pizzella, A., Corsini, E. M., Dalla Bontà, E., Sarzi, M., Coccato, L., & Bertola, F. 2005, ApJ, 631, 785

Press, W. H., Teukolsky, S. A., Vetterling, W. T., & Flannery, B. P. 1992, Numerical recipes in FORTRAN. The art of scientific computing (Cambridge: University Press)

Ravindranath, S., Ferguson, H. C., Conselice, C., Giavalisco, M., Dickinson, M., Chatzichristou, E., de Mello, D., Fall, S. M., Gardner, J. P., Grogin, N. A., Hornschemeier, A., Jogee, S., Koekemoer, A., Kretchmer, C., Livio, M., Mobasher, B., & Somerville, R. 2004, ApJ, 604, L9

Rawat, A., Kembhavi, A. K., Hammer, F., Flores, H., & Barway, S. 2007, A&A, 469, 483

Refsdal, S. 1964, MNRAS, 128, 307

Richard, J., Jones, T., Ellis, R., Stark, D. P., Livermore, R., & Swinbank, M. 2011, MNRAS, 413, 643

Riechers, D. A., Carilli, C. L., Maddalena, R. J., Hodge, J., Harris, A. I., Baker, A. J., Walter, F., Wagg, J., Vanden Bout, P. A., Weiß, A., & Sharon, C. E. 2011, ApJ, 739, L32

Rix, H.-W., Barden, M., Beckwith, S. V. W., Bell, E. F., Borch, A., Caldwell, J. A. R., Häussler, B., Jahnke, K., Jogee, S., McIntosh, D. H., Meisenheimer, K., Peng, C. Y., Sanchez, S. F., Somerville, R. S., Wisotzki, L., & Wolf, C. 2004, ApJS, 152, 163

Robertson, B., Hernquist, L., Cox, T. J., Di Matteo, T., Hopkins, P. F., Martini, P., & Springel, V. 2006, ApJ, 641, 90

Ross, N. R., Assef, R. J., Kochanek, C. S., Falco, E., & Poindexter, S. D. 2009, ApJ, 702, 472

Salucci, P., Swinbank, A. M., Lapi, A., Yegorova, I., Bower, R. G., Smail, I., & Smith, G. P. 2007, MNRAS, 382, 652

Sargent, M. T., Carollo, C. M., Lilly, S. J., Scarlata, C., Feldmann, R., Kampczyk, P., Koekemoer, A. M., Scoville, N., Kneib, J.-P., Leauthaud, A., Massey, R., Rhodes, J., Tasca, L. A. M., Capak, P., McCracken, H. J., Porciani, C., Renzini, A., Taniguchi, Y., Thompson, D. J., & Sheth, K. 2007, ApJS, 172, 434

Schlegel, D. J., Finkbeiner, D. P., & Davis, M. 1998, ApJ, 500, 525

Schneider, P., Ehlers, J., & Falco, E. E. 1992, Gravitational Lenses (Springer-Verlag Berlin Heidelberg New York)

Sersic, J. L. 1968, Atlas de galaxias australes (Cordoba, Argentina: Observatorio Astronomico)

Shen, S., Mo, H. J., White, S. D. M., Blanton, M. R., Kauffmann, G., Voges, W., Brinkmann, J., & Csabai, I. 2003, MNRAS, 343, 978

Silk, J. & Rees, M. J. 1998, A&A, 331, L1

Simard, L., Koo, D. C., Faber, S. M., Sarajedini, V. L., Vogt, N. P., Phillips, A. C., Gebhardt, K., Illingworth, G. D., & Wu, K. L. 1999, ApJ, 519, 563

Simard, L., Mendel, J. T., Patton, D. R., Ellison, S. L., & McConnachie, A. W. 2011, ApJS, 196, 11

Simard, L., Willmer, C. N. A., Vogt, N. P., Sarajedini, V. L., Phillips, A. C., Weiner, B. J., Koo, D. C., Im, M., Illingworth, G. D., & Faber, S. M. 2002, ApJS, 142, 1

Sirianni, M., Martel, A. R., Jee, M. J., van Orsow, D., & Sparks, W. B. 2003, in The 2002 HST Calibration Workshop : Hubble after the Installation of the ACS and the NICMOS Cooling System, Proceedings of a Workshop held at the Space Telescope Science Institute, Baltimore, Maryland, October 17 and 18, 2002. Edited by Santiago Arribas, Anton Koekemoer, and Brad Whitmore. Baltimore, MD: Space Telescope Science Institute, 2003., p.82, ed. S. Arribas, A. Koekemoer, & B. Whitmore, 82

Smail, I., Swinbank, A. M., Richard, J., Ebeling, H., Kneib, J.-P., Edge, A. C., Stark, D., Ellis, R. S., Dye, S., Smith, G. P., & Mullis, C. 2007, ApJ, 654, L33

Smith, G. P., Ebeling, H., Limousin, M., Kneib, J.-P., Swinbank, A. M., Ma, C.-J., Jauzac, M., Richard, J., Jullo, E., Sand, D. J., Edge, A. C., & Smail, I. 2009, ApJ, 707, L163

Soucail, G., Fort, B., Mellier, Y., & Picat, J. P. 1987a, A&A, 172, L14

Soucail, G., Mellier, Y., Fort, B., Mathez, G., & Hammer, F. 1987b, A&A, 184, L7

Springel, V., Di Matteo, T., & Hernquist, L. 2005a, ApJ, 620, L79

—. 2005b, MNRAS, 361, 776

Stark, D. P., Swinbank, A. M., Ellis, R. S., Dye, S., Smail, I. R., & Richard, J. 2008, Nature, 455, 775

Steinmetz, M. & Navarro, J. F. 1999, ApJ, 513, 555

Strauss, M. A., Weinberg, D. H., Lupton, R. H., Narayanan, V. K., Annis, J., Bernardi, M., Blanton, M., Burles, S., Connolly, A. J., Dalcanton, J., Doi, M., Eisenstein, D., Frieman, J. A., Fukugita, M., Gunn, J. E., Ivezić, Ž., Kent, S., Kim, R. S. J., Knapp, G. R., Kron, R. G., Munn, J. A., Newberg, H. J., Nichol, R. C., Okamura, S., Quinn, T. R., Richmond, M. W., Schlegel, D. J., Shimasaku, K., SubbaRao, M., Szalay, A. S., Vanden Berk, D., Vogeley, M. S., Yanny, B., Yasuda, N., York, D. G., & Zehavi, I. 2002, AJ, 124, 1810

Suyu, S. H., Marshall, P. J., Hobson, M. P., & Blandford, R. D. 2006, MNRAS, 371, 983

Tacconi, L. J., Genzel, R., Neri, R., Cox, P., Cooper, M. C., Shapiro, K., Bolatto, A., Bouché, N., Bournaud, F., Burkert, A., Combes, F., Comerford, J., Davis, M., Schreiber, N. M. F., Garcia-Burillo, S., Gracia-Carpio, J., Lutz, D., Naab, T., Omont, A., Shapley, A., Sternberg, A., & Weiner, B. 2010, Nature, 463, 781

Tacconi, L. J., Genzel, R., Smail, I., Neri, R., Chapman, S. C., Ivison, R. J., Blain, A., Cox, P., Omont, A., Bertoldi, F., Greve, T., Förster Schreiber, N. M., Genel, S., Lutz, D., Swinbank, A. M., Shapley, A. E., Erb, D. K., Cimatti, A., Daddi, E., & Baker, A. J. 2008, ApJ, 680, 246

Tacconi, L. J., Neri, R., Chapman, S. C., Genzel, R., Smail, I., Ivison, R. J., Bertoldi, F., Blain, A., Cox, P., Greve, T., & Omont, A. 2006, ApJ, 640, 228

Tremaine, S., Gebhardt, K., Bender, R., Bower, G., Dressler, A., Faber, S. M., Filippenko, A. V., Green, R., Grillmair, C., Ho, L. C., Kormendy, J., Lauer, T. R., Magorrian, J., Pinkney, J., & Richstone, D. 2002, ApJ, 574, 740

Treu, T. 2010, ARA&A, 48, 87

Treu, T., Gavazzi, R., Gorecki, A., Marshall, P. J., Koopmans, L. V. E., Bolton, A. S., Moustakas, L. A., & Burles, S. 2009, ApJ, 690, 670

Treu, T., Koopmans, L. V., Bolton, A. S., Burles, S., & Moustakas, L. A. 2006, ApJ, 640, 662

Treu, T. & Koopmans, L. V. E. 2004, ApJ, 611, 739

Trujillo, I. & Aguerri, J. A. L. 2004, MNRAS, 355, 82

Trujillo, I., Förster Schreiber, N. M., Rudnick, G., Barden, M., Franx, M., Rix, H.-W., Caldwell, J. A. R., McIntosh, D. H., Toft, S., Häussler, B., Zirm, A., van Dokkum, P. G., Labbé, I., Moorwood, A., Röttgering, H., van der Wel, A., van der Werf, P., & van Starkenburg, L. 2006, ApJ, 650, 18

Trujillo, I. & Pohlen, M. 2005, ApJ, 630, L17

Trujillo, I., Rudnick, G., Rix, H.-W., Labbé, I., Franx, M., Daddi, E., van Dokkum, P. G., Förster Schreiber, N. M., Kuijken, K., Moorwood, A., Röttgering, H., van der Wel, A., van der Werf, P., & van Starkenburg, L. 2004, ApJ, 604, 521

Tully, R. B. & Fisher, J. R. 1977, A&A, 54, 661

van Dokkum, P. G. 2001, PASP, 113, 1420

Volonteri, M., Haardt, F., & Madau, P. 2003, ApJ, 582, 559

Walsh, D., Carswell, R. F., & Weymann, R. J. 1979, Nature, 279, 381

Warren, S. J. & Dye, S. 2003, ApJ, 590, 673

Warren, S. J., Lewis, G. F., Hewett, P. C., Møller, P., Shaver, P., & Iovino, A. 1999a, A&A, 343, L35

—. 1999b, A&A, 343, L35

Weiner, B. J., Willmer, C. N. A., Faber, S. M., Harker, J., Kassin, S. A., Phillips, A. C., Melbourne, J., Metevier, A. J., Vogt, N. P., & Koo, D. C. 2006, ApJ, 653, 1049

Willis, J. P., Hewett, P. C., & Warren, S. J. 2005, MNRAS, 363, 1369

Wisnioski, E., Glazebrook, K., Blake, C., Poole, G. B., Green, A. W., Wyder, T., & Martin, C. 2012, MNRAS, 422, 3339

Wisnioski, E., Glazebrook, K., Blake, C., Wyder, T., Martin, C., Poole, G. B., Sharp, R., Couch, W., Kacprzak, G. G., Brough, S., Colless, M., Contreras, C., Croom, S., Croton, D., Davis, T., Drinkwater, M. J., Forster, K., Gilbank, D. G., Gladders, M., Jelliffe, B., Jurek, R. J., Li, I.-H., Madore, B., Pimbblet, K., Pracy, M., Woods, D., & Yee, H. K. C. 2011, MNRAS, 417, 2601

Woo, J.-H., Treu, T., Malkan, M. A., & Blandford, R. D. 2008, ApJ, 681, 925

Wright, S. A., Larkin, J. E., Barczys, M., Erb, D. K., Iserlohe, C., Krabbe, A., Law, D. R., McElwain, M. W., Quirrenbach, A., Steidel, C. C., & Weiss, J. 2007, ApJ, 658, 78

Wyithe, J. S. B. & Loeb, A. 2002, ApJ, 581, 886

—. 2003, ApJ, 595, 614

Wyithe, J. S. B. & Padmanabhan, T. 2006, MNRAS, 372, 1681

York, D. G., Adelman, J., Anderson, Jr., J. E., Anderson, S. F., Annis, J., Bahcall, N. A., Bakken, J. A., Barkhouser, R., Bastian, S., Berman, E., Boroski, W. N., Bracker, S., Briegel, C., Briggs, J. W., Brinkmann, J., Brunner, R., Burles, S., Carey, L., Carr, M. A., Castander, F. J., Chen, B., Colestock, P. L., Connolly, A. J., Crocker, J. H., Csabai, I., Czarapata, P. C., Davis, J. E., Doi, M., Dombeck, T., Eisenstein, D., Ellman, N., Elms, B. R., Evans, M. L., Fan, X., Federwitz, G. R., Fiscelli, L., Friedman, S., Frieman, J. A., Fukugita, M., Gillespie, B., Gunn, J. E., Gurbani, V. K., de Haas, E., Haldeman, M., Harris, F. H., Hayes, J., Heckman, T. M., Hennessy, G. S., Hindsley, R. B., Holm, S., Holmgren, D. J., Huang, C.-h., Hull, C., Husby, D., Ichikawa, S.-I., Ichikawa, T., Ivezić, Ž., Kent, S., Kim, R. S. J., Kinney, E., Klaene, M., Kleinman, A. N., Kleinman, S., Knapp, G. R., Korienek, J., Kron, R. G., Kunszt, P. Z., Lamb, D. Q., Lee, B., Leger, R. F., Limmongkol, S., Lindenmeyer, C., Long, D. C., Loomis, C., Loveday, J., Lucinio, R., Lupton, R. H., MacKinnon, B., Mannery, E. J., Mantsch, P. M., Margon, B., McGehee, P., McKay, T. A., Meiksin, A., Merelli, A., Monet, D. G., Munn, J. A., Narayanan, V. K., Nash, T., Neilsen, E., Neswold, R., Newberg, H. J., Nichol, R. C., Nicinski, T., Nonino, M., Okada, N., Okamura, S., Ostriker, J. P., Owen, R., Pauls, A. G., Peoples, J., Peterson, R. L., Petravick, D., Pier, J. R., Pope, A., Pordes, R., Prosapio, A., Rechenmacher, R., Quinn, T. R., Richards, G. T., Richmond, M. W., Rivetta, C. H., Rockosi, C. M., Ruthmansdorfer, K., Sandford, D., Schlegel, D. J., Schneider, D. P., Sekiguchi, M., Sergey, G., Shimasaku, K., Siegmund, W. A., Smee, S., Smith, J. A., Snedden, S., Stone, R., Stoughton, C., Strauss, M. A., Stubbs, C., SubbaRao, M., Szalay, A. S., Szapudi, I., Szokoly, G. P., Thakar, A. R., Tremonti, C., Tucker, D. L., Uomoto, A., Vanden Berk, D., Vogeley, M. S., Waddell, P., Wang, S.-i., Watanabe, M., Weinberg, D. H., Yanny, B., Yasuda, N., & SDSS Collaboration. 2000, AJ, 120, 1579

Yuan, T.-T., Kewley, L. J., Swinbank, A. M., & Richard, J. 2012, ArXiv e-prints

Zheng, X. Z., Hammer, F., Flores, H., Assémat, F., & Pelat, D. 2004, A&A, 421, 847

Zitrin, A., Moustakas, J., Bradley, L., Coe, D., Moustakas, L. A., Postman, M., Shu, X., Zheng, W., Benítez, N., Bouwens, R., Broadhurst, T., Ford, H., Host, O., Jouvel, S., Koekemoer, A., Meneghetti, M., Rosati, P., Donahue, M., Grillo, C., Kelson, D., Lemze, D., Medezinski, E., Molino, A., Nonino, M., & Ogaz, S. 2012, ApJ, 747, L9